Investigating the LES strategy for the prediction of soot production in an aero-engine combustor

Livia Pereira Tardelli

Thèse de doctorat

NNT: 2021UPAST018

université PARIS-SACLAY

Investigating the LES strategy for the prediction of soot production in an aero-engine combustor.

Thèse de doctorat de l'Université Paris-Saclay

École doctorale n° 579, Sciences mécaniques et énergétiques, matériaux et géociences (SMEMAG)
Spécialité de doctorat: Combustion
Unité de recherche: Université Paris-Saclay, CNRS, CentraleSupélec, Laboratoire EM2C, 91190, Gif-sur-Yvette, France.
Référent: : CentraleSupélec

Thèse présentée et soutenue en visioconférence, le 8 mars 2021, par

Livia PEREIRA TARDELLI

Composition du jury:

Pascale Domingo Directrice de Recherche, CORIA - CNRS	Rapportrice et Présidente
Bénédicte Cuenot CFD Combustion Project Leader, CERFACS	Rapportrice
Antonio Andreini Assistant Professor, Université dde Florence	Examinateur
Christian Angelberger Adjoint Scientifique Mobilité & Systèmes, IFP Energies Nouvelles	Examinateur
Denis Veynante Directeur de Recherche, EM2C-CNRS	Directeur
Benedetta Franzelli Chargé de Recherche, EM2C-CNRS	Co-encadrante
Nasser Darabiha Professeur, CentraleSupélec, EM2C-CNRS	Co-encadrant

Remerciements

Je tiens en premier lieu à remercier tous les membres de mon jury pour avoir accepté ce rôle. Merci à Pascale Domingo et Bénédicte Cuenot d'avoir endossé les rôles de rapporteuses de mon manuscrit de thèse et pour leurs remarques pertinentes. Je remercie Pascale Domingo d'avoir également accepté la présidence de ce jury. Je tiens aussi à leur remercier pour avoir faire en sorte que la soutenance se passe dans les conditions les plus normales possibles malgré un contexte difficile. Encore merci à Christian Angelberger et Antonio Andreini d'y avoir été examinateurs. Je vous remercie tous pour les échanges enrichissants que nous avons pu avoir lors de la séance de questions. Un grand merci également à Victor Boniou qui m'a aidé à organiser la soutenance en visioconférence en assurant la diffusion et en gérant les petits soucis techniques.

Je voudrais ensuite remercier les trois personnes qui ont constitué l'éncadrement de ma thèse et qu'on contribué énormément à la réalisation de ce travail: Denis, Nasser et Benedetta. Merci à tous les trois d'avoir partagé avec moi vos expériences, merci pour toutes discussions qu'on a eu le long de cette thèse et pour les remarques très pertinents que m'on permis à arriver au but final de cette thèse. Je les remercie également pour leur soutien lors des moments difficiles.

Il me faut également remercier le projet SOPRANO qui a financé ces travaux de recherche. Je remercie également le Grand équipement National en Calcul In-tensif (GENCI), qui m'a donné accès à des ressources de calcul intensif sur le calculateur Occigen du Centre Informatique National de l'Enseignement Supérieur, le mésocentre commun à CentraleSupélec et l'école Normale Paris-Saclay (calculateurs Fusion), financé par le CNRS et la région Île de France; et bien entendu le Centre National de la Recherche Scientifique (CNRS), cotutelle du laboratoire EM2C.

Je tiens ensuite à remercier chaleureusement l'équipe administrative, Nathalie, Brigitte et Noi, pour leur aide, leur soutien et leur amitié. Merci de prendre soin de nous! Je ne peux pas oublier Jean Michel et Sebastian Turgis pour leur disponibilité et gentillesse à régler tous mes soucis informatiques et sur les calculateurs. Je remercie également à Aymeric Vié pour m'avoir donné l'opportunité d'énseigner, ça a été une expérience formidable.

Le doctorat c'est aussi une expérience humaine. J'ai rencontré à l'EM2C des personnes extraordinaires. Je pense particulièrement à Leo, Amanda, Guillaume, Kevin Torres, Suzane, Lorella et Théa qui m'ont accompagnée et soutenue, et qui resteront des amies proches, mais aussi à Pedro qui m'a énormément aidé au début de cette aventure. Merci à tous mes co-bureaux, de Chatenay ou de Saclay, Kevin Prier, Giunio, Amanda, Yacine, Hernando, Victorien d'avoir contribué à une atmosphère à la fois studieuse et conviviale. Merci à mon "deuxième" bureau (Amanda, Davy, Léo, Giampaolo, Jan, Victor, Thea, Lorella_Linda) où je me fournissais en sucreries, beaucoup de café et des moments très joyeux. Un merci spécial à Amanda et Quentin de m'avoir embarqué dans la plus grande aventure sportive de ma vie, le RAID CentraleSupelec. Quelle aventure! Un autre grand merci à Guillaume, pour le beau voyage dans le désert de l'Arizona et de l'Utah lors de l'ASME, merci Arthur d'avoir pu nous rejoindre. Pour finir, je remercie tous les doctorants et post-doctorants que j'ai croisés au cours de ma thèse dans le labo et également mes collègues du projet SOPRANO, spécialement Lucien, Martin, Alexandre et Kevin, avec qui j'ai pu avoir des très bon échanges scientifiques et amicales.

Enfin, j'ai une pensée affectueuse à mes amis du Brèsil (Jaque, Nanda, Gustavo, Carol, Barbara) que sont là depuis toujours malgré 10000 km de distance entre nous. Il me reste à embrasser ceux qui ont largement participé à ma réussite, ma famille. Merci à mes parents Iraci et Sergio et mes deux soeurs Dalila et Camila pour leur soutien et amour. Merci à mes grands-parents Arnaldo et Neirinha qu'ont toujours cru en moi et qui m'ont permis de prendre mon envole. Enfin, merci à Vincent et à notre fille Eva, qu'ont tenu bon à mes côtés tout au long de mon doctorat. Merci pour vos soutiens, votre présence, votre amour, compression et patience.

Abstract

Predicting soot production in industrial systems using a Large Eddy Simulation (LES) approach represents a great challenge for many reasons. First, in-depth knowledge and modeling of the complex physico-chemical processes involved in soot production are still lacking. Second, multiple combustion regimes coexist in technical devices, presenting an additional difficulty for high fidelity simulations. Third, soot particles are confined in very thin structures interacting with turbulence. Because of their size, these structures may not be resolved on the LES grids, so that specific soot subgrid-scale models are required. Finally, the validation of newly developed models is difficult due to the non-linear interactions between such multi-physical phenomena and the massive computational resources required for a reliable statistical representation. In the context of the SOPRANO European project, the main objective of this thesis is to evaluate the reliability of the LES formalism for turbulent sooting flames in an aero-engine model combustor to improve the soot prediction and contribute to the development of low-emission aircraft systems. First, a sectional approach, coupled with detailed chemistry, is evaluated in laminar premixed and non-premixed ethylene-air flames. Although this model provides a good prediction of soot volume fraction and particle size distribution in premixed conditions, it fails in non-premixed flames. Therefore, an improved model is proposed in this thesis for soot growth, enabling the reproduction of the experimental soot yield in both regimes. The second part concerns the LES simulation of an aero-engine model combustor. In this case, a three-equation model is used to describe the solid phase as it provides similar accuracy for a lower CPU cost compared to the sectional approach. First, the reliability of the LES formalism is quantified through statistical analysis. This analysis reveals that numerical convergence is quite challenging to be achieved in the considered burner since it is characterized by a complex flow structure and a highly intermittent soot production. The sensitivity of results to grid resolution is also investigated in three grids with different spatial resolutions. It is found that negligible differences in the gas phase structure can lead to important discrepancies in soot prediction. Then, the impact of soot modeling in soot prediction using LES is investigated. First, the impact of the improved surface reaction model is evaluated. The statistical analysis shows that the maximum soot volume fraction

increases by a factor of three compared to the reference model due to the substantial increase of the surface reaction rates. Finally, the impact of the soot subgrid intermittency model is evaluated. A new strategy based on a unique LES transporting a duplicated set of soot equations is proposed to rigorously investigate soot models. Both sets, one accounting for the soot reference model, the other treated with the model under the scope, experience the same unique temporal and spatial gas phase evolution. Therefore, it is possible to isolate the soot model effects from the uncertainties on gaseous models and numerical sensitivities for a smaller computational cost than parametric studies. Thanks to this approach, the first indications of the soot intermittency model contribution to soot prediction in the investigated burner are proposed. Motivated by the difficulties in evaluating soot model performances in turbulent flames via LES, *a priori* analysis of the soot subgrid intermittency model based on a Direct Numerical Simulation of a turbulent counterflow 2D flame is performed to clarify its ability in describing soot-turbulence-chemistry interactions. This analysis provides first indications of the intermittency model contribution to soot prediction in turbulent flames. Besides, this provides a new database for parametric studies for soot model development.

Résumé

La prédiction de la production des suies dans une chambre de combustion à l'aide d'une approche de type Simulation aux Grandes échelles (Large Eddy Simulation - LES) représente un défi de taille pour plusieurs raisons. La modélisation des processus physico-chimiques impliqués dans la production de ces particules fait encore défaut. Ensuite, dans les dispositifs présentant un intérêt pratique, des régimes de combustion multiples coexistent, ce qui présente une difficulté supplémentaire à la modélisation haute-fidélité de tels phénomènes. De plus, les particules de suies sont confinées dans des structures soumises au transport turbulent. En raison de leur taille, un modèle de sous-maille est nécessaire. Pour finir, la validation de nouveaux modèles est difficile lorsqu'on considère ce type de flamme en raison du couplage non-linéaire entre les différents phénomènes et du besoin d'importantes ressources de calcul pour obtenir une représentation statistique fiable. L'objectif principal de cette thèse, dans le cadre du projet européen SOPRANO, est d'évaluer la fiabilité du formalisme LES pour la prédiction des émissions de particules de suies dans une configuration de type aéronautique et ainsi contribuer au développement de systèmes à faibles émissions. Initialement, un modèle sectionnel couplé à une chimie détaillé est évalué dans des flammes laminaires d'éthylène-air prémélangées et non-prémélangées. Bien qu'il fournisse une bonne prédiction de la fraction volumique des suies dans des conditions prémélangées, il échoue dans des flammes non prémélangées. Un modèle réactionnelle HACA-RC* est ainsi proposé afin d'améliorer la prédiction dans des flammes non-prémélangées. La seconde partie est consacrée à la simulation LES d'un brûleur quasi-industriel. Dans ce cas, un modèle à trois-équation est utilisé pour la description de la phase solide, fournissant une précision similaire à la méthode sectionnelle pour un coût CPU inferieur. Premièrement, la fiabilité du formalisme LES est évaluée. Une analyse statistique révèle que atteindre la convergence est difficile dans cette configuration, étant donné la complexité de l'écoulement et la forte intermittence des suies. La sensibilité des résultats à la résolution spatiale est aussi étudiée. Des différences dans la structure de la phase gazeuse, due à des résolutions différentes, entraînent des écarts importants dans la prédiction de la fraction volumique. Ensuite, l'impact des modèles de suies est également examiné. La fraction volumique maximale de suie est multipliée par trois avec le

modèle HACA-RC* en raison de l'augmentation substantielle de la croissance en surface. Enfin, une nouvelle stratégie pour évaluer la réponse des modèles de suie est proposé basée sur une unique LES où l'ensemble d'équations décrivant les suies est dupliqué. L'un des ensembles représente le modèle de référence, tandis que l'autre est traité avec le modèle à évaluer. Cela permet aux deux ensembles d'interagir avec la même évolution temporelle et spatiale de la phase gazeuse, isolant ainsi les effets du modèle de suie des incertitudes sur les modèles gazeux et des sensibilités numériques. Grâce à cette approche, les premières indications de la contribution du modèle d'intermittence de sous-maille pour la phase solide à la prédiction de suies sont proposées. Motivée par les difficultés rencontrées pour évaluer les performances des modèles de suies dans la flamme turbulente considérée, une l'analyse a priori du modèle d'intermittence basée sur une Simulation Numérique Directe d'une flamme contre-courant turbulente 2D est réalisée. Cette analyse fournit des informations sur la contribution du modèle d'intermittence à la prédiction de suies. De plus, elle réprésente une nouvelle base de données pour des études paramétriques.

Contents

Introduction

Global context: fossil-based energy supply

The world is still energetically dependent on primary fossil resources. Accordingly to the last International Energy Agency (IEA) report, in 2018, fossil resources represented more than 80% of the worldwide energy supply (Fig. 1), despite the growth of other resources for primary energy supplies. Therefore, combustion processes still represent the primary energy source. However, combustion processes generate gaseous and particulate pollutants, which have hazardous effects on the health and environment. Among the different sources of atmospheric pollutant emissions using combustion, the transport sector is one of the principal sources of greenhouse gaseous emissions due to its increasing dependence on fossil-fuel. Solely, it represented about 57% of worldwide oil consumption in 2018 (Fig. 2).

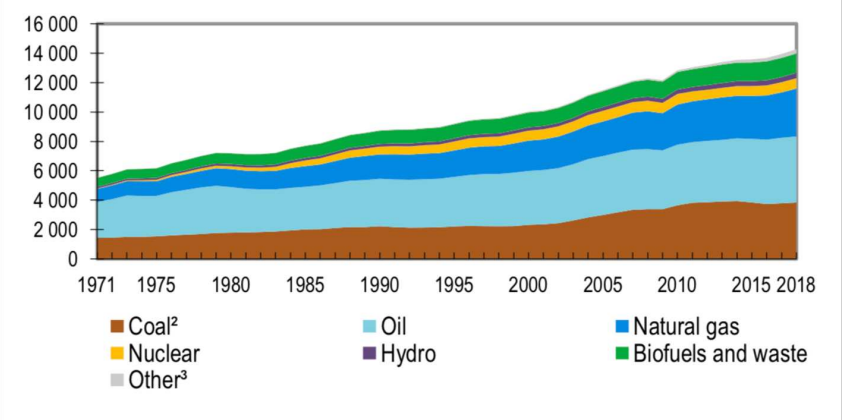

Figure 1: *Total primary energy supply by fuel ("Other" includes geothermal, solar, wind, and heat primary supply). Statistics from IEA (2020).*

Although air pollutant emissions from the transport sector have significantly reduced since 1990 in Europe, greenhouse gas emissions from transport continue

to increase since 2014, reaching 29 % above 1990 levels in 2018. According to EEA (2020), this increase in transport gas emissions is mainly attributed to international aviation, which increases by 129% compared to 1990 while the road transport has increased by 23%, with an annual increase of 3% on average since 2013. After commercial, institutional and households sector, the road transport sector is the primary source of particulate (including soot particles) emission (Fig. 3). In this scenario, achieving climate neutrality will need a 90% reduction in transport emissions by 2050 (EEA, 2020). Therefore tremendous research efforts and technological improvement are necessary to reduce pollutant emissions to respect the increasingly restrictive environmental norms and climate ambition.

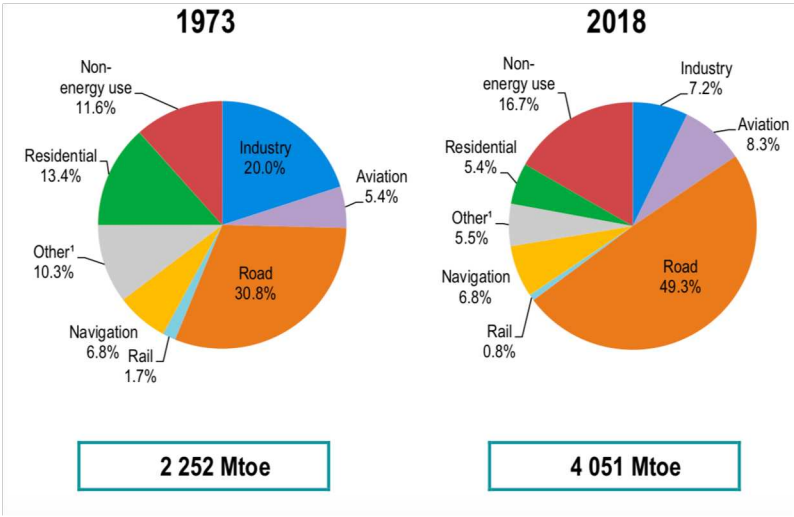

Figure 2: *Source shares of oil consumption (1973 and 2018). Statistics from IEA (2020).*

In Europe, for example, the Euro standards strict emission limits for air pollutants (including particulate matter, nitrogen oxides and carbon monoxide) from cars and vans (Euro 5 and 6), trucks and buses (Euro VI) and motorcycles (Euro V). Although more and more stringent norms (Fig. 4) and the development of low-emission vehicle technologies, atmospheric pollution is responsible for nearly 800.000 deaths per year in Europe and 8.8 million worldwide. The exposure to high particulate matter levels can indeed cause respiratory and cardiovascular diseases, reproductive and central nervous system dysfunctions, and cancer (Lelieveld et al., 2019). Besides, CO_2 and particulate matter (soot particles) contribute to climate change by changing the atmospheric radiative budget. Therefore, air quality action plans for preventing and controlling health impacts and limiting greenhouse gas and soot particle emissions are urgent.

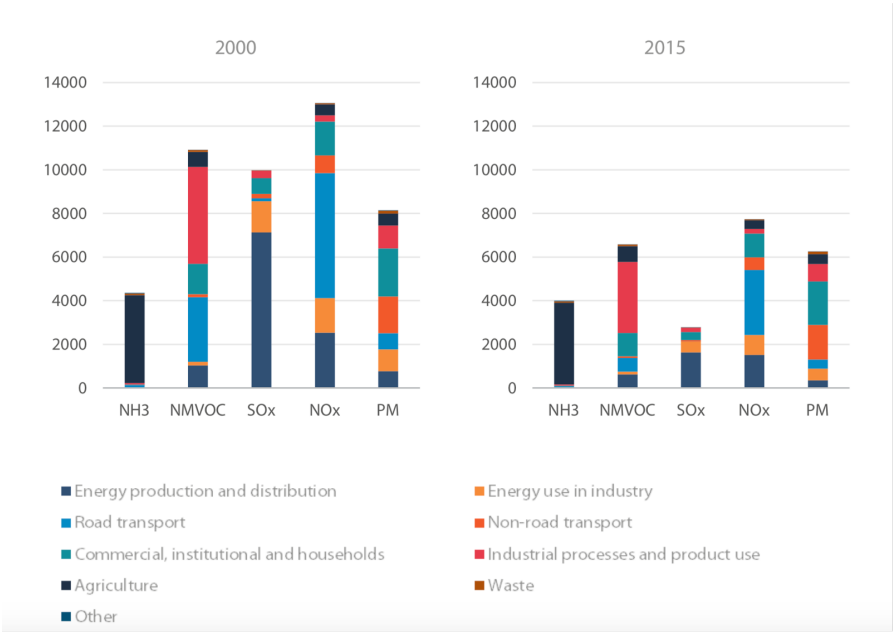

Figure 3: *Sources of air pollutants in Europe, in thousand tonnes (2000 and 2015). Source: Bourguignon (2018).*

Emission Standard/Directives, Regulations	CO (mg/km)		NO_x (mg/km)		HC (mg/km)		PM (mg/km)	
	Petrol	Diesel	Petrol	Diesel	Petrol	Diesel	Petrol	Diesel
Euro 1/91/441/EWG93/59/EWG	2 720–3 160	2 720–3 160						140–180
Euro 2/94/12/WE and 96/69/WE	2 200	1 000						80–100
Euro 3/98/69/WE	2 300	640	150	500	200			50
Euro 4/98/69/WE and 2002/80/WE	1 000	500	80	250	100			25
Euro 5/WE No. 715/2007	1 000	500	60	180	100		5	5
Euro 6/WE No. 715/2007	1 000	500	60	80	100		5	5

Figure 4: *EU Emission standards for CO, NOx, HC and PM pollutants for petrol and diesel from Kuklinska et al. (2015).*

More specifically, the fast growth of air traffic increases is a concern. Since 1978 the air traffic has doubled every 15 years despite the many economic crises (Fig. 5). In Europe, aviation emissions have increased by 16% between 2005 and 2017 (EASA, 2019) and the CO_2 emission could rise by up to 21% in 2040 compared to 2019. This alarming forecast takes into account the low-consumption and low-emission technology improvements. Beyond CO_2, aircraft engines can emit NO_x, SO_x, unburnt hydrocarbons (HC), CO and soot. In this thesis, soot production in an aero-engine model combustor is investigated. Soot is a carbonaceous product of the incomplete combustion of hydrocarbon fuels. Figure. 6 shows that during 1-hour flight with 150 passengers 2.700 kg of kerosene are consumed leading the production of 8500 kg of CO_2 and

to 0.1 kg of particulate matter including soot particles. Figure 7 shows the different contributions of aircraft pollutants to radiative forcing, the change in the balance between incoming solar radiation and outgoing infrared radiation caused by changes in the composition of the atmosphere. Even though the direct effect of soot particles remains small in the 2050 projection compared to CO_2, soot is pointed out as the principal source of contrails (Bond et al., 2013; B. Kärcher, 2018), ice clouds that nucleate on exhaust soot, and volatile plume aerosol. The contrails contribution to radiative forcing could increase by a factor of 6 in 2050. Besides the impact on the Earth's energetic budget (Bond et al., 2013), soot particles negatively affect the environment and human health (Saxon and Diaz-Sanchez, 2005) as previously said. Additionally, soot may impact the engine performance and lifetime as it promote radiative heat transfer.

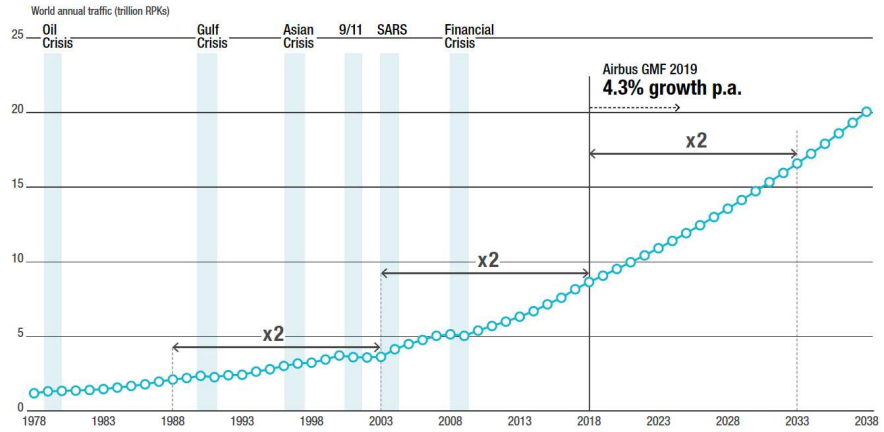

Figure 5: *World annual traffic evolution forecast. Image from (Airbus, 2019)*

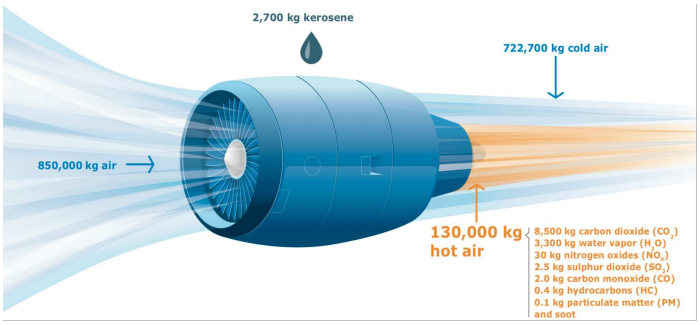

Figure 6: *Emissions from a typical two-engine jet aircraft during 1-hour flight with 150 passengers. Image from (EASA, 2019)*

Most of the international efforts to reduce pollutants emissions in aeronautic industry have been on the reduction of gaseous emissions including NO_x and CO_2, as illustrates the historic evolution of standard aircraft emissions in Fig. 8. But only recently, in January 2020, the first standard concerning non-volatile particulate matter (soot and black carbon) emissions have been proposed by ICAO (2019). The new mass standard applies to all in-production engine types of rated thrust greater than 26.7 kN from 1 January 2020 and mass and number standard from 1 January 2023. Therefore, understanding soot particle formation is of primary importance in developing low emission aircraft. However, predicting soot production is a huge challenge as discussed in the following.

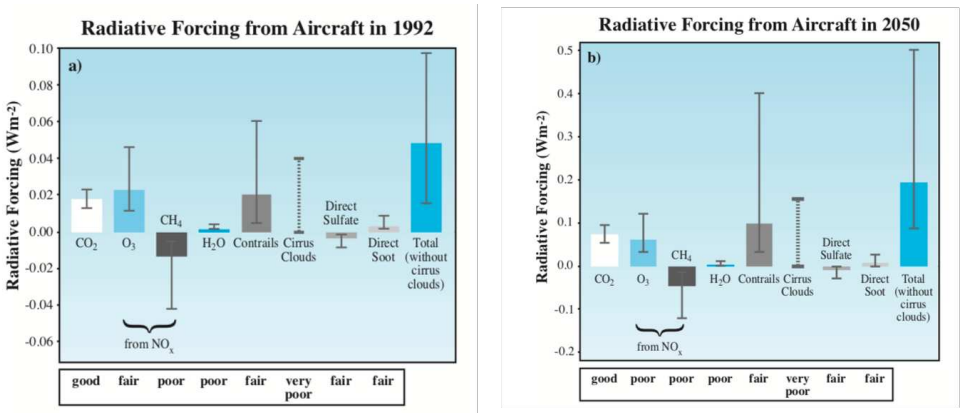

Figure 7: *Estimates of the globally and annually averaged radiative forcing (Wm^{-2}) from subsonic aircraft emissions in 1992 and in 2050. The evaluations below the graph (good, fair, poor, very poor) indicate the level of scientific understanding. Image from IPCC (1999).*

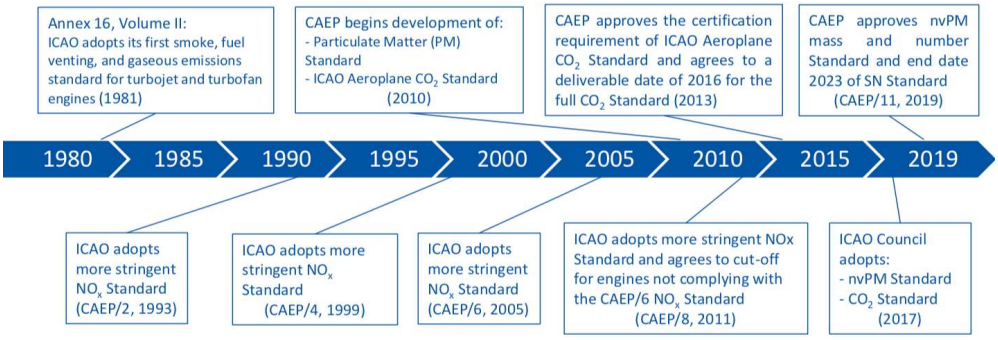

Figure 8: *History of engine emissions standards. Image from (Dickson, 2019).*

Soot modeling challenges

For the combustion community, soot is a carbonaceous product of the incomplete combustion of hydrocarbon fuels assumed to be formed from gaseous aromatic hydrocarbons products presenting a spherical and an aggregate morphology (Xu et al., 2003; Liati et al., 2014; Okyay, 2016). Another terminology currently used in the literature to designate soot is black carbon (BC), usually employed by the atmospheric chemistry and physics community. For the industrial transport sector, it is conventionally named Particulate Matter (PM) classified according to their diameter presenting different hazardous level: PM_{10} for diameter bellow 10 μm and $PM_{2.5}$ for particles smaller than 2.5 μm. The smallest particle diameter, the highest impact on human health. The different terminologies used by various scientific fields reinforce the lack of understanding of carbonaceous particle formation and the need to understand the different processes leading to such pollutant formation (Buseck et al., 2012) to guide modeling efforts.

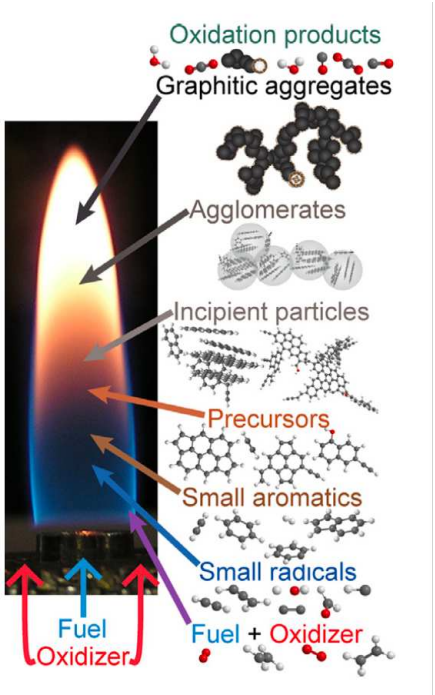

Figure 9: *Schematic representation of soot formation and evolution in a diffusion flame. The molecular species and particles are not drawn to scale. Image from Michelsen (2017).*

Figure 9, from Michelsen (2017), shows a schematic representation of soot formation in a canonical laminar diffusion-like flame. The oxidation of fuel in rich conditions leads to the formation of polycyclic aromatic hydrocarbon

(PAH) species known to be precursors to soot formation (Wang, 2011). The paths leading to the formation of large PAHs is still an open question (Richter and Howard, 2000). Numerous models exist in the literature to describe PAH growth, but they are mainly based on the HACA (H-abstraction C-addition) model (Frenklach, 1996; Appel et al., 2000; Wang et al., 2013; Slavinskaya et al., 2012; Narayanaswamy et al., 2015). The transition between the PAH species to the incipient soot particles remains elusive and is one of the main source of uncertainty in soot modeling. Although it is now widely recognized by the combustion community that soot particles are formed from large PAHs species, three conceptual mechanisms describing gas-soot transition can be found in the literature (Wang, 2011). The first mechanism is based on the growth of PAH in fullerene-like structures. The second mechanism is based on PAH coalescence forming stacked clusters. Finally, the third one is base on the chemical coalescence of PAHs generating three-dimensional structures. The second and third pathways are commonly known as dimerization (Schuetz and Frenklach, 2002; Violi, 2004; Lowe et al., 2015) and is currently adopted by the combustion community (Schuetz and Frenklach, 2002; Blanquart and Pitsch, 2007; Mueller and Pitsch, 2013; Rodrigues et al., 2018).

Once formed, the incipient particles have a carbon-hydrogen ratio (C/H) of 1.4 - 2.5 with a size range of 1 - 6 nm. These particles grow by coalescence and surface addition of gaseous species on its surface forming larger primary particles can reach diameters within 10 - 50 nm. Then agglomeration can occur, and soot takes the form of an aggregate with a fractal dimension in the range of 1.7 - 1.9. Several studies (Eaves et al., 2015; Veshkini et al., 2016; Aubagnac-Karkar et al., 2018) have shown that a two-way coupling may exist between PAH and nucleation-condensation. Although interesting results are obtained considering PAH addition reversibility, this topic is still very new and subject to recent progress. Moreover, among the many assumptions on the collision phenomena, empirical parameters are used to represent the interaction between particles (and dimers). For example, the sticking probability, the probability of two particles (or dimers) collide and stick, depends on the surface area and the mass of the colliding particles is described using an empirical correlation. However, constant values are also employed (Blanquart and Pitsch, 2007; Marchal, 2008; Yapp et al., 2015; Rodrigues et al., 2017). Historically, these empirical correlations are based on measurements in premixed conditions.

The surface reactions (surface growth and oxidation) are also subject to considerable uncertainty. While surface growth leads to mass/size increase, oxidation leads to reducing the primary particle size. Although widely accepted, the HACA model is based on the chemical similarity between soot and PAH species. Therefore, reaction constants are based on analogous PAH reactions, which is a significant source of uncertainty. The concentration of the active sites is derived assuming that the soot surface is covered with stacks of benzene rings (Appel et al., 2000; Aubagnac-Karkar et al., 2015). Veshkini et al.

(2014) found that the active site density on the soot surface decreases with the PAH size, then the assumption based on the benzene rings leads to an overestimation of the active site concentration. Besides that, surface reactivity is quite challenging to model as it depends on the particle morphology and state, which is not always accessible. Therefore an empirical parameter α was introduced to account for the soot morphology variation by temperature, aging, and residence time Veshkini et al. (2014). Classically validated in premixed flames, the HACA model failed to describe soot surface kinetics in counterflow non-premixed flames accurately (Hwang and Chung, 2001). In Chapter 3, an improved model is proposed to address this behavior. The oxidation rate is also a source of uncertainty in soot models with a significant variation of expression and empirical values in the literature (Guo et al., 2016).

Despite the huge efforts made by the scientific community to understand and model the heterogeneous mechanisms involved in soot production and its evolution into the flame, large gaps in understanding soot formation still exist. Soot formation is characterized by complex chemical and physical phenomena that may depend on the flame structure through mixing, fuel type, strain rate, and residence time (Cuoci et al., 2008; Wang and Chung, 2016; Rodrigues et al., 2017) leading to a difficult numerical representation and experimental measurements (Wang, 2011; Michelsen, 2017) of soot production. Experimental data are generally used to guide modeling. Then, the first step in soot modeling is validating the kinetics mechanisms against experimental measurements as it is strongly sensitive to the gas phase description. Whereas experimental data for dominant species is available, the PAH database is scarce. Besides the scarcity of experimental data, the kinetic model is generally validated in non-sooting flames different from those used for the soot model validation. Moreover, despite the progress made in soot optical diagnostics, uncertainty remains due to the dependence on the soot optical properties, interference of other species, and the model to obtain the soot volume fraction from the measured soot particle radiation spectrum (Zerbs et al., 2009; Migliorini et al., 2011; Leschowski et al., 2015; Yan et al., 2019).

In turbulent flames, soot prediction is even more challenging. Despite the lack of understanding of soot production and the complexity in modeling the involved process, soot production is highly coupled with the flame and flow dynamics requiring high fidelity models to obtain a reliable description of these multi-physics interactions. Moreover, in turbulent conditions, soot particles are found in ligament form due to the low soot molecular diffusion (Franzelli et al., 2015; Geigle et al., 2013). The interaction of these soot filaments with the 3D turbulent flow leads to different spatial and temporal variability. Soot production in turbulent conditions is then highly intermittent. Such features make soot modeling and measurements a great challenge. In particular, the soot filaments might not be resolved on the numerical grids used in Large Eddy Simulation formalism. Therefore, specific subgrid-scale models are required,

increasing the degree of difficulty in numerically describing soot in turbulent flames. The lack of a comprehensive experimental database in technical conditions also restricts model development. The DLR research group is a pioneer in combined diagnostics in a complex configuration (Geigle et al., 2013, 2015, 2017; Nau et al., 2017) to study soot presence correlation with flame and flow dynamics providing an extensive database to model evaluation. This configuration is adopted in this thesis within the European project SOPRANO (SOot Processes and Radiation in Aeronautical inNOvative combustors).

Soot prediction in aero-engines: the SOPRANO project

The aeronautical industry has then taken the initiative to develop methodologies for predicting soot emissions to be ahead of climate ambitions. In this context, the European project SOPRANO (SOot Processes and Radiation in Aeronautical inNOvative combustors) coordinates scientists and industrials to improve the characterization of soot particle emissions in aero-engine combustors using experimental and numerical approaches to develop low-emission aircraft combustion systems. This thesis has been supported by this project and aims to improve for Large Eddy Simulation formalism for soot prediction in an aero-engine combustor. For that purpose a lab-scale aero-engine combustor designed and experimentally study at the DLR (Geigle et al., 2013, 2015, 2017), a partner in the project, has been adopted as the reference case. Operating at elevated pressure with secondary air oxidation, this burner was designed to provide an extensive experimental database serving for evaluation of soot models under technically relevant conditions. It has been recently elected as a target flame in the International Sooting Workshop (ISF) database reference.

Objectives of the thesis

In the context of the SOPRANO project the main objectives of this thesis are defined as:

1. Proposing a model able to describe soot production in laminar and turbulent sooting flames.
2. Quantifying the reliability of the LES formalism in predicting soot production when applied in an aero-engine model combustor as the DLR burner.
3. Identifying a strategy to quantify the effect of a soot model on the LES prediction of soot production in the DLR burner.
4. Evaluating the effect of a newly developed mechanism for soot surface reactions in laminar and turbulent flames.

5. Evaluating the effect of the state-of-the-art soot subgrid intermittency model on soot prediction in the DLR burner.

Organization of the manuscript

This manuscript is organized in three parts:

Part I: This part is dedicated to the modeling and simulation of laminar sooting flames. In Chapter 1, the different models and equations for sooting flames are presented. The physical and chemical mechanisms of soot production are presented together with the different numerical methodologies to predict soot formation found in the literature. The sectional approach (Rodrigues et al., 2017), retained for the laminar simulations, is described in details. Then in Chapter 2, the retained sectional soot model is evaluated in premixed and non-premixed sooting flames. The complexity and uncertainties of soot processes and their modeling are discussed. The three-equation soot model, retained for the turbulent flames, is also described in Chapter 2.

Part II: In Part I, it has been observed that although the sectional strategy provides a good performance in predicting soot volume fraction in premixed conditions, it fails in non-premixed flames. Then, in Chapter 3, the model is improved by proposing a new soot surface reactions model called HACA-RC*. Coupled with the whole sectional strategy, the model provides a good soot volume fraction predictability in both premixed and non-premixed modes.

Part III: This third part is consecrated to the LES simulation of an aero-engine model turbulent combustor, the DLR burner (Geigle et al., 2013, 2015, 2017). In Chapter 4 the numerical approaches to solve turbulent flames are presented and the LES formalism for turbulent sooting flames, based on a tabulated approach for the gaseous phase (Ihme and Pitsch, 2008) and on the three-equation soot model (Franzelli et al., 2018) for the solid phase description, is presented. The soot subgrid-scale model is presented and the extended version of the intermittency soot model (Mueller and Pitsch, 2011) for the three-equation model is described in detail. In Chapter 5, the DLR burner is presented and its technical characteristics and available experimental data are detailed. A literature survey describes experimental evidences and numerical observations about soot formation and its interaction with turbulence. The reliability of LES of the DLR flame is quantifying analyzing the numerical convergence in Chapter 6. Then, in Chapter 7, the soot reaction surfaces model proposed in Chapter 3 is applied for the LES of the DLR flame and its impact

is evaluated. Finally, the impact of the subgrid intermittency model on the soot prediction on the DLR burner is evaluated in Chapter 8.

Motivated by the difficulties in evaluating soot model performances in turbulent flames via LES, *a priori* analysis of the soot subgrid intermittency model based on a Direct Numerical Simulation (DNS) databse of a turbulent counterflow 2D flame is performed to clarify its ability in describing soot-turbulence-chemistry interactions. The results of this preliminary analysis, presented in Appendix A, provide meaningful information about the intermittency model contribution to soot prediction in turbulent flames. Besides, this can be considered as a potential new database for parametric studies for soot model development.

Acknowledgement

The European Union funded this thesis within the SOPRANO H2020 project under the Grant Agreement No. 690724. This thesis was granted access to the HPC resources of CINES under the allocation x20162b6172 made by GENCI allocation. The Moulon Mesocentre computer resources of CentraleSupelec and ENS Paris-Saclay supported this thesis with their resources and technical assistance.

Part I

Modeling and simulating laminar sooting flames

Chapter 1

Equations and models for simulation of sooting flames

f

This chapter aims to present the numerical models and methods for the prediction of soot as to the starting point of this thesis. First, in Section 1.1, the equations governing the reacting flow are described. Then, in Section 1.2, the soot population balance equation (PBE) and the physical and chemical sub-models for the processes involved in soot production (formation + destruction) are presented. The different numerical methods existing in the literature to solve the balance equation are briefly presented in Section 1.4. The sectional method due to (Rodrigues et al., 2017) and the three equation soot model due to (Franzelli et al., 2018) are described in details in Section 1.5 and Section 1.6, respectively. The sectional method will be considered as the reference model in laminar cases investigated in Chapters 2 and 3. However, when investigating turbulent flames in Part III and IV, the three equations model will be used.

Contents

1.1 Conservation equations for compressible gaseous reacting flows

The classic set of equations used to describe a compressible multi-species reacting flow (Poinsot and Veynante, 2005) is presented in the following.

Conservation of mass:

$$\frac{\partial \rho}{\partial t} + \frac{\partial \rho u_i}{\partial x_i} = 0 \tag{1.1}$$

Conservation of momentum:

$$\frac{\partial \rho u_j}{\partial t} + \frac{\partial}{\partial x_i}(\rho u_i u_j) = -\frac{\partial P}{\partial x_j} + \frac{\partial \tau_{ij}}{\partial x_i} + \rho g_i \tag{1.2}$$

Conservation of chemical species:

$$\frac{\partial \rho Y_k}{\partial t} + \frac{\partial}{\partial x_i}(\rho u_i Y_k) = -\frac{\partial}{\partial x_i}(J_{k,i}) + \dot{\omega}_k \tag{1.3}$$

Conservation of energy:

$$\frac{\partial \rho E}{\partial t} + \frac{\partial}{\partial x_i}(\rho E u_i) = -\frac{\partial}{\partial x_i}(u_i P) + \frac{\partial}{\partial x_j}(u_i \tau_{ij}) - \frac{\partial q_i}{\partial x_i} + \dot{Q}_r + \dot{\omega}_T \tag{1.4}$$

where ρ is the gaseous density, u_i the i^{th}-component of the velocity vector, P the pressure, g_i the i^{th}-component of the gravity vector; τ_{ij} is viscous tensor; Y_k the mass fraction of the k^{th}-species, with k varying from 1 to $N_{species}$ (the number of species involved in the kinetic mechanism), $J_{k,i}$ is the molecular diffusive flux of species and $\dot{\omega}_k$ corresponds to the mass reaction rate of the k^{th} species; E is the total energy per unit mass (the sum of sensible e_s and the kinetic energies $u_i^2/2$) per unit mass. $\dot{Q}_r$ is a non-chemical energy source term, accounting for other external energy sources (as an electric spark, laser energy deposition) and radiation and $\dot{\omega_T}$ is the heat release rate due to combustion.

The thermochemistry of the gas mixture verifies the equation of state for ideal gases:

$$P = \rho r T \tag{1.5}$$

with T the gas temperature, $r = \mathcal{R}/W$ the mixture's gas constant, W the mean molar mass and $\mathcal{R} = 8.3143\ J.mol^{-1}.K^{-1}$ the universal gas constant.

The viscous stress tensor τ_{ij}, in Eqs. 1.2 and 1.4, is modeled as:

$$\tau_{ij} = \mu \left(\frac{\partial u_i}{\partial x_j} + \frac{\partial u_j}{\partial x_i} \right) - \frac{2}{3} \mu \frac{\partial u_k}{\partial x_k} \delta_{ij} \tag{1.6}$$

where μ is the dynamic viscosity. δ_{ij} is the Kronecker delta: $\delta_{ij} = 1$ if $i = j$ and $\delta_{ij} = 1$ otherwise.

The species diffusion flux $J_{k,i}$ in Eq. (1.3), is defined as:

$$J_{k,i} = \rho V_{k,i} Y_k, \tag{1.7}$$

where $V_{k,i}$ is the i^{th} component of the diffusion velocity of the k^{th} species.

To ensure the conservation of the total mass of the mixture, the chemical reaction source and diffusion velocity of the k^{th} species, $\dot{\omega}_k$ and $V_{k,i}$ respectively, must verify the following two relations:

$$\sum_{k=1}^{N} \dot{\omega}_k = 0 \tag{1.8}$$

$$\sum_{k=1}^{N} Y_k V_{k,i} = 0 \tag{1.9}$$

The mass reaction rate of the k^{th} species $\dot{\omega}_k$, is the sum of each reaction rate $\dot{\omega}_{k,j}$ (with j $\in$ [1 M] the number of reactions) for each species k^{th} composing the kinetic scheme. Each reaction rate $\dot{\omega}_{k,j}$ is obtained using an Arrhenius law.

The species diffusion velocity $V_{k,i}$ is described with the Hirschfelder and Curtis approximation to avoid the complex and costly inversion of a system of size $N^2_{species}$ in each direction for each point and time for an unsteady flow, when considering a binary mass diffusion coefficients between each species composing the mixture. This approximation describes the species diffusion velocity $V_{k,i}$ for a species k using an equivalent diffusion coefficient D_k into the mixture. For a mixture composed of only two species, the approximation relaxes to the Fick's law. In order to ensure the verification of Eq. (1.9) and the compatibility between Eqs. (1.1) and (1.3) a correction velocity V^c is also introduced:

$$V_{k,i} = -\frac{D_k}{Y_k}\frac{W_k}{W}\frac{\partial X_k}{\partial x_i} + V_i^c \tag{1.10}$$

$$V_i^c = \sum_{k=1}^{N} D_k \frac{W_k}{W}\frac{\partial X_k}{\partial x_i} \tag{1.11}$$

where W and W_k are, respectively, the molar weigth of mixture and of species k, X_k is the mole fraction of the k^{th} species ($X_k = Y_k W {W_k}^{-1}$).

In this manner, the diffusive flux of species is expressed as:

$$J_{k,i} = \rho Y_k V_{k,i} = -\rho\left(D_k \frac{W_k}{W}\frac{\partial X_k}{\partial x_i} - Y_k V_i^c\right) \tag{1.12}$$

The heat flux q_i in Eq. (1.4) is defined as the sum of two terms:

$$q_i = \underbrace{-\lambda\frac{\partial T}{\partial x_i}}_{\text{mixture's heat diffusion}} + \underbrace{\rho\sum_{k=1}^{N} h_{s,k} Y_k V_{k,i}}_{\text{species' enthalpy diffusion}} \tag{1.13}$$

where $V_{k,i}$ is the i^{th}-component of the diffusion velocity of the k^{th} species, expressed in Eq. (1.10)

The first term is the mixture's heat diffusion, following a Fourier law and the second term is the heat flux consequence of diffusion of species with different sensible enthalpies $h_{s,k}$:

Finally, the chemical reaction's heat release rate $\dot{\omega_T}$ in Eq. (1.4) is calculated from the reaction rates of species $\dot{\omega}_k$ and their mass enthalpy of formation $\Delta h^0_{f,k}$:

$$\dot{\omega}_T = -\sum_{k=1}^{N} \dot{\omega}_k \Delta h^0_{f,k} \tag{1.14}$$

1.2 Conservation equations for soot particles

Soot particles are described as a disperse phase interacting with the gaseous-phase. Thus, supplementary balance equations and models are required to take account for soot particle formation and destruction and evolution in time and

space. The evolution of non-inertial particles as soot particles is classically modeled using a population balance equation (PBE), that describes the temporal and spatial evolution of the particle population through the transport of its number density function NDF $n(t, \mathbf{x}, \xi)$:

$$\frac{\partial n}{\partial t} + \frac{\partial}{\partial x_i}(n u_i) + \underbrace{\frac{\partial}{\partial x_i}(n v_{th,i})}_{Thermophoresis} = \underbrace{\frac{\partial}{\partial x_i}\left(D_s \frac{\partial n}{\partial x_i}\right)}_{Diffusion} + \dot{\omega}_n \tag{1.15}$$

where x_i is the spatial coordinate vector, and the ξ is the internal coordinate vector describing soot particles properties as volume, surface, chemical composition and even more precise information about soot morphology as the number of primary particles per aggregate Michael (2002); Mueller et al. (2009); Zhang et al. (2009).

The third left-hand side term in Eq. (1.15), is a transport phenomenon of soot particles that moves towards the cold zones due to temperature gradient, the thermophoresis. In the presence of a high-temperature gradient, the thermophoretic effect is not negligible. This transport phenomenon is modeled by introducing a thermophoretic velocity v_{th} (Derjaguin et al., 1966):

$$v_{th} = -C_{th} \frac{\nu}{T} \frac{\partial T}{\partial x_i} \tag{1.16}$$

where ν is the gas kinematic viscosity and the model constant $C_{th} = 0.554$.

The diffusion coefficient D_s, in the diffusion term on the right-hand side in Eq. (1.15), is modeled according to Epstein (1924) and Yapp et al. (2015):

$$D_s = \frac{3}{2\rho}\left(1 + \frac{\alpha_T \pi}{8}\right)^{-1} \frac{1}{d^2} \sqrt{\frac{W_{gas} k_b T}{2\pi N_A}} \tag{1.17}$$

where W_{gas} is the gas molecular weight, ρ the density of the gas, d is the soot particle diameter, N_A is the Avogadro number, k_b is the Boltzmann constant and $\alpha_T = 0.9$ is the thermal accomodation factor expressing the fraction of heat flux exchanged between the soot particle surface and the surrounding gas molecules. In turbulent flames, soot diffusivity is usually neglected since molecular soot diffusion is small compared to the turbulent diffusivity (Bisetti et al., 2012).

The last term in right-hand side in Eq. (1.15) is the source term $\dot{\omega}_n$. It describes heterogeneous physical and chemical processes affecting the particle size distribution as nucleation, condensation, coagulation, and surface reactions (surface

growth and oxidation). The sub-models describing these processes is presented in Section 1.3.3.

1.3 Soot modeling generalities

1.3.1 Morphological description

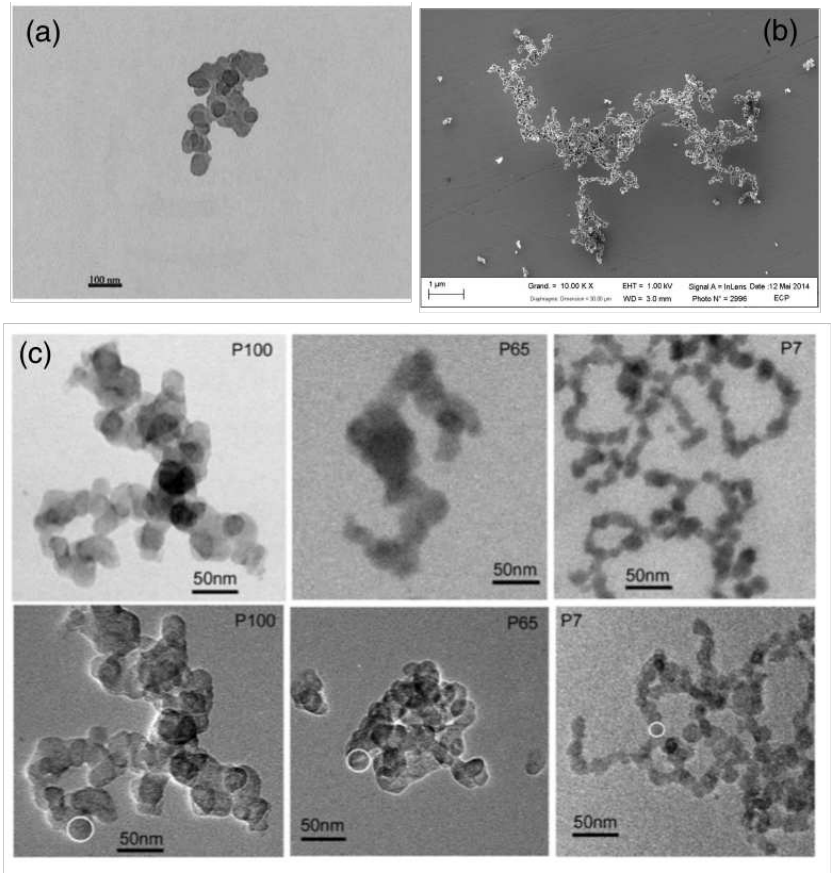

Figure 1.1: *(a) Soot aggregate extracted at the bottom of an atmospheric ethylene/air flame, where the first soot aggregates are formed extracted from Xu et al. (2003). (b) Scanning Electron Microscopy (SEM) observation of a soot aggregate sample collected from an atmospheric propane/air flame extracted from Okyay (2016). (c) Scanning Transmission Electron Microscope (BF-STEM) mode (upper row) and Transmission Electron Microscopy (TEM) mode images (lower row) of soot agglomerates from different engine thrust levels corresponding to different flight phases. Encircled in the lower row images are examples of primary soot particles extracted from Liati et al. (2014).*

Experimental evidences (Xu et al., 2003; Liati et al., 2014; Okyay, 2016) in Figure 1.1 have shown that, in addition to the spherical particles with a diameter $d = (6v/\pi)^{1/3}$, soot particles can present an aggregated form composed of $n_p = s^3/36\pi v^2$ primary spherical particle with a primary diameter $d_p = 6vs^{-1}$, where v and s are the volume and surface of a soot particle, respectively.

Therefore, accounting for soot particle shape, in addition to the particle size, is essential to predict soot correctly. To a full description of such complex geometry, a two-dimensional PBE is required in terms of volume and surface. However, the numerical solution of such equations with non-linear source terms requires complex models and a high CPU resource, which may not be conceivable in 3D turbulent flows.

According to the work of J. et al. (1987), an aggregate of soot particles follow a fractal relationship that can be described by a fractal dimension D_f linking n_p and d_p:

$$n_p \propto d_p^{-D_f} \tag{1.18}$$

where the fractal dimension D_f is often assumed equal to 1.8 by the combustion community (Köylü and G.M. Faeth and T.L. Farias and M.G. Carvalho, 1995; Blanquart and Pitsch, 2007).

This morphological definition is then retained for the model strategy adopted in this manuscript.

1.3.2 Global soot quantities

Global quantities are generally used to evaluate soot models comparing to experimental measurements. Two global quantities are of the most interest: the particle number density N_s $[m^{-3}]$ and their soot volume fraction f_v. The particle number density N_s is obtained by integrating the NDF over the total volume V of the system.

$$N_s = \int_0^\infty n(v)dv \tag{1.19}$$

The soot volume fraction f_v is generally obtained assuming that soot particles have a constant density $\rho_{soot} = 1.86\ 10^3\ kg/m^3$. Then, the total soot mass m_s and total soot volume v_s are linked through:

$$v_s = \frac{m_s}{\rho_s} \tag{1.20}$$

Finally, the soot volume fraction can be defined as:

$$f_v = \frac{v_s}{V} = \frac{m_s}{\rho_s V} = \frac{\rho}{\rho_s} Y_s \tag{1.21}$$

where Y_s is the soot mass fraction. This soot scalar is usually transported as a statistical moment of a univariate NDF based on the soot particle volume, which is the case for the sectional method retained to investigate laminar sooting flames in this manuscript, as will be described in details in Section 1.5.

1.3.3 Soot production processes

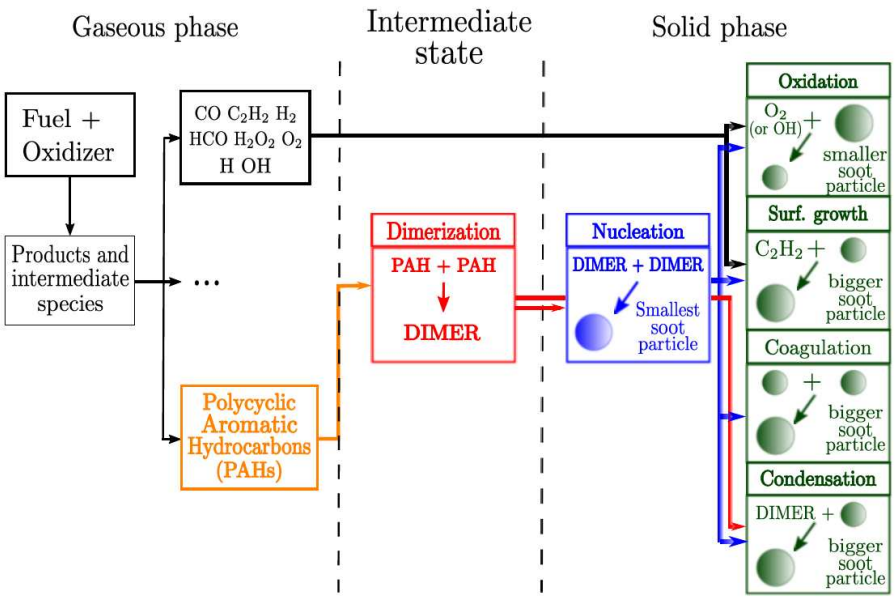

Figure 1.2: *Schematic representation of soot production processes (from Rodrigues (2018)).*

Complex physical and chemical mechanisms are involved in soot particle production during incomplete combustion of hydrocarbon fuels. The nascent particles are here assumed to be formed from aromatic species, called Polycyclic Aromatic Hydrocarbons (PAH), with large molecular weight (Wang et al., 2015). PAHs formation are modeled through the H-abstraction C-addition (HACA) mechanism (Frenklach and Wang, 1991), a sequence of chemical reactions of surface activation and cyclization until they reach a size allowing the collision and coalescence of large PAHs, via a process called dimerization (Schuetz and Frenklach, 2002). The dimerization results in a dimer, which is assumed to be an intermediate state between the gaseous and the solid/particle phases (Blanquart and Pitsch, 2007). Then, the collision between two dimers results in a new particle (Blanquart and Pitsch, 2007). Once formed, soot particles can interact between them through coagulation and grow by condensation of a dimer on the soot surface. Soot particles also grow by reactions with the surrounding

gas phase and are consumed by oxidative reactions. The soot processes considered in the present study are schematically illustrated in Fig. 1.2 and their models are described in the following.

Soot precursors formation and dimerization

The performance of a soot model is strongly correlated to the chosen kinetic mechanism, which should describe not only the global gas properties like temperature and flame speed but also the soot precursors and the other gaseous species contributing to the soot particle kinetics. Therefore, the first step to be considered in soot modeling is the formation of its gaseous precursors. Although this step still presents several uncertainties and is a central subject in soot modeling research, it is now widely accepted in the combustion community that soot particles are formed from the Polycyclic Aromatic Hydrocarbures (PAH). Among the numerous models found in the literature to describe the PAH kinetics, the HACA (H-Abstraction C-Addition) based model is the most popular. A detailed review of PAH kinetics is out of scope here. It can be found in Wang (2011).

Several gaseous kinetic schemes considering PAH formation can be found in the literature (Appel et al., 2000; Wang et al., 2013; Slavinskaya et al., 2012; Narayanaswamy et al., 2015). The selected model considered for the simulations presented in this manuscript is the KM2 mechanism due to (Wang et al., 2013). The KM2 mechanism allows PAH description up to seven aromatic rings from the pyrene (A4) with four aromatic rings up to the coronen (A7) with seven aromatic rings (see Table 1.1). Its ability to predict PAH in a counterflow nonpremixed flame of ethylene fuel mixture with benzene and propane was verified by Wang et al. (2013). Rodrigues (2018) has extended the validation to a premixed ethylene-air flame. The laminar flame speed in atmospheric pressure has also been verified considering ethylene-air, methane-air, and propane-air premixed flames. For the ethylene-air flame, the laminar flame speed was also validated at higher pressures.

The transition between gaseous PAH and soot particles is also not well understood, although the progress made in understanding soot formation. Wang (2011) also provides a comprehensive review of the state of knowledge of the process leading to soot particle formation. Here, the dimerization mechanism is retained to model this transition. Once formed, the successive collision and coalescence of PAH species produce the dimers (Blanquart and Pitsch, 2007; Mueller et al., 2009), an intermediate step between the gas-phase and the solid-phase. According to Blanquart and Pitsch (2007) the rate of dimer production

$\dot{Q}^{dim}_{PAH_i}$ is given by:

$$\dot{Q}^{dim}_{PAH_i} = 2 v_{PAH_i} \gamma_i \left(\frac{4\pi k_b T}{m_i} \right)^{1/2} d^2_{PAH_i} [PAH_i]^2 N_A^2 \tag{1.22}$$

where d_{PAH_i} is the spherical diameter of the PAH_i (i = 1 to N_{PAH}, the number of PAH species considered in the nucleation). T is the surrounding gas temperature, m_i is the mass, $v_{PAH_i} = n_{C_{PAH_i}} v_{C_2}/2$ is the volume and $\gamma_i = C_N m_i^4$ the sticking coefficient factor for the PAH_i molecule (see Table 1.1) and $C_N = 1.5\ 10^{-11} g^{-4}$.

Table 1.1: *Involved PAHs considered for the dimerization process modeling with their molar mass and sticking coefficient.*

PAH	**Chemical formula**	**Molar Mass [g/mol]**	γ_i
Pyrene (A4)	$C_{16}H_{10}$	202	0.025
Chrysene (A5)	$C_{18}H_{12}$	228	0.0406
Benzo(a)pyrene (A5)	$C_{20}H_{12}$	252	0.0606
Benzo(e)pyrene (A5)	$C_{20}H_{12}$	252	0.0606
Perylene (A5)	$C_{20}H_{12}$	252	0.0606
Benzoperylene (A6)	$C_{22}H_{12}$	276	0.0871
Coronene (A7)	$C_{24}H_{12}$	300	0.1216

In the present study, the dimerization of seven PAHs ($N_{PAH} = 7$) having four or more aromatic rings are considered, from the pyrene (A4) up to coronen (A7), according to the KM2 mechanism (Wang et al., 2013). However, instead of considering the collision between seven different PAHs, an equivalent lumped PAH accounting for all PAH_i generating soot is considered. The mass fraction Y_{PAH} and the total dimerization rate $\dot{\omega}_{dim}$ is evaluated as:

$$Y_{PAH} = \sum_{i=1}^{N_{PAH}} Y_{PAH_i} \tag{1.23}$$

$$\dot{\omega}_{dim} = \sum_{i=1}^{N_{PAH}} \dot{Q}^{dim}_{PAH_i} \tag{1.24}$$

Therefore an equivalent dimer with a volume v_{dim} is defined. It depends on the local concentration of each PAH_i and is evaluated as:

$$v_{dim} = 2\frac{\sum_{i=1}^{N_{PAH}} \dot{Q}_{PAH_i}^{dim}}{\sum_{i=1}^{N_{PAH}} \dot{Q}_{PAH_i}^{dim}/(2v_{PAH_i})} \tag{1.25}$$

The collision between two dimers leads to a newly soot particle (nucleation) and the collision with another particle leads to a particle with a bigger size (condensation). Therefore, a quasi-stationary assumption is considered between the chemical dimer production ($\dot{\omega}_{dim}$) and consumption by the nucleation ($\dot{\omega}_{nucl}$) and condensation ($\dot{\omega}_{cond}$) processes. Finally, the concentration of dimers can be obtained by solving the quadratic equation:

$$\dot{\omega}_{dim} = \dot{\omega}_{nucl} + \dot{\omega}_{cond} \tag{1.26}$$

$$\dot{\omega}_{dim} = \beta_{dim}[DIMER]^2 + \int_0^v \beta_{v,v_{dim}} n(v)[DIMER]dv \tag{1.27}$$

where $\dot{\omega}_{nucl}$ and $\dot{\omega}_{cond}$ are the source terms of nucleation and condensation, respectively.

Soot collision dynamics

Nucleation, condensation, and coagulation are modeled as collisional phenomena based on the Smoluchowski equation (Smoluchowski, 1916). The Smouchowski equation expresses the gain $\dot{n^c}(v)$ of n for a given volume v by the collision between particles of any size u and $(u-v)$, and the loss of all particles of size v colliding with any other particle. Then the coagulation ($\dot{\omega}_{coag}$), the collision between two soot particles leading to a bigger particle, can be described as:

$$\dot{n^c}(v) = \underbrace{\frac{1}{2}\int_0^v \beta_{v-u,u} n(u)n(v-u)du}_{\text{rate of gain of particle of size } v} \underbrace{-\int_0^\infty \beta_{u,v} n(u)n(v)du}_{\text{rate of loss of particle of size } v} \tag{1.28}$$

with $\beta_{u-v,u}$ and $\beta_{u,v}$ describing the collision rate of particle size $(u-v)$ with v and particle size u with v, respectively.

For the nucleation, the collision between gaseous molecules (dimers) leads to a soot particle and then to a gain of n. For condensation, soot particles col-

lide with dimers adding mass to the particles without changing n. For these phenomena, the collisional model writes as:

$$\dot{\omega}_{nucl}(v) = \frac{1}{2}\beta_{v_{dim},v_{dim}} v_{dim} N_{dim}^2 \tag{1.29}$$

$$\dot{\omega}_{cond}(v) = v_{dim} N_{dim} \int_0^v \beta_{v_{dim},u} n(u) du \tag{1.30}$$

with $\beta_{v_{dim},v_{dim}}$ and $\beta_{v_{dim},u}$ describing the collision rate of two dimers and a particle of size u with a dimer, respectively.

Therefore, nucleation contributes to the number density of particles N_s as well as to the soot mass. Condensation contributes to soot particle size and then to soot volume fraction. Finally, coagulation contributes to the soot particle size without affecting the total soot volume fraction f_v. Jointly to the nucleation, the coagulation affects the number density of particles.

The collision efficiencies β in Eqs. (1.28)- (1.30) depend on the soot particle size and morphology as well as the flow conditions. This dependence is considered through the Knudsen number $Kn = 2\lambda_{gas}/d_c$, which describes the molecular mean free path of a particle in a carrier fluid and thus the collision regime between particles (Kazakov and Frenklach, 1998). Finally, λ_{gas} is the the gas mean free path from the kinetic theory defined as:

$$\lambda_{gas} = \frac{\mathcal{R}T}{\pi\sqrt{2d_{gas}^2 N_A P}} \tag{1.31}$$

where P is the pressure and d_{gas} is the diameter of a gas particle considered constant and equal to 0.2 nm.

The collisional regime can be classified into three categories:

- Molecular regime (Kn>10): when the pressure or thermal agitation are low or the particles are small enough (generally spherical particles), the collision rate writes:

$$\beta_{u,v} = \beta_{u,v}^{fm} = \epsilon_{u,v}\left(\frac{3}{4\pi}\right)^{1/6}\sqrt{\frac{6k_bT}{\rho_s}}\sqrt{\frac{1}{u}+\frac{1}{v}}\left(\left(\frac{\pi}{6}\right)^{1/3}(d_{c,u}+d_{c,v})\right)^2 \tag{1.32}$$

with $\epsilon_{u,v}$ is the sticking coefficient taking into account the Van der Waals interactions between particles, i.e. the amplification of the collision efficiency by

the Van der Waals force. This coefficient change with the soot process being modeled (nucleation, condensation or coagulation). Constant values are taken according to the asymptotical analysis (Marchal, 2008; Rodrigues, 2018). They are: $\epsilon_{nucl} = 2.5$, $\epsilon_{cond} = 1.3$ and $\epsilon_{coag} = 2.2$, for the nucleation, condensation and coagulation, respectively. d_c is the collisional diameter defined as a function of the fractal dimension D_f and the number of primary particles composing the aggregate: $d_c = d_p n_p^{1/D_f}$.

- Continuous regime (Kn<0.1): when the pressure is sufficiently high, thermal agitation is significant or the particles are large enough (generally aggregates) the collision rate can be described as:

$$\beta_{u,v} = \beta^c_{u,v} = \frac{2k_b T}{3\mu}(d_{c,u} + d_{c,v})\left(\frac{Cu_u}{d_{c,u}} + \frac{Cu_v}{d_{c,v}}\right) \tag{1.33}$$

with $Cu_u = 1 + 1.257Kn_u$ the corrective Cunningham coefficient for a particle of size u.

- Intermediate regime (0.1<Kn<10): in this regime the collision rate $\beta_{u,v}$ is expressed as a harmonic mean of collision frequency in the molecular $\beta^{fm}_{u,v}$ and continuous $\beta^c_{u,v}$ regimes. This collision regime corresponds to a transition regime between small spherical particles and large particles as aggregates.

$$\beta_{u,v} = \beta^{tr}_{u,v} = \frac{\beta^{fm}_{u,v}\beta^c_{u,v}}{\beta^{fm}_{u,v} + \beta^c_{u,v}} \tag{1.34}$$

Soot surface kinetics

The soot surface kinetics describes soot surface reactivity through surface growth and oxidation. The surface growth contributes to the total soot mass through carbon addition at the surface of soot particles, implying an increase in the soot particle size. The oxidation acts in opposition to the surface growth by extracting carbon atoms on the surface of the primary particles, implying a decrease in particle diameter and soot volume fraction. Both surface growth and oxidation do not affect the number density of particles. The HACA-like mechanisms classically describe these two chemical processes. It was initially proposed by Frenklach and Wang (1991) for model PAH growth. By considering the chemical similarity between soot surface and PAHs chemistry, it has been introduced for soot modeling (Frenklach, 1996).

Table 1.2: *HACA-RC mechanism for surface reactions modeling (Mauss et al., 2006). The efficient parameter γ_{OH} was updated by Rodrigues et al. (2017) based on Neoh et al. (1981) and (Xu et al., 2003). $C_{n_c}H$ represents the soot particle with n_c carbon atoms on its surface while $C^*_{n_c}$ and $C^*_{n_c}C_2H_2$ represent the radicals active sites.*

N°	Reaction	A	β	E_a (kJ/mol)
$R1_f$	$C_{n_c}H + H \longleftrightarrow C^*_{n_c} + H_2$	1.00 10^{14}	0.0	0.0
$R1_b$		1.439 10^{13}	0.0	-37.63
$R2_f$	$C_{n_c}H + OH \longleftrightarrow C^*_{n_c} + H_2O$	1.63 10^{8}	1.4	6.100
$R2_b$		1.101 10^{8}	1.4	31.14
R3	$C^*_{n_c} + H \rightarrow C_{n_c}H$	1.00 10^{13}	0.0	0.0
$R4_f$	$C^*_{n_c} + C_2H_2 \longleftrightarrow C^*_{n_c}C_2H_2$	3.50 10^{13}	0.0	0.0
$R4_b$		3.225 10^{14}	0.0	181.69
$R5_f$	$C^*_{n_c}C_2H_2 \longleftrightarrow C_{n_c+2}H + H$	1.00 10^{10}	0.0	20.00
$R5_b$		8.77 10^{11}	0.0	74.44
R6	$C^*_{n_c} + O_2 \rightarrow C^*_{n_c-2} + 2CO$	1.00 10^{12}	0.0	8.4
R6'	$C^*_{n_c}C_2H_2 + O_2 \rightarrow C^*_{n_c} + 2HCO$	1.00 10^{12}	0.0	8.4
R7	$C_{n_c}H + OH \rightarrow C^*_{n_c-2} + CH + HCO$	Efficiency : γ_{OH}= 0.13		

The HACA-like mechanisms are based on the concept of surface sites (Frenklach and Wang, 1991), which are carbon atoms at the surface, either saturated ($C_{n_c}H$) or dehydrogenated ($C^*_{n_c}$) that react with the surrounding gas-phase. According to it, a radical site is formed by abstraction of an H-atom on the soot particle surface, allowing C_2H_2, the most likely soot growth precursor in premixed hydrocarbon flames (J and M, 1985; Harris, 1990), to react with the particle increasing its mass. The oxidation via the soot particle surface reaction with O_2 and OH counterbalances the surface growth, leading to loss of mass. This model has been developed by considering soot production in premixed flames, but it is currently used for non-premixed flames. However, soot production is known to strongly depend on the combustion mode, i.e., diffusion or premixed flames through factors as reactants mixing, particle trajectory through the flame, and particle residence time and particle history (Wang et al., 1996; Hwang and Chung, 2001; Khosousi and Dworkin, 2015). Therefore, it is challenging to identify a model capable of correctly reproducing the different

soot production processes in both combustion regimes. For this reason, most of the time, the model is fitted and adjusted depending on the operating conditions. Among the different mechanisms proposed in the literature to describe soot surface reactions based on the HACA mechanism (Frenklach and Wang, 1991; Frenklach, 1996; Appel et al., 2000; Mauss et al., 1994), the HACA-RC mechanism proposed by Mauss et al. (1994) is retained as the reference surface reaction model. The validity of this model in laminar flames is discussed in Chapter2 and a modification is proposed in Chapter 3.

The HACA-RC comprises 8 heterogeneous reactions between surface sites and the gas phase, as described in Table 1.2. Reactions R1 and R2 describe the formation of active radicals sites at the soot surface ($C^*_{n_c}$ and $C^*_{n_c}C_2H_2$) by the abstraction of an atom of hydrogen H, allowing the initialization of the soot growth process. This reaction is counterbalanced by the reaction R3, the recombination of H with the soot particle, limiting the surface growth process. Once the radical site is created (R1 and R2), C_2H_2 can react with them through the reaction R4 to form bigger particles. Otherwise, the reaction R5, the "ring-closure" reaction, accounts for growth limitation at high temperatures to be consistent with the assumption of chemical similarity with PAHs. Finally, reactions R6, R6' and R7 are oxidation reactions that lead to mass soot reduction by reaction with O_2 and OH. All reactions are described by an Arrhenius law of the form $A \cdot T^{\beta} \cdot e^{(-E_a/RT)}$, where A is the pre-exponential factor, E_a the reaction activation energy, with kinetic coefficients (A, β, and E_a) based on analogous reactions with the soot particle precursor with four-ring aromatic pyrene (A4) (Mauss et al., 2006). The only exception is the reaction R7. Rodrigues et al. (2017) replaced the reaction constant by an efficiency collision parameter γ_{OH}, an empirical parameter based on the works of Neoh et al. (1981) and Xu et al. (2003). In this case, the reaction constant k_{7f} is defined as:

$$k_{7f} = \frac{\gamma_{OH}}{4} s_{C_2} N_A \left(\frac{8\mathcal{R}T}{\pi W_{OH}} \right)^{1/2} \tag{1.35}$$

where s_{C_2} is the surface of two atoms of carbon and W_{OH} is the OH molar weight.

Then, following this approach, the reaction rates of the surface growth ($\dot{\omega}_{sg}$) and oxidation ($\dot{\omega}_{ox}$) phenomena are obtained based on the reactions R4 and R6/R7 respectively:

$$\dot{\omega}_{sg} = k_{4f}[C^*_{n_c}][C_2H_2] - k_{4b}[C^*_{n_c}C_2H_2] \tag{1.36}$$

$$\dot{\omega}_{ox} = k_{6f}[O_2]([C^*_{n_c}] + [C^*_{n_c}C_2H_2]) + k_{7f}[C_{n_c}H][OH] \tag{1.37}$$

where k_{4f}, k_{4b}, k_{6f} and k_{7f} are the reaction constant of the reactions R4, R6 and R7, respectively, in Table 1.2. $[C^*_{n_c}]$ and $[C^*_{n_c}C_2H_2]$ corresponds to the concentration of radical active sites on the soot surface that can react with the gaseous species (C_2H_2 and O_2), while $[C_{n_c}H]$ is the concentration of site on the soot surface.

Therefore it is necessary to know the concentration of the involved gaseous species (C_2H_2, H, OH, O_2, H_2O, $H2$, CO, HCO) and to evaluate the active sites concentration $[C_{n_c}H]$ and the related radical sites $[C^*_{n_c}]$ and $[C^*_{n_c}C_2H_2]$ concentration. Whereas the resolution of the kinetic scheme, through the balance equation of the species mass fraction Eq. (1.3), provides the gaseous species concentration, the active sites concentration $[C_{n_c}H]$ and the radical sites $[C^*_{n_c}]$ and $[C^*_{n_c}C_2H_2]$ are modeled. Their expression are described in the following.

- Expression of the active sites concentrations $[C_{n_c}H]$

The active sites concentration $C_{n_c}H$ can be expressed as:

$$[C_{n_c}H] = \int_0^\infty \frac{\alpha.\lambda_{soot}.s(v).n(v)}{N_A} dv \tag{1.38}$$

where:

- α is the fraction of sites available for a given reaction
- λ_{soot} is the number of active sites per unit surface
- s is the soot surface for a particle of volume v
- $n(v)$ is the soot particle number per unit volume unity

The density of active sites λ_{soot} is obtained assuming that each active site occupies a surface corresponding to the surface of a C_2H_2 molecule (Netzell et al., 2007), i.e., $\lambda_{soot}s_{c_2} = 1$ with s_{c_2} the surface of two carbon atoms. In order to account for aggregated soot particles in surface growth and oxidation and avoid supplementary equations to describe soot surface, a surface-volume correlation can be introduced (Netzell et al., 2007; Aubagnac-Karkar et al., 2015; Mueller et al., 2009) to describe soot surface s as shown Eq (1.39). For that purpose a function $\theta(v)$ is introduced. If the particles are considered spherical $\theta(v) = 2$, otherwise a expression for $\theta(v)$ is required. It is described in Section 1.5 in the framework of the sectional method (Rodrigues et al., 2017).

$$\frac{s}{s_{C_2}} = \left(\frac{v}{v_{C_2}}\right)^{\theta(v)/3} \tag{1.39}$$

The fraction of effectively available sites on the soot surface α is a free parameter originally introduced to accounts for soot particle morphology changing, particle aging, and temperature effects on soot surface reactivity (Michael, 2002). Modeling soot surface structure and its evolution under the local flame conditions are very complex and are often neglected, notably in simple soot models. Then, α is often tuned in order to fit soot volume fraction with experimental values depending on the flame conditions (Frenklach and Wang, 1991; Dworkin et al., 2011). Empirical relations can also be found based on the temperature (Appel et al., 2000; Veshkini et al., 2014) and residence time (Singh et al., 2005). Since soot morphology is partially taken into account through s, and no universal formulation has been determined for α, in the present work, the fraction of available sites is taken equal to 1.

Finally, the active sites concentration $C_{n_c}H$ can be expressed as:

$$[C_{n_c}H] = \int_0^\infty \frac{n(v)}{N_A} \left(\frac{v}{v_{C_2}}\right)^{\theta(v)/3} dv \tag{1.40}$$

- Expression of the radical active sites concentrations $[C^*_{n_C}]$ and $[C^*_{n_C}C_2H_2]$

At a steady state conditions, the radical sites concentration $[C^*_{n_c}]$ can be determined as a function of the gas phase environment. Mauss et al. (1994) has assumed that the $C^*_{n_C}C_2H_2$ and $C^*_{n_C}$ are in a quasi-stationary state, i.e., the number of these active radical sites is considered at equilibrium during the reactions characteristic time scales. Then, based on chemical reactions of Table 1.2, a relation can be obtained to the radicals concentrations. In fact, using:

$$\frac{d[C^*_{n_C}C_2H_2]}{dt} = 0 \tag{1.41}$$

one obtains:

$$\begin{aligned} &k_{4f}[C^*_{n_C}][C_2H_2] - k_{4b}[C^*_{n_C}C_2H_2] - k_{5f}[C^*_{n_C}C_2H_2] \\ &+ k_{5b}[C_{n_C+2}H][H] - k_{6'f}[C^*_{n_C}C_2H_2][O_2] = 0 \end{aligned} \tag{1.42}$$

which leads to:

$$[C^*_{n_C}C_2H_2] = B[C^*_{n_C}] + D[C_{n_C}H] \tag{1.43}$$

with:

$$\begin{cases} B = \dfrac{k_{4f}[C_2H_2]}{k_{4b} + k_{5f} + k_{6'f}[O_2]} \\ \\ D = \dfrac{k_{5b}[H]}{k_{4b} + k_{5f} + k_{6'f}[O_2]} \end{cases} \tag{1.44}$$

with the hypothesis that $C_{n_C+2}H \approx C_{n_C}H$.

$C^*_{n_C}$, $C^*_{n_C+2}$ and $C^*_{n_C-2}$ are considered to be equivalent. The quasi-stationary assumption for these quantities, as suggested by Mauss et al. (1994). Then, combining the results obtained in this equation with Eq. (1.43), one obtains:

$$\frac{d[C^*_{n_C}]}{dt} + \frac{d[C^*_{n_C+2}]}{dt} + \frac{d[C^*_{n_C-2}]}{dt} = 0 \tag{1.45}$$

which leads to

$$\begin{aligned} & k_{1f}[C_{n_C}H][H] + k_{2f}[C_{n_C}H][OH] - k_{1b}[C^*_{n_C}][H_2] - k_{2b}[C^*_{n_C}][H_2O] \\ & - k_{3f}[C^*_{n_C}][H] + k_{3b}[C_{n_C}H] - k_{4f}[C^*_{n_C}][C_2H_2] + k_{4b}[C^*_{n_C}C_2H_2] \\ & - k_{6f}[C^*_{n_C}][O_2] + k_{6'f}[C^*_{n_C}C_2H_2][O_2] + k_{6f}[C^*_{n_C}][O_2] \\ & + k_{7f}[C_{n_C}H][OH] = 0 \end{aligned} \tag{1.46}$$

Combining this equation with Eq. (1.43), one obtains:

$$\begin{aligned} & (k_{1f}[H] + k_{2f}[OH] + k_{3b} + k_{7f}[OH])[C_{n_C}H] + \\ & (k_{6'f}[O_2] + k_{4b})\frac{k_{4f}[C_2H_2]}{k_{4b} + k_{5f} + k_{6'f}[O_2]}[C^*_{n_C}] \\ & + (k_{6'f}[O_2] + k_{4b})\frac{k_{5b}[H]}{k_{4b} + k_{5f} + k_{6'f}[O_2]}[C_{n_C+2}H] \\ & = (k_{1b}[H_2] + k_{2b}[H_2O] + k_{3f}[H] + k_{4f}[C_2H_2])[C^*_{n_C}] \end{aligned} \tag{1.47}$$

In the same way, $C_{n_C+2}H$ and $C_{n_C}H$ are considered equivalent. Then, the following equation is verified:

$$[C^*_{n_C}] = A[C_{n_C}H] \tag{1.48}$$

Finally, combining Eq. (1.43) and Eq. (1.48), the following expression can be obtained for $[C^*_{n_C}]$:

$$[C^*_{n_C}] = (AB + D)[C_{n_C}H] \tag{1.49}$$

where B and D are defined in Eq.(1.44).

The ratio between the consumption and the production of radical active site is written as:

$$A = \frac{\overbrace{k_{1f}[H] + k_{2f}[OH] + k_{3b} + k_{7f}[OH] + k_{5b}[H](1 - f_{R4_f})}^{\text{radical formation}}}{\underbrace{k_{1b}[H_2] + k_{2b}[H_2O] + k_{3f}[H] + k_{4f}[C_2H_2]f_{R4}}_{\text{radical consumption}}} \tag{1.50}$$

with,

$$f_{R4} = \frac{k_{5f}}{k_{5f} + k_{4b} + k_{6'f}[O_2]} \tag{1.51}$$

The reaction constant ratio f_{R4} represents the surface growth progress. If the ring formation via the forward reaction R5 (k_{5f} in Table 1.2) is faster than the oxidation reaction R6 ($k_{6'f}$ in Table 1.2) and radical site $[C^*C_2H_2]$ consuming reaction (k_{5f} and k_{4b} in Table 1.2), then $f_{R4} = 1$ and the reaction of C_2H_2 addition leading to soot growth (R4 forward reaction k_{4f} in Table 1.2) is dominant. Otherwise, if oxidation and ring formation are significant $f_{R4} = 0$ and the reverse reaction R4 (k_{4b} in Table 1.2) is dominant, the growth of soot particles is limited.

- Expression of surface reaction rates

Thereby, the surface growth and oxidation rates, can be written as:

$$\dot{\omega}_{sg} = (k_{4f} A[C_2H_2] - k_{4b}(AB + D))[C_{n_c}H] \tag{1.52}$$

$$\dot{\omega}_{sg} = k_{sg}[C_{n_c}H] \tag{1.53}$$

$$\dot{\omega}_{ox} = k_{6f}[O_2](A(1 + B) + D)[C_{n_c}H] + k_{7f}[C_{n_c}H][OH] \tag{1.54}$$

$$\dot{\omega}_{ox} = k_{ox}[C_{n_c}H] \tag{1.55}$$

where $[C_{n_c}H]$ is obtained through Eq. (1.40)and the reaction constants k_{sg} and k_{ox} depend only on the gas phase composition.

1.4 Numerical approaches for soot particles evolution

Several numerical approaches exist in the literature to describe soot dynamics. They are generally classified as a function of their ability to access the particle size distribution (PSD) and its evolution once the different physical and chemical kinetics processes of soot production have been specified. Simple numerical approaches are generally based on empirical or semi-empirical correlations assuming a monodisperse soot population. On the opposite side, detailed approaches require the solution of the NDF $n(t, x, \xi)$ equation. To simplify the problem, univariate NDF, generally based on the volume of the soot particle ($\xi = \xi(v)$) is considered. In this case, global quantities as the total number density of particles and the volume fraction can be retrieved as well as the particle size distribution (PSD), but no information on the soot particle structure is available, the soot population is generally considered as spherical. Alternatively, surface-volume relations can be introduced to account for soot fractality. Finally, bivariate models, commonly based on soot particle volume and surface ($\xi = \xi(v, s)$), give particle morphology access. However, the modeling complexity and the computational cost to solve the PBE are increased.

A brief description of the numerical models used to describe soot dynamics is presented in the following. A comprehensive review has been recently proposed by Rigopoulos (2019).

1.4.1 (Semi -) Empirical models

The empirical and semi-empirical models are the first family of soot models to be developed in the early seventies. Empirical models are generally based on empirical correlations of soot formation and evolution related to temperature or mixture fraction. Kennedy et al. (1990) proposed a one-equation model considering soot particle oxidation. The model is able to correctly reproduce soot volume fraction evolution in a laminar co-flow ethylene-air flame using

a correction function depending on the mixture fraction. Moss et al. (1989) proposed a model with two equations, one for the soot mass fraction and another for the particle number density with empirical correlations describing the nucleation and surface growth as a function of the mixture fraction and temperature, while coagulation is a function of temperature and the square root of the particle number density. Since soot oxidation is not considered, the ability to describe soot volume fraction evolution is limited. Although the low computational cost and easy implementation, these models are not general since the empirical parameters are 'ad-hoc' or a function of the experimental conditions leading to a lack of physical description.

Semi-empirical models generally solve the soot mass and/or the total number density balance equations, with C_2H_2 being considered a soot precursor. Leung et al. (1991) proposed a two-equation model transporting the soot mass fraction and the number density of particles. Nucleation and coagulation are considered for the number density of particles equation, while nucleation and surface reactions (surface growth and oxidation) are considered for the soot mass equation. Nucleation and surface reactions are modeled as chemical mechanisms, whose reaction rates are expressed through the Arrhenius law. Lindstedt (1994) added the benzene (A1) as soot precursor validating the model in propane-air and ethylene-air counterflow diffusion flames. Due to its relatively low cost and easy coupling with turbulent models, this model has been extensively used to model soot production in turbulent flames (Lindstedt and Louloudi, 2005; Bolla et al., 2013; Felden et al., 2018; Gallen et al., 2018). Brookes and Moss (1999) has improved the Moss et al. (1989) empirical model, including oxidation and considering C_2H_2 as a soot precursor contributing to soot particle nucleation and surface growth, instead of the fuel concentration. Dependence of the source terms on pressure is also introduced in the semi-empirical version to simulate a turbulent methane-air jet flame at elevated pressure with good success. Even if satisfactory results are obtained for a small CPU cost once the model's parameters have been fitted on some reference test cases, this type of model provides information only on global quantities (soot particle distribution and morphology are no accessible), and their validity is quite limited.

1.4.2 Solving the Population Balance Equation

In order to access soot particles size distribution and morphology and properly accounts for soot particles dynamics, the solution of the PBE is required. In the following the main approaches used to solve the PBE in the literature are presented.

Stochastic methods

Soot particles are considered as discrete particles whose evolution is solved using an explicit Monte Carlo (MC) technique. This method allows accessing the particle size distribution without any assumption on the particle size distribution shape and soot morphology since a stochastic particle can carry different properties. However, this methodology is costly because a large number of particles are required to obtain convergence. Consequently, the application in turbulent flames is not affordable. Besides that, MC is not easily coupled explicitly to the gas-phase chemistry. The gas phase chemistry and the soot dynamics are solved separately, using a classic determinist solver for the gas phase that feeds the probabilistic solver with the chemical species profiles (Balthasar and Kraft, 2003; Singh et al., 2005). Thereby, in such a strategy, the two-way coupling is therefore not always considered, otherwise specific numerical methods are required (Celnik et al., 2007).

Discretization methods

This method are based on the discretization of the PBE. Two types can be found in the literature: the kinetic discrete sectional model and the aerosol discrete sectional model.

In kinetic models, soot particle volume is discretized in "BINs" (in terms of the number of carbons) characterized by their molecular mass and number of carbon and hydrogen atoms, which are integrated into the gaseous kinetic scheme. Then, soot evolution is resolved as the other chemical species through the transport of mass fraction and the interaction between "BINs" are treated as chemical reactions. This strategy allows for easy coupling between soot and gas phases enabling access to the particle size distribution. The particle size distribution is generally univariate based on the spherical soot particles (Richter et al., 2005; D'Anna, 2008; Blacha et al., 2012) giving access to the size distribution but not to the particle morphology. Saggese et al. (2015) proposed to include the fractal feature of soot particles through the fractal dimension D_f and adjusting the frequency factor for the surface reactions. Bodor et al. (2019) has prosed a post-processing tool to access the primary particle size. The method was applied in a premixed flat flame and non-premixed co-flow flames. The soot volume fraction was quite well reproduced for the premixed flames while it was underpredicted for the non-premixed flames, but the better prediction is obtained for the mean primary diameter compared to the results obtained assuming spherical aggregates or constant primary particle size for all aggregates. This family of methods presents the drawback of requiring high CPU cost as a detailed mechanism and a large number of BINS are needed to describe soot formation. Application is generally limited to laminar flames.

In the sectional models, soot particle is considered an individual phase and the soot particle size distribution is divided into different size (volume) classes. These volume classes called "sections" enable access to the particle size distribution without any assumption on its shape. Then, the particle size distribution is accessible through the transport of soot moments for each section. Bivariate moments enable soot particle morphology description (Zhang et al., 2009), but the CPU cost sharp increases. Thereby, this method has been limited to univariate description coupled with a surface-volume law to account for soot fractality (Rodrigues et al., 2017). The numerical accuracy of the particle size distribution depends on the number of sections leading to high CPU cost compared to the method of moments. Commonly used in RANS simulations (Netzell et al., 2007; Aubagnac-Karkar et al., 2015), it has recently been coupled with LES flow equations by Rodrigues et al. (2018) allowing the investigation of the spatial and temporal resolution of the PSD in turbulent flames.

Method of moments

The method of moments solves the PBE through the transport of statistical moments of the NDF instead of the NDF itself. These moments can be univariate or multi-variate. For a uni-variate description the moment M_x of order x based on particle volume space is formulated as:

$$M_x = \int_{v=0}^{+\infty} n(v) v^x dv \tag{1.56}$$

For a bivariate description the moment $M_{x,y}$ is based on the particle volume and surface space, with order x in the volume and order y in the surface. It is formulated as:

$$M_{x,y} = \int_{v=0}^{+\infty} \int_{s=0}^{+\infty} n(v) v^x s^y dv ds \tag{1.57}$$

The bivariate description gives access to statistical moments that correspond to physical soot properties as $M_{0,0}$, $M_{1,0}$, and $M_{0,1}$, corresponding respectively to the particle number density, the total soot volume, and the total soot surface. These first moments enable accounting for the soot particle's fractal nature without any presumed s-v correlation.

This family of models presents the advantage of requiring a low number of variables to describe soot particles resulting in a small computation cost compared to the sectional and Monte Carlo methods. However, unknown moments (non-transported moments) are needed to treat the source terms, requiring approximations and closure models. Several methods have been developed to close the source terms and reconstruct the PSD. The Method of Moments with

Interpolative Closure (MOMIC) (Frenklach, 2002) approximates the unknown moments by logarithmic interpolation from the known moments. This method is numerically well-defined and easy to implement, but it fails to describe bimodal distributions. The Direct Quadrature Method of Moments (DQMOM) (Marchisio and Fox, 2005), an extension of the original QMOM (Quadrature Method of Moments) (Marchisio et al., 2003), reconstructs the PSD by a series of delta function transporting the weights and locations of the delta functions. The moments are approximated by Gauss quadrature. In opposition to MOMIC and QMOM, the DQMOM can capture the soot population's bimodality, even for multi-variate distributions. Although it can be considered a good candidate for numerical simulations due to its accuracy and easy coupling with CFD codes, it is numerically ill-posed, leading to difficulties in its use. In order to capture the bimodality of the PSD, Mueller et al. (2009) have developed the Hybrid Method of Moment (HMOM) by associating the MOMIC and the DQMOM. Due to the relatively low computational cost, the methods of moments have been extensively used to simulate sooting turbulent flames via LES approach (El-Asrag et al., 2007; Mueller and Pitsch, 2012, 2013). The presented models are only a summary of the most common method of moments found in the literature, many other variations can be found (Blanquart and Pitsch, 2007; Salenbauch et al., 2015; Nguyen et al., 2016).

The three equation model developed by Franzelli et al. (2018) is based on a bivariate NDF transporting three soot moments: the total particles number, the total mass and the total surface. Compared to the others method of moments, the mathematical treatment of the source terms is more straightforward as it does not depend on the unknown moments. By assuming a mono-disperse distribution the sources terms are closed by a Dirac-delta function. The three equation soot model was evaluated in the DLR burner, a gas turbine model combustor. Compared to the sectional method with 25 sections (Rodrigues et al., 2018), this model reproduces with the same accuracy the global soot quantities (f_v and N_s) with a computational cost three times lower than the sectional case. However, only the evolution of global quantities of the particle population is provided. The particle size distribution (PSD) has to be reconstructed.

Lagrangian Soot Tracking (LST) Method

The previous numerical approaches are based on Eulerian formalism, where the soot population is considered a continuous phase as the carrier gas phase. In the Lagrangian-based approaches, the soot population is treated as a discrete phase where soot particles are tracked along their trajectory. Particle-particle interaction and particle-gas interaction are then considered individually. Therefore, the LST formalism provides a direct description of the polydispersity of the soot population. Very recent studies on Lagrangian soot particle tracking

methodology can be found in the literature. Ong et al. (2018) developed an LST model able to predict primary soot particle size based on the Brookes and Moss (1999) semi-empirical model, including nucleation, surface reactions (growth and oxidation) phenomena. However, the interaction between particles (coagulation) was neglected. Although the simplified model, the mean diameter distribution and the measured lognormal shape of the primary soot size distribution in n-heptane and n-dodecane spray flames were captured. Gallen et al. (2018) proposed a semi-deterministic LST model based on a Lagrangian formalism for two-phase flows. The soot model (Leung et al., 1991) included the description of C_2H_2-based nucleation, surface reactions (growth and oxidation) and coagulation phenomena. In order to reduce the computational cost, numerical particles defined as a sub-set of physical particles with the same properties at the same location and time are considered. The sub-set called *rparcels* can vary in space in time to preserve local statistical convergence. Compared to an eulerian approach based on a semi-empirical formulation for soot, it was demonstrated that the model provides the NDF with a negligible increase in the CPU cost in the DLR burner. The model was further extended to include detailed chemistry (Gallen, 2020), including PAH-based nucleation and a bivariate soot description. The improved LST model was validated in laminar flames. Applied in the DLR burner, the soot volume fraction is slightly overpredicted. Dellinger (2019); Dellinger et al. (2020) have proposed a Lagrangian formalism, also based on the concept of numerical particles, combining a sectional model for the soot precursors and a Lagrangian description for the soot particles accounting for a detailed description of the phenomena involved in soot production. The model was validated in ethylene-air premixed flames and applied to the DLR burner, where the spatial distribution of the soot volume fraction is quite well captured, including the regions near the wall.

Hybrid methods

Hybrid methods combining different categories of the model have been developed. Aksit and Moss (2006) have proposed a hybrid model for turbulent flames based on a Lagrangian Monte Carlo solution for a joint transported PDF for mixture fraction and soot quantities and an Eulerian solution for the flow field. This strategy enables tracking the evolution of soot particles, but it requires high computational resources. More recently, Yang et al. (2019) have proposed a multi-moment sectional method (MMSM) for tracking the soot number density function $n(v)$. Instead of transporting a single statistical moment for each section, many moments can be used, allowing the reconstruction of the local NDF. The model evaluation in a laminar premixed flame shown that the MMSM is computationally low cost compared to the classical sectional method. By assuming a single section, the model is reduced to a method of moments. (Bouaniche et al., 2019) have proposed a stochastic-sectional method combin-

ing Monte-Carlo and sectional methods to solve the particle size distribution. Compared to the classical sectional method, the model provides better accuracy with a comparable CPU cost for the performed canonical test cases.

To summarize, (semi-)empirical models present the lowest cost, but it does not provide morphological either PSD description required to respond to the increasingly restrictive environmental regulations. The method of moments presents a low cost since only a few moments are transported. It provides a morphological description but presents a high mathematical complexity to close the source terms which depend on the unknown moments. The three-equation model overcomes this issue by assuming a mono-disperse distribution, which was found to provides a good prediction of soot production in the DLR burner, the target flame of this thesis. Moreover, the PSD is not always accessible, requiring a PSD-reconstruction strategy. Even if kinetic and stochastic methods provide both PSD and morphological description, these methods are costly to be applied in complex turbulent flames. The sectional model provides PSD information and a morphological description with a reduced computational cost is possible through a volume-surface model. For the hybrid models, morphological and PSD description may be accessed depending on the coupled methods. Finally, the Lagrangian models may provide both morphological and PSD information. However, CPU cost and statistical convergence depend on the number of particles tracked, requiring an optimization algorithm to survey statistical convergence while keeping CPU cost affordable.

For the simulations presented in this manuscript, two soot models are retained. For the laminar flames, the sectional model is used. This model was validated in laminar premixed flames (Rodrigues et al., 2017) and used in LES simulation of a non-premixed jet flame (Rodrigues et al., 2018) and a pressurized swirl burner (DLR burner) (Rodrigues, 2018). Despite the good predictability of this model, high computational resources are required for the 3D turbulent simulations. In addition to the gaseous equations, more than 20 balance equations (sections) are generally required to accurately describe the soot population (with a monovariate description). Therefore, the three equation model is retained for the LES computations of the DLR burner since this strategy reduces the CPU cost by a factor of 3 compared to a computation using the sectional formalism with 25 sections (Franzelli et al., 2018). Both sectional and three equation models are presented in the following.

1.5 Sectional method

In the sectional method the PSD with a fixed interval of volume $[v_{MIN}, v_{MAX}]$ is divided into i = 1 to $N_{sections}$ intervals (sections) of size within $[v_i^{min}, v_i^{max}]$. A univariate sectional method has been retained here. Then a unique soot

scalar is transported for each section. By multiplying the univariate NDF $n(v)$ by the volume v and integrating it over the volume of the section, the total soot volume fraction $Q_{s,i}$ for each section is obtained and the transport equation for $Q_{s,i}$ can be written as:

$$\frac{\partial Q_{s,i}}{\partial t}+\frac{\partial}{\partial x_i}(u_i Q_{s,i})-\frac{\partial}{\partial x_i}\left(0.554\frac{\nu}{T}\frac{\partial T}{\partial x_i}Q_{s,i}\right)=\frac{\partial}{\partial x_i}\left(D_{s,i}\frac{\partial Q_{s,i}}{\partial x_i}\right)+\dot{\omega}_{Q_{s,i}} \quad (1.58)$$

with

$$Q_{s,i}=\int_{v_i^{min}}^{v_i^{max}} n(v)v dv=\int_{v_i^{min}}^{v_i^{max}} q_i(v)dv \quad (1.59)$$

where $q_i(v)$ is the volume distribution in the section i^{th}, which is considered constant for each section i, $q_i(v)=q_i(v_{mean})$, with $v_{mean}=(v_i^{max}+v_i^{max})/2$. D_s is the soot diffusion coefficient and the third left-hand side term is the thermophoresis modeled as discussed in Section 1.2.

The total number density of particles N_s and the total mass M_s are of most relevance to characterizing soot particle population, notably regarding comparison and validation against experimental data. Therefore, considering a constant density to the soot particles $\rho_s=1.86\cdot 10^3 kg/m^3$, m_s can be linked to the total soot volume v_s through the expression:

$$m_s=\rho_s v_s=Y_s M \quad (1.60)$$

with Y_s the soot mass fraction and $M=\rho V$ is the total mass of the system.

Then, the soot volume fraction of each section $Q_{s,i}$ can be expressed as a function of the soot mass fraction $Y_{s,i}$ of each section though the relation:

$$Q_{s,i}=\frac{V_{s,i}}{V}=\frac{m_{s,i}}{\rho_s V}=\frac{Y_{s,i}M}{\rho_s V}=\frac{\rho}{\rho_s}Y_{s,i} \quad (1.61)$$

Equation (1.58) finally writes as:

$$\frac{\partial \rho Y_{s,i}}{\partial t}+\frac{\partial \rho Y_{s,i}u_i}{\partial x_i}-\frac{\partial}{\partial x_i}\left(0.554\frac{\nu}{T}\frac{\partial T}{\partial x_i}\rho Y_{s,i}\right)=\frac{\partial}{\partial x_i}\left(D_s\frac{\partial \rho Y_{s,i}}{\partial x_i}\right)+\rho_s\dot{\omega}_{Q_{s,i}} \quad (1.62)$$

The soot diffusion flux, the first right-hand side term, is approximated as:

$$\frac{\partial}{\partial x_i}\left(D_s\frac{\partial \rho Y_{s,i}}{\partial x_i}\right)\approx \rho D_{s,i}\frac{\partial Y_{s,i}}{\partial x_i} \quad (1.63)$$

The production rate of the soot volume fraction $\dot{\omega}_{s,i}$ for the i^{th} section accounts for nucleation ($\dot{\omega}_i^{nucl}$), condensation ($\dot{\omega}_i^{cond}$), coagulation ($\dot{\omega}_i^{coag}$) and surface reactions ($\dot{\omega}_i^{sg}$ and $\dot{\omega}_i^{ox}$).

For a PSD assumed constant in each section, it can be considered that an infinitesimal part of soot particles volume fraction $q(v)dv$ having a volume belonging to the interval $[v;\ v+dv]$ is equal to the product of the number density of soot particles $n(v)dv$ belonging to the interval $[v;\ v+dv]$ by the volume of these soot particles v, the $n(v)$ can be defined as:

$$n(v) = q(v)/v \tag{1.64}$$

Then, the number density of particles $N_{s,i}$ of the i^{th} section can be obtained through the integral of $n(v)$ for each section i as:

$$N_{s,i} = \int_{v_i^{min}}^{v_i^{max}} \left(\frac{q(v)}{v}\right) dv = q(v_i^{mean}) \ln\left(\frac{v_i^{max}}{v_i^{min}}\right) \tag{1.65}$$

where $q(v_i^{mean})$ is the soot volume fraction density of the i^{th} section based on the mean volume of the section v_i^{mean} defined as $v_i^{mean} = (v_i^{min} + v_i^{max})/2$.

Finally, soot volume fraction f_v and total number density of particles N_s can be obtained as:

$$f_v = \sum_{n=1}^{N_{sections}} Q_{s,i} = \sum_{n=1}^{N_{sections}} q_i(v_i^{max} - v_i^{min}) \tag{1.66}$$

$$N_s = \sum_{n=1}^{N_{sections}} N_{s,i} = \sum_{n=1}^{N_{sections}} q_i \ln\left(\frac{v_i^{max}}{v_i^{min}}\right) \tag{1.67}$$

1.5.1 Soot volume discretization

The sectional method presented here is the one developed by Rodrigues et al. (2017). To define the size of each section, the model is based on the solution proposed by Netzell et al. (2007), where a power law describes the volume space occupied by each section identified by the index i. Then, for a discretization with $N_{sections}$, the maximum and the minimum particle volume v_i^{max} and v_i^{min} in the section i verifies the relation:

- For $i = 1$, the first section, has the dimension of nascent particles issued from the dimerization:

$$v_1^{min} = v^{MIN} \tag{1.68}$$

$$v_1^{max} = v^{MIN} + v_{dim} \tag{1.69}$$

where $v^{MIN} = v_{C_2}$ the volume of a spherical molecule composed of two carbon atoms and v_{dim} is the volume of a dimer.

- For $i \in [2, N_{sections-1}]$ the volume of each section follows the geometrical progression.

$$v_i^{max} = v_1^{max} \left(\frac{v^{MAX}}{v_1^{max}} \right)^{\frac{i-1}{N_{sections-2}}} \tag{1.70}$$

$$v_i^{min} = v_{i-1}^{max} \tag{1.71}$$

where v^{MAX} corresponds to the biggest soot particle and v_1^{max} is the maximum volume of the first section $i = 1$. The volume interval $[v_i^{min}, v_i^{max}]$ of each section i is bigger than the sum of all the volume intervals of the smaller sections.

In order to consider unexpected unphysical volumes and ensures soot mass conservation, Rodrigues et al. (2017) has added a special section, called "trash section", corresponding to the last section $i = N_{sections}$, where soot volume varies from v^{MAX} to v^{BIG}, where v^{MAX} corresponds to the biggest soot particle volume considered and v^{BIG} to the maximum possible volume.

1.5.2 Soot source terms

Nucleation

The source term of nucleation is modeled as:

$$\dot{\omega}_{nucl} = v_{dim} \beta_{v_{dim}}^{fm} N_{dim}^2 \delta_{i1} \frac{1}{\rho} \tag{1.72}$$

where δ_{i1} is the Kronecker delta factor enabling nucleation to be considered only in the first section and N_{dim} is the number density of dimers and $\beta_{v_{dim}}^{fm}$ is

the collision frequency between dimers in the free molecular regime in the limit of small particles:

$$\beta_{v_{dim}}^{fm} = 2.5\left(\frac{3}{4\pi}\right)^{1/6}\sqrt{\frac{6k_bT}{\rho_s}}4\sqrt{2}v_{dim}^{1/6} \tag{1.73}$$

Condensation

The source term of condensation is composed of three terms: a term describing the mass addition into a section, and two terms describing the drift of the particles into the neighboring sections due to the size changing. The global condensation rate for one section is written as:

$$\dot{\omega}_i^{cond} = \dot{\omega}_{dimer\to i}^{cond} + \dot{\omega}_{i-1\to i}^{cond} - \dot{\omega}_{i\to i+1}^{cond} \tag{1.74}$$

- Mass addition into a section:

$$\dot{\omega}_{dimer\to i}^{cond} = \frac{N_{dim}}{\rho}v_{dim}\int_{v_i^{min}}^{v_i^{max}-v_{dim}}\beta_{i,dim}^{fm}n(w)dw \tag{1.75}$$

- Mass transfer between neighboring sections:

$$\dot{\omega}_{i-1\to i}^{cond} = \frac{N_{dim}}{\rho}\int_{v_{i-1}^{max}-v_{dim}}^{v_{i-1}^{max}}\beta_{i-1,dim}^{fm}n(w)(w+v_{dim})dw \tag{1.76}$$

$$\dot{\omega}_{i\to i+1}^{cond} = \frac{N_{dim}}{\rho}\int_{v_i^{max}-v_{dim}}^{v_i^{max}}\beta_{i,dim}^{fm}n(w)wdw \tag{1.77}$$

The collisional frequency between a dimer and a soot particle, in the free molecular regime, is considered constant in the section i and is expressed as:

$$\beta_{v_{dim}}^{fm} = 1.3\left(\frac{3}{4\pi}\right)^{1/6}\sqrt{\frac{6k_bT}{\rho_s}}\sqrt{\frac{1}{v_{dim}}\frac{1}{v_i^{mean}}}\left(v_{dim}^{1/3}+\left(\frac{\pi}{6}\right)^{1/3}d_{c,i}\right)^2 \tag{1.78}$$

The collisional diameter of a section is defined as: $d_{c,i} = d_{p,i}n_{p,i}^{1/D_f}$, where D_f = 1.8 is the fractal dimension previously introduced in Section 1.3.

Coagulation

From a numerical point of view, coagulation represents the collision between two different distributions issued from different sections. Therefore, the coagulation rate for a section i is the combination of two terms, one describing the particles from the collision between others sections j and k entering the section i, the other describing the loss of particles in section i through another section j.

- Particles entering section i:

$$\dot{N}_{jk\to i}^{coag} = \int\int_{v+w\in[v_i^{min},v_i^{max}]} \beta_{j,k} n_k(k) dv dw \tag{1.79}$$

- Particles leaving section i:

$$\dot{N}_{ij}^{coag} = \int_{v_i^{min}}^{v_i^{max}} \int_{v_j^{min}}^{v_j^{max}} \beta_{i,j} n_i(v) n_j(w) dv dw \tag{1.80}$$

The global coagulation source terms writes as:

$$\dot{\omega}_i^{coag} = \frac{1}{\rho} \int_{v_i^{min}}^{v_i^{max}} \left(\sum_{j,k=1}^{i} \dot{N}_{jk\to i}^{coag} - \sum_{j=1}^{N_{sections}} \dot{N}_{ij} \to i^{coag} \right) v dv \tag{1.81}$$

The collision frequency $\beta_{i,j}$ is evaluated at the mean volume of the respective sections and is modeled according to the collisional particle size as $\beta_{i,j} = \min(\beta_{i,j}^{fm}, \beta_{i,j}^{c})$, where $\beta_{i,j}^{fm}$ is the collision between particles in the free molecular regime and $\beta_{i,j}^{c}$ is the collision between particles in the continuous regime.

$$\beta_{i,j} = \min \begin{cases} \beta_{i,j}^{fm} = 2.2 \left(\frac{3}{4\pi}\right)^{1/6} \sqrt{\frac{6k_bT}{\rho_s}} \sqrt{\frac{1}{v_{dim}} \frac{1}{v_i^{mean}}} \left(v_j^{mean} + (d_{c,i} + d_{c,j} \right)^2 \\ \beta_{i,j}^{c} = 2.2 \frac{2k_bT}{2\mu} (d_{c,i} + d_{c,j})^2 \left(\frac{Cu_i}{d_{c,i}} + \frac{Cu_j}{d_{c,j}} \right) \end{cases}$$

Recalling that the Cu_i and Cu_j are the Cunningham corrective coefficient for a particle of section i and j, respectively:

$$Cu_i = 1 + 1.257 Kn_i = 1 + 1.257 \frac{2\lambda_{gas}}{d_{c,j}} \tag{1.82}$$

where Kn_i is the Knudsen number is defined using the collision diameter $d_{c,j}$.

Surface reactions: surface growth and oxidation

Similarly to condensation, the source term of surface growth and oxidation is composed of three terms: a term describing the mass addition in a section due to reactions between the surface particle and the gaseous phase, and two terms describing the drift of the particles into the neighboring section due to the size changing. Soot surface growth results in an increase of mass by the addition of a volume of two carbons (v_{C_2}), while oxidation corresponds to a loss of mass corresponding to v_{C_2}.

The global surface growth and oxidation rates are, respectively, written as:

$$\dot{\omega}_i^{sg} = \dot{\omega}_{gas\to i}^{sg} + \dot{\omega}_{i-1\to i}^{sg} - \dot{\omega}_{i\to i+1}^{sg} \tag{1.83}$$

$$\dot{\omega}_i^{ox} = -\dot{\omega}_{gas\to i}^{ox} - \dot{\omega}_{i-1\to i}^{ox} + \dot{\omega}_{i\to i+1}^{ox} \tag{1.84}$$

- Mass addition/loss through surface reactions:

$$\dot{\omega}_{gas\to i}^{sg} = \frac{k_{sg}}{\rho} v_{C_2} \int_{v_i^{min}}^{v_i^{max}-v_{C_2}} \left(\frac{w}{v_{C_2}}\right)^{\theta_i/3} n(w)dw \tag{1.85}$$

$$\dot{\omega}_{gas\to i}^{ox} = \frac{k_{ox}}{\rho} v_{C_2} \int_{v_i^{min}+v_{C_2}}^{v_i^{max}} \left(\frac{w}{v_{C_2}}\right)^{\theta_i/3} n(w)dw \tag{1.86}$$

- Mass transfer between neighboring sections:

$$\dot{\omega}_{i-1\to i}^{sg} = \frac{k_{sg}}{\rho} \int_{v_{i-1}^{max}-v_{C_2}}^{v_{i-1}^{max}} \left(\frac{w}{v_{C_2}}\right)^{\theta_{i-1}/3} n(w+v_{C_2})dw \tag{1.87}$$

$$\dot{\omega}_{i\to i+1}^{sg} = \frac{k_{sg}}{\rho} \int_{v_i^{max}-v_{C_2}}^{v_i^{max}} \left(\frac{w}{v_{C_2}}\right)^{\theta_i/3} n(w)dw \tag{1.88}$$

$$\dot{\omega}_{i+1\to i}^{ox} = \frac{k_{ox}}{\rho} \int_{v_{i+1}^{min}}^{v_{i+1}^{min}+v_{C_2}} \left(\frac{w}{v_{C_2}}\right)^{\theta_{i-1}/3} n(w+v_{C_2})dw \tag{1.89}$$

$$\dot{\omega}_{i\to i-1}^{ox} = \frac{k_{ox}}{\rho} \int_{v_i^{min}}^{v_i^{min}+v_{C_2}} \left(\frac{w}{v_{C_2}}\right)^{\theta_i/3} n(w)dw \tag{1.90}$$

where k_{sg} and k_{ox} are the reaction constantes obtained with the HACA-RC mechanism described in Section 1.3.3. $\theta(v)$ is the fractal function introduced in Section 1.3 to describe soot surface and allows to partially take into account soot morphology Rodrigues et al. (2017) has derived a expression for $\theta(v)$ by fitting numerical results from Salenbauch et al. (2015) and Mueller et al. (2009) (see Figure 1.3).

$$\theta(v) = \begin{cases} 2 \text{ if } v < v_1 \\ 3.0\dfrac{\log(\frac{v}{v1}) + \frac{2}{3}(\log\frac{v1}{v_{c2}})}{\log(\frac{v}{v_{c2}})} \text{ if } v > v_1 \end{cases} \tag{1.91}$$

where v_{c2} and s_{c2} are the volume and surface corresponding to the volume and surface of two atoms of carbon, respectively. $v_1 = 10^{2.6}\ nm^3$ denotes the volume beyond which soot particle is no longer considered as spherical. Then for $v < v_1$ soot particles are spherical ($n_p = 1$ and $d_p = (6v/\pi)^{1/3}$). Otherwise, soot particles are considered as aggregates particles composed of n_p primary particles of diameter d_p.

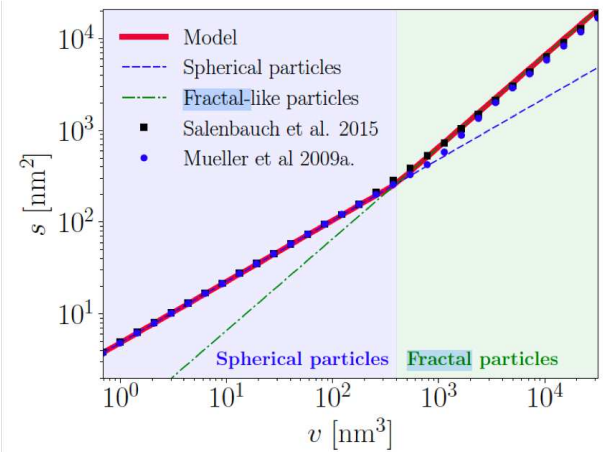

Figure 1.3: *Presumed relationship between soot particle surface and soot particle volume from (Rodrigues, 2018).*

1.6 Three-equation formalism

This section presents the three-equation soot model by Franzelli et al. (2018). The model is used in the LES simulations presented in this manuscript. It is based on a bivariate volume-surface NDF $n(x, t, v, s)$, with the soot particle

volume v and surface s as internal coordinates. Similarly to the moment methods, the bivariate NDF is represented by a finite set of its statistical moments $M_{x,y}$, which represent physical quantities. They are the total number density of particles N_s, the total soot volume fraction f_v and the total soot surface S_s:

$$M_{0,0} = N_s = \int_{v=0}^{+\infty} \int_{s=0}^{+\infty} n(v) dv ds \tag{1.92}$$

$$M_{1,0} = Y_s = \int_{v=0}^{+\infty} \int_{s=0}^{+\infty} n(v) v dv ds \tag{1.93}$$

$$M_{0,1} = S_s = \int_{v=0}^{+\infty} \int_{s=0}^{+\infty} n(v) s dv ds \tag{1.94}$$

Therefore, only three transport equations are used to describe soot population, instead of the $N_{sections}$ equations for the sectional method, as follows:

$$\frac{\partial \rho Y_s}{\partial t} + \frac{\partial}{\partial x_i} \left(\rho (u_i + v_{th}) Y_s \right) = \dot{\omega}_{Y_s} \tag{1.95}$$

$$\frac{\partial N_s}{\partial t} + \frac{\partial}{\partial x_i} \left((u_i + v_{th}) \frac{N_s}{\rho} \right) = \dot{\omega}_{N_s} \tag{1.96}$$

$$\frac{\partial S_s}{\partial t} - \frac{\partial}{\partial x_i} \left((u_i + v_{th}) \frac{S_s}{\rho} \right) = \dot{\omega}_{S_s} \tag{1.97}$$

where $\dot{\omega}_{Y_s}$, $\dot{\omega}_{N_s}$, $\dot{\omega}_{S_s}$ are the source terms and v_{th} is the thermophoretic velocity. Since this model will be used for the turbulent simulations, the diffusion term is neglected. Indeed, in high Reynolds number flows, soot particles are characterized by high Schmidt number due to negligible molecular diffusivity compared turbulent diffusivity (Bisetti et al., 2012; Attili et al., 2014) .

1.6.1 Soot source terms

The source terms $\dot{\omega}_{Y_s}$, $\dot{\omega}_{N_s}$, $\dot{\omega}_{S_s}$ are modeled by assuming a mono-disperse distribution using a Dirac-delta function $f(v, s) = N_s \delta_{v_s} \delta_{s_s}$. Compared to the classical method of moments where unknown moments are required to close the source terms, and a specific mathematical treatment is necessary, this strategy simplifies the model implementation and the physical interpretation. However, this model can predict only the evolution of global quantities of the particle population. No information on the particle size distribution (PSD) is available. In order to access the PSD, a reconstruction strategy was also proposed by

Franzelli et al. (2018) and is presented afterward in Section 1.6.2. The source terms are given as:

$$\dot{\omega}_{Y_s} = \frac{1}{\rho}\Bigg(\underbrace{v_{dim}\beta^{fm}_{v_{dim}} N^2_{dim}}_{nucleation} + \underbrace{v_{dim}\beta^{fm}_{v_{dim},v_s} N_{dim} N_s}_{condensation} + \underbrace{v_{C_2}\lambda k_{sg} s_s N_S}_{surfacegrowth} + \underbrace{v_{c_2}\lambda k_{ox} s_s N_s}_{oxidation} \Bigg) \tag{1.98}$$

$$\dot{\omega}_{N_s} = \underbrace{\frac{\beta^{fm}_{v_{dim}} N^2_{dim}}{2}}_{nucleation} + \underbrace{(1-\mathcal{H}[v_s - v_{C_2}])v_{c_2}\lambda k_{ox} s_s N_S}_{oxidation} - \underbrace{\frac{\beta_{v_s} N_s^2}{2}}_{coagulation} \tag{1.99}$$

$$\dot{\omega}_{S_s} = \underbrace{(18\pi)^{(1/3)} v_{dim}^{2/3}\beta^{fm}_{v_{dim}} N^2_{dim}}_{nucleation} + \underbrace{\delta s^{frac}_{v_{dim}}\beta^{fm}_{v_{dim},v_s} N_{dim} N_s}_{condensation} + \underbrace{\delta s^{frac}_{v_{C_2}}\lambda k_{sg} s_s N_s}_{surfacegrowth} - \underbrace{\delta s^{spher}_{v_{C_2}}\lambda k_{ox} s_s N_s}_{oxidation} \tag{1.100}$$

where $\beta^{fm}_{v_{dim}}$, β_{v_s} and $\beta^{fm}_{v_{dim},v_s}$ are the collisional frequencies already introduced in Section 1.5 for the sectional model. $\mathcal{H}[v]$ is the Heaviside function, $s_s = S_s/N_s$ is the mean soot surface, $v_s = f_v/N_s$ is the mean soot volume with $f_v = \rho_s\rho^{-1}f_v$. k_{sg} and k_{ox} are the surface reaction constantes for surface growth and oxidation respectively and λ is the number of active site per unit of surface. These three parameters (k_{sg} , k_{ox} and λ) are key parameters in the surface reaction modeling presented in Section 1.3.3.

It is interesting to note that the fractal behavior of soot particles is implicitly taken into account in the term sources where $\delta s^{frac}_{\delta v}$ represents the particle surface variation due to particle volume variation δv. Whereas the sectional approach uses a fitted surface-volume law presented, in the three-equation model, soot fractality follows the expression:

$$\frac{\delta s^{frac}_{\delta v}}{s} = \frac{2}{3}\frac{\delta v}{v} n_p^{\chi} \tag{1.101}$$

with $\chi = -0.2043$ from (Mueller et al., 2009).

Oxidation acts by extracting carbon atoms on the surface of the primary particles composing the aggregates, which are considered as spherical particles. Thus for surface oxidation source term the surface variation $\delta s_{\delta v}^{spher}$ is defined as:

$$\frac{\delta s_{\delta v}^{spher}}{s} = \frac{2}{3}\frac{\delta v}{v} \tag{1.102}$$

1.6.2 Particle size distribution reconstruction

A simple strategy was proposed by Franzelli et al. (2018) to obtain the PSD. This strategy is based on self-similar distribution of the marginal NDF $\mathcal{N}(v)$.

$$\mathcal{N}(v) = \int n(v,s)ds \tag{1.103}$$

The particle size distribution can vary along with the flame. In specific, it has been experimentally and numerically observed in both laminar (Zhao et al., 2003; Abid et al., 2009; Camacho et al., 2015; Rodrigues et al., 2017) and turbulent flames (Netzell et al., 2007; Lucchesi et al., 2017; Rodrigues et al., 2018), that the PSD generally evolves from one-peak into two-peaks distribution, as shown in Fig. 1.4a for different position in a laminar premixed flame (Abid et al., 2009).

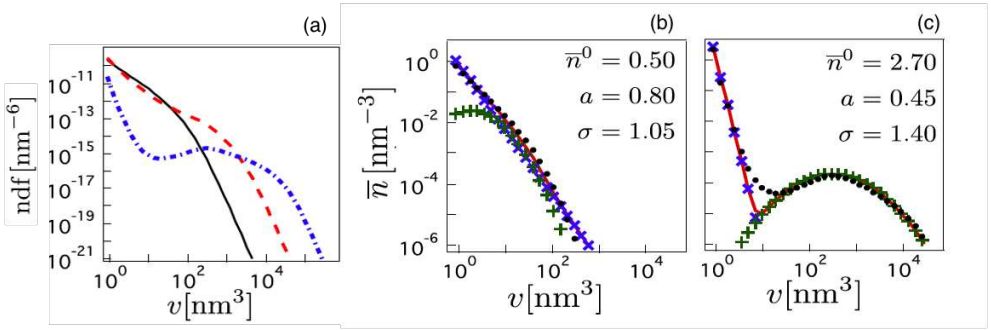

Figure 1.4: *(a) Number density function obtained with the sectional method (Rodrigues et al., 2017) in a premixed flame (Abid et al., 2009) at three axial positions above the burner. (b-c) Reconstruced NDF (red continuous line) as the sum of a Pareto (blue cross) and a log-normal (green plus) distribution for two axial positions corresponding to the black and blue line in the reference NDF (a) presented by the black circles. Image adapted from Franzelli et al. (2018)*

Then the normalized marginal NDF $\overline{\mathcal{N}}(v) = \dfrac{\mathcal{N}(v)}{N_s}$ is approximated as the sum

of two distributions expressed as:

$$\overline{\mathcal{N}}(v) \approx \bar{n}_a(v) = \alpha \bar{n}_1(v) + (1-\alpha)\bar{n}_2(v) \tag{1.104}$$

where $\bar{n}_a(v)$ is an approximation of $\overline{\mathcal{N}}(v)$. By integrating Eq. (1.104) over the volume v, the following expression is obtained:

$$v_s = \alpha v_1^{mean} + (1-\alpha) v_2^{mean} \tag{1.105}$$

where v_1^{mean} and v_2^{mean} are the soot particle mean volumes over normalized distribution $\bar{n}_1(v)$ and $\bar{n}_2(v)$, respectively.

To reproduces the first peak in a bimodal PSD a Pareto distribution was considered for $\bar{n}_1(v)$:

$$\bar{n}_1(v) = k \frac{v_{nucl}^k}{v^{k+1}} \tag{1.106}$$

where $k = \max[\bar{n}_0 \alpha^{-1}, 1.01(1-\alpha v_{nucl}/v_s)^{-1}]$ is the Pareto index, v_{nucl} is the volume of the nucleated particles and $\bar{n}_0(v) = \alpha \bar{n}_1(v_{nucl})$.

For the second peak, a lognormal function is used for $\bar{n}_2$:

$$\bar{n}_2(v) = \frac{1}{v\sigma\sqrt{2\pi}} \exp\left(-\frac{(\ln(v)\mu)^2}{2\sigma^2}\right) \tag{1.107}$$

where $\mu = \ln(v_2^{mean}) - 0.5\sigma^2$, $v_2^{mean} = (1-\alpha)^-1(v_s - \alpha v_1^{mean})$.

To capture the evolution of the NDF along the flame α, σ and $\bar{n}_0$ must vary along with the flame. For that, v_s is used as a NDF tracer, and an empirical expression is derived for these three parameters:

$$\alpha = \max\left[0, 1.0 - 0.18\left(\frac{v_s}{v_{nucl}}\right)^{0.12}\right] \tag{1.108}$$

$$\bar{n}_0 = 8(1-\alpha)^2 \tag{1.109}$$

$$\sigma = 1 + 0.65(1-\alpha) \tag{1.110}$$

α varies between 0 and 1, representing the balance between the Pareto ($\alpha = 1$) and the lognormal function ($\alpha = 0$). This enables the description of the

transition between one-peak to two-peak distributions when large soot particles are present, which has been observed numerically by Rodrigues et al. (2018) in a turbulent jet flame. The NDF is Pareto-like when only small particles are present and evolves to a lognormal distribution when bigger particles are presented. In this case, the population groups into $\overline{n}_2(v)$ since σ is also proportional to v_s. The reconstructed NDF for a premixed flame is shown in Fig. 1.4b-c.

This strategy has been validated in laminar premixed and non-premixed flames. Figure 1.5 compares the reconstructed NDF and the reference NDF obtained with the sectional method for laminar premixed and non-premixed flame (top row) and a turbulent jet flame (bottom row) for different axial positions above the burner. The evolution of the PSD shape is correctly reproduced by the reconstruction in both laminar and turbulent cases.

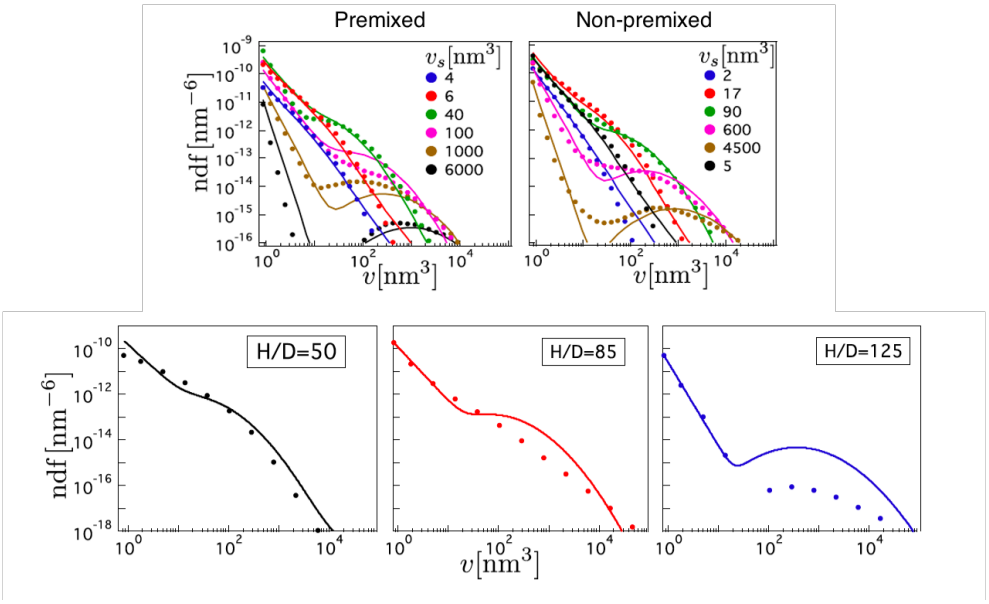

Figure 1.5: *Top: Validation of the proposed NDF reconstruction strategy (solid lines) against the sectional model (symbols) in laminar premixed (left) and non-premixed (right) flame at 6 different positions along the flame. Bottom: Validation of the NDF reconstruction strategy in a turbulent jet flame at 3 axial positions H/D along the central axis. Image adapted from Franzelli et al. (2018).*

Chapter 2

Simulation of sooting laminar flames

In this chapter, the numerical strategy to model soot production, including the model for the gas phase and the solid phase, presented in Chapter 1, is evaluated in sooting laminar flames in both premixed and non-premixed regimes. The sectional method describes the soot particle evolution, taking into account nucleation, condensation, surface reactions, and coagulation. The gas phase is described using the KM2 mechanism considering seven PAHs. The soot volume fraction is compared to the available experimental measurements. The particle number density and source terms are also investigated, as well as the particle size distribution. It is found that a good agreement with the experimental soot volume fraction is obtained for premixed flames. However, the numerical strategy fails for the analyzed non-premixed flames.

Contents

2.1 Introduction

To obtain a predictive numerical strategy for soot formation, it must consider the influence of the complex flame structure. This chapter aims to apply and compare the numerical soot strategy presented in Chapter 1 on both laminar premixed and non-premixed flames to analyze their capabilities in predicting soot formation, notably soot volume fraction.

The ability of soot models to accurately predict soot production strongly depends on the chemical kinetics. The kinetic mechanism provides the soot precursors (PAHs) concentrations involved in the nucleation and condensation processes, as well as the species involved in the surface reactions of growth (C_2H_2) and oxidation (O_2 and OH). Therefore, a detailed gas phase reaction mechanism is required to account for large PAHs formation properly. Besides soot kinetics, the flame structure and the flow governing the local conditions experienced by the particles along their trajectory, i.e., the soot particle history, also affect soot production. Consequently, soot formation may depend on the flame configuration. Radiation is also relevant for soot prediction due to the two-way coupling between soot particles and temperature. Therefore, a numerical strategy for soot prediction should be considered as a whole package, combining the gas phase kinetics, the numerical method to solve the solid phase (PSD discretization), the sub-models for the source terms (collision and reactivity models), and the radiation model.

Rodrigues (2018) has successfully validated the sectional numerical strategy (introduced in Chapter 1) in a steady laminar premixed ethylene-air flame under atmospheric pressure. Satisfactory soot volume fraction results were also obtained for a premixed flame under higher pressure, but the temperature was not compared to the available experimental measurements. Here, these flames are recalculated and new non-premixed flames are considered. Although a good agreement was observed in premixed conditions, it was found that the model still lacks in describing soot production in non-premixed flames and a new strategy will be discussed in the next Chapter 3.

For the analysis of the retained numerical soot strategy, the in-house code REGATH (Darabiha, 1992) is used with a 1D-formulation under the hypothesis that temperature, species, and soot fields are a function only of the axial coordinate. Radiation is taken into account in the energy equation considering the gaseous phase's contribution via CO_2, H_2O, and CO species through the Statistical Narrow-Band (SNB) model. The RDG/RDG-FA (Rayleigh-Debye-Gans for Fractal Aggregates) assumption (Rodrigues, 2018) is applied for soot particles, considered as aggregates of non-overlapped spherical primary particles. The flame structure and soot production are analyzed in Section 2.2 for the premixed flames and in Section 2.3 for the non-premixed flames.

2.2 Burner-stabilized stagnation premixed flames

A burner-stabilized stagnation premixed C_2H_4-O_2-Ar flame with equivalence ratio $\phi = 2.07$ (Abid et al., 2009) is used for the model evaluation on premixed condition. A schematic illustration of the flame is shown in Fig. 2.1. The diluted mixture is injected at the bottom at a velocity of 8.0 cm/s, temperature 298 K and at atmospheric pressure. The mixture's composition, in terms

of mass and molar fractions, is shown in Table 2.1. The KM2 chemical mechanism (Wang et al., 2013) is used to describe the reactive gaseous flow. The flame is stabilized few millimeters above the burner. Soot particles are formed near the flame front and evolve along their trajectories towards the stagnation plate. Soot particles are experimentally sampled through a small hole in the stagnation plate to characterize soot particle size distribution. The PSD is obtained using the technique of scanning mobility particle size (SMPS), where the particle size is obtained according to the mobility diameter of the particles. Particle number density and soot volume fraction are not directly measured. The number density of particles is obtained by integrating the PSD with respect to the mobility diameter. The soot volume fraction is obtained by integrating particle size distributions assuming spherical particles with a diameter equal to the mobility diameter. Temperature profiles obtained through thermocouple measurements are also available.

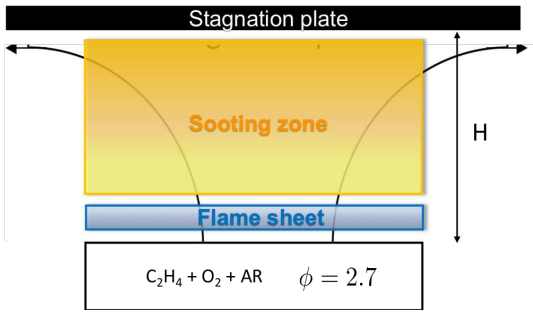

Figure 2.1: *Schematic representation of the laminar burner-stabilized stagnation premixed flame (H is the position of the stagnation plane above the burner where soot particles are collected by scanning mobility particle size (SMPS).*

Table 2.1: *Premixed composition of the burner-stabilized stagnation premixed flame (Abid et al., 2009).*

	C_2H_4	O_2	Ar
Mass fraction	0.1268	0.2098	0.6635
Molar fraction	0.1630	0.2370	0.6000

Different flame structures and soot evolution are obtained by varying the plate distance H between the burner and the stagnation plate. Table 2.2 summarizes the thermal boundary conditions for the studied configurations. A zero-velocity boundary condition is applied at the stagnation plate axis. Nevertheless, this condition is not coherent with the experimental conditions where the flow aspiration for particle sampling locally impacts the flow structure near the plane (Camacho et al., 2015; Saggese et al., 2015; Xuan and Blanquart, 2015). The

imposed zero-velocity boundary condition overpredicts the residence time experienced by the soot particles. In order to partially account for the flow aspiration effect, the numerical soot results are here shifted by −0.2 cm from the stagnation plane as proposed by Camacho et al. (2015) and Saggese et al. (2015).

Table 2.2: *Thermal boundary conditions for the studied flames with different stagnation plate positon H. T_b is the temperature of the burner; T_s is the stagnation plate temperature. Data from Camacho et al. (2015).*

H [cm]	$T_b[K]$	$T_s[K]$
0.6	473	495
0.7	473	492
0.8	473	490
1.0	473	488.7

Numerical temperature profiles are compared to the experimental profiles in Fig. 2.2. The gaseous KM2 mechanism reproduces the experimental temperature profile with good agreement for the different flames obtained by varying the stabilization plate position (H = 0.6, 0.7, 0.8, and 1 cm).

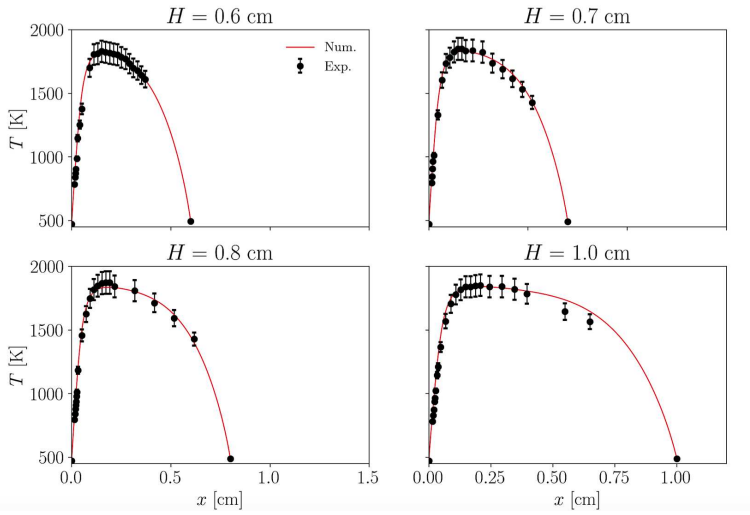

Figure 2.2: *Comparison between experimental (symbols) and numerical (solid red line) temperature profiles. Experimental data from Camacho et al. (2015)*

Figure 2.3 presents the numerical predictions of soot volume fraction and the number density of particles 0.2 cm upstream the stagnation plate (H −0.2 cm) compared with the experimental measurements for the flames with H = 0.6, 0.7, 0.8 and 1 cm. The soot volume fraction f_v presents a good agreement

with experimental measurements. On the other hand, the number density of particles is overpredicted.

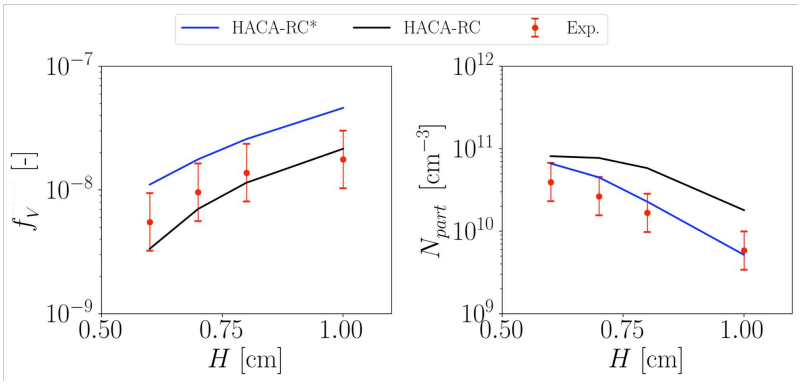

Figure 2.3: *Comparison between numerical predicted soot volume fraction (left) and number density of particles (right) with experimental measurements (symbols) (Camacho et al., 2015) for flames with burner distances from the stagnation plane H = 0.6, 0.7, 0.8 and 1 cm. The numerical values are taken at H - 0.2 cm.*

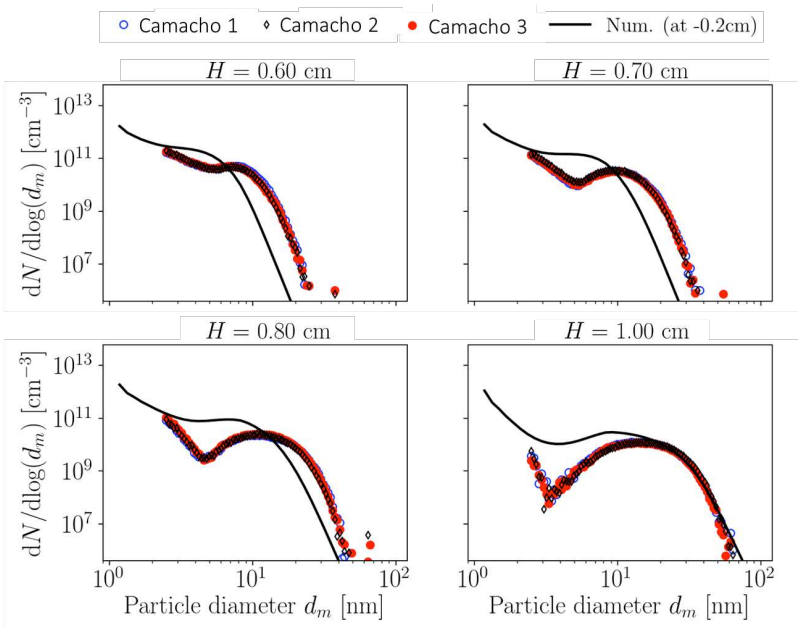

Figure 2.4: *Comparison between numerical predicted particle size distribution (solid line) with experimental measurements (symbols) (Camacho et al., 2015) for flames with burner distances from the stagnation plane H = 0.6, 0.7, 0.8 and 1 cm. The numerical values are taken at H - 0.2 cm.*

Figure 2.4 compares numerical and experimental (Camacho et al., 2015) particle size distribution. Three measurements were realized to prove their repro-

ducibility. The comparison reveals that the numerical PSD is shifted toward small particle sizes for the lower distances between the burner and stabilization plate (H = 0.6 and 0.7 cm). Besides, the transition between one-peak to a bi-modal PSD is less sharp than in the experimental PSD where a sharped second mode appears from H = 0.7 cm characterizing a bimodal PSD.

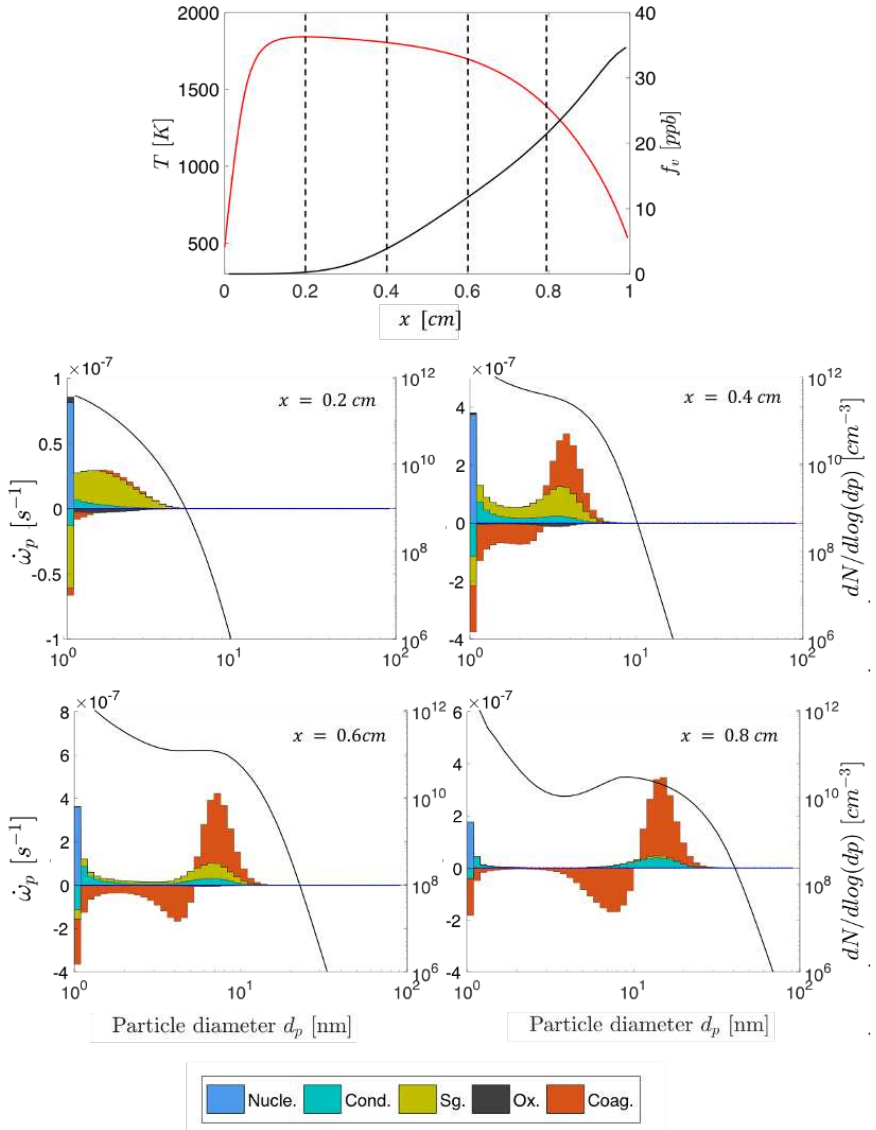

Figure 2.5: *Numerical particle size distribution (PSD) and source terms evolution along the flame for H = 1.0 cm at different axial positions x from the burner. The x-positions are illustrated with the numerical temperature profile (red line) and soot volume fraction profile (black line) at the top.*

Figure 2.5 shows the evolution of the particle size distribution along the flame for $H = 1$ cm and the source terms for each particle size (section). Looking at this evolution, one can observe that at $x = 0.2$ cm, near the flame front, the nucleation process is initially predominant. Once formed, soot particles start to grow, mainly through surface growth due to the high temperature ($x = 0.4$ cm), but nucleation persists. At $x = 0.6$ cm, coagulation and nucleation become the predominant phenomena in soot particle evolution, while surface growth has decreased due to the decrease in temperature approaching the cold stagnation plate. The presence of both nucleation and coagulation induces a change in the PSD shape, from one peak shape to a two-peak shape. At $x = 0.8$ cm the high residence time enhances coagulation and condensation, and the PSD keeps bimodal. Oxidation rarely occurs all along with the flame since O_2 was preliminary mixed with the fuel, and OH is found only near the flame front. Overall, the bimodality results from the combination of soot mechanisms. Whereas nucleation is the main responsible for the first mode (first peak), the second mode (second peak) results from the competition between coagulation and soot growth processes (condensation and surface reactions). When considering smaller H distances, lower nucleation is observed due to its dependence on the temperature that is strongly affected by the proximity of the colder stagnation plate. Consequently, the growth processes (condensation and surface growth) also decrease. Furthermore, the residence time is lower for a smaller distance between the burner and stagnation plate, reducing the time available to soot growth and collide between them, which may explain the less sharped PSD bimodality, as shown in Fig. 2.4.

2.3 Non-premixed counterflow flames

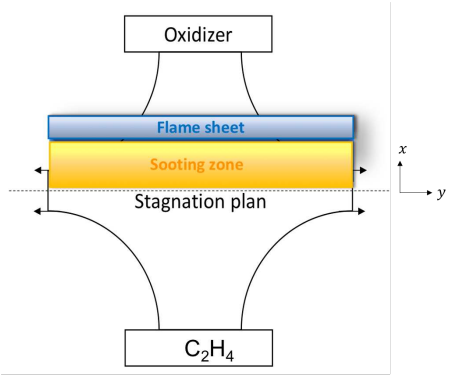

Figure 2.6: *Schematic representation of the laminar non-premixed counterflow flame.*

In order to evaluate the retained numerical approach in non-premixed conditions, the non-premixed C_2H_4-O_2-N_2 counterflow flame, experimentally studied

by Hwang and Chung (2001), is considered here with three different oxygen contents ($X_{O_2} = 0.20, 0.24, 0.28$) at atmospheric pressure. A schematic illustration of the non-premixed flame is shown in Fig. 2.6. For these conditions, the fuel diffuses through the stagnation plane and the flame establishes at the oxidizer side. Once formed on the richer side of the flame, soot particles are transported towards the stagnation plane (null velocity), evolving along with its trajectory depending on the local chemical composition, temperature, and residence time but soot oxidation rarely occurs in this type of flame.

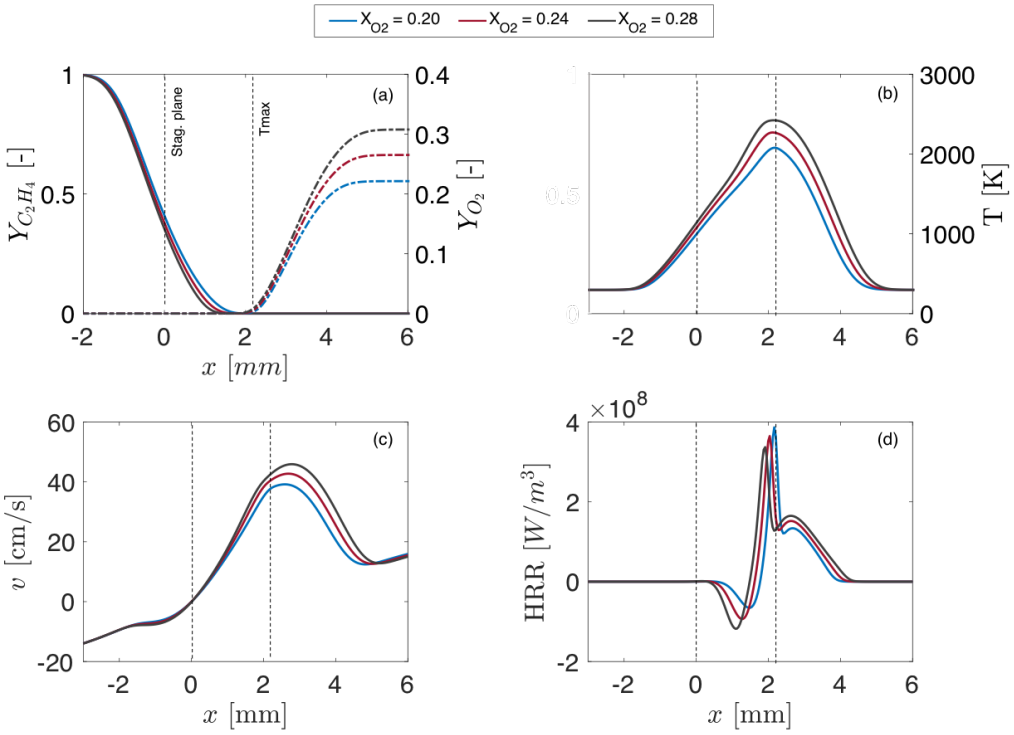

Figure 2.7: *Flame structure for the three flames with different X_{O_2} obtained using the numerical strategy from (Rodrigues et al., 2017). Species profiles are normalized by the maximum value of the respective species for the flame $X_{O_2} = 0.20$. The stagnation plane is located at $x = 0$ mm, as shown by the vertical dashed black line.*

For these flames, no experimental information about the flame structure is available. The only available measurement is soot volume fraction, obtained via laser light extinction/scattering technique. The numerical temperature, heat release rate, velocity, and species (C_2H4 and O_2) profiles in the centerline, shown in Fig. 2.7, allow the characterization of the flame structure under different oxidizer levels. The flame temperature increases due to lower N_2 dilution by increasing the oxygen addition in the oxidizer stream. Consequently,

the gas velocity increases due to the thermal gas expansion approaching the flame. Conversely, the heat release rate decreases in the reaction zone (maximum temperature) when X_{O_2} increases as a result of fuel leakage across the reaction zone, as shown by the $C_2H_4 \mid O_2$ profiles (Fig. 2.7a).

It can be expected that the observed differences in the local reacting flow conditions will affect soot production. Figure 2.8 shows the profiles of three relevant species for soot production: C_2H_2 and H (Fig. 2.8a) and the PAH with four aromatic rings A4 (Fig. 2.8b). Whereas C_2H_2 and H are involved in soot growth, pyrene (A4) is a precursor for soot particle nucleation. The species mass fractions increase with X_{O2} due to a thermal effect through the Arrhenius law. Note that C_2H_2 and $A4$ are formed on the rich side of the flame indicated by the maximum temperature (T_{max}) while H is located in the reaction zone where the maximum heat release is observed, then C_2H_2 and H coexist in small region.

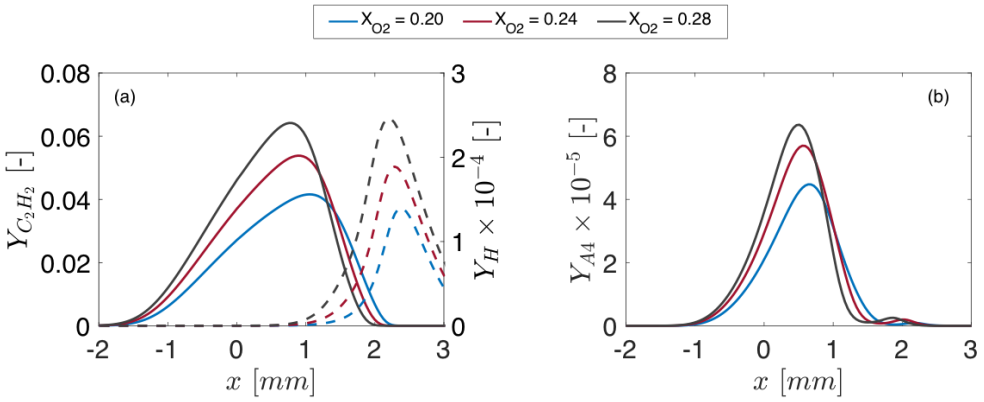

Figure 2.8: *Numerical prediction of key species for the soot model for the three flames: (a) C_2H_2 (solid lines) and H (dashed lines) profiles along the centerline; (b) A4 profile along the centerline.*

Figure 2.9 compare the numerical and experimental soot volume fraction profiles. Soot particles are formed on the rich side of the flame and are transported towards the stagnation plane. They are further transported by thermophoresis towards the fuel side beyond the gaseous stagnation plane due to the high-temperature gradient, generating a soot stagnation plane on the left side of the gaseous stagnation plan (x = 0 mm). Note that the numerical soot stagnation plane is shifted from the experimental one. This can affect the thermophoresis model, but it can also be associated with a lack of resolution in experiments that are not sufficiently resolved to correctly capture the steep gradient of soot volume fraction typical of this configuration (Yan et al., 2019). The numerical simulations underpredict the maximum experimental soot volume fraction for the three flames by a factor higher than 5, and this discrepancy increases

with X_{O_2}. Nevertheless, the increase f_v tendency with X_{O_2}, experimentally observed, is capture by the numerical model.

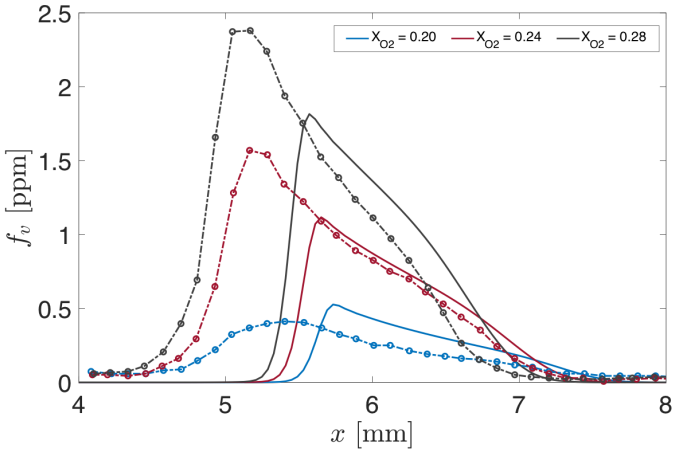

Figure 2.9: *Comparison between the numerical (solid lines) and experimental (symbols - Hwang and Chung (2001)) soot volume fraction along the centerline. Numerical results are multiplied by a factor 5 for the sake of visualization.*

To further investigation, the source terms are shown in Fig. 2.10. All processes involved in soot production increase with X_{O_2} because when increasing the oxygen concentration, the flame temperature increases, influencing the soot kinetics. Soot particle inception is enhanced, then soot growth by condensation and surface growth also increases since PAH and C_2H_2 species are further produced. Nucleation is about 5 times higher for $X_{O_2} = 0.28$ than for $X_{O_2} = 0.20$. Note that, surface reactions ($\dot{\omega}_{sg+ox}$) drives soot mass, but it occurs only in a smaller region (gray zone in Fig. 2.10) upstream the gaseous stagnation plane at a higher temperature zone where both C_2H_2 and H are present. Outside the gray zone, surface reaction decreases since H concentration sharply decreases. According to Hwang and Chung (2001), the spatial distribution of C_2H_2 and H in counterflow non-premixed flames might explain the low predictability of soot volume fraction in these flames. On the contrary, condensation persists between the soot and gas stagnation planes.The coagulation source term for the 20th section $\dot{\omega}_{coag,20}$ is also presented in Fig. 2.10. Coagulation increases with X_{O_2} consistent with the soot growth processes tendency. The coagulation is positive near the flame front since small particles collision contributes positively to the 20^{th} section and becomes negative as bigger particles collide, leaving the section.

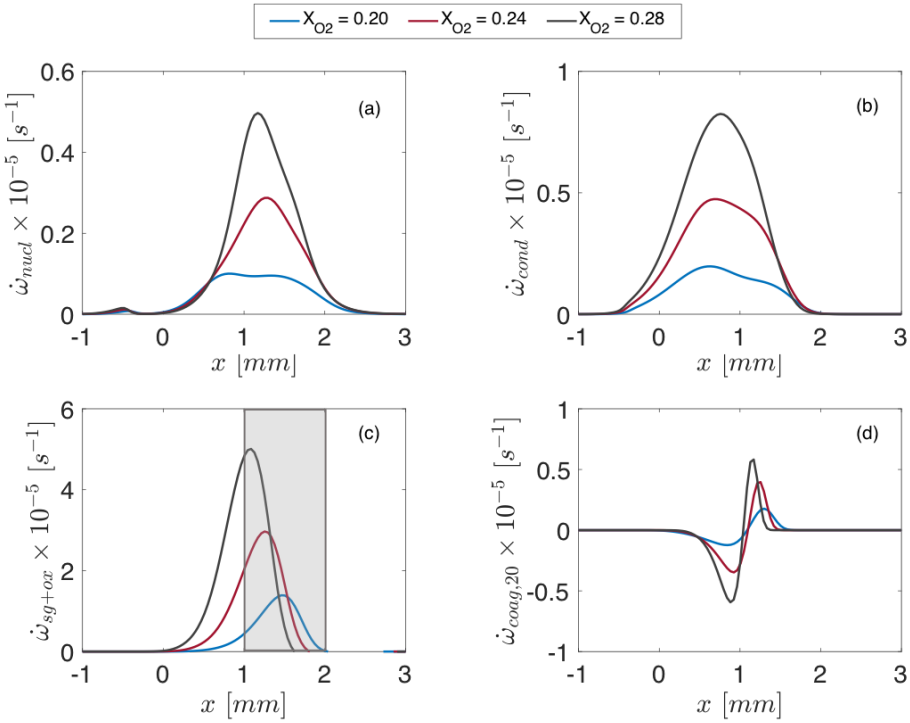

Figure 2.10: *Soot source terms. (a) nucleation $\dot{\omega}_{nucl}$, (b) condensation $\dot{\omega}_{cond}$, (c) surface reactions $\dot{\omega}_{sg+ox}$ and (d) coagulation for the 20^{th} section $\dot{\omega}_{coag,20}$ for the three studied flames obtained using the numerical approach due to (Rodrigues et al., 2017). The gray zone in the $\dot{\omega}_{sg+ox}$ profile (c) represents the zone where C_2H_2 and H coexist.*

Figure 2.11 shows the evolution of the PSD and the soot source terms for each section along the flame for $X_{O_2} = 0.24$. Particles nucleate near the flame where PAH is formed (Fig. 2.8b), so that at $x = 1.7$ cm the PSD presents a one-peak shape. Once formed, soot particles grow principally by reaction with C_2H_2. At $x = 1.2$ cm, the increasing of soot particle size results in a large collision probability between particles, enhancing coagulation, and the PSD evolves through large particle sizes. By approaching the stagnation plane, temperature decreases, resulting in decreased surface reaction ($x = 0.7$ cm). On the other hand, condensation increases as the PAH mass fraction reach its maximum near the stagnation plane. Because of the high residence time, coagulation is strongly active, and the PSD becomes bimodal. At $x = 0.2$ cm, despite the high C_2H_2 mass fraction, surface growth is low due the absence of H. At the same time, condensation is lower since the PAH mass fraction has decreased. Coagulation also decreases. Since nucleation hardly occurs in this zone, the "first" peak of a classic bimodal distribution decreases. The other flames ($X_{O_2} = 0.20$ and 0.28) present a similar PSD evolution even if very close to the flame (x = 1.7 mm) the size of particles decreases with X_{O2}, as shown in Fig. 2.12. This difference is probably due to the local lean condition for

the flames with high X_{O_2}. Note that, the flames are slightly shifted towards the oxidizer side with X_{O_2} increase (see heat release profiles in Fig. 2.7d). As shown in Fig. 2.10, soot starts to grow upstream for $X_{O_2} = 0.20$, but due to lower temperature, the growth rate is lower in the post-flame zone compared to the other flames.

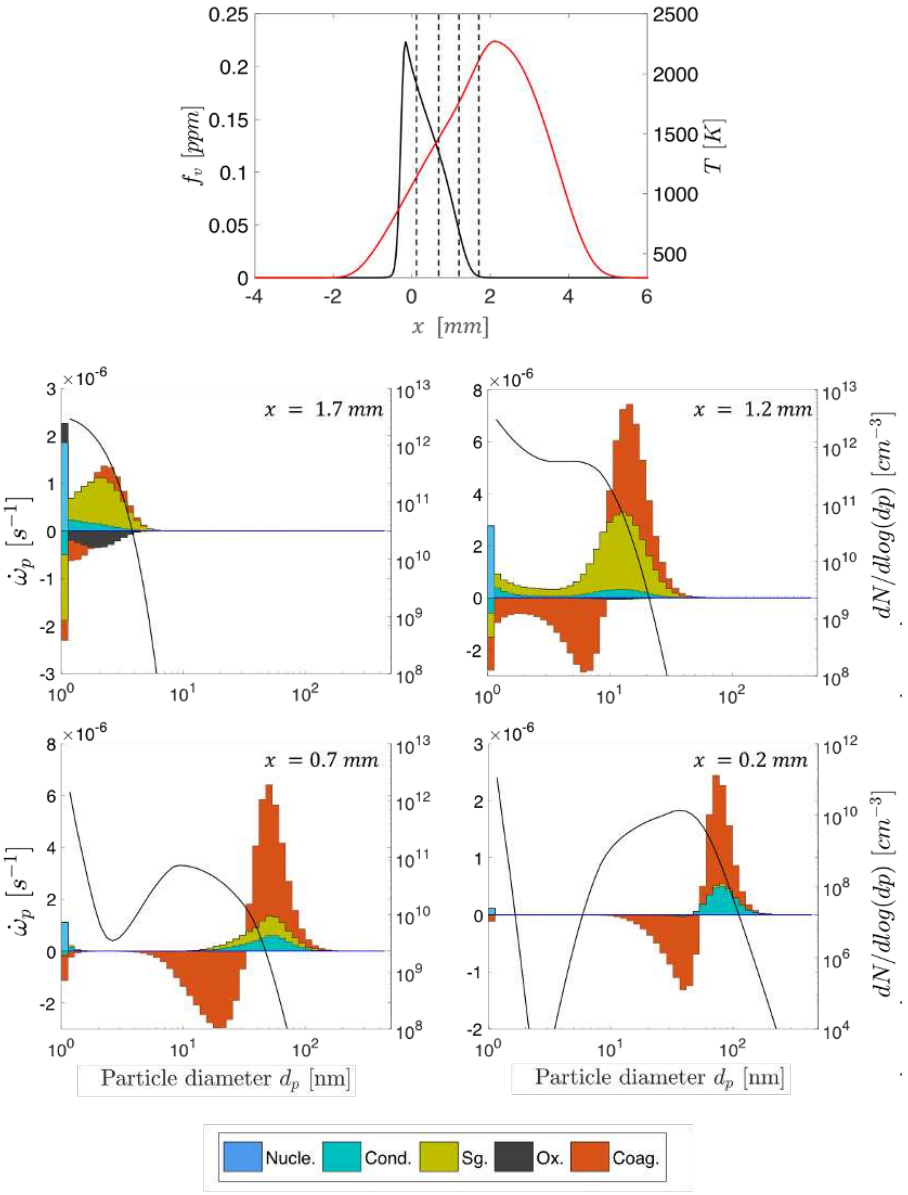

Figure 2.11: *Particle size distribution and soot source terms evolution along the counterflow flame for $X_{O_2} = 0.24$. The x-positions are illustrated with the numerical temperature profile (red line) and soot volume fraction profile (black line) at the top.*

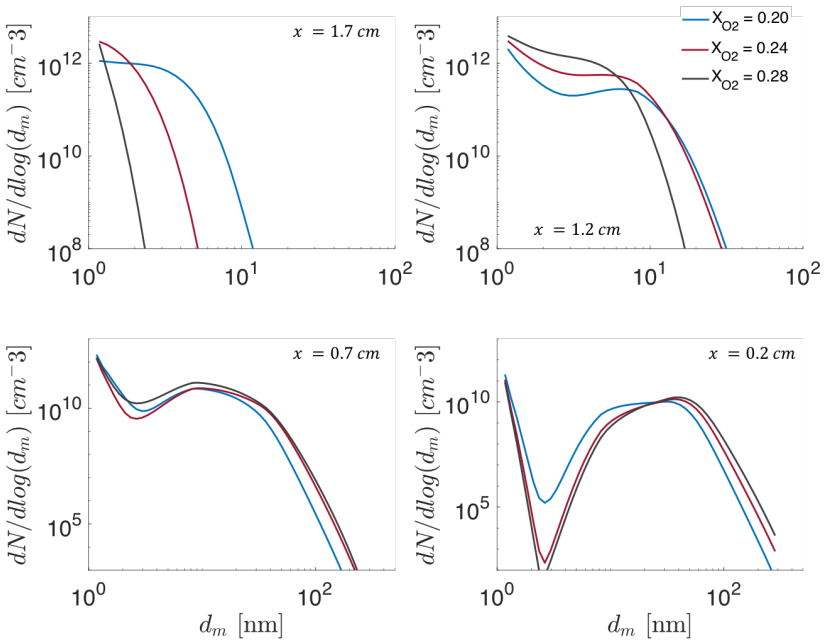

Figure 2.12: *Particle size distribution evolution at different positions along flame for the three flames with X_{O_2} = 0.20 (blue), 0.24 (red), 0.28 (black).*

Effect of strain rate on soot production

Soot production depends on the strain rate, mainly in two ways. First, PAH concentration is sensitive to the scalar dissipation rate (Bisetti et al., 2012). Second, in general, the soot processes are characterized by relatively long time scales (Rodrigues et al., 2017; Cuoci et al., 2008) and depend on the residence time experienced by the soot particles along their trajectory, which is related to the strain rate. Thereby, the impact of the proposed model is also studied for ethylene-air diffusion flames under different global strain rates, which is of interest to understand the effect of turbulence on soot production.

Two counterflow ethylene-air non-premixed flame are retained for this analysis. First, a counterflow non-premixed flame ethylene-air (gaseous composition: $X_{O_2} = 0.21$ and $X_{C_2H_4} = 1$), experimentally investigated by (Decroix and Roberts, 2000) for two different velocities corresponding to two global strain rate (15 s^{-1}, 30 s^{-1}) is considered. The global strain rate (GSR) is defined as:

$$K = \frac{2.U_o}{L} \tag{2.1}$$

where U_o is the inlet air velocity and L corresponds to the distance separating the two nozzles.

Table 2.3: *Details of the experimental conditions for the strained flames due to Decroix and Roberts (2000) and Wang and Chung (2016). T_{ini} corresponds to the cold temperature of fuel and air; U_o is the inlet velocity; L is the distance between inlets.*

	Decroix and Roberts (2000)		Wang and Chung (2016)			
K [s^-1]	15	30	37.5	50	62.5	75
${U_o}^{air}$ [cm/s]	9.53	19.0	15.0	20.0	25.0	30.0
${U_o}^{fuel}$ [cm/s]	12.1	24.2	15.0	20.0	25.0	30.0
T_{ini} [K]	294		298			
L [mm]	12.7		8.0			

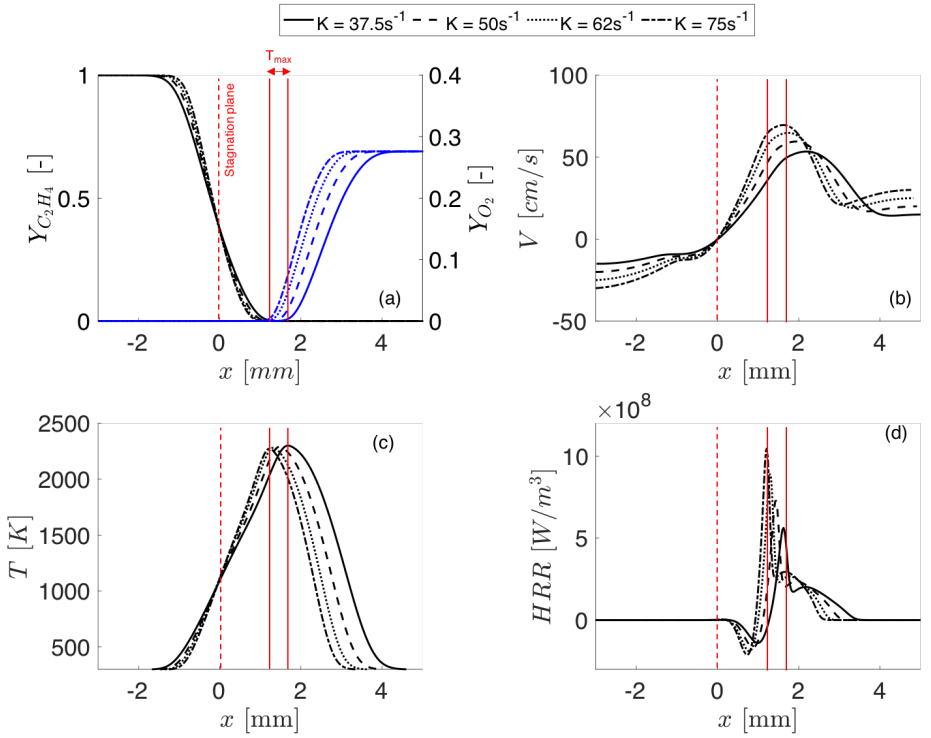

Figure 2.13: *Numerical flame structure under different strain rates corresponding to the flames experimentally studied by Wang and Chung (2016). (a) Mass fraction profiles of C_2H_4 and O_2 (b) Axial velocity profiles ; (C) Temperature profiles; (c); (d) Heat release rate profiles. The stagnation plane is located at $x = 0$ mm, as shown by the dashed black line.*

In a more recent work, Wang and Chung (2016) have experimentally studied soot production in counterflow ethylene-air non-premixed flames (gaseous composition: $X_{O_2} = 0.25$ and $X_{C_2H_4} = 1.0$) under different strain rates. Four different velocities corresponding to four global strain (37.5 s^{-1}, 50 s^{-1}, 62.5 s^{-1}, 75 s^{-1}) were considered. Whereas the work of Decroix and Roberts (2000)

provides only the soot volume fraction peak, Wang and Chung (2016) provide the soot volume fraction profile. The soot volume fraction was obtained, for both studies, using the LII technique. The flames characteristics are summarized in Table 2.3.

Figure 2.13 shows the effect of the strain rate on the flame structure obtained numerically for the flames of Wang and Chung (2016). The velocity profiles along the centerline (Figure 2.13b) shows that the stagnation plane (x = 0 mm) is located on the fuel side as reveals the temperature profiles (Fig. 2.13c) and the rate of heat release (Fig. 2.13d). The flame position (T_{max}) is slightly shifted towards the stagnation plane when the strain rate increases, as shown by the vertical red lines. The flame temperature (T_{max}) is also slightly affected by the strain rate variation, but the temperature profile is thicker for a lower strain rate. On the contrary, the maximum heat release rate (Fig. 2.13d) increases with the strain rate.

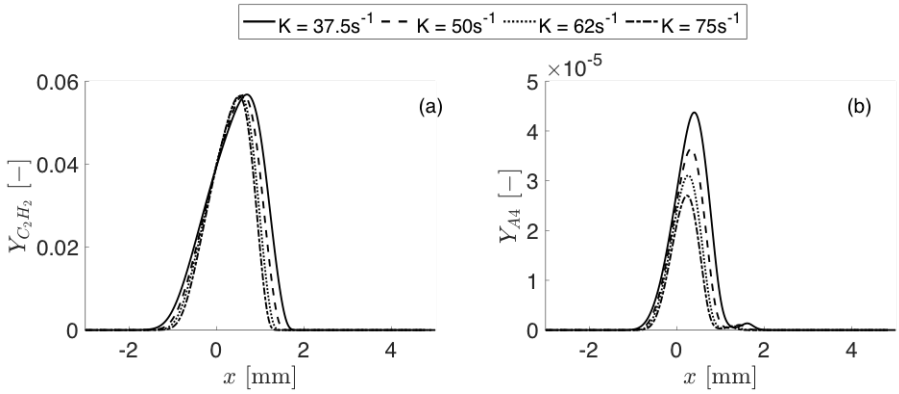

Figure 2.14: *Numerical prediction of key species in the soot model for the different strain rates: (a) C_2H_2 mass fraction; (b) pyrene (A4) mass fraction.*

Figure 2.14 shows the effect of the strain rate on two relevant species for soot production: C_2H_2 (Fig. 2.14a) and the PAH with four aromatic rings A4 (Fig. 2.14b). C_2H_2 participates in soot growth via HACA, and pyrene (A4) is a precursor for soot particle nucleation. As expected, both species are located at the fuel side, but it can be noted that A4 is more sensitive to strain rate variation than C_2H_2. C_2H_2 is an intermediate species in the combustion process, then its response to strain rate variation is related to the chemical time scale of the fuel oxidation, which is small compared to the flow time scale. On the contrary, PAHs are characterized by a longer characteristic time scale, requiring more time to be formed. The effect of the strain rate on the chemistry can be represented by the *Damköhler* number $\mathrm{Da} = \tau^{flow}/\tau^{chem}$, with τ^{flow} the characteristic time scale of the flow and τ^{chem} the chemical time scales. Here τ^{flow} is inversely proportional to the strain rate. The low sensitivity of

the flame structure and C_2H_2 to strain rate suggests that Da ≥ 1, while the high sensitivity of the PAH means that Da for PAH is close to 1. Therefore, PAH formation, and consequently, soot particles are susceptible to the flow time scale through the residence time imposed by the strain rate.

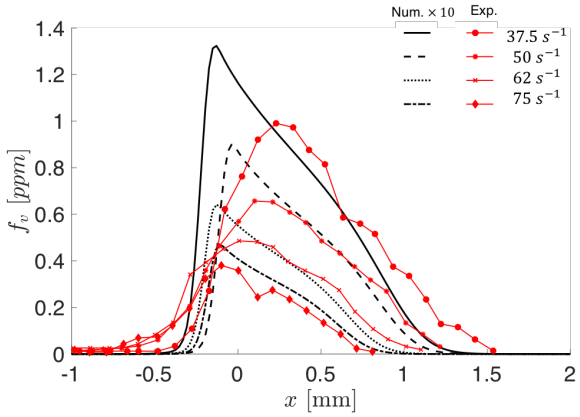

Figure 2.15: *Comparison between the numerical (lines) and experimental (symbols) soot volume fraction (Wang and Chung, 2016) for different strain rates. Numerical results are multiplied by a factor 10 for the sake of visualization.*

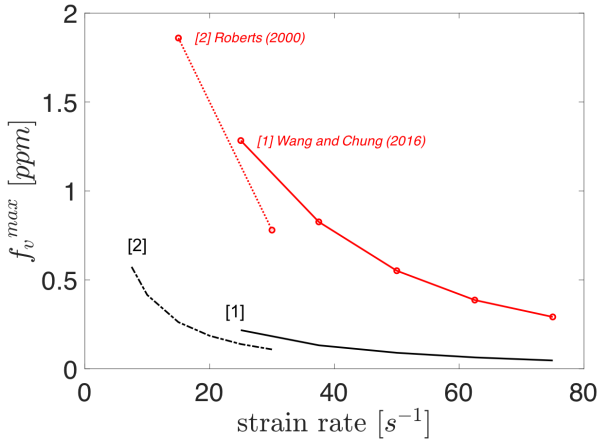

Figure 2.16: *Comparison between the numerical (lines) and experimental (black symbols from Wang and Chung (2016) and red symbols from Decroix and Roberts (2000) peak f_v as a function of strain rate.*

Numerically predicted soot volume fraction profiles are compared to the experimental profiles (Wang and Chung, 2016) in Fig. 2.15, as a function of strain rate. The numerical strategy captures the spatial distribution but underpredicts the experimental peak values by a factor of about 10. It should be noted that the disparity between numerical and experimental values increases with

the strain rate. Figure 2.16 shows the peak soot volume fraction for both experimental flames due to Wang and Chung (2016) and Decroix and Roberts (2000). The model poorly captures the decreasing tendency with strain rate in terms f_v peak. In order to understand the effect of the strain rate on soot production, the f_v source terms are shown in Fig. 2.17a-f.

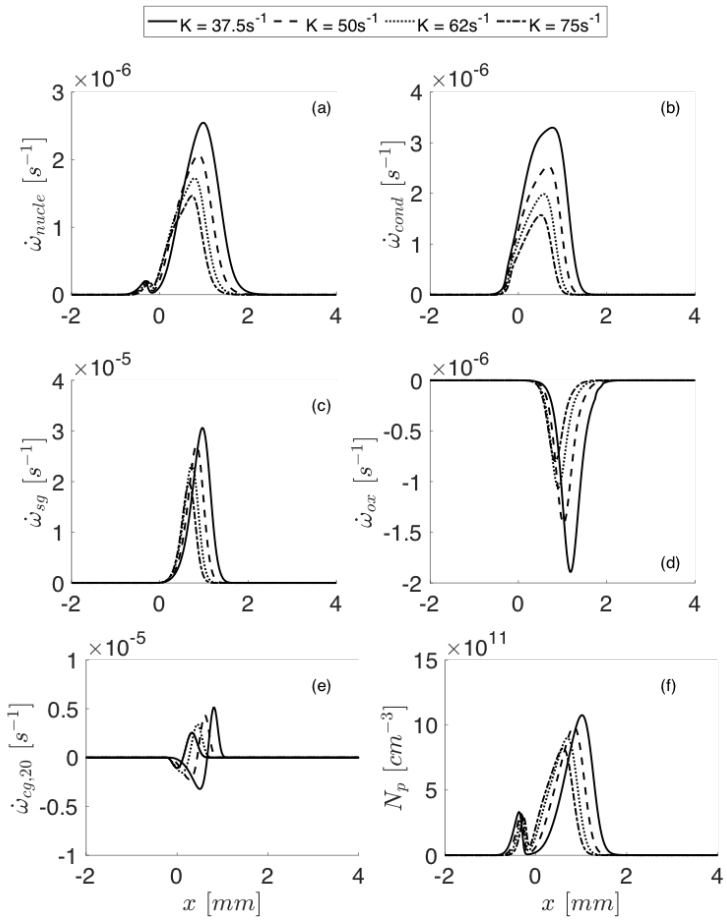

Figure 2.17: *Numerical soot source terms of nucleation (a), condensation (b), surface reactions (c - surface growth and d - oxidation) and coagulation (e - for the* 20^{th} *section) for the flames experimentally studied by Wang and Chung (2016).*

Figure 2.17 shows that all the source terms decrease with the strain rate. The effect on condensation and nucleation is significant (Fig. 2.17a-b), which can be explained by the high sensitivity of PAH on the strain rate. Consequently, the number density of particles decreases (Fig. 2.17f). Since C_2H_2 and flame temperature are slightly affected by the strain rate, the reduction of surface reactions (growth and oxidation in Figs 2.17c-d) is due to the reduction in the number of particles formed during nucleation. Furthermore, high strain rates

lead to lower residence times, restricting the collision between particles and growth. Coagulation rate (in Fig. 2.17e is shown for the 20th section) decreases with strain rate due to lower residence time experienced by the particles.

2.4 Conclusion

In this chapter, the numerical reference strategy, including the sectional method, the soot sub-models and the gaseous kinetic mechanism presented in Chapter 1, was evaluated in laminar sooting premixed and non-premixed ethylene-air flames. Good agreement with experimental measurements of soot volume fraction was obtained for the premixed tested flames. Satisfactory results were obtained for the particle number density and the PSD. However, the soot numerical strategy fails in predicting the soot volume fraction for the non-premixed tested flames. For these flames, the soot volume fraction is underpredicted by a factor higher than 5 for the flame with different oxygen concentrations and a factor 10 for the flame with different strain rates.

The prediction of soot volume fraction in counterflow laminar non-premixed flames is of most interest for sooting prediction in turbulent conditions using the tabulated chemistry approach, which uses counterflow non-premixed flamelets. However, at this point, it is impossible to identify which process is incorrectly described by the retained models since many uncertainties remain in soot modeling and due to the lack of experimental evidences, as already discussed in Chapter 1. Furthermore, the complex heterogeneous process involved in soot production is strongly coupled and can hardly be isolated. However, an accurate soot model should correctly predict soot in both premixed and non-premixed flames to obtain a predictive numerical strategy when applied in realistic combustors, like gas turbines, where multiple flame regimes may coexist.

According to (Hwang and Chung, 2001), the surface reaction modeling based on the HACA mechanism, classically validated in premixed conditions, can explain the soot model's inability to predict soot volume fraction in counterflow non-premixed flame. It was demonstrated that for counterflow non-premixed flames, the HACA species C_2H_2 and H do not coexist as in premixed flames. Therefore, the classical HACA models are not able to describe soot surface kinetics in non-premixed flames. In the next chapter, the HACA-RC model retained for the simulation performed for this manuscript is extended based on Hwang's work and is then investigated in the same ethylene-air flames studied in the present chapter.

Part II

Improving soot surface reaction model to predict premixed and non-premixed flames

Chapter 3

Improving soot surface reaction model: HACA-RC* model

In this chapter, the HACA-RC model presented in Chapter 1 is extended to improve soot volume fraction prediction in non-premixed flames. The proposed model, called HACA-RC, is inspired by the work of Hwang and Chung (2001). The new soot reaction mechanism is then coupled with the sectional strategy proposed by Rodrigues et al. (2017), presented in Chapter 1 and evaluated in the Chapter 2. The proposed model is tested for different laminar flames. A good compromise was obtained for f_v prediction in both premixed and non-premixed flames. A better agreement is obtained for the non-premixed flames, while the accuracy level is kept for the premixed flames. Therefore the HACA-RC* mechanism is retained for all turbulent simulations presented in this manuscript. Part of the discussion presented in this chapter has been published as: "Impact of the reaction mechanism model on soot growth and oxidation in laminar and turbulent flames", in Proceedings of ASME Turbo Expo 2019: Turbomachinery Technical Conference and Exposition.*

Contents

3.1 Introduction

The numerical prediction of soot production, i.e., the net product of formation and destruction phenomena, in applied systems is exceptionally challenging for many reasons. First, the involved processes are complex phenomena with a heterogeneous nature that is still not entirely well understood. Many assumptions have to be made when modeling these phenomena leading to considerable uncertainty. Second, most practical interest devices often work under specific operating conditions, leading to multi-regime combustion (premixed and non-premixed). Hence the soot model has to be able to reproduce soot production in both premixed and non-premixed regimes without any parameter fitting depending on the investigated case, making the problem even more complicated. Finally, the model has to be simple enough to perform Large Eddy Simulations (LES) of the industrial configurations in terms of CPU time.

This chapter aims to generate and fully validate a soot model with as few fitted parameters as possible that can be applied to premixed or non-premixed systems using ethylene fuel. Ethylene is one of the most important intermediate species in the oxidation of aliphatic hydrocarbons and the experimental combustion community commonly uses it for soot formation studies. The model will also be used in the LES simulations of the DLR burner experimentally investigated using ethylene as fuel (Chapters 6- 8).

Among the different mechanisms involved in soot production, soot kinetics is challenging since it depends on the soot particle's surface state, which is very complicated to access experimentally and numerically. The Hydrogen-Abstraction-Carbon-Addition (HACA) model has been historically validated in premixed flames (Frenklach and Wang, 1991; Appel et al., 2000) but is known to fail the description of laminar non-premixed sooting flames (Lindstedt, 1994; Khosousi and Dworkin, 2015), even if it is employed as a reference reaction mechanism for surface growth and oxidation reactions, as discussed shown in Chapter 2. In order to mitigate this undesirable behavior, a parameter α, corresponding to the fraction of surface sites available for chemical reaction, is often used to reproduce the reactivity loss of soot particles due to thermal effects or time history (Appel et al., 2000; Michael, 2002; Veshkini et al., 2014; Singh et al., 2005). However, this approach lacks generality since its value is tuned to match the experimental data as a function of the flame conditions and the investigated configurations. More recently, Xu et al. (2018) proposed changing the constants of the C-addition reaction to control the concentration of active sites, but, once again, this modification is configuration-dependent. Alternatively, Hwang and Chung (2001) proposed to add some radical species into the original HACA mechanism. This modification allowed to enhance soot surface activation in counterflow diffusion-like flames with a small impact on the premixed flames, then it can be applied independently of the considered combustion regime.

Here the HACA-RC mechanism (Mauss et al., 1994), presented in Chapter 1, is extended following Hwang's strategy. The mechanism is then coupled with a sectional method (Rodrigues et al., 2017) and the KM2 detailed chemistry (Wang et al., 2013). In Section 3.2, model modification is described. The new reaction mechanism, called HACA-RC*, is then tested on the laminar premixed and diffusion flames studied in Section 3.3. This model has been published as *"Impact of the reaction mechanism model on soot growth and oxidation in laminar and turbulent flames"*. in Proceedings of ASME Turbo Expo 2019: Turbomachinery Technical Conference and Exposition.

3.2 Model modification

Hwang and Chung (2001) studied experimentally and numerically the structure of the sooting zone in counterflow non-premixed flames, focusing on the soot growth by surface reactions with the surrounding gas phase. According to them, the classic HACA reaction model can not describe surface growth in this type of flame because the sooting zone structure differs from the premixed flames, usually used to validate soot models. It was found that, in opposition to the premixed flames, the H atom is rarely found in the sooting growth zone, limiting the soot reactivity and then the HACA reaction model's ability to describe surface growth in counterflow non-premixed flames. Then, they showed that hydrocarbon radical species as C_3H_3, CH_3, and C_2H, can be considered to significantly improve soot reactivity through H-abstraction reactions in the high-temperature zone. To illustrate this point, the flame structure, the species profiles (C_2H_4, O_2, C_2H_2, C_3H_3, CH_3 and C_2H), the soot volume fraction and the involved soot source terms (nucleation, condensation, surface growth and oxidation) are shown in Fig. 3.1 for a counterflow premixed and non-premixed flame, both studied in Chapter 2.

The premixed flame structure and the sooting zone is shown in Figs. 3.1b-d-f. For this flame, the C_2H_2 and H species involved in the HACA-RC reaction model (Fig 3.1d) coexist near the flame front (T_{max} at x = 1.6 mm (Fig. 3.1d). Thus, soot particles, once formed by nucleation, can react with these species, and the original HACA-RC mechanism (surface growth and oxidation) is activated (Fig 3.1f) under favorable conditions. However, the non-premixed flame structure, shown in Figs 3.1b-d-f, is quite different. The flame front (T_{max} at x = 2.0 mm in Fig. 3.1a) is located on the lean side of the flow, but soot particles form on the rich side where PAHs are present (represented by the A1 and A4 profiles Fig. 3.1c). Then, they grow while traveling away from the flame. However, soot oxidation rarely occurs. For this flame, C_2H_2 profile (solid blue line in Fig. 3.1c) is shifted compared to the H profile (dotted blue line in Fig. 3.1c) since C_2H_2 is formed on the rich side of the flame whereas H is located close to the temperature's peak. Therefore, additionals species

may be taken into account in the HACA-RC mechanism in order to predict soot particle activation in counterflow non-premixed flames. The carbonated radical species (CH_3, C_3H_3 and C_2H in Fig. 3.1c) proposed by Hwang and Chung (2001) are formed on the rich side of the flame and, consequently, partially coexist with the species C_2H_2. Soot particles can then react with the new H-abstraction species increasing soot reactivity and, consequently, soot mass addition by reaction with C_2H_2.

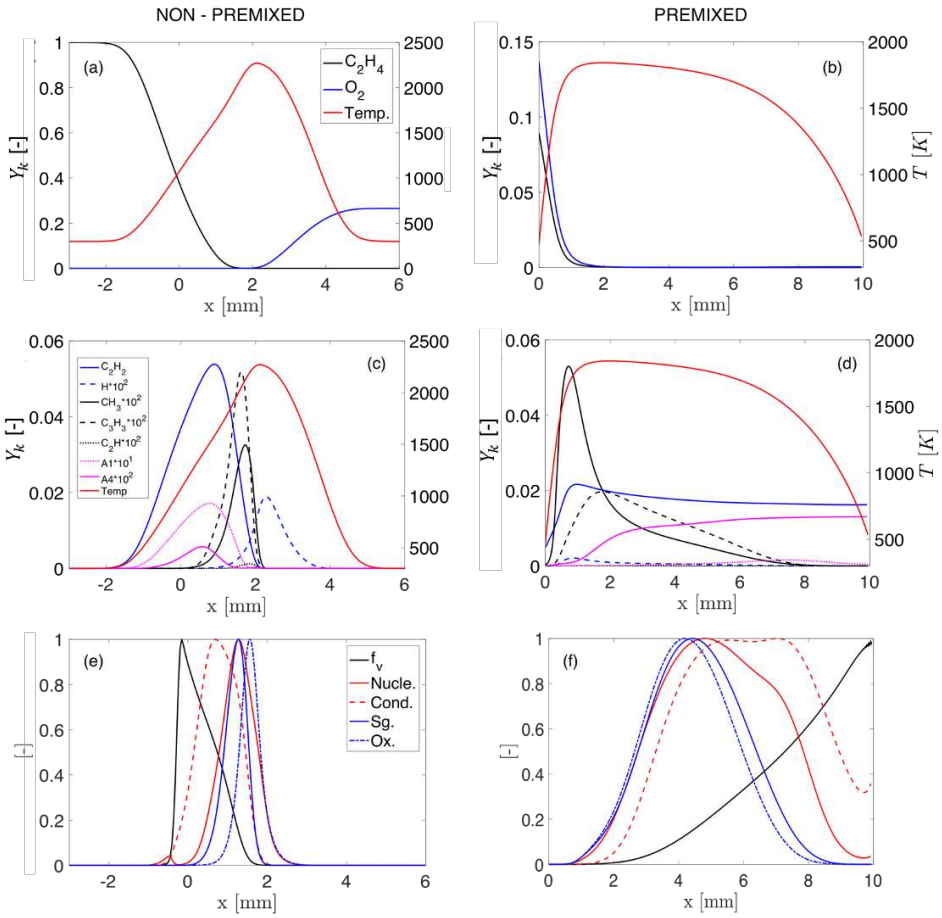

Figure 3.1: *Flame structure and sooting zone. Left: counterflow non-premixed flame. Right: premixed flame. a-b; Temperature, C_2H_4 and O_2 profiles; c-d: Temperature, HACA species (C_2H_2 and H) and the radicals mass fraction (C_2H, CH_3, C_3H_3 - Hwang and Chung (2001)); e-f: normalized soot volume fraction and source terms.*

3.2.1 Chosing the radical species to add

Inspired by Hwang and Chung (2001), three different new H-abstraction reactions, resumed in Table 3.1, have been added into the HACA-RC reaction

mechanism in order to extend the validity of the numerical strategy to non-premixed laminar flames. They are tested separately to identify the impact of each additional species. The reaction constants of the respective reactions are also shown in Table 3.1. Note that they are all not dependent on temperature.

Table 3.1: *Additional H-Abstraction reaction.* $k_{reac}^{[+]}$ *is the reference reaction constant from Hwang and Chung (2001).* k_{reac}^{*} *and* k_{reac}^{**} *are the modified reaction constants.*

N°	Reaction	$k_{reac}^{[+]}$	k_{reac}^{*}	k_{reac}^{**}
$R8$	$C_{n_c}H + C_2H \xrightarrow{k_8} C_{n_c}^{*} + C_2H_2$	2.0 10^{13}	1.0 10^{14}	-
$R9$	$C_{n_c}H + C_3H_3 \xrightarrow{k_9} C_{n_c}^{*} + AC_3H_4$	5.0 10^{12}	1.0 10^{14}	5.0 10^{14}
$R10$	$C_{n_c}H + CH_3 \xrightarrow{k_{10}} C_{n_c}^{*} + CH_4$	2.0 10^{13}	1.0 10^{14}	-

reaction constants units: $[s^{-1}]$

Figure 3.2 shows the soot volume fraction prediction with different version of the HACA-RC mechanism. In Fig. 3.2a, HACA-RC* including each new species separarely (black lines) and considering all species togheter (blue line) with with the reference reaction constants $k_{reac}^{[+]}$ (Hwang and Chung, 2001) are compared to the reference HACA-RC model (red line). In Fig. 3.2b the reaction constants are modified, corresponding to the reaction k_{reac}^{*}.

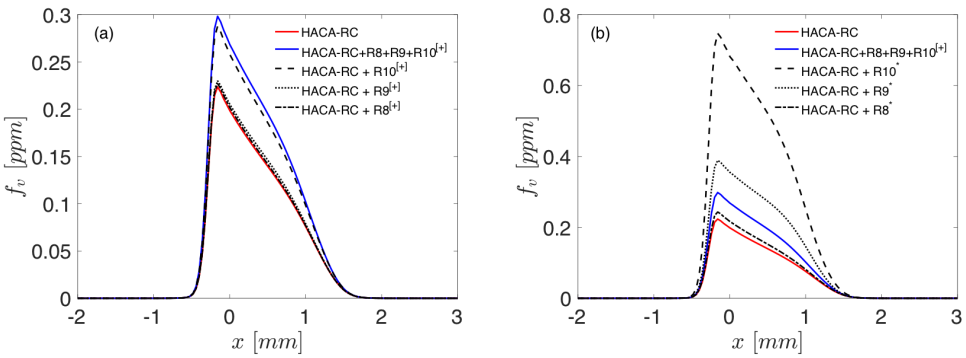

Figure 3.2: *Soot volume fraction prediction using different versions of the HACA-RC model. (a) results using the reference HACA-RC (red line) and with the additional reactions using the reactions parameters proposed by Hwang and Chung (2001) (*$k_{reac}^{[+]}$ *in Table 3.1) considering the three radical (solid blue line) and considering individually each radical (black lines); (b) the reaction rates of the radical species are modified (*k_{reac}^{*} *in Table 3.1) and compared to the original version (Rodrigues et al., 2017).*

If all species are considered together, using $k_{reac}^{[+]}$ (Hwang and Chung, 2001), the expected effect on soot volume fraction is not obtained, as soot volume fraction

slightly increases. Hwang and Chung (2001) have used a method of moments coupled with a less detailed chemistry ABF (Appel et al., 2000). These first results reinforce the idea that soot models should be considered a whole strategy considering the gas chemistry and the method to solve the PBE.

By considering each radical individually, it is identified that the radical CH_3 is the main contributor for f_v increasing, while CH_2 and C_3H_3 have a negligible impact on soot volume fraction prediction. However, if the reaction constants are modified (k^*_{reac} in Table 3.1), the soot volume fraction increases when adding separately CH_3 and C_3H_3 to the HACA-RC mechanism, as shown in Fig. 3.2b. Concerning the C_2H reaction, no matter which value of reaction constants was considered, the impact on f_v is negligible since this species is hardly present in the post-flame region. On the contrary, the C_3H_3 reaction with the reaction constant k^*_{reac} (Table 3.1) affects not only the solid phase description but also the gaseous phase. It has been observed that when surface reactions are enhanced by adding the modified C_3H_3 reaction, the PAH concentrations drastically decrease.

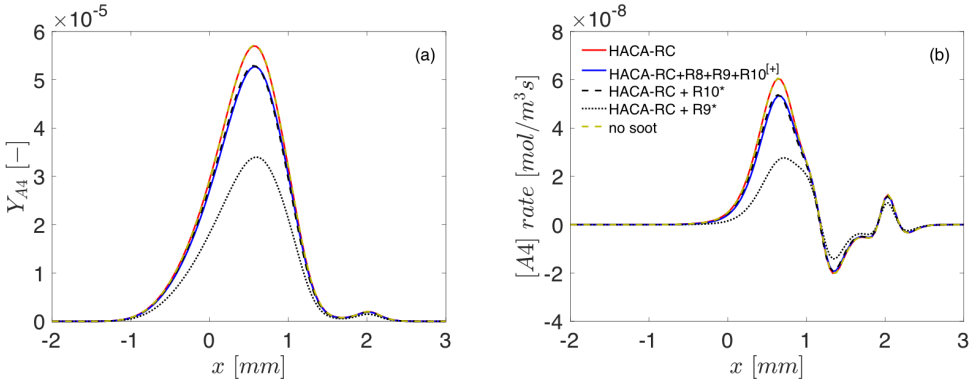

Figure 3.3: *Impact of the surface kinetics on PAH prediction for the non-premixed flame. (a) Pyrene (A4) mass fraction with the reference HACA-RC (red line), with the three proposed radicals (blue line) without modification ($k^{[+]}_{reac}$ in Table 3.1), with only C_3H_3 (dashed black lines) with modified reaction constants (k^*_{reac} in Table 3.1), with only CH_3 using k^*_{reac} (dotted black line) and not considering soot production (yellow dashed line); (b) the corresponding A4 chemical production rate.*

To illustrate the effect of considering C_3H_3 in the reaction soot model on the PAH prediction, the same counterflow diffusion flame has been calculated with and without soot production (while activating the dimerization in both cases). Results for the soot precursor pyrene (A4) are reported in Fig. 3.3. When soot production is considered, four variations of the surface reaction mechanism were tested: the original HACA-RC model, the HACA-RC model with all radicals with the reference reaction constants (k_{reac}), the HACA-RC with the C_3H_3 reaction and the HACA-RC model with the CH_3 reaction, both with modified

reaction rates (k^*_{reac} in Table 3.1). The profiles of pyrene ($A4$) in Fig. 3.3b indicate that when the C_3H_3 reaction is included in the soot reaction model, the A4 concentration sharply decreases. When considering the CH_3 reaction, only a slight decrease in the maximum value is observed. Figure 3.3b shows that when considering C_3H_3, the production rate of pyrene considerably decreases. This is because the C_3H_3 self-recombination reaction is known to be one of the main pathways for the first aromatic ring formation (Miller and Melius, 1992). It can also contribute to large PAHs formation as described by the KM2 mechanism (Wang et al., 2013). Therefore, considering this species in the HACA-RC model could affect the PAH formation using the KM2 kinetic mechanism. This effect was not reported in the work of Hwang and Chung (2001) probably because their strategy relied on a different kinetic scheme (Appel et al., 2000) that does not include C_3H_3 into larger PAH formation mechanism (up to four-ring aromatic species).

It should be recognized that the retro-coupling effect of soot surface reactions on the gaseous PAHs concentrations is possibly correct, as suggests by the studies due to (Eaves et al., 2015; Veshkini et al., 2016; Aubagnac-Karkar et al., 2018) in laminar flames. However, this topic is only subject to recent progress with no experimental evidence. It must then be avoided here since the primary purpose of this work is to develop a strategy for LES of sooting turbulent flames based on state-of-the-art look-up tables techniques (Mueller and Pitsch, 2012; Xuan and Blanquart, 2014, 2015; Rodrigues et al., 2018). In this approach, information on PAH is pre-tabulated from purely gaseous flames. To guarantee a consistent description, the soot production has to slightly alter the gaseous phase results, excluding the possibility of adding C_3H_3 radicals to the HACA-RC model. If such retro-coupling has to be considered in the LES, new strategies to account for detailed chemistry effects for LES of sooting turbulent flames alternatively to look-up tables have to be developed, which is out of the scope of this thesis.

Additionally, it was observed that using the C_3H_3 reaction leads to a strong over-prediction of the soot volume fraction in premixed flames compared to the reference HACA-RC which correctly reproduces the soot load (Fig. 2.3). To obtain the same level of soot volume fraction in the non-premixed flame using the reaction CH_3 and the reaction C_3H_3, the reaction constant for the reaction C_3H_3 has to be strongly modified. Since this species coexists in high concentration with C_2H_2 in the post-flame zone of the premixed flame, the soot volume fraction is strongly affected in this flame, which is not desired since results were in good agreement with experiments for premixed flames as shown in Chapter 2.

Figure 3.4a shows the soot volume fraction for the burner stagnation stabilized premixed flame, obtained with four variations of the HACA-RC model: HACA-RC, HACA-RC + CH_3 with the modified reaction constant $k_{reac}*$ (Table 3.1) and HACA-RC + C_3H_3 with two different reaction constants k^*_{reac} and k^{**}_{reac}

(Table 3.1). The soot volume fraction increases in premixed conditions with the addition of any radical reactions. Nonetheless, with equivalent reaction constants (equivalent soot volume fraction in non-premixed flame), the addition of reaction C_3H_3 leads to a strong overprediction of the soot volume fraction, twice the prediction considering the reaction CH_3. In addition to that, the production rate of A4 is strongly affected, as shown in Fig. 3.4b. Similarly to the non-premixed flame, this effect is not desirable. Thereby, only the CH_3 species (reaction $R10$ in Table 3.1) is kept allowing to enhance f_v production in counterflow non-premixed flames without affecting much the PAH concentrations in both premixed and non-premixed flames, and f_v yield in the premixed flames.

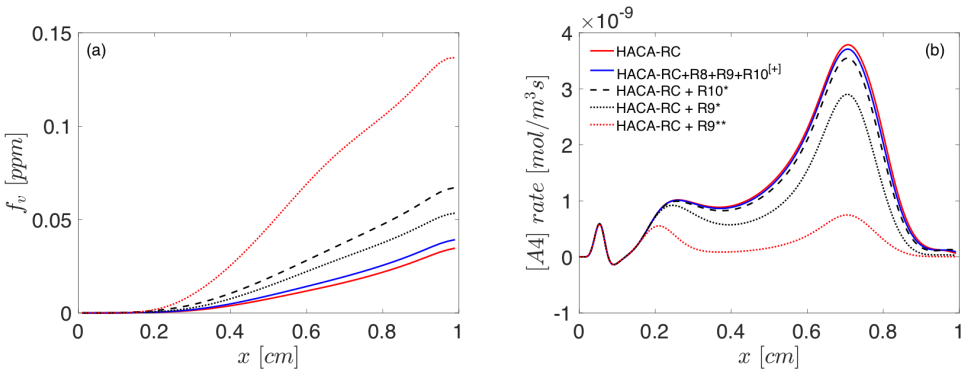

Figure 3.4: *Impact of the surface kinetics on soot volume fraction and PAH prediction for the premixed flame. (a) Soot volume fraction prediction with the reference HACA-RC (solid red line), with the three proposed radicals (blue line) using $k^{[+]}_{reac}$, with only C_3H_3 using k^*_{reac} (dotted black line) and k^**_{reac} (dotted red line) and with only CH_3 (dashed black line) using k^*_{reac}; (b) the corresponding A4 chemical production rate.*

3.2.2 Chosing the reaction parameters

The choice of the reaction parameters is not straightforward. The HACA constants are generally based on similar reactions between PAHs reactions and the gaseous species assuming a chemical similarity between soot surface and PAH molecules. This assumption leads to many uncertainties so that a large variety of the models can be observed in the literature (Frenklach and Wang, 1991; Appel et al., 2000; Mauss et al., 1994), even for PAHs growth application (Appel et al., 2000; Michael, 2002; Slavinskaya et al., 2012; Wang et al., 2013), showing that surface reactions kinetics is still far from being a well-understood soot phenomenon. In the work of Hwang and Chung (2001), the reactions constants were derived from similar reactions with naphthalene. Here, we have adjusted the rate coefficient of CH_3 reaction ($R10$) in order to obtain a reasonable agreement between numerical and experimental results for all investigated non-premixed and premixed flames (Section 3.3), respecting the PAH forma-

tion using the KM2 chemical mechanism. It is then important to mention that the application of the HACA-RC* with other kinetic mechanisms should be verified.

Table 3.2: *New H-Abstraction reaction.* [+] *Hwang and Chung (2001)*

N°	Reaction	$k_{reac}^{[+]}$	New k_{reac}
$R10$	$C_{n_c}H + CH_3 \xrightarrow{k_{10}} C_{n_c}^* + CH_4$	2.0 10^{13}	1.0 10^{14}

reaction constants units: $[s^{-1}]$

Finally, the obtained reaction Arrhenius parameters, with no dependency on temperature, are: A = 1.0 10^{14}, $\beta = 0.0$, $E_a = 0.0$ as summarized in Table 3.2. Once fitted, the reaction soot model has not been modified anymore. Therefore, the new reaction model, called HACA-RC* (HACA-RC + R10), is coupled with the sectional model (Rodrigues et al., 2017) and the KM2 chemistry (Wang et al., 2013).

3.3 Model validation

3.3.1 Non-premixed flames

The comparison between results obtained with the reference model HACA-RC and the proposed HACA-RC* model for the atmospheric counterflow non-premixed flames with different oxygen content (Hwang and Chung, 2001) is shown in Fig. 3.5. A better prediction of the maximum soot volume fraction is obtained with the proposed HACA-RC* model. The maximum soot load is increased by a factor 3 compared to the coupling with the reference HACA-RC.

Figure 3.6 compares the soot sources terms obtained with the two models. Surface growth is strongly enhanced with the HACA-RC* model (solid lines in Fig. 3.6c). Oxidation also increases (Fig. 3.6d) as it also depends on the soot surface reactivity. Due to the increase in particle size by soot growth, soot collision with PAH via condensation (Fig. 3.6b) and between particles via coagulation increase. While the negative contribution of coagulation increases, as shown in Fig. 3.6e) for the 20th section, the positive contribution is slightly affected. It can be explained by the fact that, although nucleation decreases, leading to lower particle number density (Fig. 3.7b), the soot particle size increases, balancing the reduction in the number of particles. The nucleation rate decreases mainly due to the assumption of quasi-stationarity with condensation (Chapitre 1) since PAH is slightly affected by the model as show Fig. 3.7a. However, the joint contribution of nucleation and condensation is

similar between computations (Fig. 3.6f).

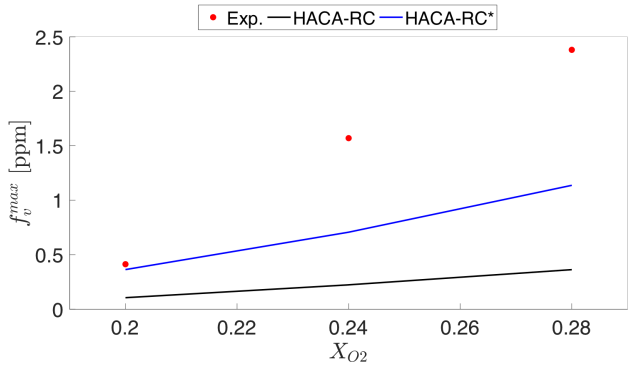

Figure 3.5: *Comparison of the soot volume fraction peak between the reference model (black line), the HACA-RC* model (blue line) and experimental data (symbols) from Hwang and Chung (2001).*

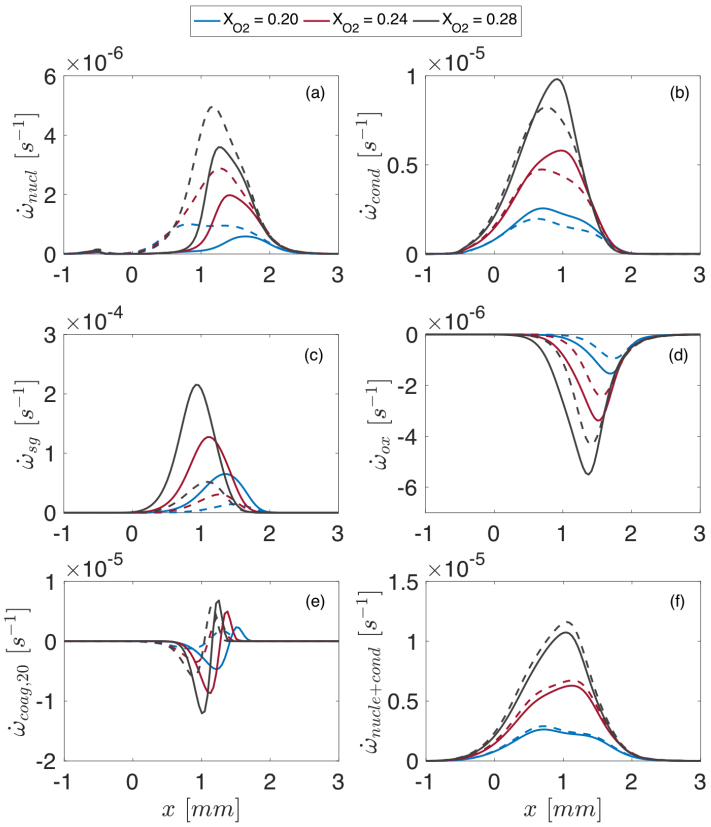

Figure 3.6: *Soot source terms comparison between HACA-RC (dashed lines) and HACA-RC* (solid lines) for the three studied flames (X_{O_2} = 0.20, 0.24, 0.28). The $\dot{\omega}_{coag}$ profile (e) represents the coagulation rate for the 20th section.*

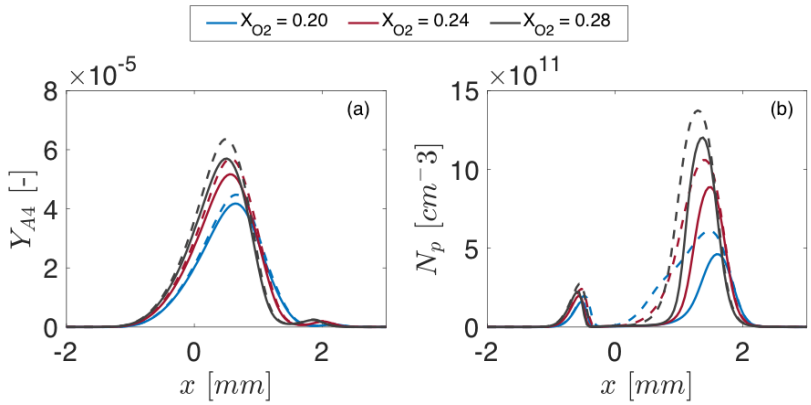

Figure 3.7: *(a) A4 mass fraction (b) particle number density with the HACA-RC (dashed lines) and HACA-RC* (solid lines) for the flames varying X_{O_2} (= 0.2, 0.24, 0.28).*

Despite the increase in soot volume fraction (Fig. 3.5) due to the increase in surface growth rate, the discrepancy between experimental and numerical prediction still increases with X_{O_2}. In order to explain this behavior Fig. 3.8 shows the reaction constant k_{sg} from the surface growth model (defined in Chapter 1) obtained with the reference model HACA-RC and the proposed model HACA-RC*. It is interesting to note that k_{sg} is similar between the flames with different X_{O_2}. The thermochemical conditions in the three flames leads to similar reaction constant. Actually, increasing X_{O_2}, soot is further produced due to thermal effects. Therefore more surface is available. Since species concentrations in high to large X_{O_2}, soot surface reactivity increases with X_{O_2}. However, it appears that the thermochemical conditions limit surface growth which might explain the higher discrepancy between experiments and numerical prediction for high X_{O_2}.

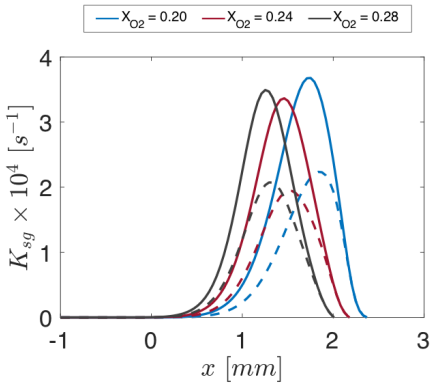

Figure 3.8: *Surface growth reaction constant K_{sg} with HACA-RC (dashed lines) and HACA-RC* (solid lines) for different X_{O2}.*

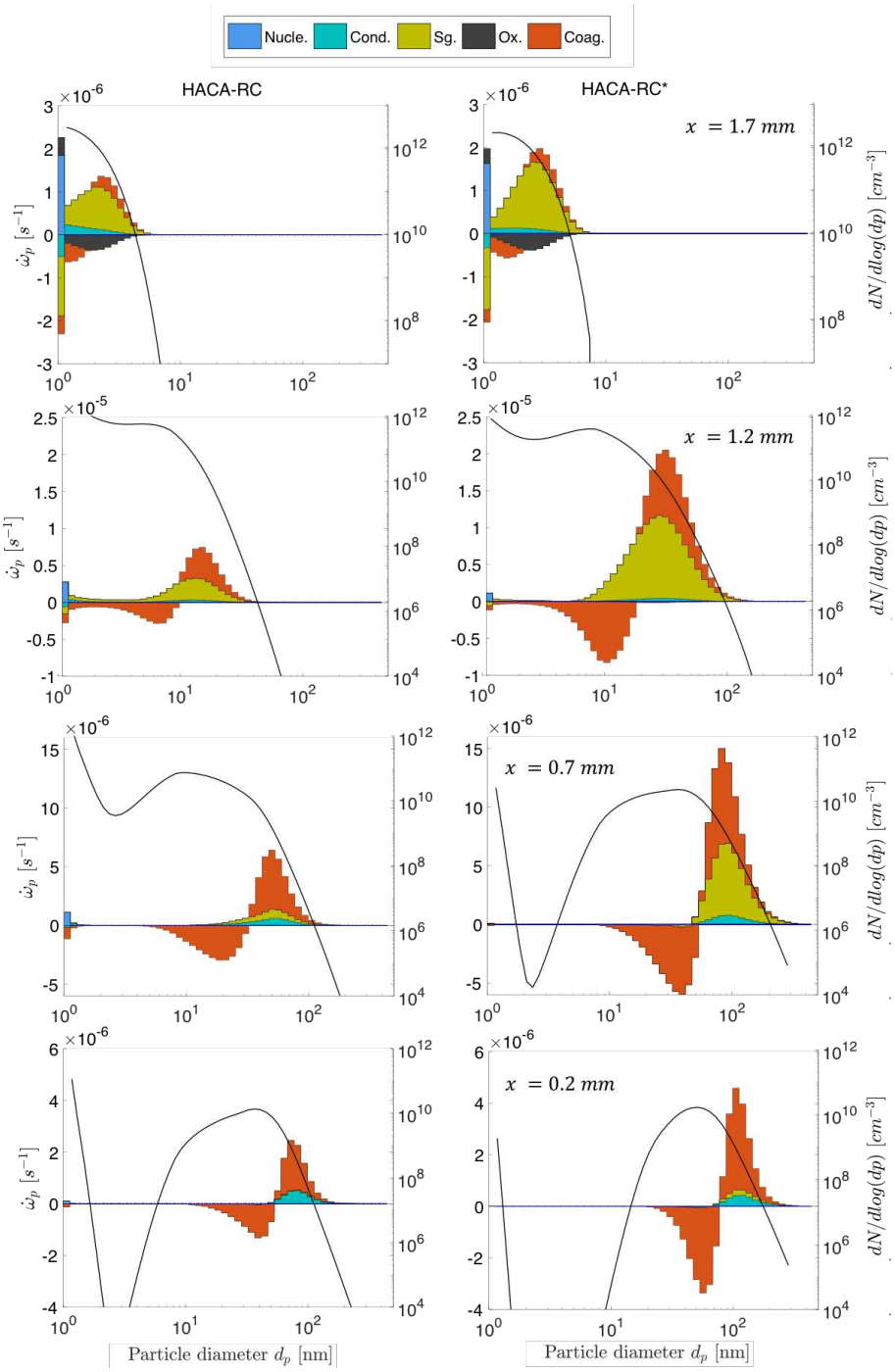

Figure 3.9: *Evolution of the particles size distribution (PSD) and source terms (nucleation, condensation, surface growth, oxidation and coagulation) at different axial positions along the flame with $X_{ox} = 0.24$ for the HACA-RC (left) and HACA-RC* (right) cases.*

Overall, the increase in surface growth changes the soot population: the soot particle size increases, and the particle density decreases. Thus, it can then be expected that the evolution of the PSD is also impacted. Figure 3.9 compares the evolution of the PSD, and the soot source terms, along with the flame ($X_{ox} = 0.24$) with the two models. At $x = 1.7$ cm near the flame front, the

PSD is quite similar between cases since surface growth and coagulation have slightly increased with the HACA-RC* model. At $x = 1.2$ mm, the PSD shape is still similar between cases, but soot particles are bigger using the HACA-RC* since surface growth rate has increased by a factor 3 compared to the reference model, while nucleation reduces. In the presence of bigger particles, coagulation also increases. Further approaching the stagnation plan, the PSD changes drastically in shape, and at $x = 0.7$ cm, the bimodality is sharpened. For the HACA-RC*, the increase in coagulation and surface growth combined with the decrease of nucleation leads to a lower number of small particles. Near the stagnation plane, at $x = 0.2$ cm, the surface growth decreases due to the decrease in H concentration and temperature, but coagulation continues to impact the PSD.

3.3.2 Model response to strain variation

Figure 3.10 shows the comparison between the predicted evolution of the maximum soot volume fraction as a function of the strain rate using the reference HACA-RC model and the new HACA-RC* for the flames experimentally investigated by Decroix and Roberts (2000) and Wang and Chung (2016), both introduced in Chapter 1. The maximum soot volume fraction and the decreasing tendency with strain rate are better reproduced with the HACA-RC* model
.

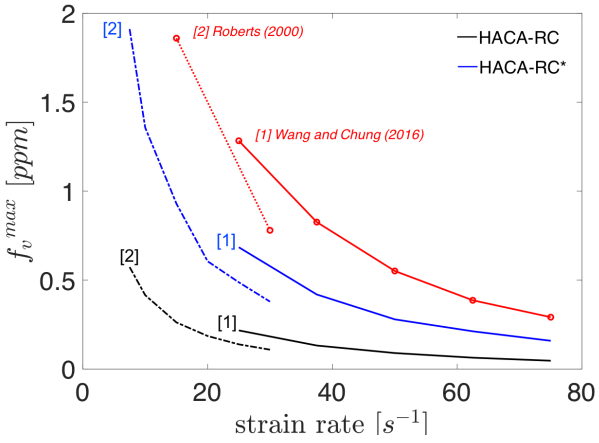

Figure 3.10: *Comparison of the soot volume fraction peak between HACA-RC (blue lines), HACA-RC* (black lines) and experimental measurements from Decroix and Roberts (2000) (red dotted line) and from Wang and Chung (2016) (red solid line).*

Figure 3.11 shows the computed sources terms for the flames studied by Wang and Chung (2016). Similarly to the flame with different oxygen dilution, the surface growth has significantly increased with the HACA-RC* model (solid lines Fig.3.11c). The increase in surface reaction leads to an increase in particle size, leading to an increase in condensation and coagulation as well (Fig.3.11b and Fig.3.11e). The increase in condensation leads to a decrease in the nucleation rate (Fig.3.11a), and consequently, on the number density of particles (Fig.3.11f), as previously observed for the diluted flames.

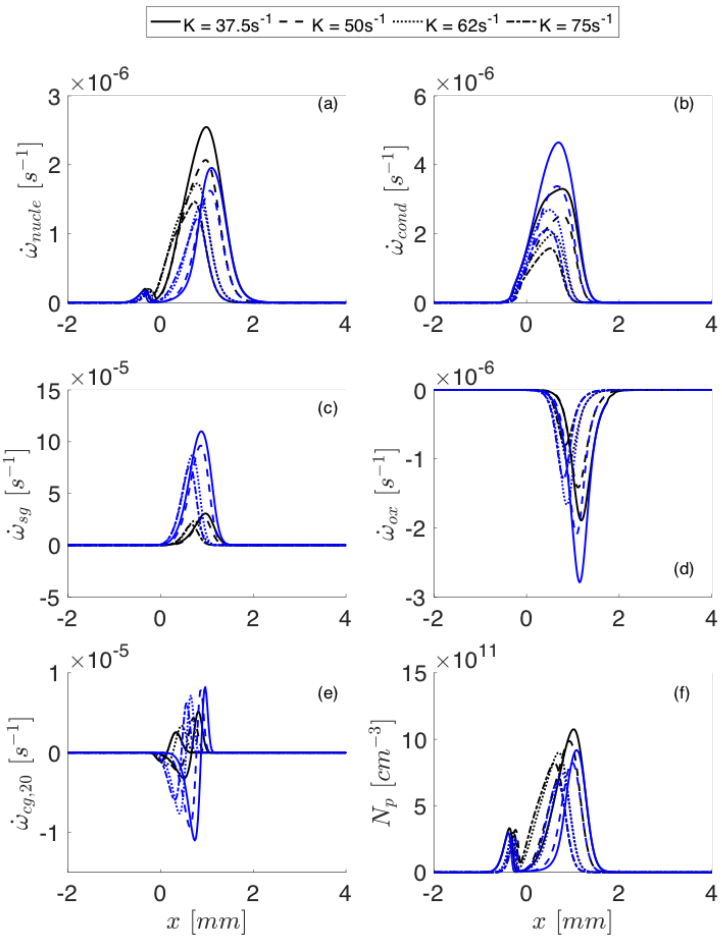

Figure 3.11: *(a-e) Soot source terms comparison between HACA-RC (black lines) and HACA-RC* (blue lines) and particle number density (f) for the flame due to Wang and Chung (2016).*

This study brings to light the complexity of modeling soot. The modification of a sub-model leads to a change in the overall soot formation, reinforcing the necessity in considering the soot model as a global strategy englobing gas

phase description, soot modeling for the physical and chemical process, and the method to solve the soot equations. Therefore, considering the experimental and numerical uncertainty, as discussed in Chapter 1, the improvement of the soot load with the simple proposed model is notable. The persistent lack of soot prediction in this type of flame can be associated with different reasons: PAH chemistry, nucleation, and condensation modeling, soot morphology, and surface reactivity assumptions. Detailed PAH measurements are still hardly performed to enable accurate comparison with numerical predictions and kinetic model validation. Similarly, the measurement of soot morphology in flame conditions is quite complicated. The assumption of quasi-stationarity between nucleation, condensation, and dimer can also partially explain the lack of soot volume fraction prediction. Veshkini et al. (2016) and Aubagnac-Karkar et al. (2018) have shown that the retro-coupling between soot and gas phase via the nucleation and condensation reversibility may significantly affect soot prediction. Additionally, surface reaction constants are based on similar PAH reactions even though that soot surface state can differ from the PAH structure.

3.3.3 Premixed flames

In this section, the proposed model is evaluated in the burner-stabilized premixed stagnation flame. Figure 3.12 presents the comparison of the soot volume fraction and the number density of particles for the different flames. In opposition to the HACA-RC predictions, now soot volume fraction is overpredicted wheres particle number density is correctly reproduced. Nevertheless, the soot volume fraction predicted with the HACA-RC* mechanism is satisfactory.

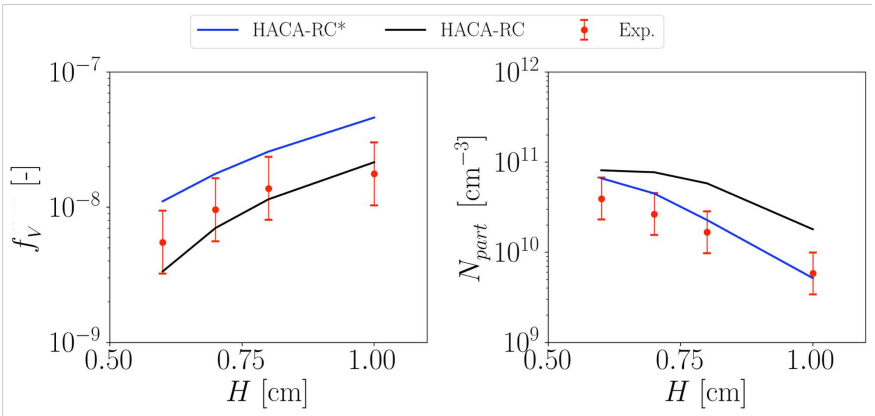

Figure 3.12: *Comparison between numerical predicted soot volume fraction (left) and number density of particles (right) using the HACA-RC and HACA-RC*, with experimental measurements (symbols - (Camacho et al., 2015)) for flames with H = 0.6, 0.7, 0.8 and 1 cm. The numerical values are taken at H - 0.2 cm.*

Figure 3.13 shows the PSD for each flame. For flames with a small distance between the burner and the stagnation plate (H= 0.6 and 0.7 cm), the PSD shape is not much affected by the new model, even though bigger particles are predicted. On the other hand, for higher distances (H = 0.8 and 1.0 cm), differences between the two models are greater. If the original model seems to capture the big particles mode better, a more accurate description of the small particles mode is obtained with the HACA-RC* model. In general, by enhancing surface reactions, big particles are more likely to be observed since condensation, surface growth and coagulation are increased.

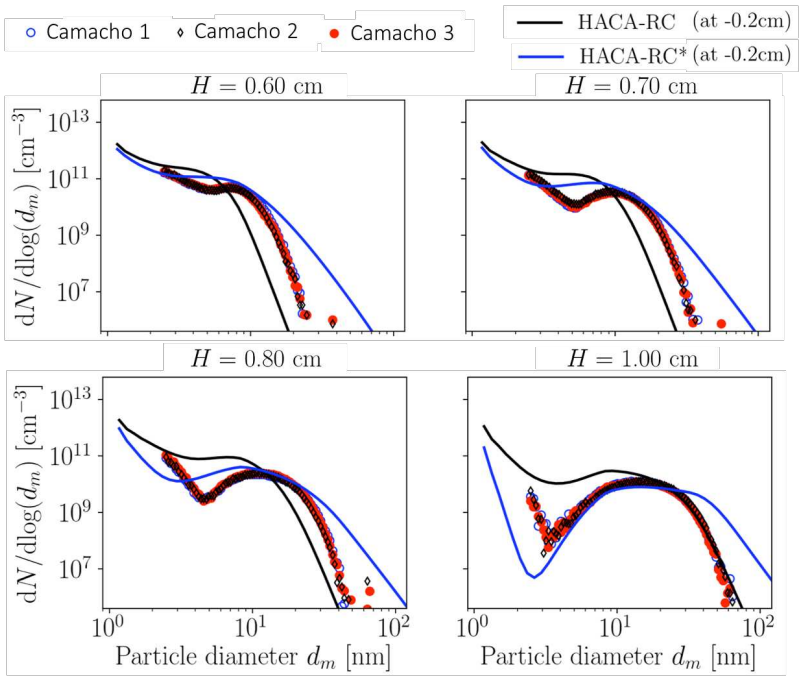

Figure 3.13: *Comparison between numerical predicted particle size distribution using the HACA-RC and HACA-RC* with experimental measurements protect (Camacho et al., 2015) for flames with H = 0.6, 0.7, 0.8 and 1 cm. The numerical values are taken at H - 0.2 cm.*

To illustrate the soot evolution along the flame, the particle size distribution and the soot source terms evolution are analyzed for the flame with H =1 cm (Fig. 3.14). At x = 0.2 and 0.4 cm, surface growth increase with HACA-RC* by about a factor 2. Due to the production of bigger particles, coagulation increases. However, nucleation and condensation slightly change between cases and the PSD keeps a similar shape. Approaching the stagnation plate (x = 0.6 and 0.8 cm), nucleation is more affected and the second peak of the bimodal distribution becomes predominant using the HACA-RC* model. In this case, surface growth and nucleation have similar contributions, while for the HACA-

RC case, nucleation and coagulation are the primary soot process in the post-zone flame.

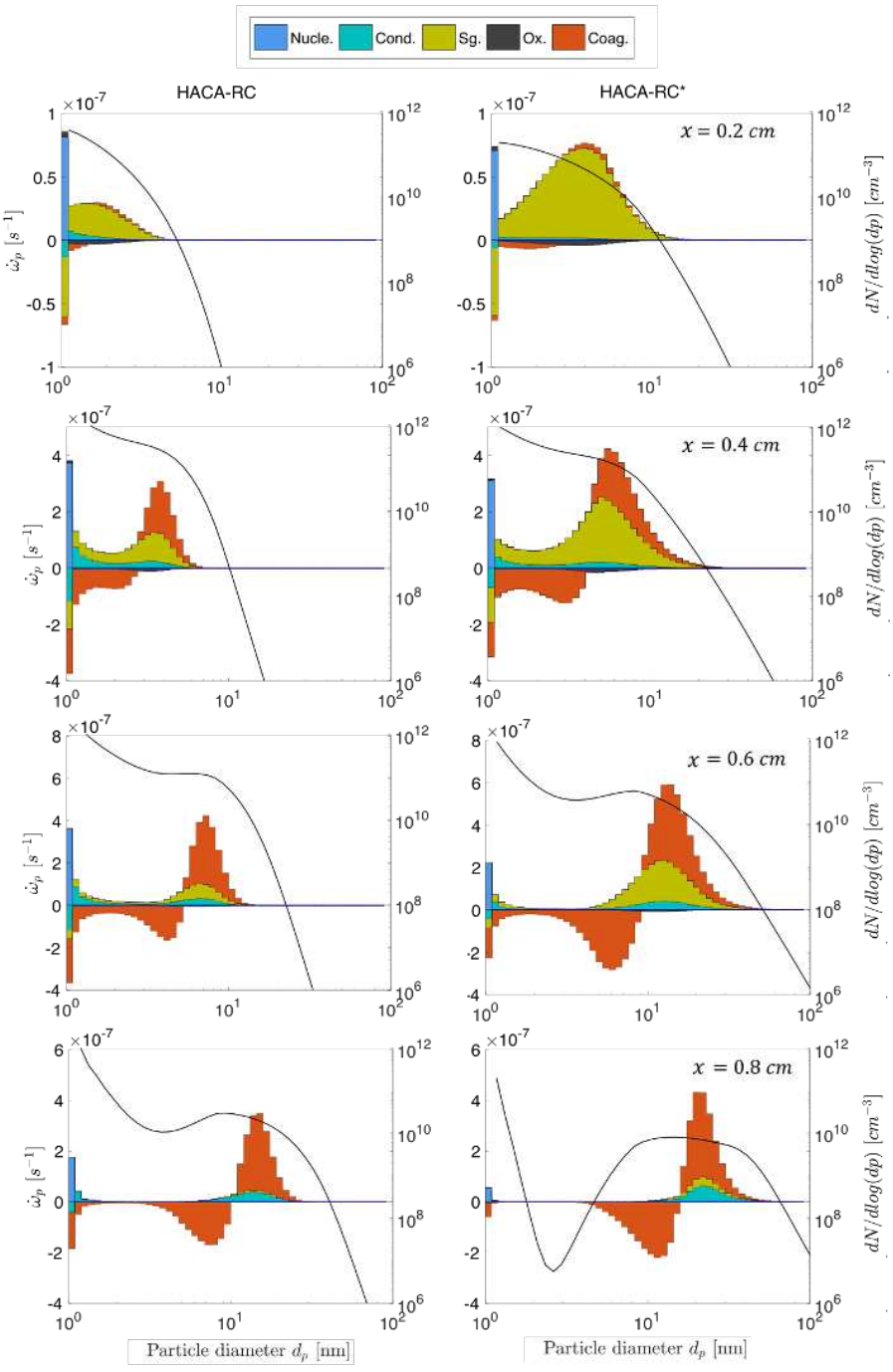

Figure 3.14: *Evolution of the particles size distribution (PSD) and source terms (nucleation, condensation, surface growth, oxidation and coagulation) at different x-positions above the burner for the flame with H = 1.0 cm.*

Overall, considering the uncertainties involved in soot modeling, the improvement obtained for the non-premixed flames in terms of soot load to the detriment of the premixed flame prediction is very satisfactory since the same accuracy level can be accessed in both combustion regimes and any additional fitting is required. This is quite relevant in multi-regime turbulent configurations where both regimes coexist.

3.4 Conclusion

In this chapter, the HACA-RC model introduced in Chapter 1 was modified based on the study of Hwang and Chung (2001) to improve soot volume fraction predictability in counterflow non-premixed ethylene-air flames. Therefore, a new reaction H-abstraction reaction was included in the reaction model, leading to the model called HACA-RC*. The model was coupled with the sectional method and the KM2 mechanism and evaluated in numerous laminar flames.

The aim is to apply the model in turbulent flames with tabulated chemistry. Thereby, two constraints guided the model development: not to affect soot prediction in premixed flames and not affect PAH formation. The investigation in laminar flames showed that with the new model, better results compared to experimental data are obtained in terms of soot volume fraction for the studied counterflow non-premixed flames under atmospheric pressure. The soot volume fraction is overpredicted for the premixed flames while the number density of particles decreases, reaching a better agreement with experimental values. Better results have also been obtained for counterflow non-premixed flames with different strain rates. A negligible impact was observed concerning PAH concentrations, ensuring the model's applicability in turbulent sooting flames with the tabulated chemistry model.

The analysis of the soot source terms revealed a significant increase in surface growth with the HACA-RC* model. With the increase in surface growth, coagulation and condensation increase as well, as they depend on the soot particle size. On the other hand, nucleation decreases, leading to a decrease in the number of soot particles. Therefore the particle size distribution (PSD) is affected, notably close to the stagnation plane, where the residence time is high.

Finally, the present study brings to light the complexity of modeling soot. The modification of a sub-model leads to a change in the overall soot structure formation. Thereby, the model should be considered as a global strategy, englobing gas-phase description, physical and chemical soot sub-models, and the soot equations method. The coupling of the HACA-RC* model with other kinetic mechanisms and solving methods needs additional validation since its performances strongly depend on the prediction of CH_3, C_2H_2 as well as PAH. However, the proposed model diminishes the need for arbitrary or tuned un-

physical parameters, providing the good tendency and the order of magnitude of soot volume fraction in ethylene-air flames in both premixed and non-premixed conditions. The proposed model will be used in the following LES calculations. Its impact is evaluated in a turbulent sooting flame, a gas turbine model combustor, in Chapter 7.

Part III

Large Eddy Simulation of soot production in a gas turbine combustor model

Chapter 4

LES formalism for sooting flames

This chapter presents the retained numerical formalism to solve soot production in turbulent conditions. In Section 4.1, the computational methods to solve turbulent reacting flow with soot formation are briefly presented and the gaseous filtered soot equations for LES are introduced. Then the retained soot LES formalism (Rodrigues et al., 2018) is described. In Section 4.3, the classical tabulated RFPV approach (Ihme and Pitsch, 2008) for the gaseous description coupled with a β subgrid model for mixing is presented. PAH species require a particular treatment as it is characterized by a high Damköhler number (Bisetti et al., 2012) compared to the other chemical species. Then a transport model for a lumped PAH (Mueller et al., 2009) is described in Section 4.4. The filtered soot equations (Franzelli et al., 2018) are given in Section 4.5. Finally, a brief review of the soot subgrid scale models is done. The soot subgrid intermittency model due to Mueller and Pitsch (2011) is retained for the LES simulations presented in this manuscript.

Contents

4.1 Computational approaches for reacting turbulent flows

The numerical resolution of the Navier-Stokes equations for turbulent flows is challenging due to the complex nature of the flow, characterized by unsteady and chaotic motions over a broad range of time and spatial scales. The aerodynamic structures vary from the system dimension (the most energetic flow structure) to the smallest eddies (Kolmogorov scale), dissipating kinetic energy in heat (Pope, 2000). In reaction conditions with soot production, the two-way coupling between turbulence, combustion, radiation and soot particles presents an additional difficulty. The combustion process can be affected by the turbulent flow altering the flame structure. At the same time, the flow can be affected by heat release and temperature variations. When soot production is considered, this is even more challenging due to its non-linear dependence on flow parameters, flame characteristics, and the competition between soot time scales, kinetically controlled, and turbulence scales. Moreover, the turbulence-combustion interactions may also occurs at the smallest scales as the chemical reactions are controlled by molecular mixing. Soot particles, characterized by low molecular diffusivity are confined in very thin flow structures which may also interacts with the smallest flow scales. Therefore, the numerical treatment of such a wide range of time and spatial scales determines the computational approaches to solve turbulent reacting flows.

In principle, to represents all scales, the grid used to solve NS equations needs to be fine enough. In non-reacting conditions, the number of grid points in each direction of the flow should be $N_{grid} > Re_t^{9/4}$ (Pope, 2000) ($Re_t = l_t u'/\nu$, where l_t is the integral length scale and u' is the turbulent velocity fluctuation). This approach corresponds to the Direct Numerical Simulation (DNS), which solves the instantaneous equations without any subgrid scale model. The high number of points and the large range of time scales result in a prohibitive computational cost. This approach is then impracticable in industrial applications. It is limited to simple applications with simple small geometries and low-moderate Reynolds number. When considering combustion, the computing cost grows with the *Damköhler* number ($\mathrm{Da} = \tau_t/\tau_c$), involving the turbulence and chemical time scales. A highly refined grid is required since the flame front is generally smaller than the cell size. It is similar to the soot particles that are confined in thin structures subjected to turbulence. Hence, few DNS studies

on turbulent sooting flames are found in the literature. Most of these studies are performed with two-dimensional flames (Lignell et al., 2007; Bisetti et al., 2012; Attili et al., 2014, 2015, 2016).

Numerical methods to solve turbulent flows have been developed to overcome the prohibitive computational cost of DNS. The Reynolds Averaged Navier-Stokes (RANS) solves the time-averaged equations providing only the mean properties of the flow and its evolution. Grid size is then much coarser than the grids required for DNS, leading to much affordable simulation costs. This approach was extensively used to predict soot formation in turbulent conditions, notably in IC engines and gas turbine model combustors (Balthasar et al., 2000; Netzell et al., 2007; Aubagnac-Karkar et al., 2015; Bolla et al., 2013; Eberle et al., 2015). However, RANS cannot resolve transient phenomena, and specific models, based on severe assumptions, are required to account for the turbulence-chemistry-soot interactions.

An intermediary approach between DNS and RANS has been developed in the last decades. The Large Eddy Simulations (LES) consists of resolving the large scales of the flow by applying a spatial filtering operator on the NS equations and modeling the small scale effects. Since the large scales are the most energetic scales of the flow, the transient features are captured with this technique. Similarly to the RANS approach, subgrid models are needed, but in LES, only the small scales, considered as universal, are modeled. Combustion interacts with turbulence at a subgrid level since the flame structure is not resolved on the LES grids. Turbulent combustion modeling is the subject of interest for accurate reacting flow LES. A comprehensive review can be found in Peters (2000) Poinsot and Veynante (2005) and Pitsch (2006). Although many efforts have been made to model turbulent-chemistry interaction, the effect of turbulence on soot production is still an open subject. The complex non-linear coupling between the soot and gas phase and the yet lack of understanding of soot formation made the task even more challenging.

Figure 4.1 illustrates with a turbulent energy spectrum how LES differently treat the large and subgrid dissipative scales. The gain in resolution over computational cost made LES an excellent approach to study complex multi-physical transient and unsteady phenomena in lab-scale geometries under technical conditions of practical interest for industrials (Gicquel et al., 2012; Mueller and Pitsch, 2013; Stohr et al., 2018). In practice, the mesh size implicitly controls the LES filter size. Then LES is expected to tend to DNS when the mesh is sufficiently refined to capture all the flow length scales.

The present work deals with the numerical simulation of a turbulent sooting flame in a gas turbine model combustor, the DLR burner. Thereby, to study soot production and its interaction with turbulence in such a complex configuration, the LES approach is suitable, as it captures instantaneous local flow structures. In the following, the retained LES formalism (Rodrigues et al.,

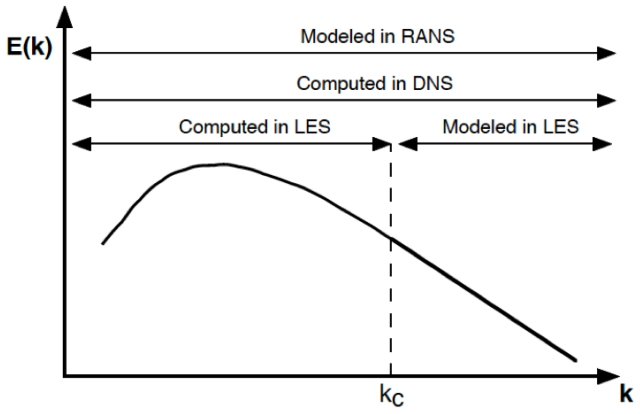

Figure 4.1: *Turbulent energy spectrum as a function of the wave number illustrating the scales modeled and/or resolved according to the numerical approach (DNS, LES or RANS). For LES, the cut-off value is shown and noted k_c from Poinsot and Veynante (2005).*

2018; Franzelli et al., 2018) for both gaseous and solid phases is presented.

4.2 Filtered gaseous conservation equations for LES

The filtered conservation equations for LES are obtained by the convolution product between the instantaneous variables and the normalized filter F with the characteristic length Δ (Pope, 2000). A filtered quantity $\overline{f}$ is then obtained by space filtering of the variable f.

$$\overline{f}(x,t) = \int f(x',t)F(x-x')dx' \tag{4.1}$$

The filtered quantity $\bar{f}$ represents the resolved turbulent structure in the LES approach. The subgrid unresolved structures are denoted as

$$f'(x,t) = f(x,t) - \overline{f}(x,t) \tag{4.2}$$

In the case of reacting flows where the density ρ is variable, it is convenient to apply the mass-weighted Favre average, which consists of spatial filtering of the variables weighted by their density. For the physical variable f, its Favre average $\widetilde{f}$ is:

$$\widetilde{f} = \frac{\overline{\rho f}}{\overline{\rho}} \tag{4.3}$$

The filtering procedure is expressed as:

$$\overline{\rho}\widetilde{f}(x) = \overline{\rho f(x)} = \int \rho(x')f(x',t)F(x-x')dx' \tag{4.4}$$

Different filter functions F can be used to obtain filtered quantities, but the filtering function becomes implicit in practice. Indeed, the separation between the resolved scales and the non-resolved scales, which have to be modeled, is dictated by the size of the grid cells. Accordingly, the filtered Navier-Stokes equations for multi-species in a reactive flow are the following (Poinsot and Veynante, 2005):

$$\frac{\partial \overline{\rho}}{\partial t} + \frac{\partial \overline{\rho}\widetilde{u}_i}{\partial x_i} = 0 \tag{4.5}$$

$$\frac{\partial \overline{\rho}\widetilde{u}_j}{\partial t} + \frac{\partial}{\partial x_i}(\overline{\rho}\widetilde{u}_i\widetilde{u}_j) = -\frac{\partial \overline{P}}{\partial x_j} + \frac{\partial}{\partial x_i}(\overline{\tau}_{ij} + \overline{\tau}_{ij}^{sgs}) \tag{4.6}$$

$$\frac{\partial \overline{\rho}\widetilde{Y}_k}{\partial t} + \frac{\partial}{\partial x_i}(\overline{\rho}\widetilde{u}_i\widetilde{Y}_k) = -\frac{\partial}{\partial x_i}\left(\overline{J}_{i,k} + \overline{J}_{i,k}^{sgs}\right) + \overline{\dot{\omega}}_k \tag{4.7}$$

$$\frac{\partial \overline{\rho}\widetilde{E}}{\partial t} + \frac{\partial}{\partial x_i}(\overline{\rho}\widetilde{u}_i\widetilde{E}) = -\frac{\partial \overline{Pu_i}}{\partial x_i} + \frac{\partial \overline{\tau_{ij}u_i}}{\partial x_j} - \frac{\partial}{\partial x_i}(\overline{q}_i + \overline{q}_i^{sgs}) + \overline{\dot{\omega}}_T + \overline{\dot{Q}}_r \tag{4.8}$$

where $\bar{.}$ and $\tilde{.}$ denote the filtering and the density-weighted filtering operations, respectively.

The filtering procedure, which separate the large scales to be resolved from the small scales, leads to unknown terms "sgs" that must be modeled. They are: the unresolved transported terms τ_{ij}^{sgs}, $J_{i,k}^{sgs}$ and q_i^{sgs}. The filtered laminar diffusion fluxes in momentum, species and energy equations $\overline{\tau}_{ij}$, $\overline{J}_{k,i}$, $\overline{q}_i$, respectively, also need to be modeled, as well as the filtered chemical reaction rates $\overline{\dot{\omega}}_k$.

4.2.1 Approximations and subgrid closure models

The approximations and models considered in the AVBP code, developed at CERFACS/IFP Energies Nouvelles (Schonfeld and Rudgyard, 1999), used to perform the simulations presented in this manuscript, are generally based on the resolved quantities assuming similarity between scales based on the Kolmogorov cascade theory. They are given in the following.

Laminar filtered stress tensor $\bar{\tau}_{ij}$:

$$\bar{\tau}_{ij} = \overline{\mu\left(\frac{\partial u_i}{\partial x_j} + \frac{\partial u_j}{\partial x_i}\right) - \frac{2}{3}\mu\frac{\partial u_k}{\partial x_k}\delta_{ij}} \approx \bar{\mu}\left(\frac{\partial \tilde{u}_i}{\partial x_j} + \frac{\partial \tilde{u}_j}{\partial x_i}\right) - \frac{2}{3}\bar{\mu}\frac{\partial \tilde{u}_k}{\partial x_k}\delta_{ij} \quad (4.9)$$

with $\bar{\mu} \approx \mu(\widetilde{T})$.

Diffusive flux vector $\bar{J}_{k,i}$:

$$\bar{J}_{k,i} = \overline{\rho Y_k V_{k,i}} \approx -\bar{\rho}\left[\overline{D}_k \frac{W_k}{W}\frac{\partial \widetilde{X}_k}{\partial x_i} - \widetilde{Y}_k \widetilde{V}_i^c\right] \quad (4.10)$$

with $\bar{D}_k = \bar{\mu}/(\bar{\rho} Sc_k)$ and $\widetilde{V}_i^c = \sum_{k=1}^{N} \bar{D}_k \frac{W_k}{W}\frac{\partial \widetilde{X}_k}{\partial x_i}$.

Filtered heat flux $\bar{q}_j$:

$$\bar{q}_i = \overline{-\lambda\frac{\partial T}{\partial x_i}} + \sum_{k=1}^{N} \overline{J_{k,i} h_{s,k}} \approx -\bar{\lambda}\frac{\partial \tilde{T}}{\partial x_i} + \sum_{k=1}^{N} \bar{J}_{k,i}\tilde{h}_{s,k} \quad (4.11)$$

with $\approx \bar{\mu}\bar{C}_p(\tilde{T})/Pr$.

Subgrid scale (SGS) fluxes

The unknown subgrid scales terms describing the interactions between the resolved and non-resolved scales are:

$$\overline{\tau_{ij}}^{sgs} = -\bar{\rho}(\widetilde{u_i u_j} - \widetilde{u}_i\widetilde{u}_j) \quad (4.12)$$

$$\overline{J_{i,k}}^{sgs} = \bar{\rho}(\widetilde{Y_k u_i} - \widetilde{Y}_k\widetilde{u}_i) \quad (4.13)$$

$$\overline{J_{i,k}}^{sgs} = \bar{\rho}(\widetilde{Y_k u_i} - \widetilde{Y}_k\widetilde{u}_i) \quad (4.14)$$

It is assumed that the unresolved transported terms have a purely dissipative effect on the resolved scales. Then, a subgrid turbulent viscosity is introduced to models the dissipation of energy from the large to the smaller turbulence scales. The subgrid terms are then approximated as:

$$\overline{\tau_{ij}}^{sgs} \approx \bar{\rho}\nu_t \left(\frac{\partial \tilde{u}_i}{\partial x_j} + \frac{\partial \tilde{u}_j}{\partial x_i} \right) - \frac{2}{3}\bar{\rho}\nu_t \frac{\partial \tilde{u}_k}{\partial x_k}\delta_{ij} \tag{4.15}$$

$$\overline{J_{i,k}}^{sgs} \approx -\bar{\rho} \left(D_k^t \frac{W_k}{W} \frac{\partial \widetilde{X}_k}{\partial x_i} - \widetilde{Y}_k \widetilde{V}_i^{c,t} \right) \tag{4.16}$$

$$\overline{q_i}^{sgs} \approx -\lambda^t \frac{\partial \widetilde{T}}{\partial x_i} + \sum_{k=1}^{N} J_{i,k}^{sgs} \widetilde{h}_{s,k} \tag{4.17}$$

with ν_t the subgrid turbulent viscosity, $D_k^t = \nu_t / Sc_k^t$ the turbulent molecular diffusion coefficient and $\lambda^t = \bar{\rho}\nu_t \bar{C}_p / Pr^t$ the turbulent thermal diffusion coefficient. Sc_k^t and Pr^t are the turbulent Schmidt and Prandlt subgrid numbers, fixed both at 0.6.

The subgrid turbulent viscosity ν_t is estimated from the unresolved Reynolds stresses model. In the simulations presented in this manuscript, the SIGMA model due to Nicoud et al. (2011) is used. This model is based on the singular values of the locally-resolved velocity gradient tensor and has the property to vanish in two-dimensions or two-components flow where subgrid turbulence viscosity is not expected as well as for resolved scales in pure axisymmetric or isotropic expansion/contraction situations. Near-wall regions are also adapted, since turbulence is damped due to the no-slip condition, with a cubic order decay of the turbulent viscosity. Then, the turbulent viscosity is defined as:

$$\nu_t = (C_\sigma \Delta)^2 \frac{\sigma_3(\sigma_1 - \sigma_2)}{\sigma_1^2} \tag{4.18}$$

with $\sigma_1 > \sigma_2 > \sigma_3$ the three singular values of the resolved velocity gradient tensor $\dfrac{\partial \tilde{u}_j}{\partial x_i}$. Δ denotes the filter characteristic length ($\Delta = V_{node}^{1/3}$) and $C_\sigma = 1.5$ is the constant model.

Filtered chemical reaction $\overline{\dot{\omega}_k}$

The state-of-the-art of turbulent combustion models is abundant, many models are available in the literature (Poinsot and Veynante, 2005). They generally rely on the combustion mode, i.e., premixed or non-premixed mode. For the simulations presented in this manuscript, a tabulated approach is retained. Since fuel and oxidizer are separately introduced in the chamber, the RFPV approach is coupled with a presumed PDF to model the subgrid scales. The model is presented in the following.

4.3 Turbulent combustion modeling

The description of the gas phase is one of the main challenges of modeling turbulence combustion. It is even more challenging when predicting pollutants since the chemistry model has to describe the fuel oxidation and the key species involved in the gaseous or solid pollutant formation. In sooting flames, soot precursors, gaseous species with high molecular weight and long chemical time scales have to be included in the kinetic mechanism resulting in chemical models with more than 100 species (Appel et al., 2000; Wang et al., 2013). Due to their high computational cost, these mechanisms are generally reserved for one-dimensional laminar flames. Three reduction techniques are available in the literature to prevent prohibitive computational costs while preserving accuracy in turbulent flames. They are: (1) skeletal reduction (Lu and Law, 2005a; Pepiot-Desjardins and Pitsch, 2008); (2) optimization-based techniques including analytical reduced chemistry (ARC) (Felden et al., 2019) and the recent virtual chemistry (Cailler et al., 2017); (3) the tabulation techniques. The ARC techniques have been successfully applied in purely gaseous and spray flames (Jaravel et al., 2017, 2018; Felden et al., 2018) and in a sooting flame coupled with a C_2H_2-based model (Felden et al., 2018; Gallen et al., 2018). However, including large PAHs remains a challenge to be overcome. Recently Gallen (2020) have addressed this issue by including PAH up to A4 in a chemistry model via ARC. The virtual chemistry has only recently been validated in a laminar premixed sooting flame coupled with a kinetic soot model (Colmán et al., 2019). The tabulation approach is widespread in the sooting and non-sooting flames literature (Balthasar et al., 2000; Mueller et al., 2009; Fiorina et al., 2010; Franzelli et al., 2013; Mercier et al., 2015; Rodrigues et al., 2018) as it provides an excellent accuracy-cost compromise despite the many model assumption. The Radiation-Flamelet Progress variable (RFPV) approach is retained for this work since it has been previously coupled and validated with the three-equation soot model by Franzelli et al. (2018) in the target flame (the DLR burner).

4.3.1 RFPV approach coupled with a β PDF model

In order to incorporate complex detailed chemistry in LES of sooting flames, tabulated chemistry models have been extensively used in the literature (Mueller and Pitsch, 2012, 2013; Franzelli et al., 2015; Chong et al., 2018; Franzelli et al., 2018; Rodrigues et al., 2018; Chong et al., 2019). Instead of transporting a large number of chemical species and closing the associated non-linear chemical source terms, a reduced number of tracking scalars are used to retrieve information on the chemical kinetic processes involved in combustion, enabling a considerable reduction of the CPU cost.

The RFPV (Radiation Flamelet-Progress Variable) approach due to Ihme and

Pitsch (2008) is used in the LES calculations performed during this thesis. This model is an extension of the FPV (Flamelet-Progress Variable) approach developed by Pierce and Moin (2004), proposed in the context of LES of non-premixed flames. For this approach, the flamelet database is composed of thermochemical variables from the laminar counterflow non-premixed flames. The model is based on the assumption of fast chemistry, then only flamelets in a steady-state are considered and it is parameterized by only two scalars, the mixture fraction Z, and the reaction progress variable Y_C. The RFPV model introduces a supplementary coordinate, the enthalpy H, to describe radiative heat loss effects through the solution of unsteady flamelets since radiation occurs on relatively slow time scales (Ihme and Pitsch, 2008). Rodrigues (2018) has found that accounting for radiative heat loss effects is crucial to flame stabilization in this configuration studied in this manuscript and, consequently, to soot prediction.

4.3.2 Flamelets generation

For the generation of the look-up table, counterflow ethylene-air non-premixed 1D flames at $T = 298\ K$ and $p = 3\ atm$ (DLR operating conditions) are considered. The adiabatic steady flamelets are then solved in the physical space imposing strain-rate and using the detailed KM2 kinetic mechanism (Wang et al., 2013) with a unity Lewis diffusion model in the REGATH in-house code (Darabiha, 1992). In order to account for PAH consumption by soot, the 1D flames are calculated considering the dimerization process, which depends on the concentration of PAH itself, .

When plotting the maximum temperature as a function of the scalar dissipation rate, the considered solutions generate the classical "S-curve", which gives access to the different steady thermochemical states found by the flame as a function of the strain rates. This curve is composed of three states: the stable and unstable burning branches and the extinction line, as indicated in Fig. 4.2. The maximum temperature decreases with increasing strain rate due to a competition between mixing time and chemical time on the steady burning branch. According to the Arrhenius law, close to the critical turning point, the flame temperature becomes too low to overcome the activation energy to keep the reaction rate. Thus, when the dissipation rate becomes higher than the critical value, the flame extinguishes. The extinction line corresponds to the pure mixing of reactants. Between these two states, the unstable conditions characterize burning under partially extinguished states. The turning point ("critical point") between the steady and unsteady branches corresponds to the critical scalar strain rate at which quenching occurs. This curve is obtained through the continuation technique, based on the curvilinear abscissa parametrization by the temperature and the strain rate (Kee et al., 1989).

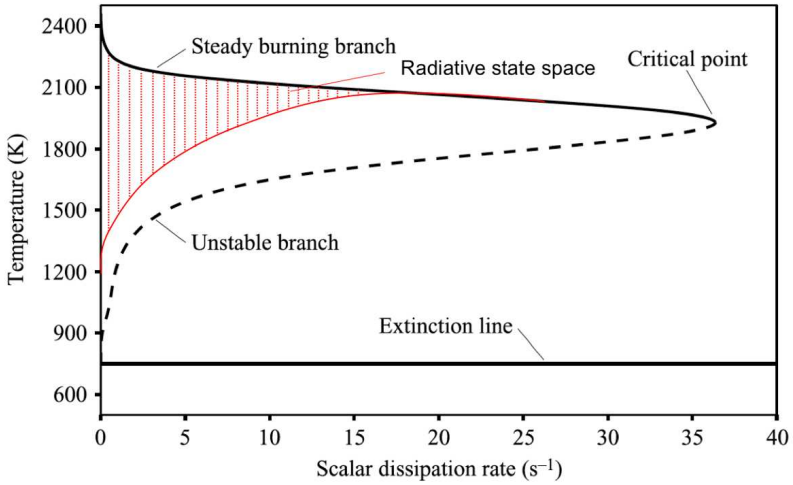

Figure 4.2: *Schematic "S-curve" representing the set of steady flamelet solutions (solid and dashed black lines) and the unsteady radiation space (red lines). The red dotted lines denote the intermediate unsteady flamelet solutions composing the look-up table. Figure adapted from Pierce and Moin (2004)).*

The FPV formulation cannot account for radiation effects that are of most relevance for pollutant predictions, as for soot particles (Rodrigues, 2018). Soot and radiation are coupled in two-way, then soot contributes to radiative transfer and radiation affects temperature that is a crucial parameter for soot production mechanisms. In order to account for heat loss effects, unsteady flamelets from each steady stable-branch solution are solved by imposing the radiation source term, assuming optically thin radiation of CO, CO_2, and H_2O species. A set of intermediate solutions obtained during calculation is stored in the RFPV library. These flamelets are represented by the red dot lines in Fig. 4.2.

4.3.3 Tabulation methodology

For the generation of the RFPV library, the first step involves defining the mixture fraction Z and the reaction progress variable Y_C since the flamelets are solved in the physical space. This definition should describe the S-curve without bijection in the reduced space (Y_C, Z). In the AGATH in-house code, the mixture fraction Z, a passive scalar not influenced by the chemical reactions, is defined in terms of the N_2 species mass fraction so that Z is one in the fuel-stream and zero in the oxidizer stream.

$$Z = \frac{Y_{N_2} - Y_{N_2}\,|_{ox}}{Y_{N_2}\,|_{fuel} - Y_{N_2}\,|_{ox}} \tag{4.19}$$

The reaction progress variable Y_C is defined as a linear combination of reaction product mass fraction. For this thesis, the reaction progress variable describing

the combustion process based on the KM2 kinetic scheme is defined following (Rodrigues, 2018) :

$$Y_C = \frac{Y_{H_2O}/W_{H_2O} + Y_{CO_2}/W_{CO_2} + Y_{CO}/W_{CO} - 3Y_{CH_4}/W_{CH_4}}{1/W_{H_2O} + 1/W_{CO_2} + 1/W_{CO} + 3/W_{CH_4}} \tag{4.20}$$

where Y_k is the mass fraction of the k^{th} species (H_2O, CO_2, CO and CH_4) and W_k are the molecular weight of the k^{th} species.

Therefore, each flamelet in the S-curve can be identified by a parameter defined as:

$$\Lambda = Y_C \mid_{Z_{st}=0.064} \tag{4.21}$$

which corresponds to the value of Y_C for each steady adiabatic flamelet evaluated at the stoichiometric condition Z_{st}. Then, each thermochemical variable ξ stored in the flamelet library can be accessed as:

$$\xi = \mathcal{F}_\xi(Z, \Lambda) \tag{4.22}$$

where $\mathcal{F}_\xi$ denotes the FPV thermochemical library.

The chemical space is then reduced to only two scalars Z and Λ. Instead of transporting an equation for each species composing the chemistry, the transport of the introduced scalars Z and Λ gives access to the thermochemical state. However, the transport of Λ is not trivial since it requires additional models (Pierce and Moin, 2004). Instead, the transport equation for Y_C is solved. This is possible under the assumption of bijectivity of $\mathcal{F}_{Y_C}$, i.e., one flamelet corresponds to a unique value of Y_C. Then Λ can be written as:

$$\Lambda = \mathcal{F}_{Y_C}^{-1}(Z, C) \tag{4.23}$$

with

$$C = \frac{Y_C - Y_C^f(Z)}{Y_C^{eq}(Z) - Y_C^f(Z)} \tag{4.24}$$

where Y_C^{eq} is the progress variable value for the lowest strain rate flamelet on the stable branch of the S-curve representing the flame when steady state is reached and Y_C^f is the unburnt mixture solution when chemical reactions are neglected.

Finally, all thermochemical quantities can be expressed as:

$$\xi = \mathcal{G}_{\xi}^{FPV}(Z, C) \tag{4.25}$$

with

$$\mathcal{G}_{\xi}(Z, C) = \mathcal{F}_{\xi}(Z, \mathcal{F}_{C}^{-1}(Z, C)) \tag{4.26}$$

According to Ihme and Pitsch (2008), a new parameter is necessary to describe the radiative heat loss, ψ. Then, assuming statistical independence between the parameters Λ and ψ, the non-adiabatic flamelets can be written as:

$$\psi = H\,|_{Z_{st}} \tag{4.27}$$

where the normalized heat loss coordinate writes as:

$$H = \frac{h - h^{rad}(Z)}{h^{adiab}(Z) - h^{rad}(Z)} \tag{4.28}$$

with h^{adiab} the enthalpy of the adiabatic flamelet corresponding to the steady state and h^{rad} the enthalpy of the flamelet presenting the maximum of radiation heat loss.

Finally, the extended RFPV library should be written as:

$$\xi = \mathcal{G}_{\xi}^{RFPV}(Z, C, H) \tag{4.29}$$

whith $\mathcal{G}_{\xi}^{RFPV}$ representing the relationship obtained now with this RFPV database.

Figure 4.3 illustrate the parametrization of the flamelet library by Λ and ψ. It can be noted that each flamelet of the RFPV database is parameterized by a unique set of parameters (Λ, ψ).

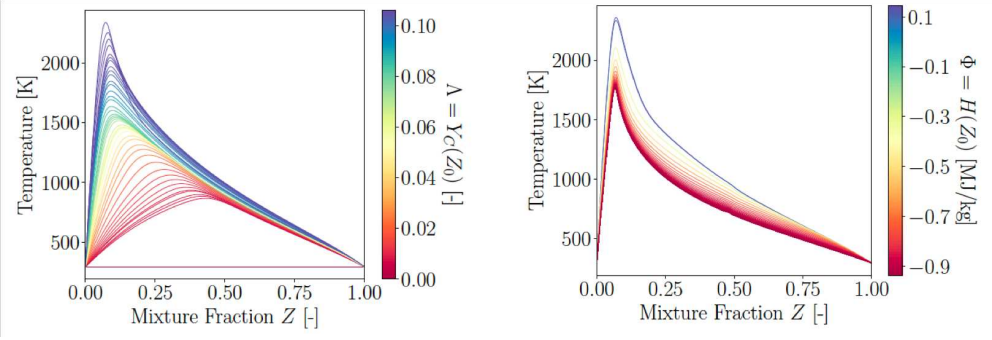

Figure 4.3: *Left: Evaluation of the temperature in the mixture fraction space. Each steady flamelet can be identified by the parameter* Λ *evaluated at the mixture fraction* $Z_0 = Z_{st}$*. Right: Impact of the enthalpy defect on the temperature. Each unsteady flamelet can be identified by the parameter* ψ *evaluated at the mixture fraction* $Z_{st} = 0.064$*. Image from Rodrigues (2018).*

4.3.4 Gaseous subgrid model

A presumed PDF is used to link non-resolved quantities ξ to the resolved scales $\tilde{\xi}$. Then any filtered quantities ξ depending on the thermochemical state can be expressed as:

$$\widetilde{\xi} = \int \xi(Z, \Lambda, \psi)\widetilde{P}(Z, \Lambda, \psi)dZd\Lambda d\psi \tag{4.30}$$

with $\widetilde{P}$ is a density-weighted joint PDF.

Assuming a statistical independence between the table coordinates ξ, $\widetilde{P}(Z, \lambda, \phi)$ can be modeled using marginal presumed distributions for each coordinate. Thus, a β-pdf is used for the mixture fraction (Lien et al., 2009) and a Dirac δ function is considered for the reaction progress variable and enthalpy:

$$\widetilde{P}(Z, \Lambda, \psi) = \beta(Z; \widetilde{Z}, Sz)\delta(\Lambda - \widetilde{\Lambda})\delta(\psi - \widetilde{\psi}) \tag{4.31}$$

where S_Z is the mixture fraction segregation factor required by the β distribution.

The filtered variable $\tilde{\xi}$ from the table can finally be obtained through:

$$\widetilde{\xi} = \widetilde{\mathcal{G}}_{\xi}^{RFPV}(\widetilde{Z}, S_Z, \overline{C}, \overline{H}) \tag{4.32}$$

where $\widetilde{Z}$, S_Z, $\overline{C}$ and $\overline{H}$ are the non-dimensional coordinates of the table.

The non-dimensional coordinates (S_Z, $\overline{C}$ and $\overline{H}$) used to retrieve the variables of the table are computed from the transported scalars ($\widetilde{Z}$, $\widetilde{Z_v}$, $\widetilde{Y_C}$, $\widetilde{h}$) as:

$$S_Z = \frac{\widetilde{Z_v}}{\widetilde{Z}(1-\widetilde{Z})} \tag{4.33}$$

$$\text{with } \widetilde{Z_v} = \widetilde{Z''^2} = \widetilde{Z^2} - \widetilde{Z}^2 \tag{4.34}$$

$$\overline{C} = \frac{\widetilde{Y}_C - \widetilde{Y}_C^f(Z)}{\widetilde{Y}_C^{eq}(Z) - \widetilde{Y}_C^f(Z)} \tag{4.35}$$

$$\overline{H} = \frac{\widetilde{h} - \widetilde{h^{rad}}(Z)}{\widetilde{h^{adiab}}(Z) - \widetilde{h^{rad}}(Z)} \tag{4.36}$$

where S_Z is the normalized mixture fraction variance Z_v, required in the β-PDF model. For S_z= 0 the variance Z_v is nulle then $\widetilde{\xi}(\widetilde{Z}) = \xi(Z)$, otherwise for S_z = 1, the mixture between fresh gases at Z = 0 and Z = 1 follows a linear variation as a function of $\widetilde{Z}$. Y_C^{eq} is the progress variable value for the lowest strain rate flamelet and Y_C^f its frozen value when chemical reactions are neglected. h^{adiab} is the enthalpy of the adiabatic flamelet, h^{rad} is the enthalpy of the flamelet presenting the maximum of radiation heat loss.

Therefore, the gaseous phase chemistry can be described by a reduced set of equation ($\widetilde{Z}$, $\widetilde{Z_v}$, $\widetilde{Y_C}$, $\widetilde{h}$). The multi-species mass fraction conservation equations Eq.(4.7) are then replaced by the following set of equations:

$$\frac{\partial \bar{\rho}\widetilde{Z}}{\partial t} + \frac{\partial}{\partial x_i}(\bar{\rho}\widetilde{u_i}\widetilde{Z}) = \frac{\partial}{\partial x_i}\overline{(\rho D_Z \frac{\partial Z}{\partial x_i})} - \frac{\partial}{\partial x_i} J_{ij,Z}^{sgs} \tag{4.37}$$

$$\frac{\partial \bar{\rho}\widetilde{Z_v}}{\partial t} + \frac{\partial}{\partial x_i}(\bar{\rho}\widetilde{u_i}\widetilde{Z_v}) = \frac{\partial}{\partial x_i}\overline{(\rho D_{Z_v} \frac{\partial Z_v}{\partial x_i})} - \frac{\partial}{\partial x_i} J_{ij,Z_v}^{sgs} - 2\tau_Z \frac{\partial \widetilde{Z}}{\partial x_i} - \overline{s_{\chi_z}} \tag{4.38}$$

$$\frac{\partial \bar{\rho}\widetilde{Y_C}}{\partial t} + \frac{\partial}{\partial x_i}(\bar{\rho}\widetilde{u_i}\widetilde{Y_C}) = \frac{\partial}{\partial x_i}\overline{(\rho D_{Y_C} \frac{\partial Y_C}{\partial x_i})} - \frac{\partial}{\partial x_i} J_{ij,Y_C}^{sgs} + \overline{\rho}\widetilde{\dot{\omega}}_{YC} \tag{4.39}$$

$$\frac{\partial \bar{\rho}\widetilde{h}}{\partial t} + \frac{\partial}{\partial x_i}(\bar{\rho}\widetilde{u_i}\widetilde{h}) = \frac{\partial}{\partial x_i}\overline{(\rho D_h \frac{\partial h}{\partial x_i})} - \frac{\partial}{\partial x_i} J_{ij,H}^{sgs} + \overline{\dot{q}}_R \tag{4.40}$$

The unclosed terms require some closure models detailed in the following.

Unresolved scalar fluxes $J^{res}_{ij,\xi} = \bar{\rho}(\widetilde{u_i\Theta} - \widetilde{u}_i\widetilde{\Theta})$ with $\Theta = \widetilde{Z}$, $\widetilde{Y_C}$, $\widetilde{h}$.

The subgrid scalar fluxes for $\widetilde{Z}$, $\widetilde{Y}_C$ and $\widetilde{h}$ are closed by a simple gradient assumption:

$$\bar{\rho}(\widetilde{u_i\Theta} - \widetilde{u}_i\widetilde{\Theta}) = -\frac{\nu_t}{Sc_\Theta}\frac{\partial\widetilde{\Theta}}{\partial x_i} \tag{4.41}$$

where ν_t is the turbulent viscosity given by the SIGMA model as discussed in Section 4.2, with constant Schmidt number $Sc_\xi = 0.6$.

To close the subgrid fluxes for Z_v, information from the mixture fraction and the square of the mixture fraction (Poinsot and Veynante, 2005; Vicquelin, 2010) are used, so that:

$$J^{sgs}_{ij,Z''} = \bar{\rho}(\widetilde{u_iZ_v} - \widetilde{u}_i\widetilde{Z_v}) = \bar{\rho}(\widetilde{u_iZ^2} - \widetilde{u}_i\widetilde{Z^2}) - 2\widetilde{Z}\bar{\rho}(\widetilde{u_iZ} - \widetilde{u}_i\widetilde{Z}) \tag{4.42}$$

$$\Rightarrow \bar{\rho}(\widetilde{u_iZ_v} - \widetilde{u}_i\widetilde{Z_v}) = -\frac{\nu_t}{Sc_{S_Z}}\frac{\partial S_Z}{\partial x_i} \tag{4.43}$$

Turbulent scalar dissipation rate $\overline{s_{\chi Z}}$

This term is modeled using a relaxation assumption (Poinsot and Veynante, 2005; Vicquelin, 2010), expressed as:

$$\overline{s_{\chi Z}} = 2\overline{\rho}c_\chi D^t\frac{S_Z}{\Delta^2} \tag{4.44}$$

with the constant model $c_\chi = 1$.

It is fundamental to remind that the β-pdf model, although classically used with tabulated models, is not suitable for describing non-binary-mixing (Floyd et al., 2009), as the mixing in the recirculation zones where burnt gases mix up with fresh inflow reactants. In the DLR burner case, retained for the present work (presented in Chapter 5), an additional constraint exists. The additional secondary air injection also dilutes the burnt gases. In both situations, the mixture fraction range is narrow due to the vigorous swirl, but the β-pdf will always describe mixing over the entire mixing range within the LES cell. (Floyd et al., 2009) has also shown that the suitable cell size to be used with the β-pdf model is not consistent with the cell size needed to resolve the scales of the flow, introducing additional uncertainties on the accuracy of LES results. Additionally, (Mueller and Pitsch, 2012) has shown that soot volume fraction is sensitive to the subfilter scalar dissipation rate model in a turbulent jet flame.

The choice of the scalar dissipation constant model c_χ from the $\widetilde{Z_v}$ equation can strongly impact soot prediction. A sensitivity analysis in the DLR burner might be meaningful but not affordable in the context of this thesis.

Filtered laminar viscous terms:

$$\frac{\partial}{\partial x_i}\overline{(\rho D_\Theta \frac{\partial \Theta}{\partial x_i})} \approx \frac{\partial}{\partial x_i}(\overline{\rho D_\Theta}\frac{\partial \widetilde{\Theta}}{\partial x_i}) \tag{4.45}$$

with Θ = Z, Z_v, Y_C, h.

Radiative source term $\overline{q_R}$

It accounts for the radiation contribution from the gas (CO_2, H_2O and CO) and soot particles, under the assumption of optically-thin radiation. For the gaseous phase, Planck mean absorption coefficients $a_{Pl,i}$ (i = CO_2, H_2O and CO) are used based on polynomial fits (Rodrigues, 2018). For the soot particles, the Rayleigh scattering assumption is considered and a Planck mean absorption coefficient κ_{soot}^{Planck} is used. The radiative source term is then expressed as:

$$\overline{\dot{q}_R} = -4\sigma \left(\sum_i (a_{Pl,i} p_i) + \kappa_{soot}^{Planck} \right) \widetilde{T}^4 \tag{4.46}$$

where σ is the Stefan-Boltzmann constant, p_i is the partial pressure of species i and $\kappa_{soot}^{Planck}(T) = 3.83 C_0 f_v T / C_2$. The first constant Planck C_0 is based on a refractive index, that considered here as a contanst $m = 1.57 - 0.56i$ (Smyth and Shaddix, 1996).

Source term of reaction progress variable $\widetilde{\dot{\omega}_{Yc}}$: is directly obtained from the table.

4.4 PAH model for tabulated chemistry

Soot precursors are characterized by long chemical time scales compared to turbulence, resulting in a more delayed response to turbulence fluctuations compared to other major species (Bisetti et al., 2012; Attili et al., 2014). Therefore, the PAH mass fraction can not be accurately described by the tabulated values based on the fast chemistry assumption. In order to model the unsteady response of the soot precursors to the turbulent flow, a supplementary equation for a lumped PAH is transported (Mueller and Pitsch, 2012; Rodrigues, 2018).

The filtered equation for the lumped PAH mass fraction $\widetilde{Y}_{PAH}$ is written as:

$$\frac{\partial \bar{\rho}\widetilde{Y}_{PAH}}{\partial t} + \frac{\partial}{\partial x_i}(\bar{\rho}\widetilde{u_i}\widetilde{Y}_{PAH}) = \overline{\frac{\partial}{\partial x_i}\left(\rho D_{Y_{PAH}} \frac{\partial Y_{PAH}}{\partial x_i}\right)} - \frac{\partial}{\partial x_i} J^{sgs}_{ij,Y_{PAH}} + \bar{\rho}\widetilde{\dot{\omega}}_{PAH} \tag{4.47}$$

The right-hand terms on the Eq. (4.47) need additional modeling:

Unresolved viscous flux $J^{sgs}_{ij,PAH}$:

$$J^{sgs}_{ij,Y_{PAH}} = (\bar{\rho}\widetilde{u_i Y}_{PAH} - \bar{\rho}\widetilde{u}_i\widetilde{Y}_{PAH}) \approx -\bar{\rho}D^t_{PAH}\frac{\partial \widetilde{Y}_{PAH}}{\partial x_i} \tag{4.48}$$

with $D^t_{PAH} = \dfrac{\nu^t}{Sc^t_{PAH}}$ and $Sc^t_{PAH} = 0.6$.

Source term of lumped PAH mass fraction $\widetilde{\dot{\omega}}_{PAH}$:

The model of term source of the lumped PAH can be split into three different terms: the chemical PAH production rate $\dot{\omega}_{PAH,+}$, the chemical PAH consumption rate $\dot{\omega}_{PAH,-}$ and the dimerization rate $\dot{\omega}_{dim}$ representing the transfer of mass between the gas phase and the soot particles. The chemical consumption is linear with Y_{PAH}, while the term of dimerization is quadratic with Y_{PAH} (as shown in Section 1.3.3 by Eq. (1.22)), then the source of the lumped PAH is modeled as:

$$\widetilde{\dot{\omega}}_{PAH} = \widetilde{\dot{\omega}}_{PAH,+} + \underbrace{\left(\frac{\widetilde{\dot{\omega}}_{PAH,-}}{\widetilde{Y}_{PAH}}\right)\widetilde{Y}_{PAH}}_{\dot{\omega}_{PAH,-}} + \underbrace{\left(\frac{\widetilde{\dot{\omega}}_{dim}}{\widetilde{Y}^2_{PAH}}\right)\widetilde{Y^2}_{PAH}}_{\dot{\omega}_{dim}} \tag{4.49}$$

Assuming a scale-similarity between transported and tabulated soot precursors, similarly to the assumption made by Ihme and Pitsch (2008) for the NO_x, the $\widetilde{\dot{\omega}}_{PAH}$ is modeled as (Mueller and Pitsch, 2012; Rodrigues et al., 2018):

$$\widetilde{\dot{\omega}}_{PAH} \approx \overline{\dot{\omega}}_{PAH} = \widetilde{\dot{\omega}}^{tab}_{PAH,+} + \widetilde{\dot{\omega}}^{tab}_{PAH,-}\left(\frac{\widetilde{Y}_{PAH}}{\widetilde{Y}^{tab}_{PAH}}\right) + \widetilde{\dot{\omega}}^{tab}_{dim}\left(\frac{\widetilde{Y}_{PAH}}{\widetilde{Y}^{tab}_{PAH}}\right)^2 \tag{4.50}$$

where $\widetilde{\dot{\omega}}^{tab}_{PAH,+}$, $\widetilde{\dot{\omega}}^{tab}_{PAH,-}$ and $\widetilde{\dot{\omega}}^{tab}_{dim}$ are the source terms of the lumped PAH stocked in the table. $\widetilde{Y}^{tab}_{PAH}$ is the mass fraction of PAH, also from the look-up table. These terms are obtained considering the contribution of 7 PAHs (pyrene A4 - coronen A7) from the KM2 mechanism (Wang et al., 2013):

$$\widetilde{\dot{\omega}}^{tab}_{PAH,+} = \sum_{i=1}^{N_{PAH}} \widetilde{\dot{\omega}}^{tab}_{PAH_i,+} \tag{4.51}$$

$$\widetilde{\dot{\omega}}^{tab}_{PAH,-} = \sum_{i=1}^{N_{PAH}} \widetilde{\dot{\omega}}^{tab}_{PAH_i,-} \tag{4.52}$$

$$\widetilde{\dot{\omega}}^{tab}_{DIM} = \sum_{i=1}^{N_{PAH}} \widetilde{\dot{\omega}}^{dim,tab}_{PAH_i} \tag{4.53}$$

$$\widetilde{Y}^{tab}_{PAH} = \sum_{i=1}^{N_{PAH}} \widetilde{Y}^{tab}_{PAH_i} \tag{4.54}$$

The diffusion term $\overline{\frac{\partial}{\partial x_i}\left(\rho D_{PAH}\frac{\partial Y_{PAH}}{\partial x_i}\right)} \approx \frac{\partial}{\partial x_i}\left(\overline{\rho D_{PAH}}\frac{\partial \widetilde{Y}_{PAH}}{\partial x_i}\right)$

For high turbulent flows, the turbulent diffusivity is higher than the molecular diffusivity. Then, the unity Lewis number is generally considered in turbulent computations. Therefore, the flamelets are computed using a diffusion model assuming a unity Lewis number. Nevertheless, differential diffusion is not always negligible, notably in weakly turbulent zones (Pitsch, 2000). (Attili et al., 2016) have found that PAH is sensible to the diffusion model. Therefore, considering non-unity Lewis numbers for PAHs is necessary to describe the turbulence effect on soot formation adequately. Rodrigues et al. (2018) has proposed to partially account for differential diffusion effects on PAH production by using the real molecular diffusivities of the lumped PAH, D_{PAH}. The inconsistency with the flamelet table is tempered by a relaxation model, which allows the transported lumped PAH to deviate from the flamelet manifold. The lumped PAH diffusivity is then modeled as:

$$\overline{D}_{PAH} = \frac{(\overline{D}_{PAH_i}\nabla\widetilde{Y}^{tab}_{PAH})}{\nabla\widetilde{Y}_{PAH}} \tag{4.55}$$

4.5 Filtered soot conservation equations for LES

The corresponding filtered transport equation for the three-equation soot model (Franzelli et al., 2018) is:

$$\frac{\partial\widetilde{\Psi}}{\partial t} + \nabla\cdot(\widetilde{\mathbf{u}}\widetilde{\Psi}) - \underbrace{\nabla\cdot\overline{\left(C_{th}\nu\frac{\nabla T}{T}\Psi\right)}}_{I} = \underbrace{+(\nabla\cdot(\widetilde{\mathbf{u}}\widetilde{\Psi}) - \nabla\cdot(\widetilde{\mathbf{u}\Psi}))}_{II} + \underbrace{\widetilde{\dot{\Phi}}_{\Psi}}_{III} \tag{4.56}$$

with $\Psi = Y_s, N_s, S_s$. The terms I, II and III correspond to the filtered laminar thermophoresis flux, unresolved soot scalar flux and the source terms, respectively. Note that the diffusion is neglected since soot molecular diffusivity is negligible in turbulent conditions (Bisetti et al., 2012).

The unclosed terms are modeled as follows.

I - Filtered laminar thermophoresis flux:

$$-\nabla \cdot \overline{\left(C_{th} \nu \frac{\nabla T}{T} \Psi \right)} \approx -\nabla \cdot \left(C_{th} \bar{\nu} \frac{\nabla \widetilde{T}}{\widetilde{T}} \widetilde{\Psi} \right) \tag{4.57}$$

with $C_{th} = 0.554$.

II - Unresolved soot scalar flux: this term represents the unresolved transport of soot particles. It is modeled using a classical gradient assumption:

$$\nabla \cdot (\widetilde{\mathbf{u}} \widetilde{\Psi}) - \nabla \cdot (\widetilde{\mathbf{u}\Psi}) \approx D_s^t \nabla \widetilde{\Psi} \tag{4.58}$$

where $D_s^t = \nu^t / Sc_s^t$ is the soot turbulent diffusivity, v^t is the turbulent viscosity obtained from SIGMA model and the turbulent Schmidt number is $Sc_s^t = 0.6$.

III - Filtered source terms: it accounts for nucleation $\dot{\omega}_{nucl}$, condensation $\dot{\omega}_{cond}$, coagulation $\dot{\omega}_{coag}$ and surface reactions (surface growth $\dot{\omega}_{sg}$ and oxidation $\dot{\omega}_{ox}$). The closure model for this term is presented in the following.

4.6 Soot subgrid model

The probability density function (PDF) approach is generally used to account for turbulence fluctuations effect on chemistry and soot process. Lindstedt and Louloudi (2005) combined a reduced mechanism describing gas phase, the method of moments for the soot dynamics, and a transported high-dimensional joint-PDF including soot scalar, mixture fraction and enthalpy to account for interactions between turbulence, soot particles and chemistry in a turbulent ethylene-air jet flame. It was found that experimental soot volume fraction profiles along the flame are better reproduced when soot-turbulence interaction is considered, notably when the number of statistical moments is increased. Good results were also obtained, considering a simple two-equation soot model (Lindstedt, 1994). Aksit and Moss (2006) coupled an Eulerian reactive flow field with a Lagrangian Monte Carlo joint transported PDF for mixture fraction and soot scalars. To reduce the computational cost, the gas phase was described using a laminar flamelet approach (Young and Moss, 1995), while soot was modeled

using a semi-empirical two-equation model (Brookes and Moss, 1999), yet the computational cost remains high compared to the presumed pdf approach. The model underpredicted the soot volume fraction in a non-premixed methane-air flame. The simple soot dynamics description might explain such disagreement. However, coupling a more detailed soot model with a Monte Carlo method is not practicable in turbulent flames. El-Asrag et al. (2007) proposed extending the subgrid mixing and combustion linear eddy model (LEM) to include soot subgrid scale effects. For that, the LEM is coupled with the method of moments MOMIC (Michael, 2002). Although an acetylene-based nucleation model and a reduced kinetic model (Lu and Law, 2005b) were used, this model has a high computational cost, notably if coupled with detailed chemistry required to PAHs description. Mueller and Pitsch (2011) have developed a presumed PDF approach. The model was evaluated using the DNS database of a two-dimensional non-premixed flame. By assuming statistical independence between gas and soot solid phases, the marginal PDF of the soot moments are modeled by a double delta distribution weighted by the subfilter intermittency. This model is the most widely used in the literature in jet and confined non-premixed flames (Mueller and Pitsch, 2012, 2013; Rodrigues et al., 2018; Franzelli et al., 2018). Similarly to Aksit and Moss (2006), Donde et al. (2013) have proposed to solve a joint-PDF of soot moments and gas-phase scalars using a Lagrangian Monte Carlo technique coupled to an Eulerian flow field. Donde et al. (2013) have used the method of moment HMOM (Mueller et al., 2009) to describe soot dynamics and the RFPV model (Ihme and Pitsch, 2008; Mueller and Pitsch, 2012) to describe the gas phase. The proposed strategy was evaluated in a piloted natural gas flame. It was found that soot moments present a large subfilter variance and a strong correlation with mixture fraction. However, the experimental soot volume fraction profiles are only qualitatively reproduced. This overprediction of soot volume fraction was attributed to errors in the flamelet assumption, PAH reaction model, and subfilter dissipation. More recently, Eberle et al. (2018) has opted to extend the QLC (Quasi Laminar Chemistry) approach to soot subfilter dynamics. However, this model requires a relatively high grid resolution, potentially increasing the computational cost. Very recently, two works have extended the intermittency soot model due to Mueller and Pitsch (2011). First, Yang et al. (2019) have considered the dependence of the soot scalar on in the mixture fraction space. The PDF is then conditioned by a mixture fraction characterizing soot presence. Applied to a turbulent non-premixed sooting jet flame, the model provides better soot volume fraction prediction. Second, Berger et al. (2020) have proposed a log-normal distribution to accounts for the sub-structure of the soot distribution at the subgrid. Compared to the intermittency model of Mueller and Pitsch (2011), two additional transport equations are required. Tested for different Damköhler number using the same large-scale DNS data of temporally evolving non premixed n-heptane jet flames from (Attili et al., 2014, 2015), the model provides improved coagulation source term.

In the present work, the soot equations are closed using a PDF presumed model. The retained PDF is based on the subgrid soot model due to Mueller and Pitsch (2011). This model is easy to implement and does not affect much the computational cost.

4.6.1 Closing soot equations

The filtered soot source term can be described using a joint subfilter PDF split into a thermochemical component and a soot component conditioned on the thermochemical variables (Mueller and Pitsch, 2012):

$$\widetilde{\dot{\Phi}}_{\Psi} = \int\int \dot{\Phi}_{\Psi}(\xi_j, \Psi_i)\widetilde{P}(\xi_j)P(\Psi_i \mid \xi_i)d\xi_j d\Psi_i \tag{4.59}$$

where ξ_i is the vector of gaseous variables ($\widetilde{Z}$, S_Z, $\overline{C}$, $\overline{H}$) and Ψ_i is the vector of soot scalars, ($\tilde{Y}_s$, $\tilde{N}_s$, $\tilde{S}_s$) according to the three equation soot model.

The time scales of the soot mechanisms are generally slower than the combustion time scales. Therefore, by assuming a disparity between the time scales of gaseous chemistry and soot, the joint PDF can be separated into a PDF for the gas phase and a marginal PDF for the solid phase (Mueller and Pitsch, 2011). This simplification enables the treatment of the soot source term as a contribution of two independent parts, with a first-term depending only on the gaseous phase and a second depending on the solid phase (Mueller and Pitsch, 2012; Rodrigues et al., 2018):

$$\widetilde{\dot{\Phi}}^{p}_{\Psi} = \underbrace{\int \dot{\Phi}_{gas}(\xi_j)\widetilde{P}(\xi_j)d\xi_j}_{I} \times \underbrace{\int \dot{\Phi}^{p}_{soot}(\Psi_i)P(\Psi_i)d\Psi_i}_{II} \tag{4.60}$$

with p is the superscript representing the considered soot phenomena (*nucl*, *cond*, *coag*, *sg*, *ox*). The term I correspond to the subgrid scale distribution for the gas phase quantities obtained with the RFPV approach (Section 4.3). The term II corresponds to the filtered solid phase quantities modeled using a double-delta distribution function in analogy with Mueller and Pitsch (2011) model as described in the following.

4.6.2 Intermittency subgrid model

The intermittency subgrid model due to Mueller and Pitsch (2011) was developed in the context of the hybrid method of moment (HMOM) (Mueller et al., 2009) and has been lately derived for the soot sectional model (Rodrigues et al.,

2018) and to the three equations model (Franzelli et al., 2018). Based on DNS observations, a two delta distribution function has been proposed to capture the intrinsic spatial intermittent feature of soot production in turbulent reacting flows. The soot subfilter PDF is expressed as:

$$P(\Psi_i) = \omega\delta(\Psi_i) + (1-\omega)\delta(\Psi_i - \Psi_i^*) \tag{4.61}$$

where ω is the subfilter intermittency of soot scalars representing the probability of not finding soot within an LES filter width. Two modes can be distinguished, a "non-sooting" mode and a "sooting" mode with a constant value Ψ_i^*.

Then the filtered soot scalars Ψ_i can be evaluated as :

$$\widetilde{\Psi}_i = \int \Psi_i P(\Psi_i) d\Psi_i = (1-\omega)\Psi_i^* \tag{4.62}$$

Rewriting Eq. (4.62), the "sooting" mode value of the soot scalars in the LES cell is obtained:

$$\Psi_i^* = \frac{\widetilde{\Psi}_i}{(1-\omega)} \tag{4.63}$$

Similarly, the filtered soot source terms $\widetilde{\dot{\Phi}^p}_\Psi(\Psi_i)$ can be obtained and writes as:

$$\widetilde{\dot{\Phi}^p}_\Psi(\Psi_i) = \dot{\Phi}^p_\Psi\left(\frac{\widetilde{\Psi}_i}{1-\omega}\right)(1-\omega) \tag{4.64}$$

Accordingly to Mueller and Pitsch (2011), the subfilter intermittency ω can be evaluated using the filtered number density of particles $\overline{N}_s$ and the filtered square of the number density $\overline{N_s^2}$:

$$\omega = 1 - \frac{\overline{N}_s^2}{\overline{N_s^2}} \tag{4.65}$$

- If $\omega < 1$ - ϵ_{num} the subgrid model is active and $\Psi_i^* = \Psi$ /(1- ω).

- If $\omega >$1 - ϵ_{num}, corresponding to $\overline{N}_s^2/\overline{N_s^2} \approx 0$, very few soot are presented and the subgrid model is no applied.

with the numerical threshold $\epsilon_{num} = 10^{-3}$.

Thereby, in addition to the transported equation for number density of particles N_s, a transported equation for N_s^2 is necessary. The filtered equation for $\overline{N_s^2}$ is:

$$\begin{aligned}\frac{\partial \overline{N_s^2}}{\partial t} + \nabla \cdot (\widetilde{\mathbf{u}}\overline{N_s^2}) = \underbrace{2\overline{\rho}\widetilde{m_N \dot{N}_s}}_{I} - \underbrace{\overline{N_s^2 \nabla \cdot \mathbf{u}}}_{II} - \underbrace{\overline{N_s^2 \nabla \cdot \mathbf{v_{th}}}}_{III} \\ + \underbrace{\nabla \cdot (-\overline{\mathbf{v_T} N_s^2})}_{IV} + \underbrace{\nabla \cdot \left(\overline{\rho}\widetilde{\mathbf{u}}\frac{\widetilde{N_s^2}}{\rho} - \overline{\rho}\widetilde{\mathbf{u}}\frac{\widetilde{N_s^2}}{\rho} \right)}_{V}\end{aligned} \tag{4.66}$$

with $m_N = N_s/\rho$ and $\dot{N}_s = \dot{\omega}_{N_s}$ the particles number density source terms.

The unclosed terms are modeled similarly to Eq. (4.56) as follows:

I: $\overline{\rho}\widetilde{m_N \dot{N}_s}$ is closed with Eq. (4.59)

II: $\overline{N_s^2 \nabla \cdot \mathbf{v}_{th}} \approx \overline{N_s^2} \nabla \cdot \left(-C_{th}\overline{\nu}\frac{\nabla \widetilde{T}}{\widetilde{T}} \right)$

III: $\overline{N_s^2 \nabla \cdot \mathbf{u}} \approx \overline{N_s^2} \nabla \cdot \widetilde{\mathbf{u}}$

IV: $\overline{\mathbf{v_{th}} N_s^2} \approx -\overline{\rho} C_{th} \overline{\nu} \frac{\nabla \widetilde{T}}{\widetilde{T}} \frac{\overline{N_s^2}}{\overline{\rho}}$

V: $\left(\overline{\rho}\widetilde{\mathbf{u}}\frac{\widetilde{N_s^2}}{\rho} - \overline{\rho}\widetilde{\mathbf{u}\frac{N_s^2}{\rho}} \right) \approx \overline{\rho} D^t_{s,Ns^2} \nabla \left(\frac{\overline{N_s^2}}{\overline{\rho}} \right)$

with $D^t_{s,Ns^2} = v^t / Sc^t_{Ns^2}$ ($Sc^t_{Ns^2} = 0.6$).

It should be noted that applying Eq. (4.64) to each source term ($p = nucl$, $cond$, $coag$, sg, and ox), the subfilter model acts solely on the coagulation source term since it is the only term that has a quadratic dependence on the transported quantity used to evaluate the subgrid intermittency subfilter ω,

N_s. The resultant filtered coagulation source term is expressed as:

$$\widetilde{\dot{\Phi}}_{N_s}^{coag}(\Psi_i) = \frac{\dot{\Phi}_{N_s}^{coag}(\widetilde{\Psi}_i)}{(1-\omega)} \tag{4.67}$$

Whereas all other filtered terms simplify to :

$$\widetilde{\dot{\Phi}}_{\Psi_i}^{p}(\Psi_i) = \dot{\Phi}_{\Psi_i}^{p}(\widetilde{\Psi}_i) \tag{4.68}$$

Table 4.1: *Working equation set for LES.*

Gaseous equations
$\frac{\partial \overline{\rho}}{\partial t} + \nabla \cdot \overline{\rho}\widetilde{\mathbf{u}} = 0$
$\frac{\partial \overline{\rho}\widetilde{\mathbf{u}}}{\partial t} + \nabla \cdot \overline{\rho}\widetilde{\mathbf{u}}\widetilde{\mathbf{u}} = -\nabla \overline{P} + \nabla \cdot \overline{\tau} + \nabla \cdot \overline{\tau}_{\mathbf{u}}$
$\frac{\partial \overline{\rho}\widetilde{Z}}{\partial t} + \nabla \cdot \overline{\rho}\widetilde{\mathbf{u}}\widetilde{Z} = \nabla \cdot (\overline{\rho}(D + D^t)\nabla \widetilde{Z}$
$\frac{\partial \overline{\rho}\widetilde{Z_v}}{\partial t} + \nabla \cdot \overline{\rho}\widetilde{\mathbf{u}}\widetilde{Z_v} = \nabla \cdot (\overline{\rho}(D + D^t)\nabla \widetilde{Z}_v) + 2\overline{\rho}D^t \mid \nabla \widetilde{Z} \mid^2 - \overline{s_{\chi_Z}}$
$\frac{\partial \overline{\rho}\widetilde{Y_C}}{\partial t} + \nabla \cdot \overline{\rho}\widetilde{\mathbf{u}}\widetilde{Y_C} = \nabla \cdot (\overline{\rho}(D + D^t)\nabla \widetilde{Y}_C) + \overline{\rho}\widetilde{\dot{\omega}}_{Y_C}$
$\frac{\partial \overline{\rho}\widetilde{h}}{\partial t} + \nabla \cdot \overline{\rho}\widetilde{\mathbf{u}}\widetilde{h} = \nabla \cdot (\overline{\rho}(D + D^t)\nabla \widetilde{h}) + \overline{\dot{q}_R}^{gas+soot}$
$\frac{\overline{\rho}\widetilde{Y}_{PAH}}{\partial t} + \nabla \cdot (\overline{\rho}\widetilde{\mathbf{u}}\widetilde{Y}_{PAH}) = -\nabla \cdot \overline{\rho}((D_{PAH} + D^t)\nabla \widetilde{Y}_{PAH}) + \overline{\rho}\widetilde{\dot{\omega}}_{PAH}$
Soot equations
$\frac{\partial \overline{\rho}\widetilde{Y_s}}{\partial t} + \nabla \cdot (\overline{\rho}(\widetilde{\mathbf{u}} + \widetilde{\mathbf{v}_{th}})\widetilde{Y_s}) = \nabla \cdot (\overline{\rho}D^t \nabla \widetilde{Y}_s) + \overline{\rho}\widetilde{\dot{\omega}}_{Y_s}$
$\frac{\partial \widetilde{N_s}}{\partial t} + \nabla \cdot ((\widetilde{\mathbf{u}} + \widetilde{\mathbf{v}_{th}})\widetilde{N_s}) = \nabla \cdot \left(\overline{\rho}D^t \nabla \widetilde{\left(\frac{\widetilde{N}_s}{\rho}\right)}\right) + \widetilde{\dot{\omega}}_{N_s}$
$\frac{\partial \widetilde{S_s}}{\partial t} + \nabla \cdot ((\widetilde{\mathbf{u}} + \widetilde{\mathbf{v}_{th}})\widetilde{S_s}) = \nabla \cdot \left(\overline{\rho}D^t \nabla \widetilde{\left(\frac{\widetilde{S}_s}{\rho}\right)}\right) + \widetilde{\dot{\omega}}_{S_s}$
$\frac{\partial \overline{N_s^2}}{\partial t} + \nabla \cdot \widetilde{\mathbf{u}}\overline{N_s^2} = 2\overline{\rho}\widetilde{m_N \dot{N}_s} - \overline{N_s^2}\nabla \cdot (\widetilde{\mathbf{v}}_{\mathbf{T}} + \widetilde{\mathbf{u}}) + \nabla \cdot (\widetilde{\mathbf{v}_{\mathbf{T}}}\overline{N_s^2}) + \overline{\rho}D^t \nabla \left(\frac{\overline{N_s^2}}{\overline{\rho}}\right)$

Chapter 5

A aero engine model combustor: the DLR burner

This chapter presents the gas turbine combustor model retained for the numerical simulations of this Part. Experimentally studied at the DLR (Geigle et al., 2013, 2015, 2017) and Geigle et al. (2015)b, this burner was designed to provide an extensive experimental database serving for evaluation of soot models under technically relevant conditions. It has been recently selected as a target flame in the International Sooting Workshop (ISF) database. In addition, the flame under 3 bar with secondary air oxidation was adopted as the reference test case in the SOPRANO project, the funding program of this thesis.

The experimental configuration are presented in Section 5.1, including a brief description of the available experimental measurements. Then in Section 5.2 a literature survey on the reacting flow characteristics and soot production is done from the experimental perspective. A literature survey on the numerical prediction of soot production in the DLR burner is also presented. Finally, the numerical set-up used to performer the simulations is presented in Section 5.3.

Contents

5.1 The DLR burner

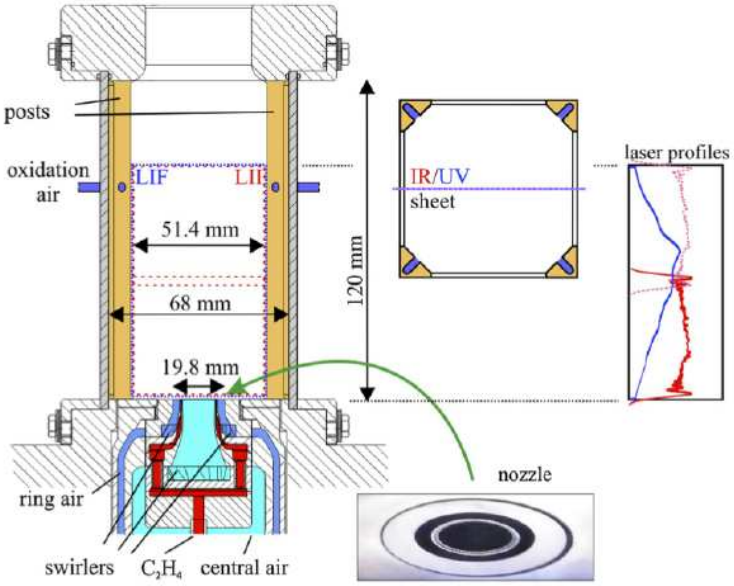

Figure 5.1: *Experimental burner geometry. Image from Geigle et al. (2015).*

The DLR burner (Geigle et al., 2013, 2015, 2017), schematically shown in Fig. 5.1 is a gas turbine model combustor that was developed to provide reliable data for soot model validation. It is a confined swirled burner composed of two systems of injectors operating at P = 1, 3 or 5 bar. The primary injection consists of three concentric flows, where the air is supplied to the combustor by separate plenums and passes through a central (diameter 12.3 mm) and an annular nozzle (inner diameter 14.4 mm and outer diameter 19.8 mm). Both air injectors are radial swirlers with the central nozzle comprising 8 channels (width of 4.2 mm and height of 5.4 mm) and the annular nozzle 12 channels (width of 3.2 mm, height of 4.5 mm). The gaseous fuel (ethylene C_2H_4) is injected in between the two air flows through 60 straight channels (0.5 × 0.4 mm^2), mimicking a liquid spray injection currently found in real combustors. Using a gaseous fuel instead of a liquid spray simplifies the numerical investigation avoiding the complexity of modeling sprays to focus on soot modeling. The combustion chamber measures 120 mm in height and has a square section of 68 x 68 mm^2. The secondary oxidation air injection is composed of four transver-

sal injectors (diameter 5 mm) located at a distance of z = 80 mm from the primary injector's exit (at z = 0 mm coinciding with the combustor chamber inlet). It was initially designed to mimic the dilution effects, classically found in rich-quench-lean (RQL) combustors, widely used in aero-engines. Besides, it enables the study of soot oxidation processes.

The numerical simulation of such systems is a great challenge due to the complex turbulent flow that interacts with the non-linear phenomena of combustion and soot formation. The presence of secondary jets leads to an additional difficulty, as will be discussed in Chapter 6.

5.1.1 Operating conditions

The operating condition at 3 bar with the secondary air injection was adopted as the reference case in the SOPRANO project. The experimental operating conditions are summarized in Table 5.1. Whereas the equivalent ratio ϕ and the thermal power P are calculated from the primary injection considering the air flow rate Q_{air} as the sum of both central $Q_{air,c}$ and ring $Q_{air,r}$ swirl air flows, the global equivalence ratio ϕ_{global} and global thermal power P_{global} are obtained from the total air flow accounting for the secondary air flow Q_{oxi}, $Q_{air} + Q_{oxi}$. The secondary air injection represents 40% (Q_{oxi}/Q_{air}) of the air flow injected in the combustor. In the swirl, the air split ratio between the central nozzle and the total combustion air ($Q_{air,c}/Q_{air} = 0.3$) in the primary combustion zone avoids high soot deposition in the inner surface of the chamber windows, which can presents an additional difficulty to measurements.

Table 5.1: *Flame parameters of the reference studied case (flow rates are referenced at in standard liters per minute (slpm) conditions: 1.013bar and 273K)*

p	ϕ	P	$Q_{air,c}$	$Q_{air,r}$	Q_{fuel}	Q_{oxi}	$\frac{Q_{air,c}}{Q_{air}}$	$\frac{Q_{oxi}}{Q_{air}}$	ϕ_{global}	P_{global}
[*bar*]		[kW]	[slpm]	[slpm]	[slpm]	[slpm]	[slpm]	[slpm]		[kW]
3.0	1.2	32.2	140.8	328.5	39.3	187.4	0.3	0.4	0.86	38.6

5.1.2 Available experimental data

The DLR burner is equipped with a set of optical diagnostics enabling the characterization of the flow and soot production. A large amount of comprehensive validation data is then available. A brief summary of the techniques used to obtain the experimental results, compared to LES simulations in this manuscript, is given here. An exhaustive description of these methods can be found in Geigle et al. (2013, 2015, 2017), Geigle et al. (2015)b and Nau et al. (2017).

Particle image velocimetry (PIV): the three velocity components of the swirl flow were obtained through Stereo PIV technique (Geigle et al., 2017). Two methods were used, the SoC (sum of correlations) and the FoV (field of view) methods. The latter, in addition to the mean flow, provides detailed information about the instantaneous flow, and a better suppression of soot luminosity is possible using a thicker bandpass filter, resulting in more reliable data. The measurements were carried out at different locations in the mid-plane of the combustor chamber, enabling the full characterization of the swirling flow in reacting and non-reacting conditions. However, no information on the plane of the secondary oxidation jets is available.

Coherent Anti-Stokes Raman (CARS): temperature is obtained by CARS technique (Geigle et al., 2015). In order to obtain accurate temperature measurements in the sooting zone, the excitation wavelength was shifted away from 532 nm, to avoid CARS signal interferences with laser-induced C2 emissions. This technique provides the probability density function of temperature at several positions in the chamber.

Phosphor thermometry: internal and external wall temperature along the center of the quartz window was made available through Phosphor thermometry (Nau et al., 2017). This optical technique, based on the phosphorescence phenomenon, correlates the temperature to the phosphorescence signal. The data is used as a boundary condition for all simulations performed in this thesis.

Laser-Induced Incandescence (LII): Soot volume fraction is obtained through LII (Geigle et al., 2013) using a laser at 1064 nm and a fluence of 0.4 mJ/cm^2 $\pm$ 15% and a interference filter at 450$\pm$10nm. The estimated uncertainty is 30%. Time-average soot distribution is obtained from 400 instantaneous images with an acquisition frequency of 2.5 Hz.

PAH spectroscopy (PAH-LIF): PAH intensity was obtained using the PAH LIF technique. Geigle et al. (2015)b used a laser at 283 nm with a pulse of approximately 20-30 mJ. The detection range used was between 300-350 nm, which corresponds to small PAH with two to four-ring aromatic species.

OH* chemiluminescence and planar laser-induced fluorescence of OH (OH- PLIF): OH* chemiluminescence was simultaneously performed with PAH-LIF and LII to capture the flame zone (Geigle et al., 2015)b, and OH-PLIF (Geigle et al., 2015) was performed simultaneously with LII to have access to the instantaneous flame front and its correlations with spatial soot distribution.

5.2 Literature survey

5.2.1 Experimental evidences

As in a classical gas turbine, the flame is aerodynamically stabilized by a swirled injection system in the DLR burner. The dynamics of a confined swirling flow depend on many parameters as the Reynolds number, the swirl number, the confinement, and the equivalence ratio (Syred et al., 1997). The presence of two typical structures generally characterizes the flow: (1) the Inner/Central Recirculation Zone (IRZ), enabling the flame anchoring by the recirculation of burnt hot gas and radical species in the flame zone; (2) the Outer Recirculation Zones (ORZ) induced by the presence of the walls. These typical features (a high-velocity conical jet inflow, a strong IRZ and an ORZ) were identified in the average flow field of the DLR burner, in reacting and non-reacting conditions, using the PIV technique (Geigle et al., 2017).

An unsteady coherent structure usually found in swirled flows, known as precessing vortex core (PVC), has been identified in the inner shear layer between the inflow jets and the inner recirculation zone (Geigle et al., 2017). Geigle et al. (2017) found that the PVC has a local influence on the spatial soot distribution due to enhanced mixing. Stohr et al. (2018), in a joint numerical and experimental study, highlight the time-history dependence of the soot particles on the flow conditions and estimate the PVC frequency of 440 Hz. According to this work, soot production is driven by the intermittent local mixture conditions entering the IRZ which might be affected by the secondary air dynamics. Soot particles are then formed in rich-fuel pockets where residence time is long enough to promote soot formation. Thanks to the simultaneous PIV and OH measurements, this work also revealed the complex flame structure, which presents both premixed and non-premixed local flame fronts, typical of partially-premixed flames due to the mixture inhomogeneity (Domingo et al., 2002; Masri, 2015; Boxx et al., 2010).

Additional oxidation air injection through four counterflow radial jets was included in the burner to mimics dilution effects, typically found in Rich-Burn/Quick-Mix/Lean-Burn (RQL) combustor, also allowing the investigation of soot oxidation (Geigle et al., 2013). The cold flow structure with and without the secondary injection is illustrated in Fig. 5.2 from Geigle et al. (2017). The impinging jets creates a stagnation zone near the secondary injection (z = 80 mm) reducing the IRZ length compared to the case without the additional air injection. Qualitatively similar results are observed under reacting conditions. The side jet flows split into a part that goes towards the flame zone and another that follows the combustor exit. The additional downward air enhances the reverse flow within the IRZ, affecting the tangential flow. In reacting conditions, the incoming secondary air reacts with the remaining unburned rich-fuel gases from the primary combustion resulting in an additional OH formation

that propagates downstream in the IRZ (Geigle et al., 2015). The distribution of OH restrains the soot particle distribution in the burner through oxidation. Simultaneous OH, PAH and soot volume fraction measurements Geigle et al. (2015) and Geigle et al. (2015)b show that soot is confined between the OH zones from the primary and the "secondary" combustion. In contrast, in the case without secondary injection, the soot volume fraction is found downstream in the IRZ.

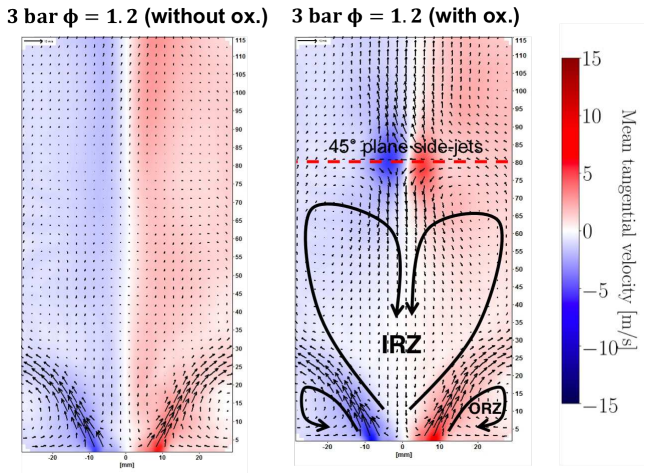

Figure 5.2: *Mean tangential velocity field in non-reacting conditions without (left) and with (right) the secondary oxidation air at z = 80 mm. Image adapted from Geigle et al. (2017).*

The effect of operating conditions on soot production, as the equivalence ratio, the amount of oxidation air, and pressure is reported in Geigle et al. (2013). It was found that increasing pressure leads to an increase in soot volume fraction, while decreasing the equivalence ratio leads to a decrease in the soot volume fraction. Soot production was found to be highly intermittent in this configuration as revealed by instantaneous imaging of soot volume fraction Geigle et al. (2015)b. A significant number of soot filaments are observed without the oxidation air compared to the diluted case. Moreover, these soot filaments are shorter than in atmospheric conditions, like soot pockets exhibiting a sharp gradient. Figure 5.3 shows the ensemble-averaged fields of OH, PAH, and soot volume fraction experimentally obtained with and without the secondary air injection under pressure of 3 bar and for two different cases without the secondary injection (higher pressure at 5 bar and lean injection at 3 bar).

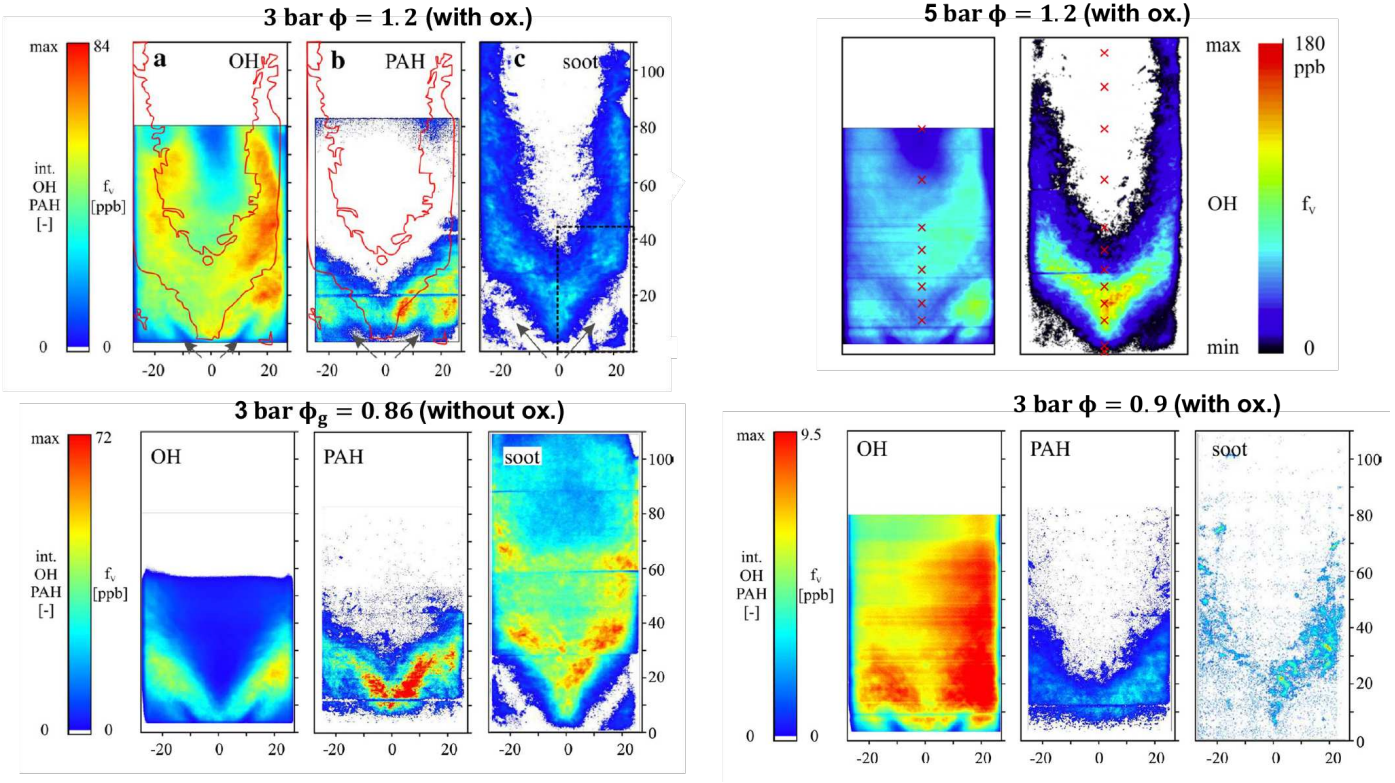

Figure 5.3: *Ensemble-averaged OH, PAH and soot volume fraction at different operating conditions. On the top and bottom left images, measurements at 3 bar in rich primary combustion with $\phi = 1.2$ with (reference case) and without (with $\phi_{global} = 0.86$) secondary air injection, respectively. On the bottom right, OH, PAH and soot volume fractions images from measurements under lean conditions $\phi = 0.9$ with secondary air injection. On the top right OH and soot volume fraction for measurements at 5 bar without secondary oxidation . Images from Geigle et al. (2015)b.*

5.2.2 Numerical observations

The DLR burner has been extensively used by different research teams to evaluate soot models using RANS and LES. This section presents a review of the LES performed using the DLR burner, notably for the reference case (3 bar with oxidation air) used in the SOPRANO project.

Franzelli et al. (2015) performed a sensitivity analysis of soot production on the chemistry model. This work is the first LES of soot production in a laboratory-scale gas turbine reported in the literature. A hybrid chemical approach combining a reduced mechanism for combustion and a tabulated approach for soot precursors is compared to a full tabulation method. The hybrid method has the advantage of not imposing a local flame structure and can potentially reproduce different combustion modes and transient phenomena such as dilution and auto-ignition. In contrast, the fully tabulated approach uses premixed flamelets. Soot was described using a semi-empirical model with C_2H_2 as the only soot precursor (Leung et al., 1991). The hybrid model predicts ten more soot volume fraction than the fully tabulated model. The discrepancies in the concentration of C_2H_2 and OH between models explained the different predictions. Comparing to the experimental soot volume fraction field both models underpredicted the soot volume fraction. In addition, the experimental soot spatial distribution is poorly reproduced. Soot is mainly located close to the shear-layer and is rarely predicted in the bottom of the inner recirculation zone. Nevertheless, the obtained results are remarkable, considering the simplicity of the models and the state-of-the-art numerical soot prediction in gas turbines at the study time.

Dupoirieux and Bertier (2016) have simulated the reference DLR case using a tabulated combustion model based on premixed flamelets and the two-equation soot model (Leung et al., 1991), based on the formalism of Lecocq et al. (2013). The flame is found located upstream compared to the experimental flame position. However, the soot model seems not sensitive to this discrepancy, which is attributed to the nucleation C_2H_2-based model (as well as surface growth). C_2H_2 is found upstream in the flame and is known to be less sensitive to turbulence fluctuations than large molecules as PAHs. In contrast to the results from Franzelli et al. (2015), obtained with a similar modeling framework, the maximum soot volume fraction and spatial distribution agree quite well with experimental measurements. It is partially attributed to the modifications of the reaction rates involved in the soot sub-models (Lecocq et al., 2013).

Wick et al. (2017) also studied soot production on the reference DLR burner using the RFPV model coupled with the HMOM soot approach. An additional transport equation is solved for a lumped PAH and C_2H_2 to consider the two-way coupling between gas and soot phases via nucleation and surface growth. However, the soot volume fraction prediction based 20 ms of time-averaging

over-predicts the soot measurements by a factor 1000. Such discrepancies could be a result of a lack in the physical-chemical description by the used model. On the other hand, considering the strong soot intermittency and the long residence time typical of flows with recirculation zones, statistics based on 20 ms seem to be not representative of the soot production in such a complex configuration.

Chong et al. (2018) also performed an LES using the RFPV model for the gas phase and the HMOM for soot description. It was found that the key process for soot mass addition is surface growth. For the first time, grid sensitivity and temporal convergence analysis were performed in this burner. According to this study, the soot volume fraction decreases with grid resolution because the dissipation rate is better captured in fine grids, reducing the PAH concentration and consequently soot production. The temporal convergence revealed that the gas phase appeared to be converged within 100 ms while the soot volume fraction needs about 135 ms to be statistically converged. In opposition to Koo et al. (2016), who considered a soot subgrid model in a similar configuration, Chong et al. (2018) claims that soot intermittency is driven only by the large scale turbulence motions coupled with the slow soot time scale neglecting the subgrid scales effects, even though the thin soot structures can be affected by LES filtering.

In more recent work, Chong et al. (2019) studied the impact of the soot sub-models, the soot dynamics model (HMOM, Conditional Quadrature Method of Moments - CQMOM, and a semi-empirical model), and the chemistry kinetics on soot prediction in the DLR burner without the side-jets. This study demonstrates that soot prediction is very sensitive to the chosen models. The nucleation model based on C_2H_2 is found to predict high soot concentration, mainly in the bottom part of IRZ. In contrast, PAH-based models predict soot in the shear layer, which is in better agreement with experimental observations Geigle et al. (2015)b. The choice of the statistical approach was also found to significantly impact soot prediction, notably in the number density of particles and the coagulation rate. HMOM was found to produce a lower number density of particles than CQMOM, but bigger particles were observed due to a high coagulation rate. Finally, the final soot mass fraction seems not to be sensible to the choice of the chemistry model since the surface growth appears to dominate nucleation and condensation.

Eberle et al. (2018) compared LES results with URANS (Unsteady-RANS) results from Eberle et al. (2015). In this study, a finite rate chemistry approach is used for the fuel oxidation and a sectional model for the soot precursors describing PAH growth up to the nascent soot particles. Soot evolution is then described through a two-equation model considering surface reactions, condensation, and coagulation according to the modeling strategy due to Domenico et al. (2010). In opposition to tabulated approaches, this strategy accounts for the differential diffusion of the PAHs and soot feedback on the gas phase. Heat

losses are also easily considered. Whereas adiabatic conditions have been used up to now, isothermal boundary conditions are assumed by imposing measured temperature (from thermocouples) for the first time in the DLR burner. Both URANS and LES quite well retrieve the flame position, temperature, and velocity fields. However, LES predicted a higher soot volume fraction showing the LES capability to capture the intermittent soot behavior. In the same research team (DLR - the German Aerospace Center), Grader et al. (2018) used a more detailed soot model based on a sectional approach for both soot and PAH coupled, allowing an easy retro-coupling between soot particle and gas phase. The subgrid soot model due to Mueller and Pitsch (2011) was also considered. Unlike the semi-empirical model and the HMOM currently used in the previous studies, the soot size distribution is easily accessible. Grader et al. (2018) evaluated the soot model predictability under different conditions (3 and 5 bar), with and without side-jets. A good agreement was obtained concerning the soot load, but there is still a lack of predicting soot along the combustor walls as for all previous works.

Felden et al. (2018) compared an alternative chemistry model based on an analytically reduced chemistry (ARC) approach with an FPI tabulated approach. The soot semi-empirical model (Leung et al., 1991) was used to describes soot. Both models were able to reproduce the experimental temperature and velocity fields correctly. However, the soot volume fraction is better predicted using the ARC chemistry model, and the spatial soot distribution agrees quite well with the experimental one. In the same research team (CERFACS), the DLR burner was used to evaluate a new semi-deterministic Lagrangian particle tracking methodology (Gallen et al., 2018) combined with the semi-empirical two equations model (Leung et al., 1991). The new approach is promising, and efforts have been made to include more detailed soot chemistry and physical phenomena as PAH-based nucleation and soot morphology description (Gallen, 2020).

Rodrigues (2018) has computed the reference case using the RFPV table coupled with a sectional soot model. The effects of thermal boundary conditions and radiation model on soot production and flame stabilization were evaluated for the first time. A strong impact of the heat losses on the flame position and, consequently, on soot production was observed. Adiabatic case predicts two times more soot than cases considering heat losses. The adiabatic case predicts the spatial soot location quite well but underpredicts the experimental soot peak by a factor of 1.8. According to Rodrigues (2018), in adiabatic conditions, PAH is formed upstream in the IRZ, where residence time is high, which is favorable to soot formation. However, considering heat losses, PAH concentration is lower. Another interesting information from this work is that the particle size distribution (PSD) has a one-peak shape in the entire combustor, in opposition to the PSD obtained in turbulent jet flames, also studied by Rodrigues (2018); Rodrigues et al. (2018). This found suggests that the soot

population is characterized by small particles, consistent with the low soot load in this burner (≈ ppb). However, no experimental evidences are available to confirm this observation.

Although the sectional model provides detailed information about the soot population, it demands high computational resources. Franzelli et al. (2018), also from the EM2C research team, have proposed an alternative model to the sectional approach (Rodrigues et al., 2018). Similar to the methods of moments, this model accounts for soot fractality via the transport of the total soot surface, the total mass and the particle number density under a monodisperse assumption. This assumption seems acceptable considering the low soot load in this configuration and the one peak PSD found by (Rodrigues et al., 2018). Comparable soot volume fraction prediction to the sectional model (Rodrigues, 2018) was obtained for a CPU cost three times lower than the sectional model with 25 sections.

Very recently Paccati et al. (2020) compared a mutli-physics LES simulation coupling fluid, solid and radiative heat transfer (conjugated heat transfert CHT simulation) and a LES under adiabatic conditions. The gas phase was modeled by a FMG and soot was modeled using a semi-empirical model Brookes and Moss (1999). The temperature discrepancies between the CHT simulation and experiments was attributed to the underestimation of the lean gas recirculation from the secondary injection. Despite spatial soot distribution is correctly reproduced, the discrepancies in gas-phase flow (temperature and velocity) and the adoption of a simplified soot model resulted in an underprediction of the soot volume fraction by one order of magnitude for both adiabatic and CHT simulation.

Figure 5.5 compares the time-averaged soot volume fraction fields from the literature for the DLR reference case discussed in this section. The spatial distribution is quite similar between simulations, with soot being predicted mainly in the cone-shaped region in the primary combustion zone. Compared to experimental measurement, a wider angle is generally observed and no soot volume fraction is predicted along the lateral walls suggesting a lack of physical description of soot production in this region. The soot volume fraction peak strongly varies between studies. Such differences can be explained by the different chemistry and soot models, the used thermal boundary conditions and the description of the reacting flow (Chong et al., 2019; Rodrigues, 2018; Paccati et al., 2020). Besides soot modeling, the simulation parameters, gaseous models and the numerical grids may affect the swirl flow structure. Consequently, soot production is affected. Additionally, since soot is highly intermittent in this configuration, statistical convergence should be considered in the analysis of soot volume fraction production. Table 5.2 summarizes the differences between these studies in terms of gas and soot phase modeling, simulation parameters (numerical grid and turbulent subgrid model) and LES statistics.

In this thesis, the effect of soot models on soot prediction in the DLR burner is discussed. First, the effect of the surface kinetics model HACA-RC* (introduced in Chapter 1) is discussed in Chapters 7. Then the effect of the soot subgrid model is evaluated in Chapter 8. Statistical convergence as well as a gas and solid phases sensitivity to the grid resolution are discussed in Chapter 6 in order to evaluate the reliability of the LES formalism in predicting soot particles in DLR

combustor. For that purpose, the numerical simulation set-up is presented in the following.

5.3 Numerical set-up

This section presents the reference numerical set-up used to perform LES of the DLR burner discussed in the next chapters.

5.3.1 Geometry

Figure 5.4: *Global view of the numerical geometry and inlets.*

The numerical geometry is presented in Fig. 5.4. The axial direction, the main flow direction, is referred to as the z-axis while the x-axis and the y-axis denote the transverse directions. The computational geometry, obtained through a collaboration with CERFACS, presents some simplifications compared to the experimental configuration. A continuous annular nozzle models the 60 channels found in the experimental fuel injection to facilitate meshing in this zone.

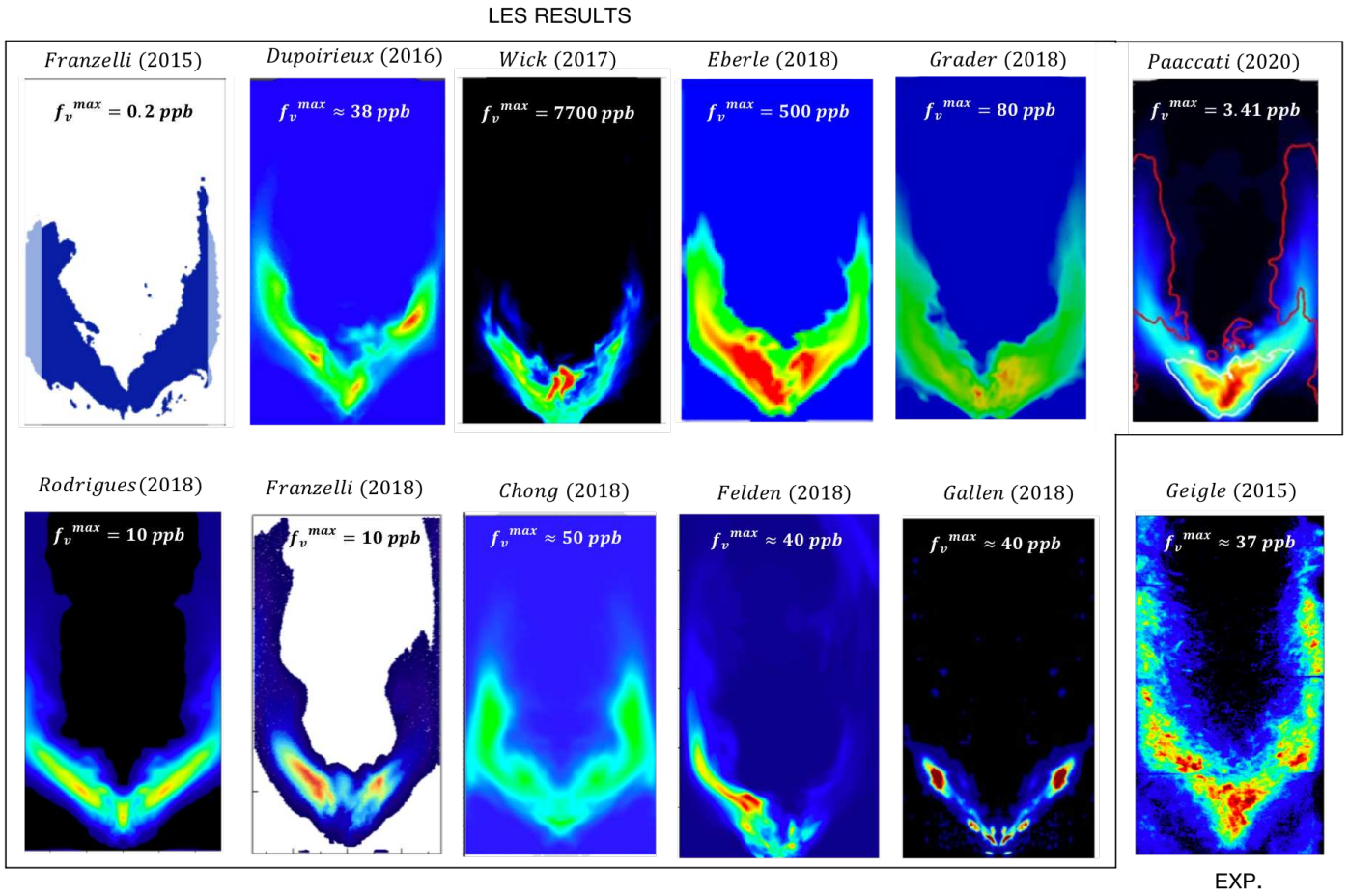

Figure 5.5: *LES predictions of soot volume fraction f_v from the literature for the reference operating condition. Experimental prediction from Geigle et al. (2013) is shown in the right bottom. The soot volume fraction peak value is shown for each field. The f_v field from Franzelli et al. (2015) corresponds to the soot presence index. The f_v field from Paccati et al. (2020) correspond to the f_v prediction obtained with the CHT simulation.*

Table 5.2: *Numerical state-of-the-art soot production in the DLR burner under reference conditions (3 bar + secondary oxidation).*

Authors	Code	Combustion model	Soot model	Turbulence	Grid	Statistics
Franzelli et al. (2015)	AVBP	Full and hybrid FPI chem. [1] + ATF	Two-eqns [6]	WALE [11]	17.5 Mcells	30 ms
Dupoirieux and Bertier (2016)	CEDRE	FPI + ATF[*]	Two-eqns [6]	Smagorinsky	12.8 Mcells	-
Wick et al. (2017)	VIDA	RFPV chem. [2]	HMOM [10]	Vreman [7]	21 Mcells	20 ms
Eberle et al. (2018)	THETA	FRC chem. [3] + PAH sectional	Two-eqns [5]	WALE [11]	36.5 Mcells	60 ms
Grader et al. (2018)	THETA	FRC chem. [3] + PAH sectional	Sectional	WALE [11]	36.5 Mcells	60 ms
Rodrigues (2018)	AVBP	RFPV chem. [4]	Sectional	SIGMA [13]	40 M cells	40 ms
Franzelli et al. (2018)	AVBP	RFPV chem. [4]	Three-eqns	WALE [11]	40 Mcells	40 ms
Felden et al. (2018)	AVBP	DTFLES[**] (ARC [****] vs FPI)	Two-eqns [6]	WALE [11]	40 Mcells	30 ms
Gallen et al. (2018)	AVBP	DTFLES[**] + ARC	Two-eqns [6] + Lagrangian	WALE [11]	40 Mcells	-

Chong et al. (2018)	OpenFOAM	RFPV chem. [2]	HMOM [10]	Dynamic [8]	6-12-77 Mcells	200 ms
Chong et al. (2019)	OpenFOAM	RFPV chem. [3]vs[6]	HMOM [10] CQMOM Two-eqns [6]	Dynamic [8]	12 Mcells	-
Paccati et al. (2020)	ANSYS Fluent	FGM[***] (chem. [12])	Two-eqns [9]	Dynamic Smagorinsky [11]	18-32 Mcells	38-57 ms [!]

[0][1] Wang and Laskin (1998), [2] Narayanaswamy et al. (2015), [3] Slavinskaya et al. (2012), [4] Wang et al. (2013), [6] Domenico et al. (2010), [6]Leung et al. (1991), [7] Vreman (2004), [8] Moin et al. (1991), [9] Brookes and Moss (1999), [10] Mueller et al. (2009), [11] Nicoud and Ducros (1999), [12] Wang and Laskin (1988), [13] Nicoud et al. (2011). [*] Artificially Thickened Flame, [**] Dynamically Thickened Flame for LES, [***] Flamelet Generated Manifold, [****] Analytically Reduced Chemistry. [!] including flushing.

The plenums upstream of the swirler system are also not considered to avoid numerical acoustics instabilities. Velocity is imposed at the inlet of the injectors. The secondary ducts are also reduced to an imposed velocity at the inlets. The inlets (primary and secondary) are illustrated in the right of Fig. 5.4. Finally, part of the atmosphere is included to impose a pressure boundary condition far from the burner outlet.

5.3.2 Boundary conditions

Table 5.3: *NSCBC conditions applied on the boundary for the DLR burner.)*

Boundary conditions	**Physical parameters**	**Relax coefficient**
Fuel inlet	$\dot{m}_{fuel} = 8.191510^{-4} kg/s$ $T_{fuel} = 293K$ Z = 1 $Y_c = 0$ H = 1863431.52 J/kg $Y_s, N_s, S_s, Y_{PAH} = 0$	5000000 s^{-1}
Central air inlet	$\dot{m}_{ox,c} = 3.019310^{-3} kg/s$ $T_{ox,c} = 293K$ Z = 0 $Y_c = 0$ H = -5162.75 J/kg $Y_s, N_s, S_s, Y_{PAH} = 0$	1000000 s^{-1}
Annular oxidizer inlet	$\dot{m}_{ox,ext} = 7.049610^{-3} kg/s$ $T_{ox,ex} = 293K$ Z = 0 $Y_c = 0$ H = -5162.75 J/kg $Y_s, N_s, S_s, Y_{PAH} = 0$	5000000 s^{-1}
Secondary air inlet	$\dot{m}_{ox,sec} = 4.016910^{-3} kg/s$ $T_{ox,sec} = 293K$ Z = 0 $Y_c = 0$ H = -5162.75 J/kg $Y_s, N_s, S_s, Y_{PAH} = 0$	1000000 s^{-1}
Atmosphere inlet	$v_{atm} = 0.3m^3/s$	100000 s^{-1}
Outlet	P = 303975 Pa	20000 s^{-1}
Lateral wall	T from experimental profile Wall law isotherm	- -
Bottom wall	T = $650K$ Wall law isotherm	- -
Wall air swirl injectors	Wall no slip adiabatic	-
Wall fuel and secondary injection	Wall slip adiabatic	-

Navier-Stokes Characteristic Boundary Conditions (Poinsot and Lele, 1992) are used to prescribe the boundary conditions with imposed temperature, velocity, and scalar (thermochemical gas phase and solid phase scalars) values at the inlets and pressure at the outlet. Adiabatic no-slip boundary conditions are imposed at the walls of the swirlers air injectors. The slip boundary condition is imposed for the fuel injector to avoid too small cell sizes that can compromise the time-step. For the combustor chamber walls, a wall law model (Jaegle et al., 2010) is considered with imposed temperature. The lateral walls' temperature is extrapolated from the quartz windows centerline temperature measurements (Nau et al., 2017), as shown in Fig. 5.6. At the bottom walls, a temperature equal to 650 K has been considered with experimental uncertainty of about +/- 100 K quantified and communicated by the DLR research group. A summary of the imposed conditions can be found in Table 5.3.

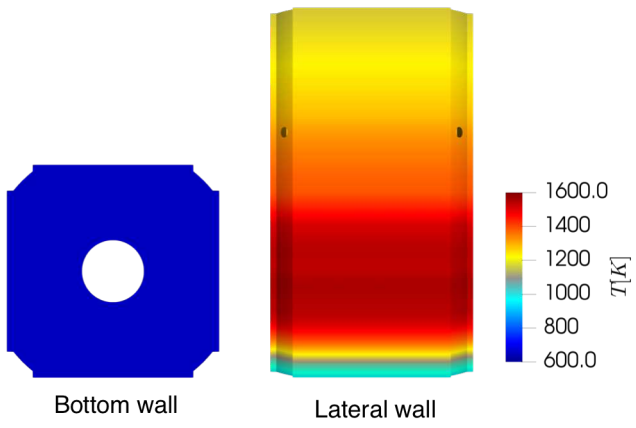

Figure 5.6: *Imposed temperature on the lateral wall (right) and on the bottom of the combustor chamber at $z = 0mm$ (left).*

Rodrigues (2018) has performed a fully-coupled LES simulation accounting for a conjugated heat transfer (CHT) at the solid walls and radiative transfer through the Monte Carlo technique. The impact of the wall heat flux distribution and thermal radiation on temperature, flame stabilization and soot production was investigated. The time-averaged temperature at the inner and outer wall obtained with the CHT simulation is shown in Fig. 5.7a-b. The CHT simulation better represents the transverse evolution of the wall temperature. The high temperature gradient corresponds to the damaged zones observed at the quartz wall used for the experimental measurements (Fig. 5.7c). Compared to an adiabatic simulation and a non-coupled simulation (imposed experimental temperature at the wall and with optically thin radiation assumption), the fully-coupled simulation presents a better agreement with experimental temperature. However, a similar flame position is obtained with the non-coupled

and the fully-coupled simulations even if the optically thin assumption leads to an over-prediction of the radiative heat losses in the inner recirculation zone. In terms of computational cost, an increase of 123% is obtained when considering a fully multi-physics simulation. Besides, a similar soot load is obtained with a tendency of soot volume fraction decrease with the increase of heat losses. Therefore, the state-of-the-art non-coupled set-up with imposed temperature and an optically thin assumption is adopted in this manuscript.

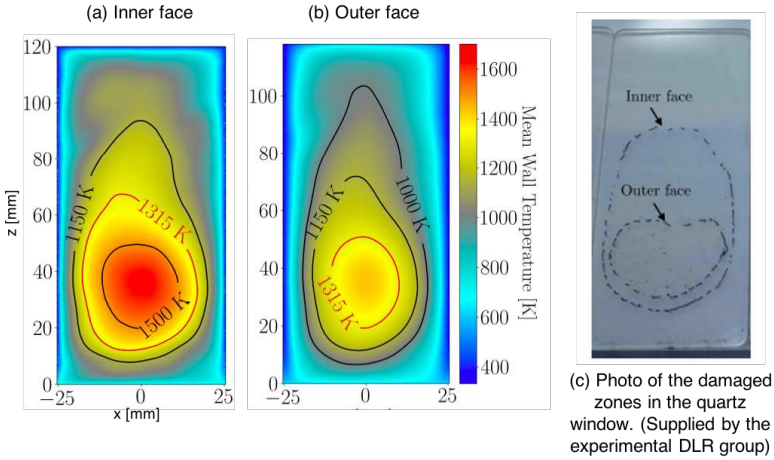

Figure 5.7: *(a-b) Numerical temperature fields of the inner and outer faces of quartz window obtained with a coupled CHT simulation. Isolines of temperature are also shown, the red isoline corresponds to the quartz annealing temperature. (c) The inner line corresponds to the surface damage at the outer side of the window whereas the outer line corresponds to the damage in the inner side. Images from Rodrigues (2018)..*

5.3.3 Numerical grid

The numerical grid, shown in Fig. 5.8, is a fully unstructured tetrahedral grid of 26.1 million cells and 4.7 million nodes. Mesh refinement has been considered mainly in the flame region (the rectangular zoomed region in Fig. 5.8), where the radial cell size range is within 0.084 - 0.6 mm. The number of points resolving the flame front varies in space and time depending on the flame localization and characteristics, governed by the local mixing. The instantaneous filtered flame front analysis reveals that at least 5 points resolve the source term of the reaction progress variable. The smallest cell size, 0.06 mm, is localized on the fuel injector (the circular zoomed zone in Fig. 5.8), allowing its resolution over 7 cells to impose the mass flow rate correctly.

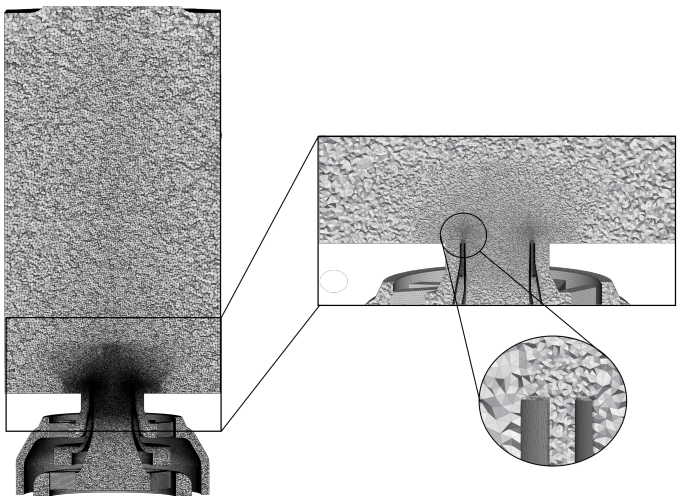

Figure 5.8: *Half-portion of the numerical grid and zoomed view in the flame zone and in the fuel injector.*

5.3.4 Modeling

The LES formalism used for the simulations presented in the next chapters were presented in detail in Part I. Summarily, the gas phase is described using the RFPV model (Ihme and Pitsch, 2008) presented in Section 4.3. The corresponding flamelet library is generated using the detailed mechanism KM2 (Wang et al., 2013) with 202 species and 1351 reactions enabling soot precursors formation up to seven aromatic rings. The consumption of soot precursors (PAH) by dimerization is taken into account in the flamelet computation. Four variables parameterize the lookup table: the filtered mixture fraction $\tilde{Z}$, the filtered reaction progress variable $\overline{Y}_C$, the filtered heat loss $\overline{H}$ and the sub-filter mixture fraction variance S_z, required by the β-pdf sub-grid scale combustion model (Lien et al., 2009), allowing to access the thermochemical quantities. An additional transport equation for the lumped PAH mass fraction is considered, as described in Section 4.4.

The solid phase is described using the three-equation model (Franzelli et al., 2018), introduced in Section 1.6. Nucleation, condensation, coagulation, and surface reactions (oxidation and surface growth) phenomena are considered source terms. Surface reactions are described using the recent HACA-RC* model (Tardelli et al., 2019) introduced in Chapter 3. The soot-turbulence interaction is considered through the soot intermittency model (Mueller and Pitsch, 2011) accounting for soot-turbulence interaction based on a presumed PDF, as introduced in Section 4.5.

Radiation is taken into account using an optically thin assumption (OTA) (Modest, 1991; Smyth and Shaddix, 1996). The impact of the radiative heat

losses in flame stabilization and soot production was evaluated by Rodrigues (2018). Assuming optically thin radiation, the flame position and temperature profiles were satisfactorily reproduced compared to a multi-physics simulation fully solving radiation from gas and solid phases, which requires massive computational cost.

The solver used is AVBP, a parallel CFD code developed at CERFACS and IFPEN (Schonfeld and Rudgyard, 1999). This explicit code solves the three-dimensional compressible Navier-Stokes equations on unstructured meshes. The third-order in space and time finite element TTGC scheme (Colin and Rudgyard, 2000) is retained for the simulations, and the SIGMA turbulence subgrid-scale model (Nicoud et al., 2011) is considered.

Chapter 6

Quantifying LES reliability of the DLR burner: temporal and grid convergence

Before evaluating the effect of a soot model for LES prediction of soot production, it is essential to quantify the quality and sensitivity of the retained numerical strategy. In this chapter, the effects of grid resolution and the temporal interval used for time-average are investigated in terms of gaseous and solid phases prediction in the DLR burner. It is observed that obtaining a statistical analysis in this burner is quite challenging due to the complexity of its flow structure and the high intermittency of soot volume fraction. Three sources of soot production unsteadiness in the DLR burner are discussed in Sec. 6.1 from the literature results and the current simulations. First, a precessing vortex core (PVC), usual in swirling flows, has been observed both experimentally (Geigle et al., 2017; Stohr et al., 2018) and numerically (Eberle et al., 2015). Second, the secondary air jets dynamics appear to substantially impact the flow structure inside the inner recirculation zone (IRZ). Finally, the turbulence-soot-flame interaction leads to a highly intermittent soot production (Geigle et al., 2017; Stohr et al., 2018). In Section 6.2 a statistical analysis of both gaseous and solid fields is performed by looking at time-averaged quantities over different temporal intervals, as well as scatterplots and pdf. It is observed that rare local gaseous conditions drive soot production. A long time averaging is required to guarantee the statistical convergence and establish a convincing results interpretation, notably for soot quantities, requiring high CPU resources. Then, the impact of grid resolution in both gas and soot description is be discussed in Section 6.3 to evaluate the reliability of the numerical results proposed in the following chapters.

Contents

6.1 Unsteady soot production in the DLR burner

Statistical stability is fundamental to ensure the reliability of the LES results. Nevertheless, achieving convergence becomes a heavy computational task, especially when low-frequency motions are present. In the DLR burner, three sources of unsteadiness of soot production were identified: (1) a coherent large scale motion, known as precessing vortex core (PVC), already experimentally and numerically characterized (Eberle et al., 2015; Geigle et al., 2017; Stohr et al., 2018); (2) the dynamics of the secondary jets, not experimentally reported; (3) the soot-turbulence interaction (Stohr et al., 2018). The PVC and secondary jets potentially affect the flow structure and mixing. The stagnation point induced by the secondary jets may be a source of slow motions in the inner recirculation zone (IRZ), which may affect the flame and soot dynamics. The effect of turbulence on soot formation leads to intermittent soot dynamics. Finally, to capture all these phenomena, a long computational time and an accurate spatial description are required. In this chapter, the unsteady phenomena and their impact on the gas and soot statistics are discussed based on results from the literature and from the current LES performed with the reference numerical set-up detailed in Section 5.3.

6.1.1 Precessing Vortex Core

Besides the turbulent velocity fluctuations, swirling flows present typical unsteady large scales structures that substantially impact mixing (Stohr et al.,

2015) and flame stabilization (Galley et al., 2011; Stohr et al., 2012). The most common is a hydrodynamic instability known as precessing vortex core (PVC), usually found in gas turbine combustors (Syred et al., 1997). The presence of a PVC in the DLR burner was characterized, numerically and experimentally by Eberle et al. (2015) and Geigle et al. (2017); Stohr et al. (2018), respectively. Eberle et al. (2015) estimated the PVC frequency to be about 500 Hz based on UNRANS computation. The PVC presence was later confirmed by Geigle et al. (2017) using a proper orthogonal decomposition for a slightly different operating conditions ($\phi = 0.9$) compared to the reference case ($\phi = 1.2$). Stohr et al. (2018) estimated a frequency of 440 Hz for the reference case in a joint LES-experimental study. Geigle et al. (2017) experimentally showed that the PVC strongly affects the spatial distribution of soot particles due to its impact on mixing.

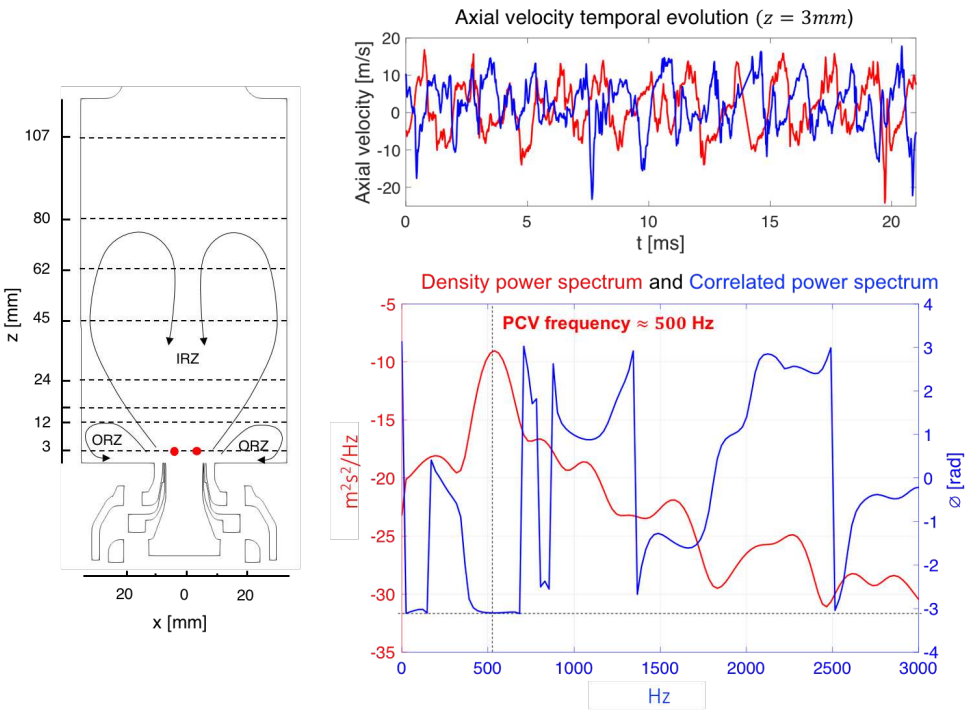

Figure 6.1: *Temporal evolution of axial velocity (top right) in two faced probes (red points in the schematic chamber on the left) in the PVC zone. The corresponding density power spectrum (red line) is superposed to the correlated spectrum (blue line) between the two probes (bottom right).*

The PVC occurrence in the current work is confirmed using the power spectrum of the axial velocity. According to Geigle et al. (2017), the PVC is located in the inner shear layer of the swirling flow between the recirculation zones (IRZ and ORZ). Two probes close to the fuel injector are used here to obtain the density

power spectrum. Figure 6.1 shows the temporal signal of axial velocity (top) for two-faced probes (P1 and P2) on the primary zone at the height of z = 3 mm (x = 4 mm and x = -4 mm) and the respective power density spectrum (red line in the bottom plot) and the correlated power spectrum (blue line in the bottom plot). The power density spectrum obtained using Welch's averaging method (Welch, 1967) characterizes the frequency of the unsteady motion. It reveals a predominant frequency at about 500 Hz. The correlated power spectrum shows a phase-shift of 2π between the velocity signals that can be interpreted as rotational motion, characteristic of a helicoidal precessing vortex core. The observed frequency is similar to the values obtained in Eberle et al. (2015) and Stohr et al. (2018).

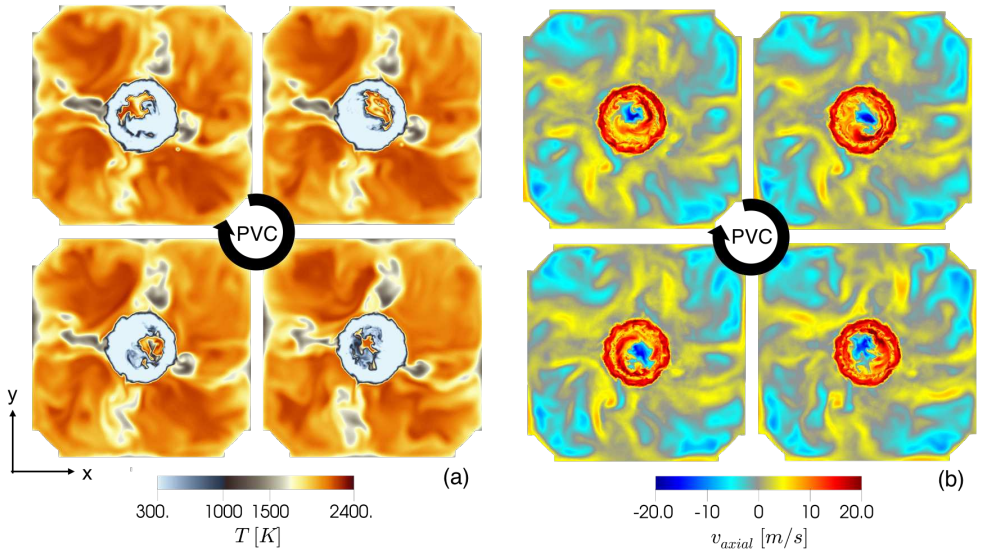

Figure 6.2: *Snapshots of temperature (left) and axial velocity (right) at z = 3 mm in a precessing period (f_{PVC} = 500 Hz).*

Figure 6.2 (on the left) shows instantaneous snapshots of temperature at the plane at z = 3 mm during a PVC precessing period (t_{PVC} = 2 ms). The flame root moves with the PVC motion. The PVC controls the stagnation point of the IRZ that controls the flame stabilization (Stohr et al., 2012), as shown by the axial velocity fields also in Fig. 6.2 (on the right). To prove the correlation between flame position and the PVC motion, Fig. 6.3 shows the power density spectrum of the temperature (Fig. 6.3a) and the axial velocity (Fig. 6.3b) at z = 3 mm and x = 4 mm. The flame presents an oscillating behavior at the same frequency as the PVC, confirming the effect of the PVC on the flame root position. A similar effect of the PVC on flame stabilization was experimentally observed by Galley et al. (2011) in a gas-turbine model combustor.

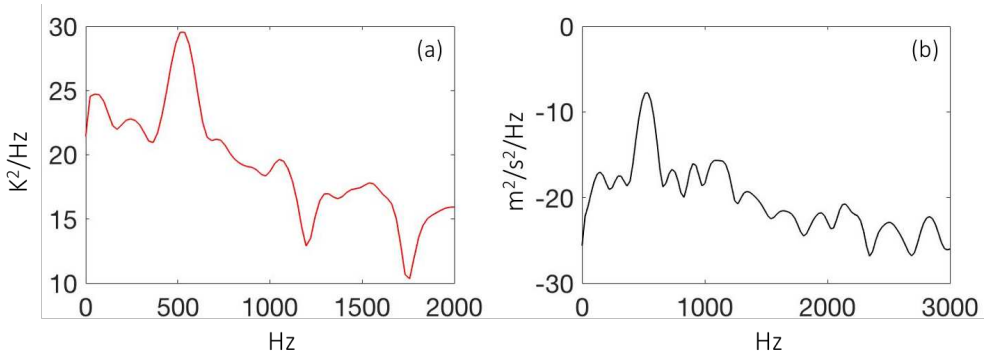

Figure 6.3: *Density power spectrum for the temperature (a) and axial velocity (b) at probe P1 close to the primary injection (z = 3 mm, x = 4 mm).*

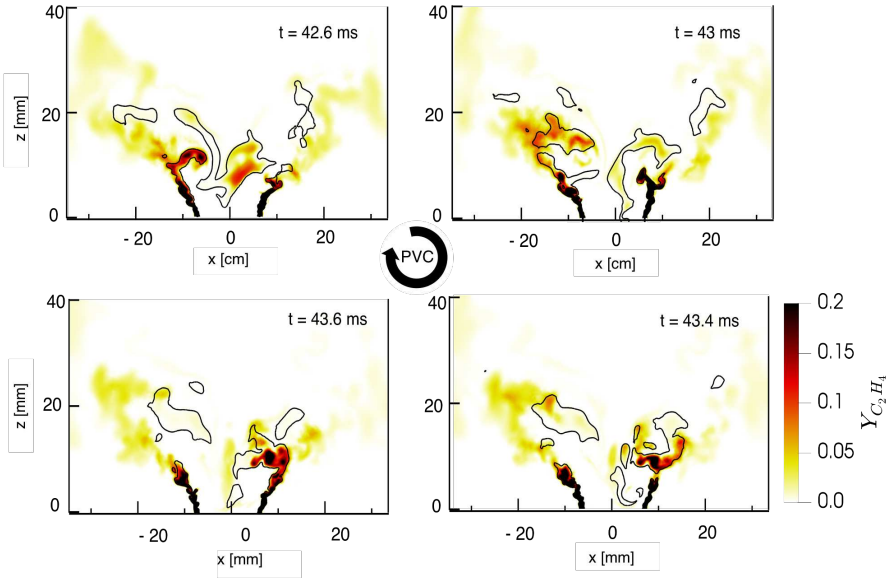

Figure 6.4: *Instantaneous C_2H_4 mass fraction fields with the iso-line of Z = 0.1 over a half precessing period.*

Besides the effect on flame stabilization, the PVC can impact the mixing close to the fresh reactant inflow (Masri, 2015; Stohr et al., 2015). Figure 6.4 shows the instantaneous field of C_2H_4 mass fraction with the iso-line of mixture fraction Z = 0.1. The sequence of snapshots corresponds to a half precessing period of the PVC. The left-right alternation of the jet flapping occurs at the half-time of the precessing motion (t_{PVC} = 2 ms), confirming the effect of the PVC motion on the mixing process. As discussed by Stohr et al. (2015), the fuel jet is entrained into the vortex roll-up action, entraining rich-fuel pockets in the IRZ. The fuel jets can eventually break down through the vortex passage creating local rich-

fuel pockets. The PVC's effect on the fuel jet induces an unsteady mixing, with the formation of localized fuel-rich zones leading to strong intermittent inhomogeneity. Geigle et al. (2017) and Stohr et al. (2018) have found that soot formation is more likely to occur at these zones of rich, fresh gases at high temperatures, which residence time are affected by the secondary jets contribution. Eberle et al. (2015) reported that a long time simulation should be necessary to obtain a statistical convergence of the results due to the PVC motion. According to them, the PVC impacts the IRZ structure, and a lack of statistical stability results in an asymmetric mean axial velocity field. In our simulations, it appeared that not only the PVC has an effect on the IRZ, but also the secondary air injection dynamics, as discussed in the following.

6.1.2 Secondary jets dynamics

Additional oxidation air is injected through four radial jets under the reference operating conditions to mimic dilution effects as in real aero-engine combustors. Traditionally, the numerical treatment of such complex flow is not straightforward, and the interaction with swirling flow in reacting conditions makes the numerical investigation even more complicated. Jet in crossflow is a canonical flowfield vastly studied in the literature. Kartaev et al. (2018) have experimentally and numerically investigated the behavior of multiple counterflow jets in a confined high temperature mainstream in a cylindrical duct. They found that increasing the momentum flux ratio increases the mixing within the IRZ and that the secondary jets can become unstable. Ivanova et al. (2012) have numerically studied a single jet in crossflow channel by comparing RANS and LES simulations. The authors found that simulation parameters such as the Schmidt number and the choice of Reynolds stress closure model can significantly affect the results. Yuan et al. (1999) found that the jet inflow conditions can significantly affect the mean jet flow. Prescribing the inflow boundary conditions can lead to unphysical behavior that could be mitigated by extending the admission pipe. Schluter and Schonfeld (2000) shows that mesh resolution and boundary conditions can significantly affect jet penetration and trajectory. Investigating the effect of radial injection in mixing a confined cross-flow, Kartaev et al. (2018) and Thong et al. (2005) have experimentally and numerically, respectively, observed that the jets become unsteady. Then jets flapping occurs for high jets momentum relative to the main flow affecting the mixing in the upstream recirculation zone. Kartaev et al. (2018) evaluated the frequency of flapping to be within $1 - 2$ Hz, based on the elapsed time of UNRANS calculations. Yoda and Fiedler (1996) investigated the structure and concentration field of a round water jet in a uniform mainstream. The author also found that for a large jet to mainstream flow velocity ratio, the jet becomes unstable and sensitive to directional perturbations affecting the jet penetration and leading to asymmetric oscillations at the jet base for a Stroudal number of 0.2 - 0.3.

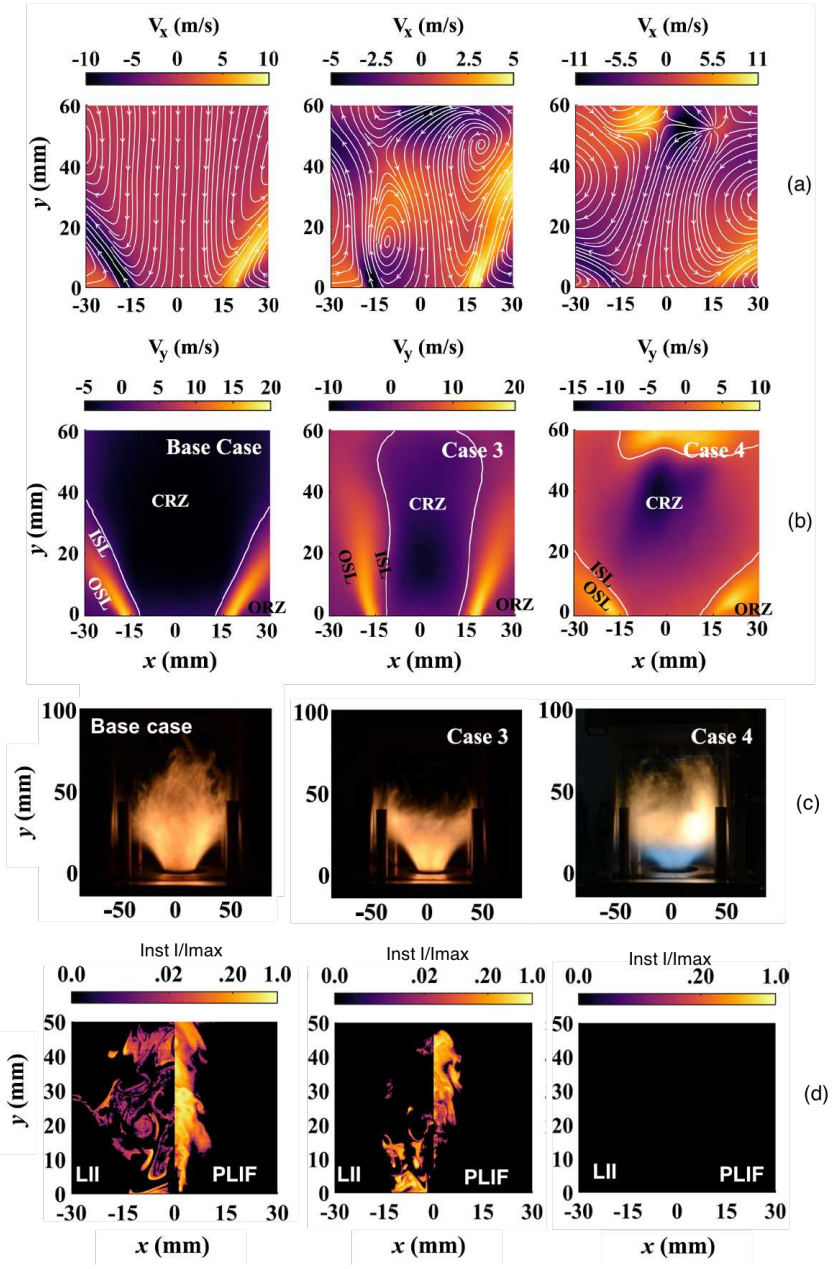

Figure 6.5: *Measurements from Helou et al. (2020) for three different cases with different dilution levels: Base Case = no dilution, Case 3 = 20 % of dilution air, Case 4 = 40 % of dilution air. Dillution stage at y = 47 mm (a) Time-averaged radial velocity field in cold conditions. (b) Time-averaged axial velocity field in cold conditions with the flow structures inner (ISL), outer (OSL) shear layers and central recirculation zone (CRZ). (c) Long exposure flame photographs. (d) Instantaneous LII/PLIF images normalized by the maximum PLIF/LII signal of the Base Case plotted.*

Tracey et al. (2018) have recently developed at the University of Cambridge an RQL model combustor similar to the DLR burner to investigate the mechanisms of soot formation as well as the dilution effects in flame structure and soot formation. For that purpose, the dilution secondary jets can be moved along the axis of the combustor. Giusti et al. (2018) performed LES simulations of the Cambridge burner to investigate the effect of the split air ratio between the primary and secondary air injection in the reacting flow and soot formation. It was found that increasing the secondary jet momentum affects the dynamics of the fuel jet in the primary zone. Part of the secondary air entrains the IRZ increasing its strength and penetrating the primary zone. High velocity fluctuation levels lead to an unstable jet fuel penetration, and the mixture becomes leaner in the primary combustion zone. The intense mixing leads to lower residence time and leaner mixture resulting in a decrease in soot mass fraction. Helou et al. (2020) have experimentally studied the effect of the secondary jets under different axial locations and split ratio in the flame structure and soot formation. It was found that the introduction of secondary air affects the IRZ structures by changing their shape, size, and strength. Similarly to the DLR burner, when the momentum of the secondary jet increases, a stagnation zone is formed near the axial injection height. Then part of the flow goes towards the flame zone, increasing the reverse velocity within the IRZ, whereas the other part is convected upward towards the burner exit. Increasing the distance between side-jet injection and primary injection leads to an increase in turbulent mixing and reduces jet penetration. Then the flame location and shape change and the residence time reduces. For high side jet momentum close to the primary injector, the OH distribution is very similar to those found in premixed flames even though fuel and oxidizer are injected separately. Such differences in flame and turbulence levels result in different soot formation. Increasing the dilution air flow rate leads to a decrease in soot volume fraction while moving the dilution injection downstream reduces the recirculated oxidation air effects on soot formation in the primary zone. Figure 6.5 illustrate some flame structure and soot volume fraction measurements obtained by Helou et al. (2020) under different operating conditions.

In the current work, it was observed that the secondary jets present an unstable behavior. However, it should be pointed out that this unsteadiness has not been reported in experiments. To illustrate the dynamics of the secondary jet, Fig. 6.6 shows two instantaneous fields of velocity magnitude at independents instants at three perspectives: the two secondary jets injection planes (Plane Jet1 and Plane Jet2), and the parallel plane to the secondary jets at z = 8 cm (Plane Jet3). The jets arrangements are revealing an unstable interaction between the four secondary jets. For the first considered instant (t = 37 ms), the four jets penetrate the chamber towards the combustor centerline and seem to be aligned. In contrast, for the second considered instant (t = 43 ms), the counterflow jets are aligned only in the Plane Jet2. Simultaneously, in Plane

Jet1, the jets trajectories deviate from each other, and jets are no longer aligned.

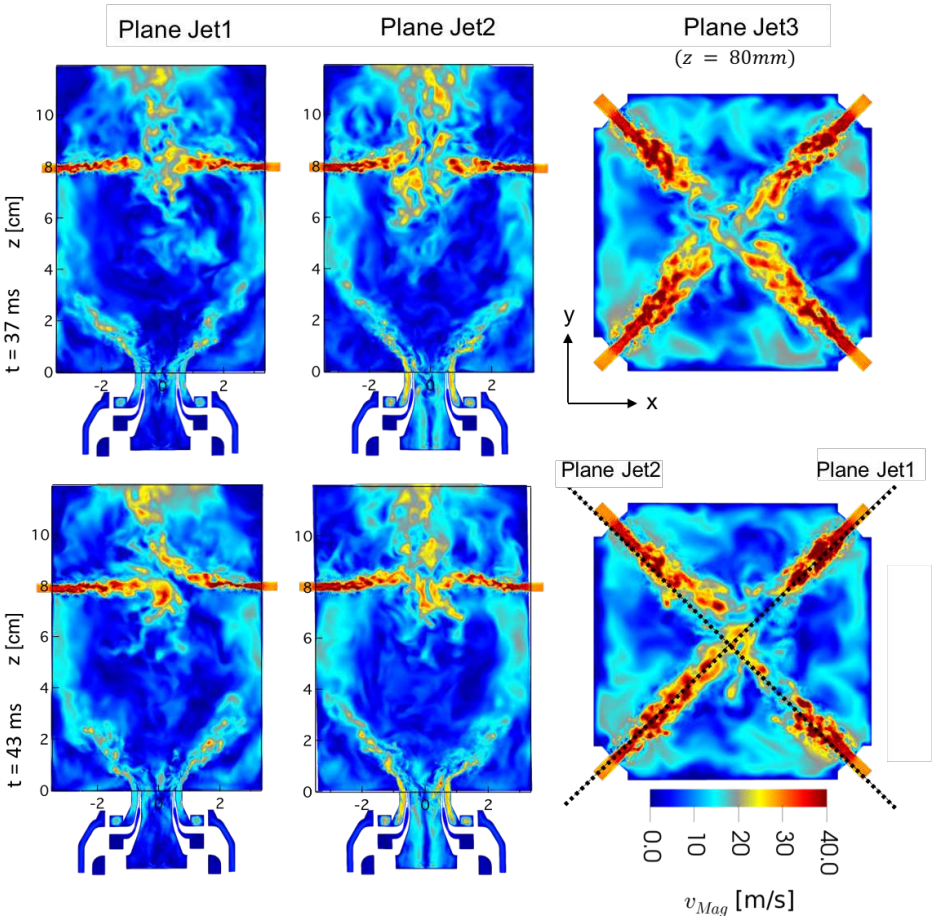

Figure 6.6: *Two instantaneous (t = 37 and 43 ms) axial velocity fields for three different perspectives: the two vertical secondary injection planes (Plane Jet1 and Jet2) and a top view (z = 80 mm) of the injection (Plane Jet3).*

The characterization of the secondary air dynamics in the DLR burner is not straightforward. The four jets in the turbulent swirl flow appear to have an intermittent and asymmetric behavior. Based on the instantaneous solution analysis, the frequency of flapping is estimated to be within 30-50 Hz, assuming that flapping is altering between the jets. Such low-frequency motion is expected to affect the quality of time-averaged statistics requiring a very long simulation time to be achieved. It should be recognized that a more in-depth analysis is necessary to accurately evaluate the unsteady interaction between jets, which is out of the scope of this work. Only qualitative insights into the effect of the jet dynamics on the flow structure and mixing are provided in the following.

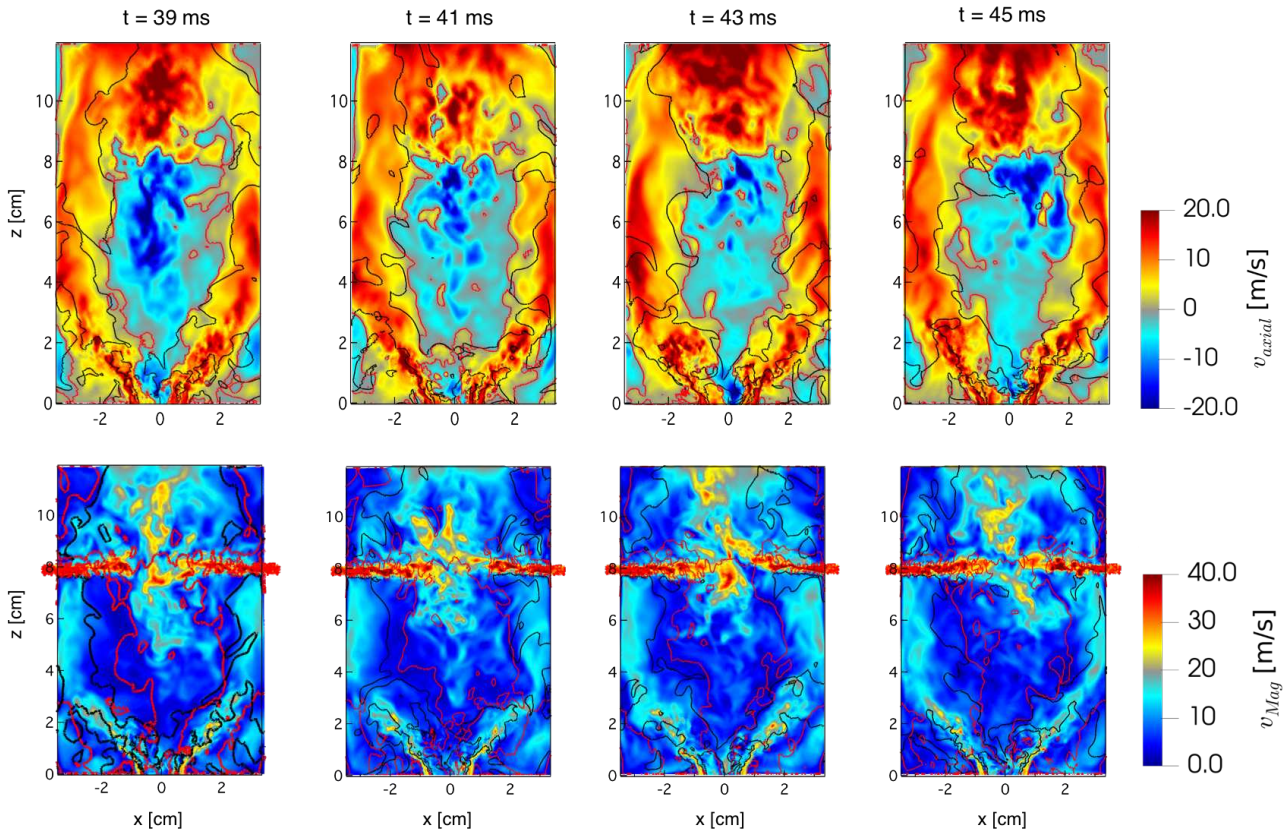

Figure 6.7: *Four instantaneous axial velocity fields in the central mid-plane (top) and in the Planes Jet1 and Jet2 in Fig. 6.6). Isolines of mixture fraction Z = 0.03 (red) and Z = 0.064 (black) are added to illustrate the mixing.*

In the present simulations, it has been observed that the secondary jets induce an intermittent behavior within the IRZ, as already suggested by Stohr et al. (2018), although no quantification or characterization of the secondary zone was reported. Figure 6.7 shows instantaneous snapshots of axial velocity in x-z plane and velocity magnitude in Plane Jet1 before and after jet deviation. Before the interaction between jets loses its symmetry, the IRZ zone aligns with the combustor chamber axis (t = 39 ms), and the flow inside the IRZ goes straight down the primary combustion zone. Approaching the non-symmetric state, the IRZ becomes disturbed and loses strength (t = 41 ms). When the jets finally deviate (t = 43 ms), the downward jet pushes the IRZ that strongly deviates.

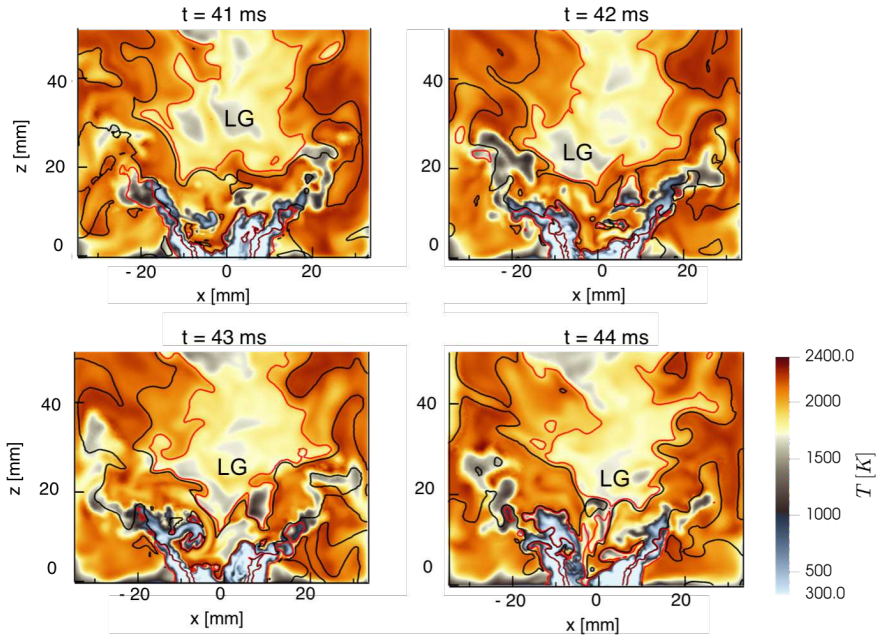

Figure 6.8: *Instantaneous temperature in the primary injection in the burner mid-plane. Isolines of mixture fraction Z = 0.03 (red) and Z = 0.064 (black) are shown to localize rich and stoichiometric mixture zones. LG: lean gas.*

The jets may affect the mixing process upstream in the primary combustion zone. The primary combustion zone is filled with hot burned gases, but lean gases can intermittently enter this zone. Figure 6.8 shows instantaneous temperature fields overlaid by the isolines of mixture fraction Z = 0.03 (red line) and 0.064 (black line), the stoichiometric value. Lean gases (LG) from the secondary zone propagate in the primary swirled zone (t = 41 - 43 ms). They are mixed with the rich-fuel gases by the swirling flow leading to a leaner mixture in the central IRZ (t = 44 ms). Additionally, the mixing zone becomes thinner,

and temperature decreases in the IRZ. It is then expected that flame structure and then soot production might be affected by the unsteady jets dynamics as observed by the Cambridge team.

However, it should be recognize that the flapping observed in the present work could be a numerical artifact due to the numerical setup, including boundary condition, numerical grid, and turbulent subgrid-scale model (Yuan et al., 1999; Schluter and Schonfeld, 2000; Ivanova et al., 2012). Large Eddy Simulation of gas turbine combustors still present limitations in modeling such complex flow structure even when using state-of-art LES models. The grid resolution and boundary conditions are critical for LES (Pope, 2004; Gicquel et al., 2012), notably in such complex reacting flow where multi-regime combustion coexists and a wide range of scales characterize the flow. Including multi-physics phenomena, as soot formation, is an additional challenge.

6.1.3 Soot - turbulence interactions

Soot production can be affected by turbulence in two major ways. First, soot precursors are very sensitive to the local scalar dissipation rate since a long chemical time scales characterize them as evidenced by Bisetti et al. (2012); Attili et al. (2014, 2015) through a Direct Numerical Simulation (DNS) of a non-premixed flame. Consequently, nucleation and condensation can be inhibited in the high dissipation rate zone, while strong soot production can be found in low dissipation rate zones. Second, it was also found that soot particles are characterized by a high Schmidt number, i.e., soot molecular diffusivity is negligible. Soot particles are then confined in thin structures. These structures can be convected and transported by the turbulent flow field, leading to a soot distribution drifted in the mixture fraction space and the presence of deformed soot ligaments of different scales. Therefore, soot particles experience various thermochemical conditions (temperature and gas composition), moving along the flow pathlines, promoting or inhibiting soot growth leading to high intermittency in space and time. In jet flames, soot production is characterized by a stratified-like soot formation and the intermittency strongly varies in the axial and radial direction (Shaddix et al., 2010; Mueller and Pitsch, 2012; Rodrigues et al., 2018). In the DLR burner, a confined swirled flame, the swirl flow induces an intense mixing and the soot mechanisms seem to overlap (Geigle et al., 2017). The secondary jets further restrict the sooting zone between the two OH fronts (Geigle et al., 2013). These phenomena result in temporal soot intermittency of about 90% (Geigle et al., 2013), i.e., only 10% of the experimentally observed soot events are characterized by a soot volume fraction higher than a specific threshold (not provided in Geigle et al. (2013)).

Figure 6.9 shows instantaneous fields of the soot volume fraction with iso-line of mixture fraction $Z = 0.1$ (representing the inflow fuel jets) to illustrate the

effect of the turbulence on soot yield on the DLR reference case. In the primary combustion zone where soot is formed, turbulence intensity is high due to the swirl flow. The soot particles are concentrated in localized zones coinciding with the flow structures displaying a vortex-like structure. At t = 42.6 ms, the soot patch is deformed by the vortical structure (as shown by the roll-up of the mixture fraction red iso-line) issued from the PVC motion and at t = 43.6 ms after a half PVC cycle. Through the action of the PVC and the turbulent flow field, they are eventually transported downstream towards the lateral walls and towards the IRZ, where residence time is higher, promoting soot growth.

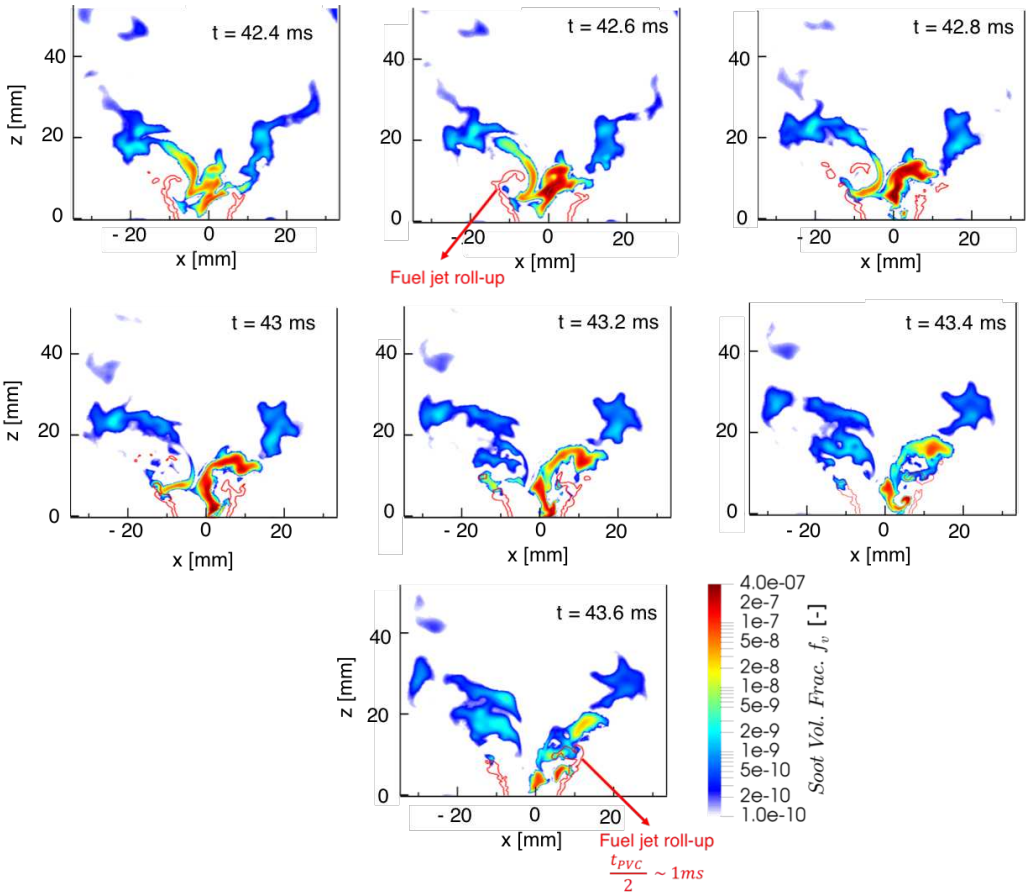

Figure 6.9: *Temporal evolution of soot ligaments, colored by the soot volume fraction, in the central mid-plane of the combustor during a half precessing period.*

Figure 6.10 shows the particles number density, soot volume fraction, PAH, and C_2H_2 mass fraction in the mixture fraction space at different times at x = 0 plane, corresponding to the instantaneous snapshots in Fig. 6.9. The scatter plot of the number density of particles shows an almost steady distribution. The peak value of N_p is located within Z = 0.1 - 0.2, in the high PAH concentration

zone related to the nucleation mechanism. However, while the particle number density remains relatively steady localized in mixture fraction space, the soot volume fraction distribution varies in the same space. Sometimes, the soot volume fraction peak can be found in lean mixtures. However, C_2H_2 and PAH concentrations are very low for Z < 0.1, meaning that f_v peak in lean regions is most likely the result of turbulent convection and not because of soot production processes. Note that the soot volume fraction peak decreases when it is localized in leaner mixtures. The movement of soot volume fraction in the mixture fraction space is a clear effect of the turbulence interaction, as already observed by Bisetti et al. (2012). Additionally, the intermittent IRZ motion can affect the dynamics of soot evolution as previously discussed. Lean burnt gases enter the primary mixing zone filling it up with OH, as shown in Fig. 6.11 by the iso-line of Z = 0.05 (blue line). The lean condition can inhibit soot formation or oxidize the existing soot in the central zone of the IRZ (yellow iso-line of f_v = 1 ppb), as already observed by Stohr et al. (2018).

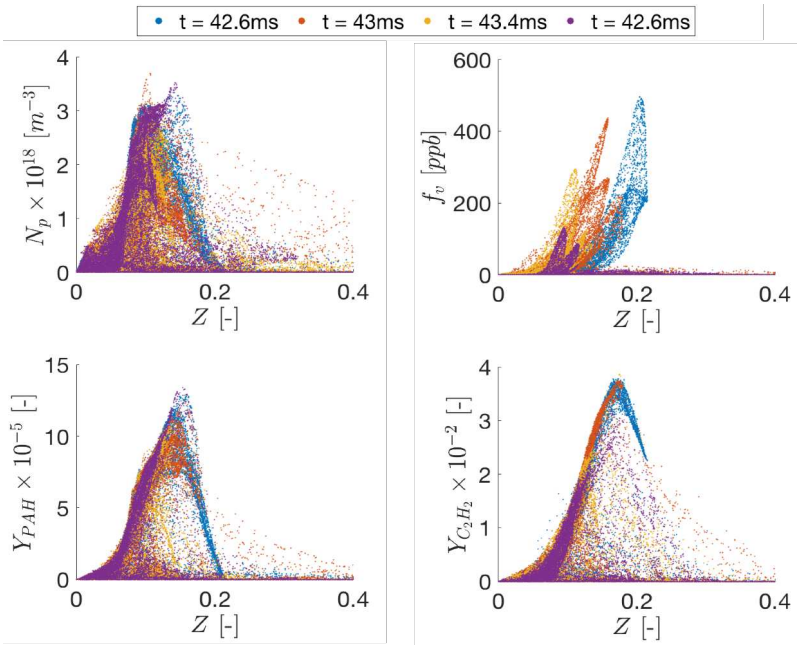

Figure 6.10: *Temporal scatter plots of particle number density (top left), soot volume fraction (top right) and gaseous key species for soot production (bottom - PAH and C_2H_2) as a function of the mixture fraction. The same instants as in Fig. 6.9 are considered.*

Based on the previous discussions, the unsteadiness of soot production is strongly coupled with the complex flow structure found in the DLR burner. To guarantee the reliability of the LES simulations performed during this thesis, statistical

and grid resolution analyses are required. Nevertheless, it will be shown in the next chapter that achieving statistical convergence, both in space and time, of soot production and even of the reactive flow structure is quite challenging in the DLR reference configuration.

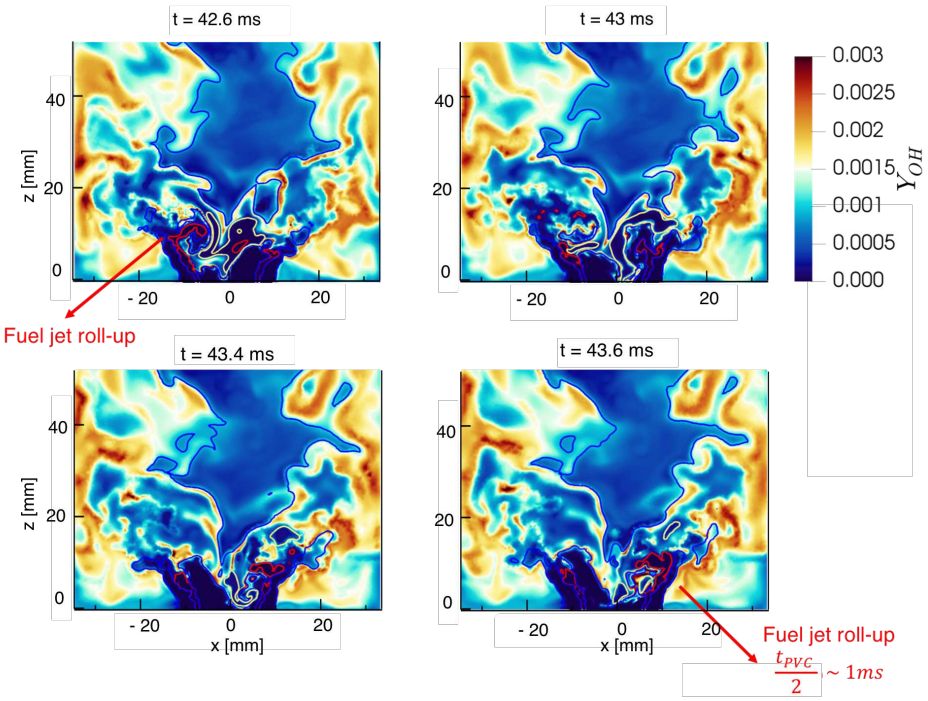

Figure 6.11: *Instantaneous OH filed in the central plan zoomed in the primary injection. Same instants as in Fig. 6.9 are considered. Isolines of Z = 0.05 (blue) and Z = 0.1 (red), f_v = 1 ppb (yellow) are added.*

6.2 Statistical analysis

An LES simulation of the DLR burner was performed over 90 ms. Statistics were collected over the last 60 ms corresponding to seven flow-through times (estimated based on the inflow velocity and the axial length of the combustor). The total time-averaged statistics (60 ms) were split into a sequence of three successive sub-periods of 20 ms, called MEAN 1, MEAN 2 and MEAN 3. In order to perform a statistical analysis, results are considered for three different intervals: MEAN 1 + 2 (40 ms), MEAN 2 + 3 (40 ms) and MEAN 1 + 2 + 3 (60 ms), called MEAN 12, MEAN 23 and MEAN 123, respectively. First, time-averaged 2D fields of gaseous and solid phases will be considered. Then, scatterplots and probability density functions will be discussed to highlight the difficulties in obtaining an accurate statistical description of soot quantities in

such complex turbulent configuration.

6.2.1 Time-averaged quantities

Figure 6.12a shows the cumulative time-averaged MEAN 12 (40 ms), MEAN 23 (40 ms) and MEAN 123 (60 ms) of the temperature with the isoline of T = 2000 K. The temperature field seems to be statistically converged at 40 ms. Only small differences are notably between 40 ms and 60 ms. However, it is important to observe that some discrepancies are found when considering the sub-intervals of 20 ms represented in Fig. 6.12b. In specific, the flame position is very similar for the three periods, except in the post-flame zone (18 - 24 mm) where the temperature is lower for MEAN2 compared to MEAN1 and MEAN3. In the vicinity of the secondary air injection (z = 62 - 80 mm), the cold air seems to penetrate farther in the IRZ for MEAN2 due to a higher negative axial velocity prediction (shown in Fig. 6.13). As already said, the dynamics of the secondary jet are characterized by long time scales affecting the position of the IRZ motion. Therefore, the statistical description of the IRZ seems to require a physical averaging time longer than 40 ms.

Concerning the mixture fraction, the fields for each time-averaged intervals are presented in Fig. 6.12c with an iso-line of the mean stoichiometric mixture fraction (Z_{st}=0.064). Globally the three mean subinterval fields present the same features, i.e., an asymmetric field in the primary swirling zone as well as along the lateral walls. The skewed distribution between left and right is due to fuel jets roll-up induced by the PVC motion, as previously shown in Section 6.1. This unsteady effect induces an asymmetric fuel distribution, which can be explained by fuel jet break down, leading to an intermittent formation of fuel-rich pockets and a skewed mixture fraction time-averaged field. Additionally, the thickness of the primary mixing zone varies between mean fields due to the irregular motions of the IRZ, which also induces an asymmetry in the chamber, as discussed early in Section 6.1. The variability of the mixture fraction field in the region close to the fuel injection is evident when looking at the three 20 ms sub-intervals in Fig. 6.12d. Although the swirling flow mainly controls the mixing in the primary region, the intermittent propagation of the lean gas from the secondary zone in the primary zone also affects the mixing by reducing the local equivalent ratio and leading to a compact mixing zone, which is similarly predicted by the three intervals in Fig. 6.12c.

Mixing has a significant impact on soot production through gaseous species concentration. Figure 6.14a shows the 2D fields for MEAN 12, MEAN 23 and MEAN 123 of three critical species for soot production: the lumped PAH involved in nucleation and condensation processes, the C_2H_2, involved in soot surface growth and the OH, involved in the soot particles oxidation. As expected from results on the mixture fraction, the species fields seem to be statistically

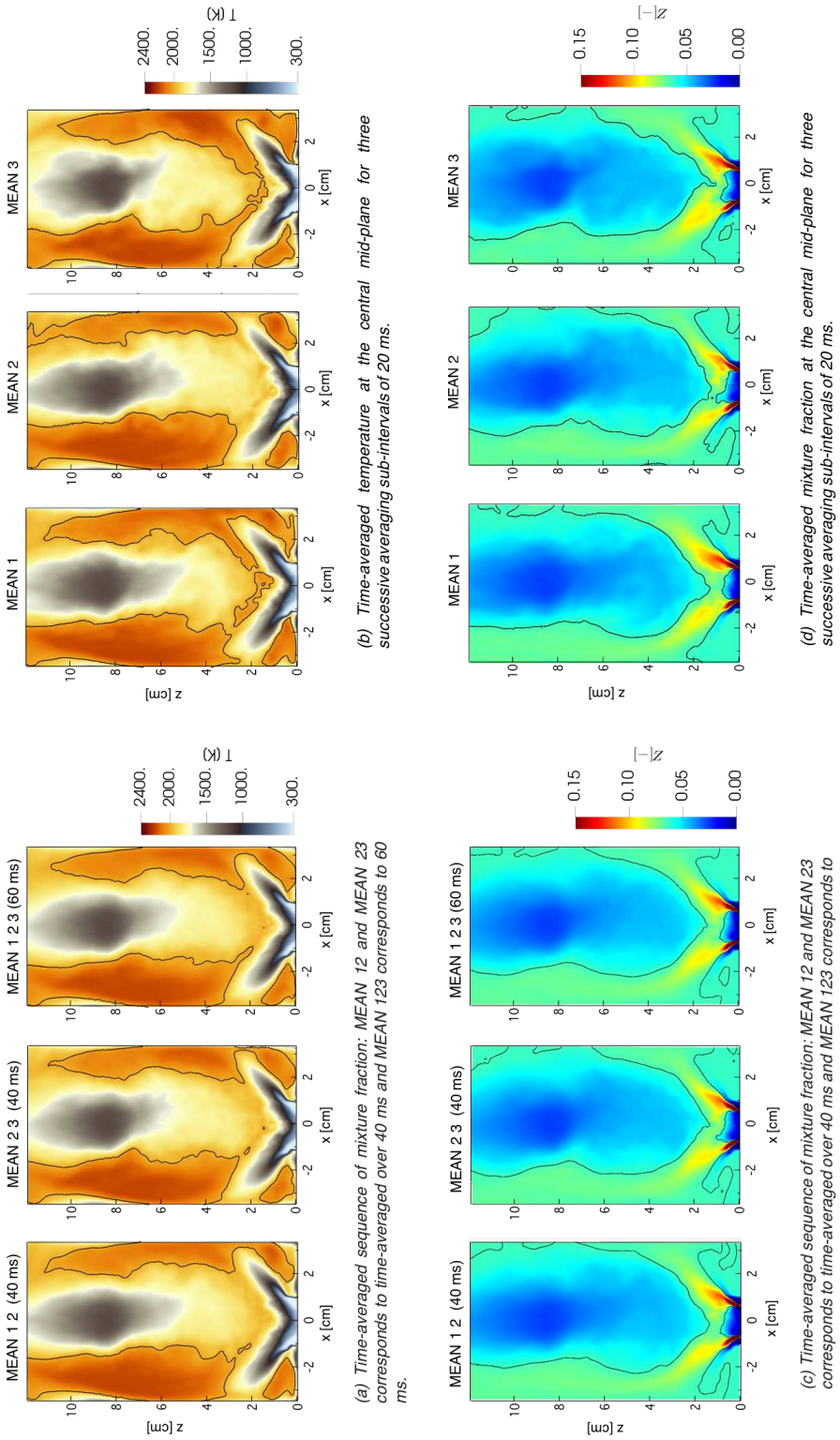

(a) Time-averaged sequence of mixture fraction: MEAN 12 and MEAN 23 corresponds to time-averaged over 40 ms and MEAN 123 corresponds to 60 ms.

(b) Time-averaged temperature at the central mid-plane for three successive averaging sub-intervals of 20 ms.

(c) Time-averaged sequence of mixture fraction: MEAN 12 and MEAN 23 corresponds to time-averaged over 40 ms and MEAN 123 corresponds to 60 ms.

(d) Time-averaged mixture fraction at the central mid-plane for three successive averaging sub-intervals of 20 ms.

Figure 6.12: *Time-averaged temperature and mixture fraction fields.*

converged at 40 ms. Similarly to the temperature and mixture fraction, only small differences are notably between 40 ms and 60 ms. OH is present mainly in the primary combustion zone and along the wall. The central IRZ is free of OH due to the local lean conditions induced by the supplementary oxidation air at z = 80 mm. C_2H_2 is concentrated close to the flame zone while PAH is observed in the primary reaction zone but also along the walls. The mixture fraction asymmetry is also retrieved in the C_2H_2 and PAH fields. Note that the peak mass fraction for both C_2H_2 and PAH is found in the fuel-rich zones, represented by the isoline of Z = 0.09. The asymmetric feature observed in the mixture fraction filed is retrieved in the C_2H_2 and PAH fields. Similarly to the mixture fraction field, the high variability of results in the bottom zone of the IRZ is observed when looking to the 20 ms sub-intervals of Figure 6.14b. Thereby, an asymmetric effect on soot production is expected.

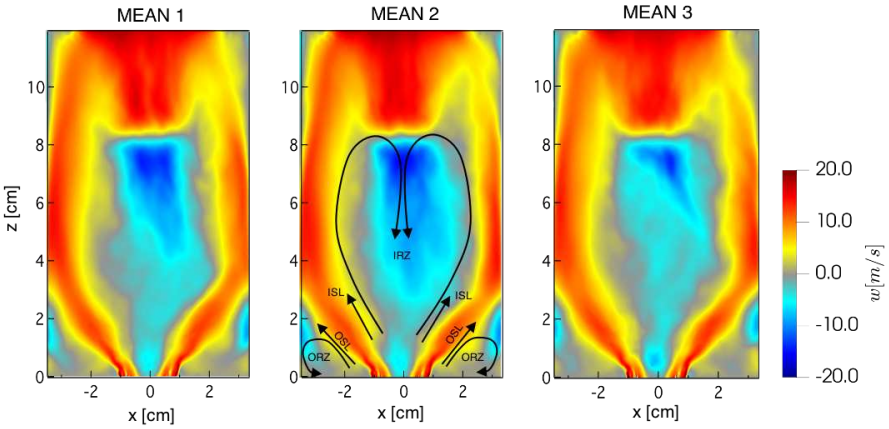

Figure 6.13: *Time-averaged axial velocity at the central mid-plane for three successive averaging sub-intervals of 20 ms. The inner, outer recirculation zones and inner shear layer (IRZ, ORZ and ISL, respectively) are schematically shown in MEAN 2.*

Figure 6.15 shows the cumulative time-averaged MEAN 12 (40 ms), MEAN 23 (40 ms) and MEAN 123 (60 ms) of particle number density and soot volume fraction. The particle number density seems to be converged. On the contrary, the soot volume fraction appears to be not converged even for 60 ms. Instantaneous fields of N_p and f_v for three independent instants (t_1, t_1 + 10 ms and t_1 + 20 ms) presented in Fig. 6.16 reveals that N_p field is more homogeneously distributed in the chamber compared to f_v, which is found at very localized regions that vary in time. Particles number density depends on the PAH concentration. Comparing instantaneous PAH (shown in Fig. 6.17) and N_p (in Fig. 6.16) fields it can be noticed that the presence of soot particles (N_p) in the primary zone and along the lateral wall is due to the presence of PAHs in these regions leading to the nucleation of soot particles as shown by the instantaneous nucleation source term in Fig. 6.18. On the contrary, the

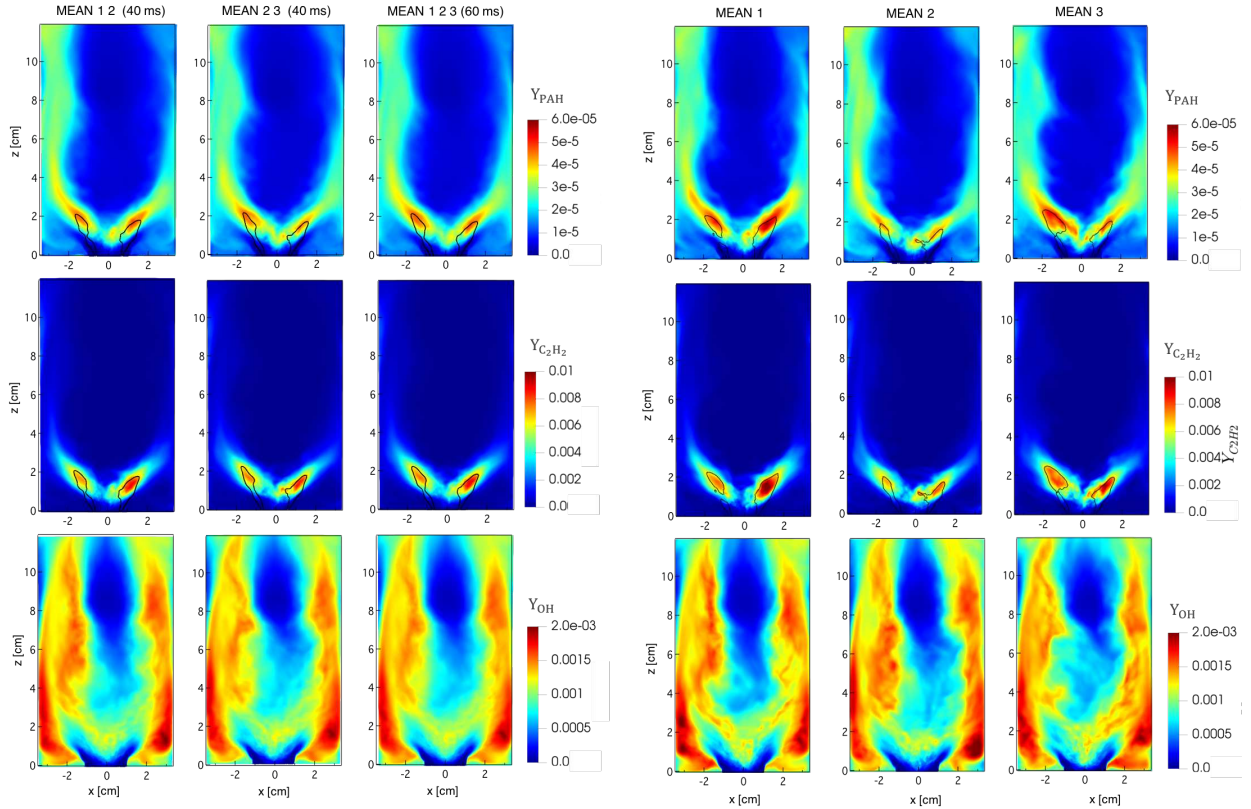

(a) Time-averaged sequence of species mass fraction: MEAN 12 and MEAN 23 corresponds to time-averaged over 40 ms and MEAN 123 corresponds to 60 ms.

(b) Time-averaged species mass fraction for three successive averaging sub-intervals of 20 ms.

Figure 6.14: *Time-averaged fields of OH, C_2H_2 and PAH mass fraction. Isolines of $Z = 0.1$ are display with the C_2H_2 and PAH fields.*

soot volume fraction, whose production is mainly driven by surface reactions via HACA-RC* mechanism as will be discussed in Chapter 7 (twice nucleation and condensation in Fig. 6.18) is then localized in small regions where C_2H_2 is present (shown in Fig. 6.17). Since C_2H_2 is present only in the primary zone, surface growth does not occur along the walls, where condensation occurs since PAHs are present. Soot particles are also highly oxidized (Fig. 6.18) due to the presence of OH in this region (Fig. 6.17), leading to a very low soot load. The dependence on temperature, species concentration, scalar dissipation as well as the strong coupling between all involved mechanisms are responsivle for the strong intermittent nature of the soot volume fraction. To provide a deep characterization of the observed soot intermittent feature, the temporal variability of the gaseous and solid fields will be investigated in the following by looking at instantaneous scatterplots and probability density functions.

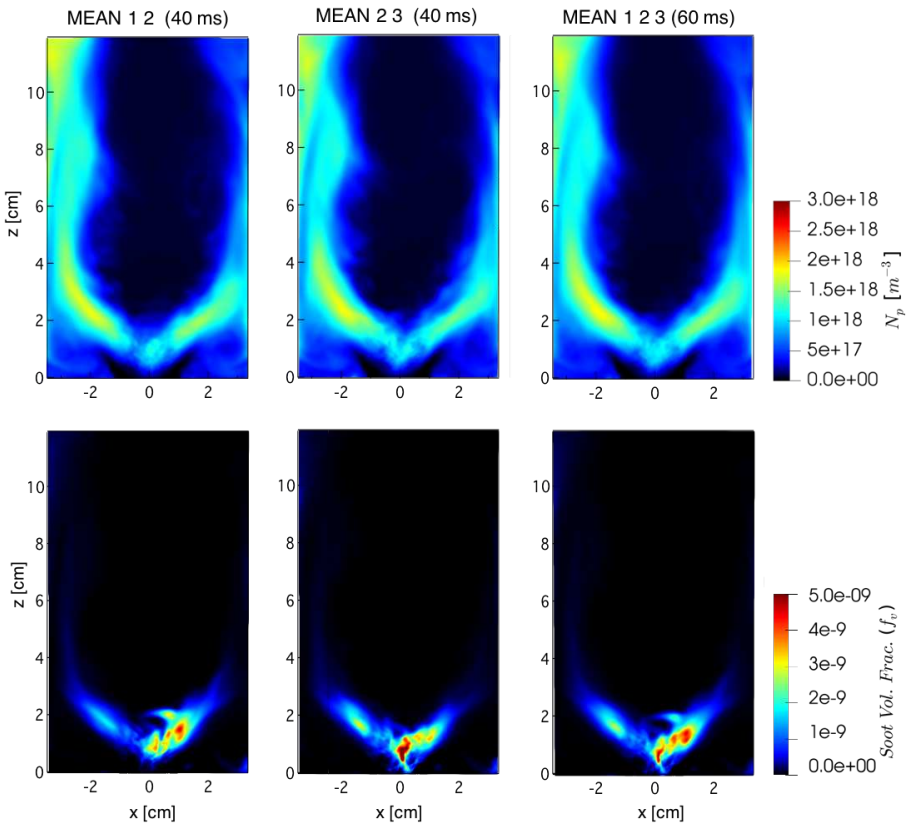

Figure 6.15: *Time-averaged fields of particle number density (top) and soot volume fraction (bottom). MEAN 12 and MEAN 23 correspond to time-averaged over 40 ms and MEAN 123 corresponds to 60 ms.*

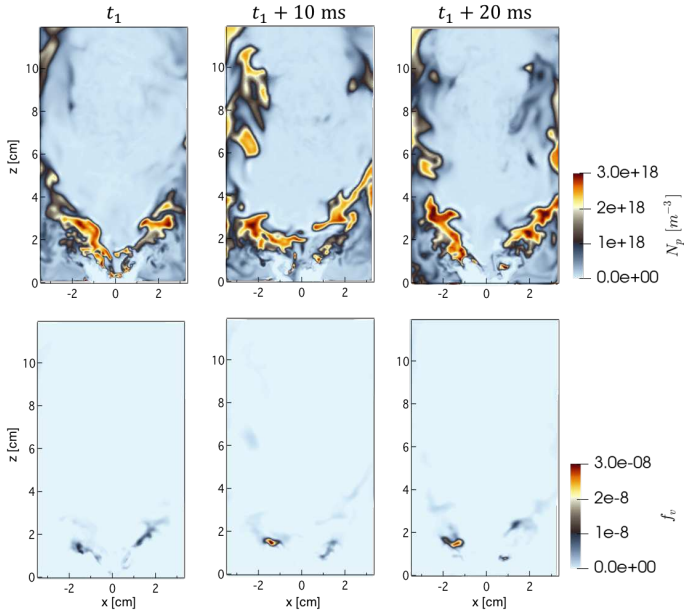

Figure 6.16: *Instantaneous particle number density (top) and soot volume fraction (bottom) fields.*

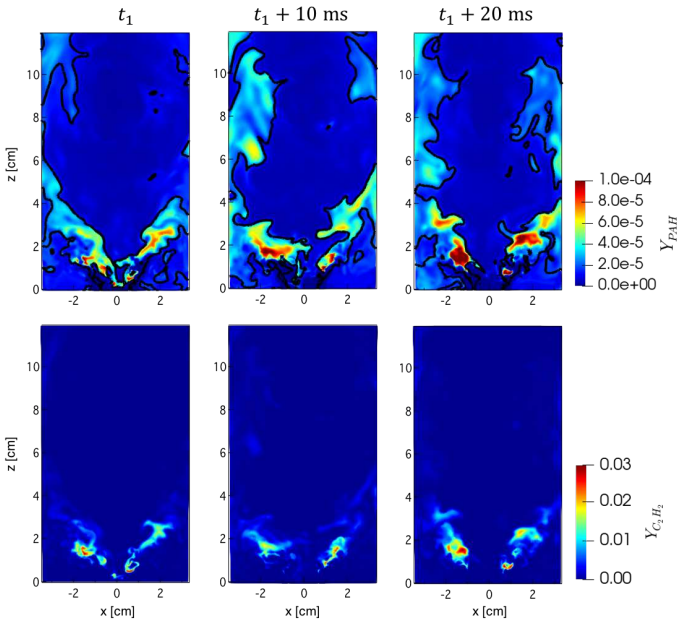

Figure 6.17: *Instantaneous PAH (top) and C_2H_2 (bottom) mass fraction fields. Isolines of mixture fraction $Z = 0.064$ (black) are shown to localize stoichiometric mixture zones.*

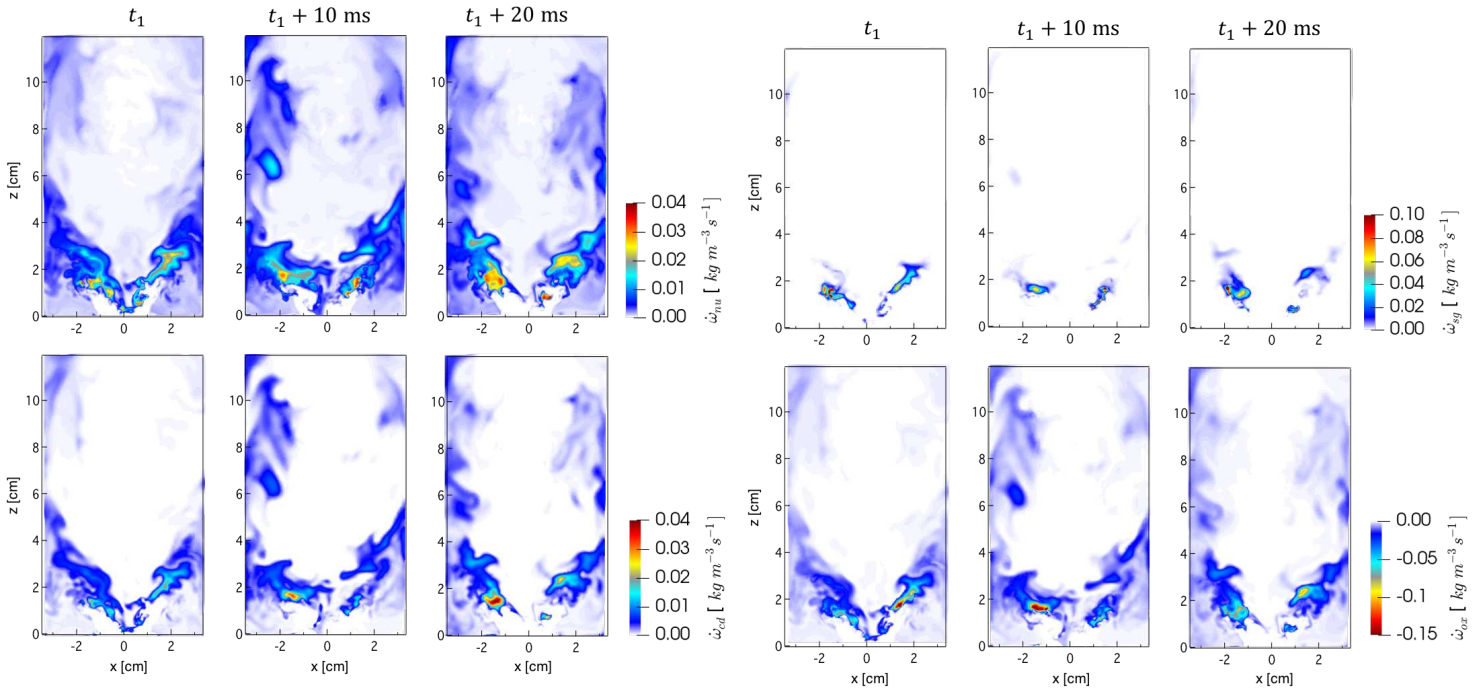

Figure 6.18: *Instantaneous soot source term fields corresponding to the same instants from Figs. 6.16 and 6.17. Top: nucleation (left) and condensation (right). Bottom: Surface growth (left) and oxidation (right).*

6.2.2 Scatterplots and PDF

As previously said, soot prediction is strongly dependent on local gas properties. It is, therefore, essential to characterize its temporal and spatial evolution. For this, the probability density function (pdf) of temperature and mixture fraction are compared in Fig. 6.19. Temperature and mixture fraction pdfs are similarly predicted for the three time-averaged periods. Only small discrepancies are observed, in analogy with the gaseous statistics (Fig. 6.12).

Figure 6.20 shows the mixture fraction, temperature, soot volume fraction and number density of particles pdfs conditioned by the presence of soot ($f_v > 1$ ppb) at different locations in the sooting zone (z $<$ 30 mm). Compared to the global pdfs (shown in Fig. 6.19), the conditioned mixture fraction and temperature pdfs present more significant discrepancies between the temporal intervals, notably at z = 18 mm. It suggests that soot particles experience different thermochemical conditions during the considered time-averaged periods along the flow pathline leading to different soot events, as shown by the pdfs of particle number density and soot volume fraction.

Table 6.1 shows the conditioned mean gaseous and soot quantities. It can be noted that the mean mixture fraction and temperature are quite similar between time-averaged intervals (ΔT $<$ 20 K and ΔZ $<$ 0.005), except at z = 3 mm where ΔT $\approx$ 68 and 115 K for MEAN 12 and MEAN 23 compared to MEAN 123. The mean conditioned soot volume fraction present large discrepancies for z = 12, 18 mm x = 0 mm, with MEAN 23 (40 ms) predicting 50% higher soot volume fraction than MEAN 12 (40 ms). On the contrary, at z = 18 mm x = 4 mm, MEAN 12 predicts a higher soot volume fraction than MEAN 23. Therefore, although similar mean gaseous conditions, soot prediction is quite different. This is associated to the intermittent soot nature.

The intermittency, defined as the probability to found $f_v > 1ppb$ is only 1 % for MEAN 12 and increase up to 5 % for the period MEAN 23 at z = 18 mm x = 4 mm. Then, considering the mean values and the high intermittency, it can be concluded that soot production is not only intermittent in space and in time, but the magnitude of such rare events is also highly variable. This is illustrated by the scatter plots of temperature as a function of mixture fraction colored by joint T-Z probability in Fig. 6.21. The three intervals are statistically similar, as confirmed by the cumulative distribution function of temperature and mixture fraction in Figs. 6.23 and 6.24 but, the occurrence of soot events, illustrated by conditioned T-Z scatter plot colored by f_v in Fig. 6.22, is very rare. This is because soot production is observed for specific conditions of the gaseous phase.

The cumulative distribution functions of temperature and mixture fraction in Figs. 6.23 and 6.24 conditioned by the presence of soot ($f_v > 1$ ppb) shows that

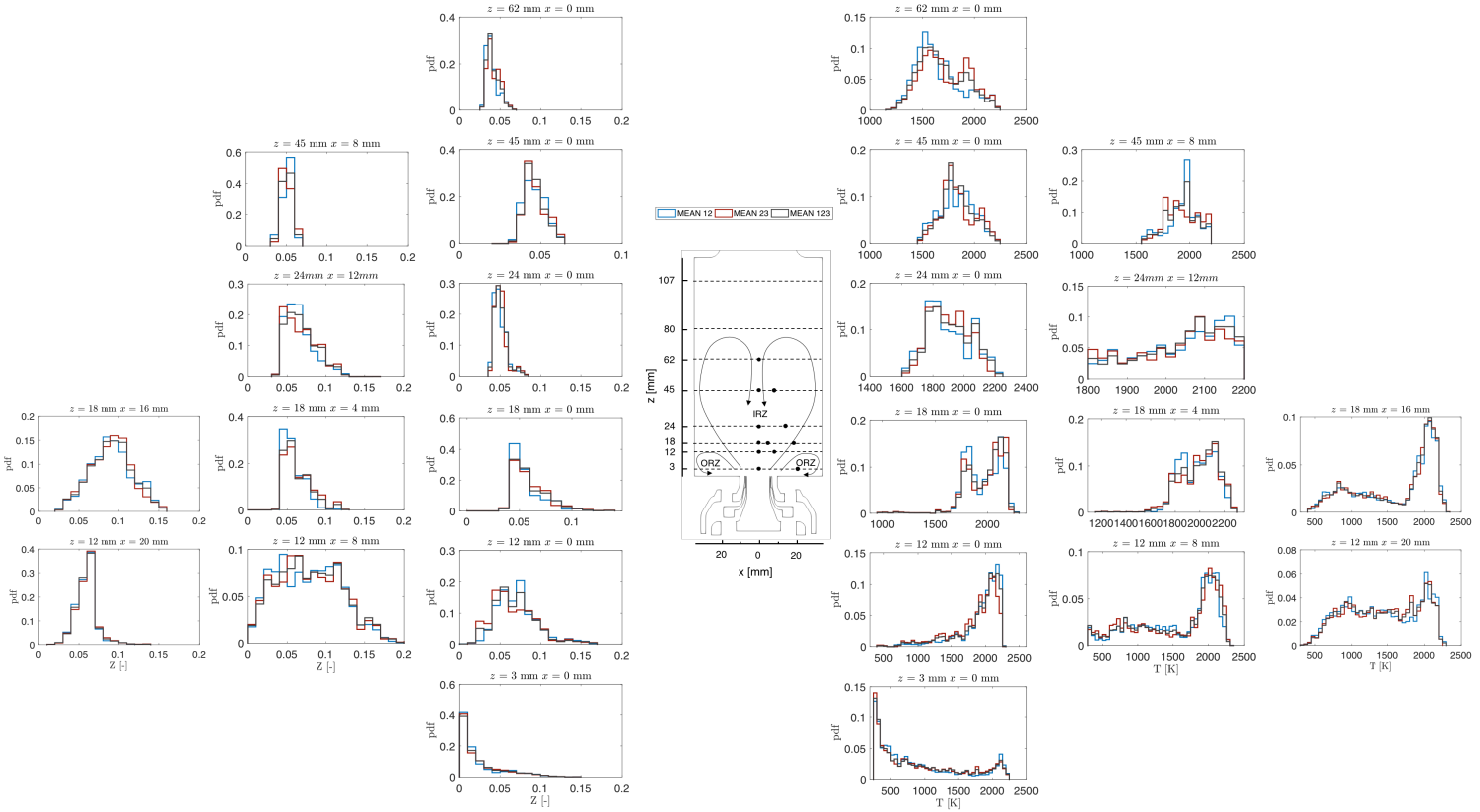

Figure 6.19: *Probability density function of mixture fraction (left of the schematic DLR burner) and temperature (right of the schematic DLR burner) for MEAN 12 (blue), MEAN 23 (red) and MEAN 123 (black) at different locations in the chamber as indicated in the schematic illustration of the DLR burner (in the center). The radial coordinate x corresponds to - x in the 2D fields.*

soot is most probable to be found for temperature higher than 2000 K and mixture fraction higher than 0.1 while most of the gaseous events are characterized by leaner mixture fraction. Moreover, as already mentioned, the soot load is quite different between the considered time-averaged intervals. This implies that to statistically describe soot volume fraction, a longer simulation time is necessary to capture a representative number of soot events which may requires massive computational resources. Therefore, this analysis reveal that the statistical convergence for the gas phase does not assure statistical convergence for the solid phase that is highly sensitive to the local fluctuations of combined gaseous variables.

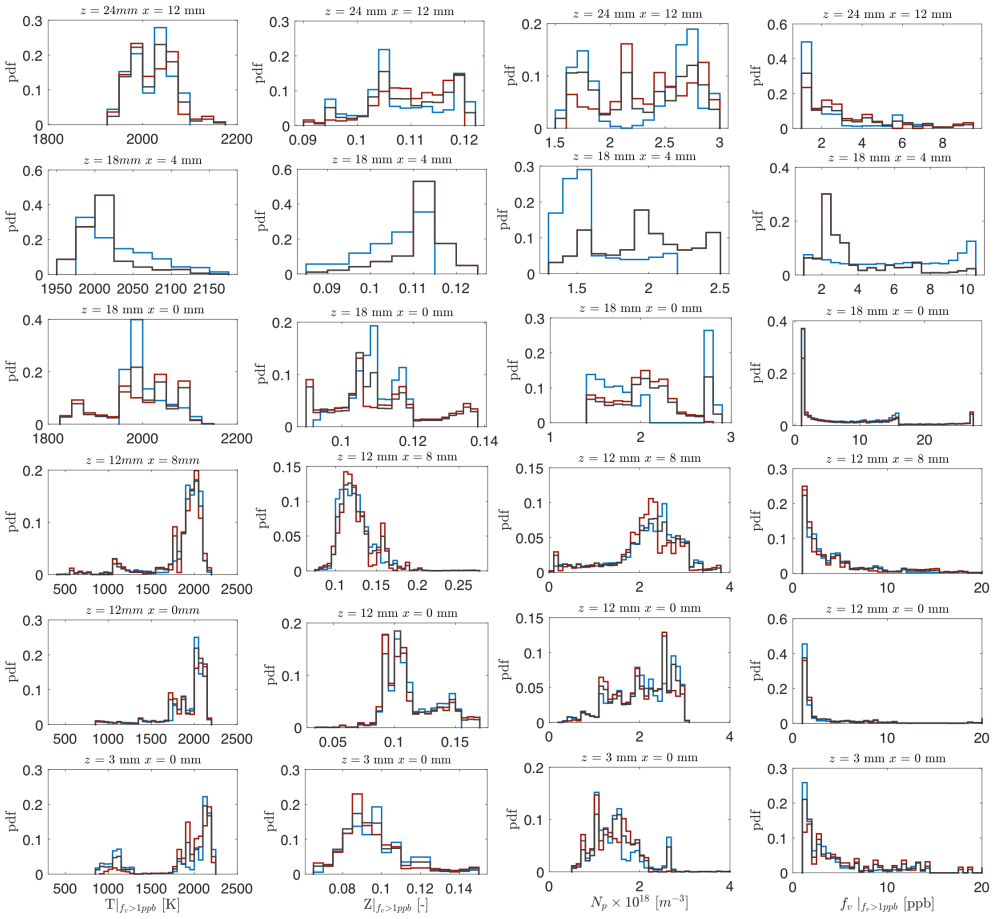

Figure 6.20: *Probability density function of mixture fraction, temperature, particle number density and soot volume fraction (from the left to the right) for $f_v > 1$ ppb at different locations in the sooting zone. The radial coordinate x corresponds to - x in the 2D fields.*

Table 6.1: *Gaseous and soot time-averaged values conditioned by the presence of soot (f_v > 1 ppb) at different probes in the sooting zone.*

z | - x [mm]	T$\|_{f_v>1ppb}$ [K]			Z$\|_{f_v>1ppb}$ [-]			f_v $\|_{f_v>1ppb}$ [ppb]		
	M12	M23	M123	M12	M23	M123	M12	M23	M123
3 | 0	1782	1965	1850	0.098	0.095	0.095	4.06	6.02	4.99
12 | 0	1906	1890	1906	0.111	0.112	0.112	10.02	16.41	13.60
12 | 8	1816	1816	1877	0.123	0.126	0.126	4.69	5.58	4.98
18 | 0	2005	1995	1994	0.108	0.110	0.110	6.05	9.07	7.87
18 | 4	2032	2012	2012	0.105	0.110	0.101	6.05	3.65	3.65
24 | 12	2022	2019	2024	0.108	0.110	0.109	2.33	3.12	2.96

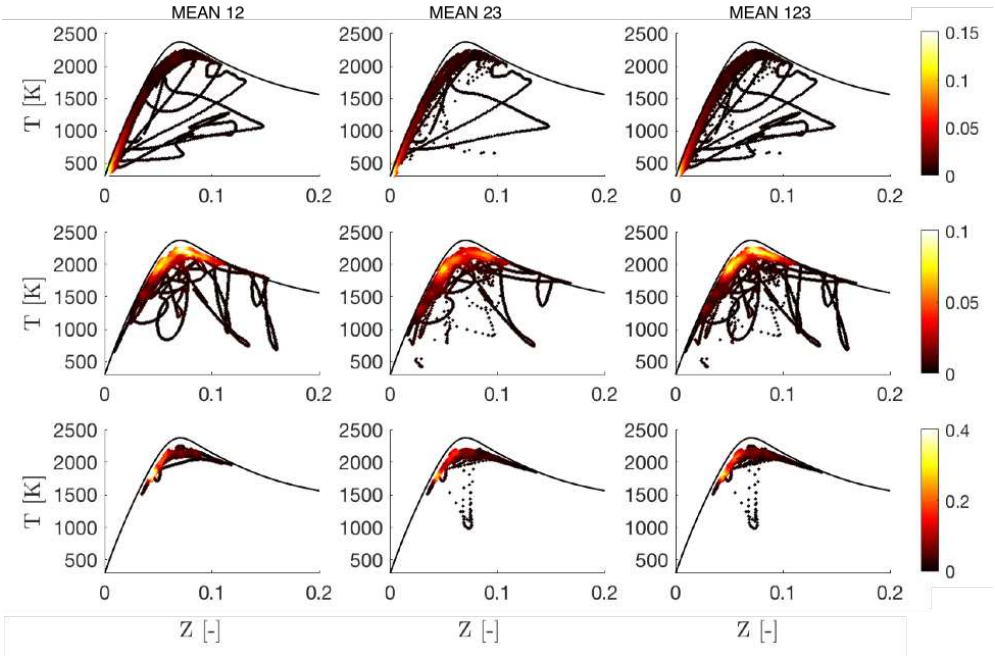

Figure 6.21: *Scatter plot of temperature in the mixture fraction space colored by joint T-Z probability at different locations in the sooting zone. The black line represents the adiabatic flame temperature from the look-up table. From top to the bottom: z = 3, 12, 18 mm x = 0 mm.*

It should be noticed that the studies presented in the following will be based on time-averaged statistics taken over about 60 ms, which is good enough to describe the gas-phase compared to the time-ensemble experimental measurements, notably in the sooting zone. Although the soot fields might not reach

statistical stability, the trends can be a capture, which is still acceptable considering the many uncertainties involved in soot modeling and the computational resources required to compute such complex turbulent configuration. In addition considering 60 ms is still CPU - affordable in the industrial context of the SOPRANO project, which represents the framework of this PhD work. Finally, prior LES studies of the DLR burner are based on statistics lower than 60 ms (summarized in Table 5.2). It should also be mentioned that it is a common practice to azimuthally average the time-averaged fields. However, it is not suitable for this non-axisymmetric configuration, especially when the second injection stage is considered. This averaging strategy can bias the interpretation of soot formation as well as the flow structure. For these reasons, in the current work, results are always shown in the combustor's mid-plane, consistent with the experimental procedure. However, it should be remembered that the experimental ensemble-average f_v field contains 400 instantaneous images obtained with a frame rate of 400 ms (Geigle et al., 2013), which corresponds to a few minutes, while the computations capture only a few ms of physical time.

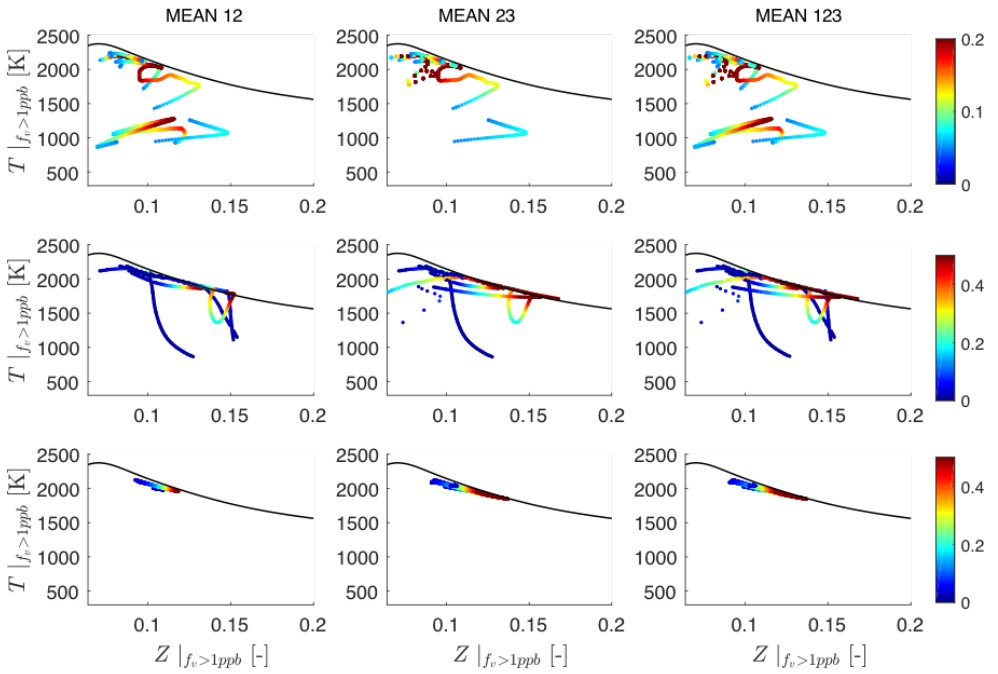

Figure 6.22: *Scatter plot of temperature in the mixture fraction space conditioned by the presence of soot (f_v > 1 ppb) colored by the normalized f_v at different locations in the sooting zone. Soot volume fraction f_v is normalized by the maximum f_v from MEAN 123. The black line represents the adiabatic flame temperature from the look-up table. From top to the bottom: z = 3, 12, 18 mm x = 0 mm.*

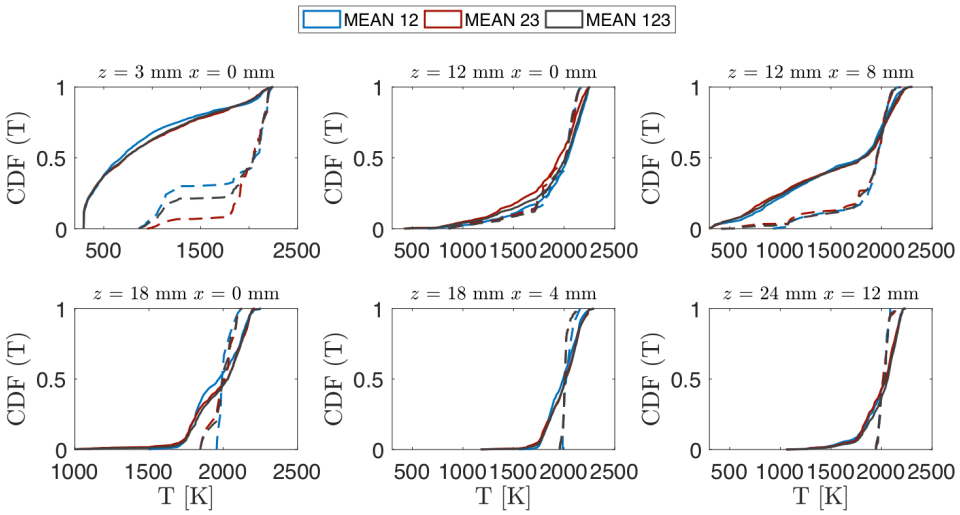

Figure 6.23: *Cumulation density function (CDF) of temperature at the probes in Table 6.1. Dashed lines represents the CDF conditioned by the presence of soot (f_v > 1 ppb).*

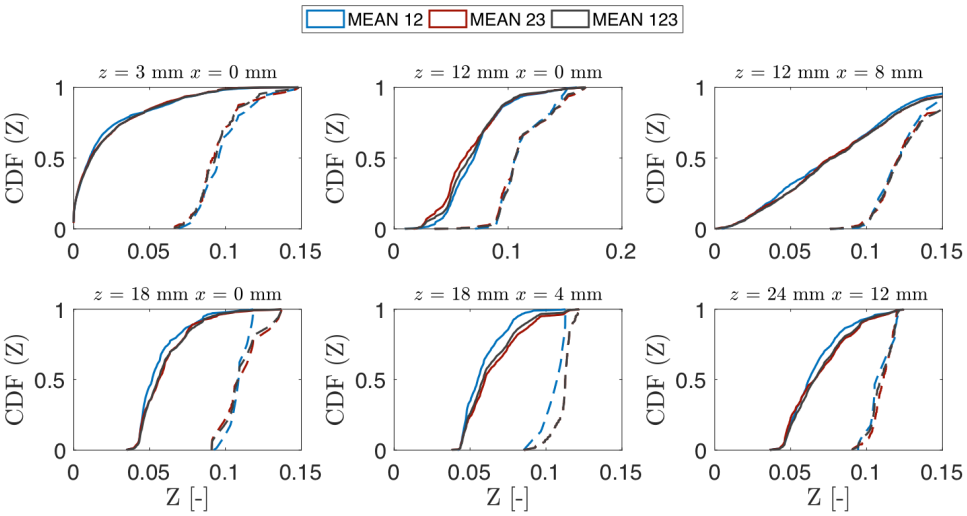

Figure 6.24: *Cumulation density function (CDF) of mixture fraction at the probes in Table 6.1. Dashed lines represents the CDF conditioned by the presence of soot (f_v > 1 ppb)*

6.3 Effect of grid resolution

From a theoretical point of view, LES depends on the filter width and type used in the filtering procedure, on the grid resolution and on the numerical methods (Pope, 2004). In practice, the numerical grid acts as an implicit filter. LES results are then very sensitive to the grid resolution, which drives the resolved and non-resolved scales contribution on the LES statistics (Pope, 2004; Klein, 2005; Pitsch and Duchamp de Lageneste, 2002). Therefore, evaluating the grid resolution impact on LES results is a fundamental step to assess reliable results (Pope, 2004; Vervisch et al., 2010). It is even more critical for turbulent sooting flames since an additional length scale is introduced. Soot particles are found in a ligament form that may not be resolved on the LES grids, requiring specific subgrid-scale models similar to the flame. However, grid dependence is seldom evaluated, notably in realistic configurations, since it requires high computational resources. Chong et al. (2018) have recently reported the impact of grid resolution on an LES of the DLR burner. In this study, three fully unstructured numerical grids (6, 12, and 77 million cells) were tested. They observed that the soot volume fraction, obtained using the soot HMOM model, decreases while increasing the mesh resolution. Such an effect was attributed to the increase of the scalar dissipation rate with mesh resolution, enhancing mixing and reducing PAH concentrations involved in nucleation and condensation processes. Nevertheless, the study is very brief, i.e., the effect on the reacting scalar quantities is not evaluated, which is essential considering the dependence of soot fields on the gaseous phase.

Table 6.2: *Time averaging and computational cost for each simulation. Simulations were run on Intel E5-1920 processors.*

Grid	τ_{sim} [ms]	τ_{ave} [ms]	CPU_{ave} [h]
Coarse	60	30	96.000
Reference	90	57	180.000
Fine	90	57	330.000

Thereby, the present study aims to evaluate the effect of grid resolution on both gaseous and solid phases and evaluate their ability to reproduce the experimental measurements. For this, three numerical grids with different resolutions are employed. In addition to the reference grid used in the previous section, a finer and a coarser grid are tested. The choice for a coarser grid has been made to limit the computational cost. The same numerical set-up detailed in Section 5.3 is used for the simulations presented here. The initial solutions for the fine grid and the coarse grid computations were obtained by interpolating the statistically stabilized solution from the reference grid. Once interpolated,

the simulations are computed for $\tau_{sim} = 90$ ms, time-averaged statistics are collected over the last 57 ms. For the coarser grid, however, only $\tau_{sim} = 60$ ms were performed due to the occurrence of a flame instability, as will be discussed in the following sections. The time averaging τ_{ave} and the CPU cost for each numerical grids are summarized in Table 6.2. Detailed information on the resolution of each grid is presented in the following.

6.3.1 Numerical grids

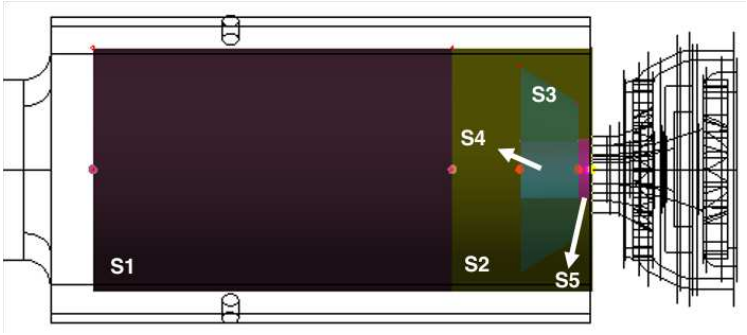

Figure 6.25: *Schematic burner showing the zones (S_x with x = 1-5) with different refinement.*

Table 6.3: *Cell size in extremities (top and bottom, respectivelly) of the meshing zones (S1, S2, S3, S4, S5) for the primary zone and inner recirculation zone.*

Grid	S1 [mm]	S2 [mm]	S3 [mm]	S4 [mm]	S5 [mm]
Coarse	0.60 - 0.80 0.65 - 0.75	0.20 - 0.50 0.65 - 0.75	0.08 - 0.40 0.70 - 0.70	0.07 0.70 - 0.70	0.07
Reference	0.72 - 0.96 0.60 - 0.84	0.24 - 0.60 0.60 - 0.84	0.084 - 0.240 0.36 - 0.60	0.084 0.24 - 0.36	0.07
Fine	0.60 - 0.80 0.50 - 0.70	0.20 - 0.50 0.50 - 0.70	0.07 - 0.20 0.30 - 0.50	0.07 0.20 - 0.30	0.07

Three fully unstructured tetrahedral numerical grids with different resolutions were employed to evaluate the impact of the grid resolution on the numerical simulation of the DLR burner using the LES formalism. The fine grid contains 40.5 million tetrahedra cells and 7.15 million nodes. The reference grid contains 26.1 million tetrahedra cells and 4.7 million nodes. Due to the small difference between the fine and reference grid in the primary zone (zones S3 and S4 in Table 6.3), it could be expected that the flame stabilization and the soot production will be quite similar. Finally, the coarser grid contains 19.8 million

tetrahedra cells and 3.6 million nodes. This grid was coarsed in the primary zone (zones S2-S4 in Table 6.3), but in the IRZ and the vicinity of the secondary jets (zone S1 and the top of zone S2 in Table 6.3) the resolution is higher than in the reference grid in an attempt to avoid the supposed numerical secondary jet flapping. Along the wall and inside the swillers, cell sizes are quite similar between the three grids. For all considered grids, the smallest cell size (0.06 mm) is located in the fuel injector (width 0.4 mm) to guarantee the correct mass flow rate on the inlet. Figure 6.25 shows the zones with cell size variations between grids. The cell size ranges are summarized in Table 6.3.

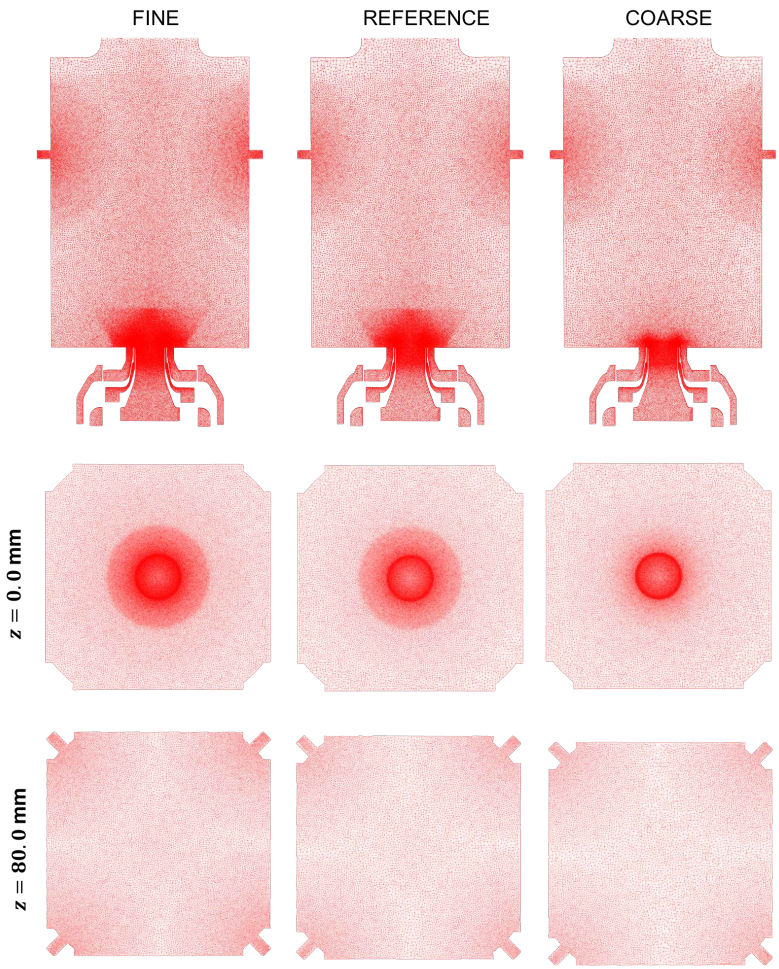

Figure 6.26: *Numerical grids at three different planes. Top: the secondary jets plane. Center: the transversal plane at the inlet (z = 0.0 mm). Bottom: the transversal plane at the secondary injection (z = 80 mm).*

Figure 6.26 shows the numerical grids at three different planes. The instantaneous flame thickness and soot structures depend on the local flow conditions.

Thereby, the flame and soot filament characteristics size strongly vary in space and time. In this configuration, the soot pockets are found to be, in general, larger than the flame front. According to the experimental observations, the soot filament size can vary from 1 mm to 10 mm in the DLR burner (Geigle et al., 2015). Considering the high soot intermittency and the non-homogeneous grid, it is not easy to precise the resolution of the soot structures. From the experimental results and instantaneous numerical solutions, soot pockets are expected to be resolved in a wide size range.

6.3.2 Gas phase statistics

Velocity

Figure 6.27 displays the time-averaged fields of the three velocities components under reacting conditions for the three grids. The iso-line of nul axial velocity $v_{axial} = 0.0$ m/s, superposed to the axial velocity fields, enables the localization of the IRZ and the ORZ. It can be observed that the IRZ intensifies when decreasing the grid resolution: the reverse flow within the IRZ is more intense for the reference and coarse grids. The radial component appears to be also sensitive to the grid resolutions, except for the radial inflow jets in the swirling region (z $<$ 30 mm). The isoline of null tangential velocity shows that the rotational motion is also affected by the grid resolution.

For further investigations, Figs. 6.28 and 6.29 compare numerical and experimental radial profiles of the three velocity components at the primary combustion zone (z $<$ 30 mm) and downstream towards the secondary injection (z $>$ 40 mm), respectively. In Fig. 6.28, the swirling flow feature is quite well described by the three tested grids, even if the jet angle is narrower in the numerical simulations compared to the experimental one. The IRZ strength is slightly high for the coarse grid, which leads to flame instability and stabilization problems, as discussed afterward.

Downstream (z = 44 - 62 mm in Fig. 6.29), the IRZ strength is well captured by the reference and coarse grids, but the fine grid under-predicts the IRZ intensity. The axial velocity profiles show that the negative axial velocity, typically found in reverse flows, is not well captured by the fine grid. It is ascribed to the secondary dynamics that affect the flow split and the amount of recirculated dilution air. In fact, the profiles at the secondary injection stage, at z = 80 mm, shows a good agreement with experiments for all velocity components for the reference and coarse grids. However, the fine grid over-predicted the axial and tangential velocity components, which is quite surprising since it could be expected that fine grids would be able to capture better high-gradient regions such as the cross jets in the secondary zone. The radial velocity is differently described by the grids, revealing that the interaction between radial

secondary jets is sensible to the grid resolution. It should be reminded that such conclusions can be affected by a lack of statistical convergence in this highly turbulent zone, notably for the coarse grid whose statistics period is two times shorter than in the other two cases.

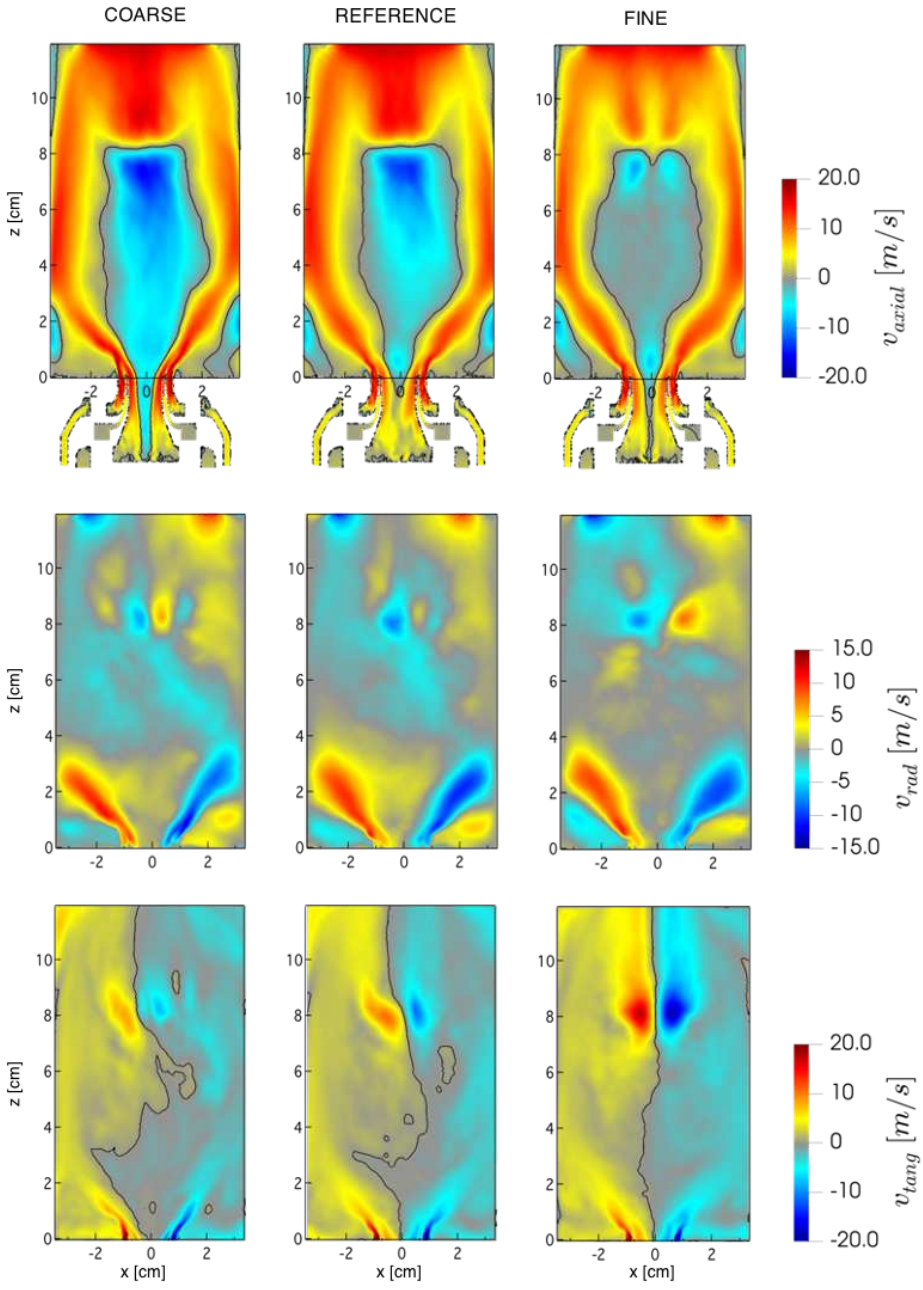

Figure 6.27: *Time-averaged 2D fields of velocity components for the fine (right), reference (center) and coarse (left) grids. Null axial and tangential velocities isolines are shown in the respective axial (top) and tangential (bottom) fields.*

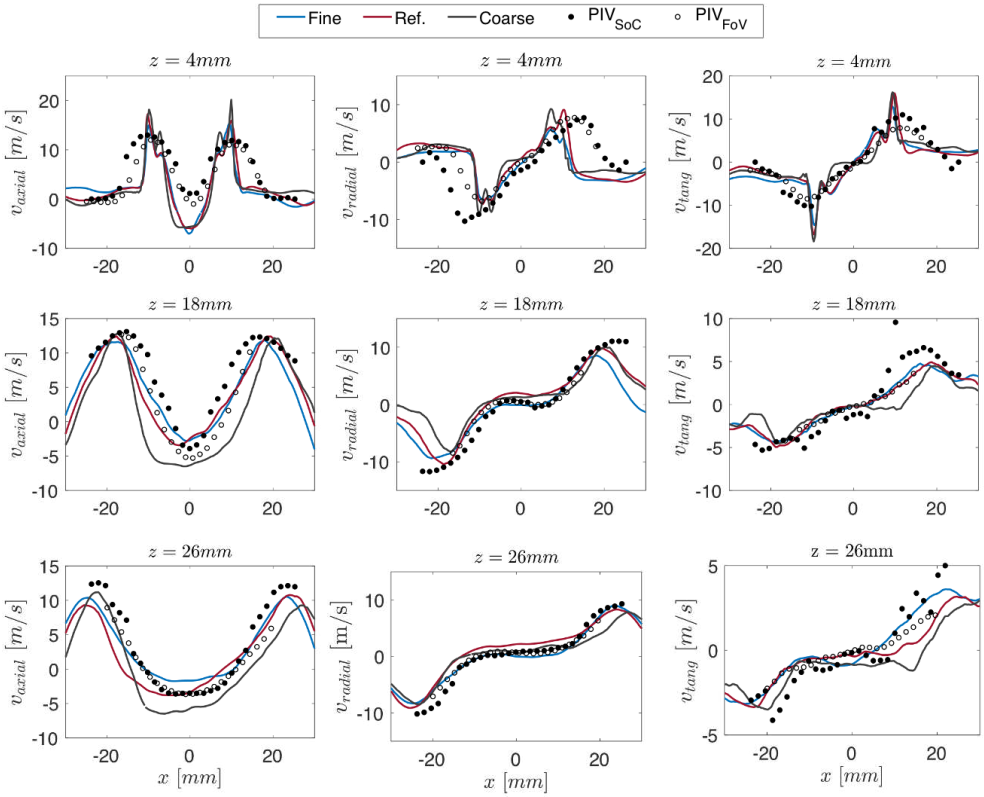

Figure 6.28: *Time-averaged velocity components profiles under reacting conditions obtained with the three grids (fine grid in blue, reference grid in red and coarse grid in gray) compared to the experimental measurement (symbols - Geigle et al. (2017)) in the primary zone ($z < 30$ mm).*

Fig. 6.30 shows the velocity fields on the top view of the secondary air injection (Jet3 plane) illustrating the effect of the grid resolution on the description of secondary jets. The jet penetration is quite similar between grids. However, for the fine grid, a more intense tangential velocity induces a jet rotational motion, which is weakly observed in the other cases. The impact of secondary jet dynamics on the IRZ was discussed in Section 6.1 for the reference grid. It was shown that the secondary jets interact intermittently, affecting the IRZ structure by inducing an unsteady motion. Additionally, lean gases can intermittently penetrate the primary mixing zone. However, the secondary jets unsteady behavior is not observed for the finer and coarser grids. In the fine grid, the jets are driven by the tangential velocity, and the downward flow seems to be aspired by the created vortex core, while in the coarse case, the instantaneous lower jets penetration prevents the jet flapping. Henceforth, it is evident that grid resolution has a substantial impact on the secondary air injection and, consequently, on the IRZ structure, which may impact the mixing upstream and then the flame structure and soot production.

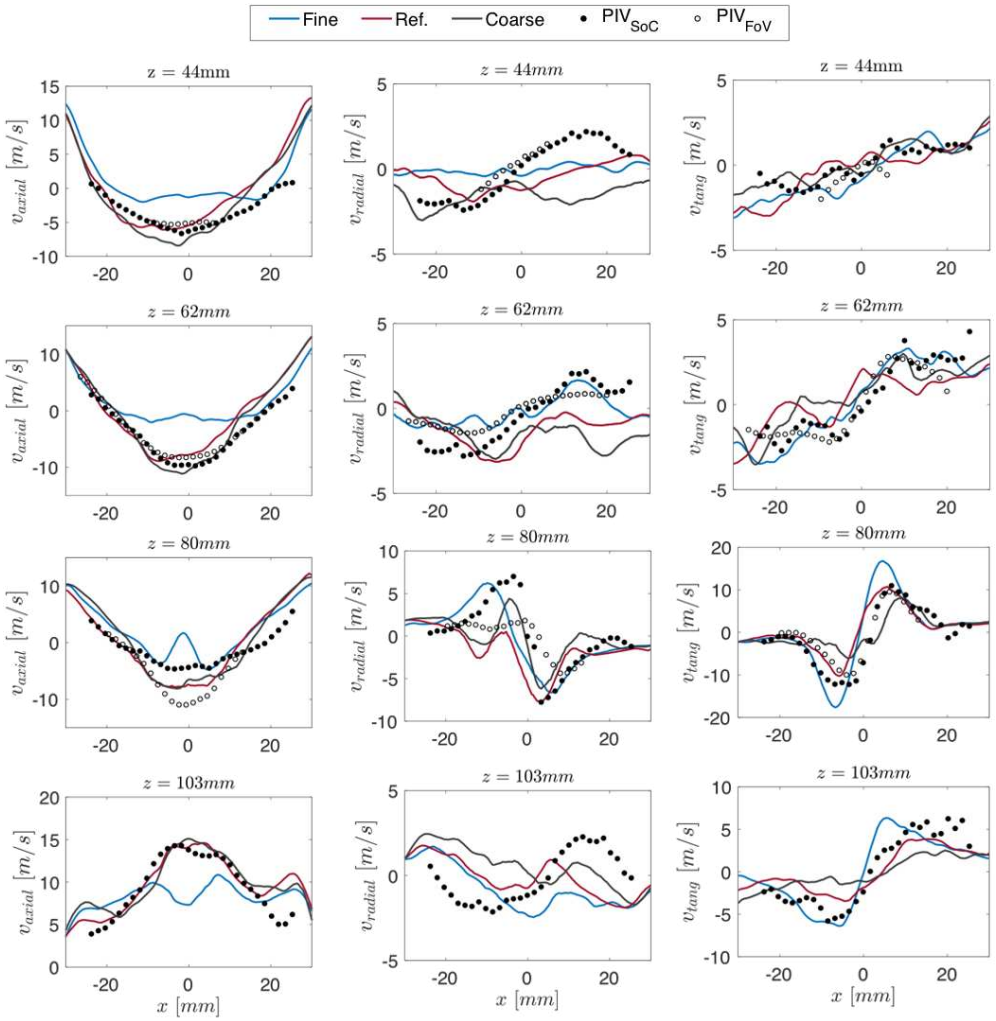

Figure 6.29: *Time-averaged velocity profiles under reacting conditions obtained with the three grids (fine grid in blue, reference grid in red and coarse grid in gray) compared to the experimental measurements (symbols - Geigle et al. (2017)) in the vicinity of the secondary zone (40 < z < 80 mm).*

The turbulence intensity, shown in Figs 6.31 - 6.32 in terms of resolved RMS velocity, is globally well captured for all grids in the primary combustion zone (z = 4, 18 and 26 mm in Fig. 6.31) and downstream (z = 44, 62, 80 and 103 mm in Fig. 6.32) for axial and radial components. However, the tangential component is underpredicted in the IRZ (z = 18 - 62mm). For the coarse and reference grids, this underprediction is associated with the stronger reverse flow, which interacts with the swirling flow. By comparing the different numerical results, it can be noted that the fine grid predicts lower RMS velocity in the IRZ (z = 26, 44 and 62 mm). This is ascribed to the moderate reverse flow, which is a source of unsteadiness in the IRZ. Downstream, in the close vicinity of

the secondary injection (z = 62 - 103 mm), the turbulence level is very similar between grids.

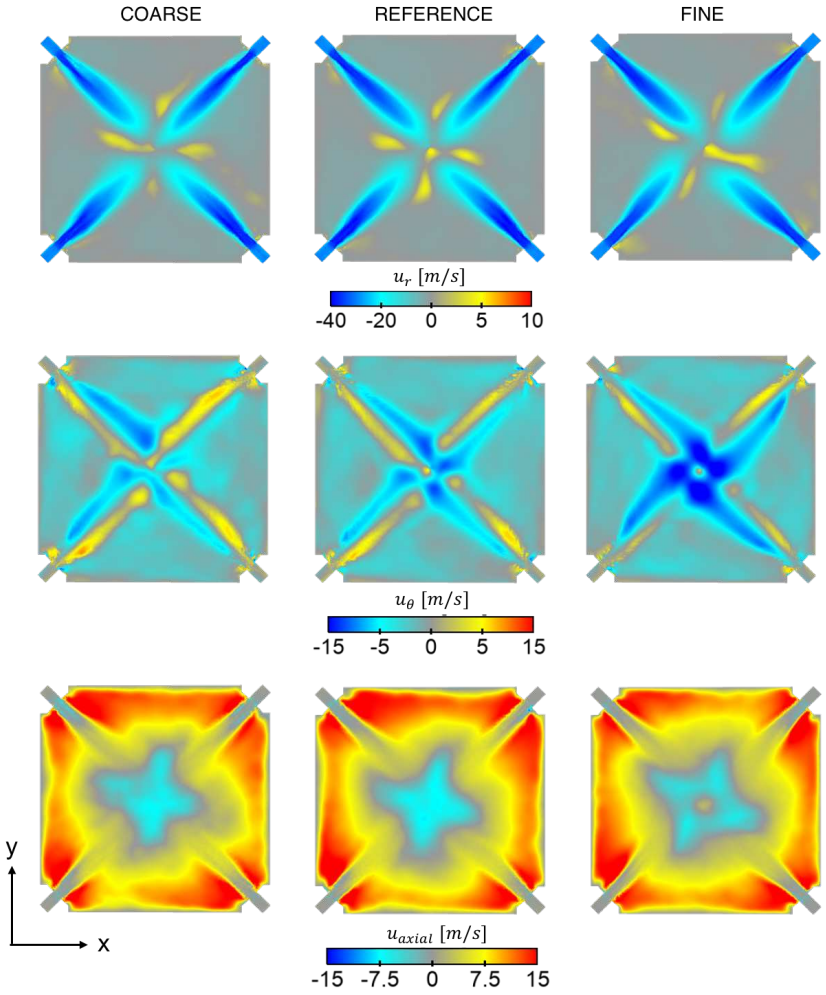

Figure 6.30: *Time-averaged velocity fields (u_r radial, u_θ tangential and u_{axial} axial velocities from the top to the bottom) a the secondary air injection plane (z = 80 mm) for the coarse, reference and fine grids, respectively.*

These results highlight the difficulty in numerically reproducing such a complex flow, notably the secondary injection flow. Considering the LES state-of-the-art of the DLR burner, the complexity of the flow and the experimental uncertainties, if each grid was considered distinctly, it could have been considered in good agreement with experiments, validating the numerical simulation but better agreement with experiments could result from numerical and modeling errors compensation, leading to reduced total errors (Vreman et al., 1996; Meyers et al., 2003; Vervisch et al., 2010). An additional CPU-expensive simulation

on an even finer mesh should be helpful but out of the scope of this thesis since it is related to the difficulty in numerically predicting jet in crossflow and not directly linked with the simulation of soot production.

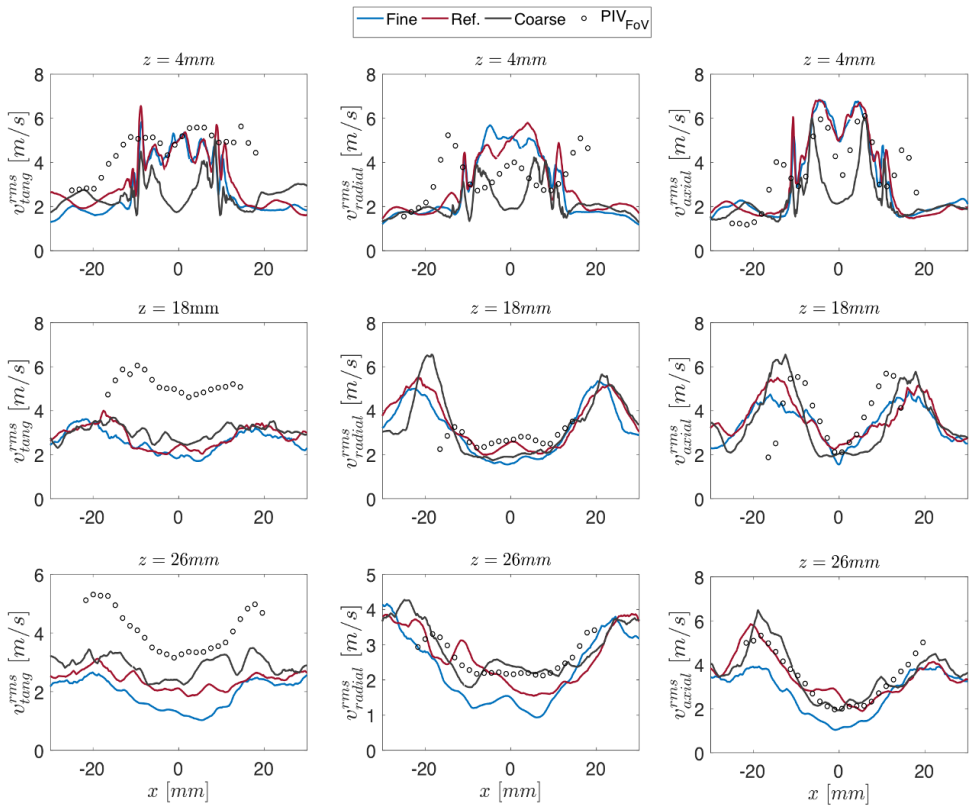

Figure 6.31: *Resolved rms velocity components profiles under reacting conditions obtained with the three grids (fine grid in blue, reference grid in red and coarse grid in gray) compared to the experimental measurement (symbols - Geigle et al. (2017)) in the primary zone ($z < 30$ mm).*

Temperature

The numerical time-averaged temperature fields for the three grids are compared in Fig. 6.33. Comparison with experimental measurements along the centerline is also shown in Fig. 6.33. All numerical flames are stabilized upstream compared to the experimental flame slightly lifted and stabilized few millimeters above the burner inlet. In specific, for the coarse grid, the flame stabilizes inside the central air injector with a narrow flame angle touching the lateral combustor walls, which can be explained by the high negative axial velocity within the IRZ leading to the flame dragging inside the injector. However, no flame flashback was experimentally reported in the DLR burner.

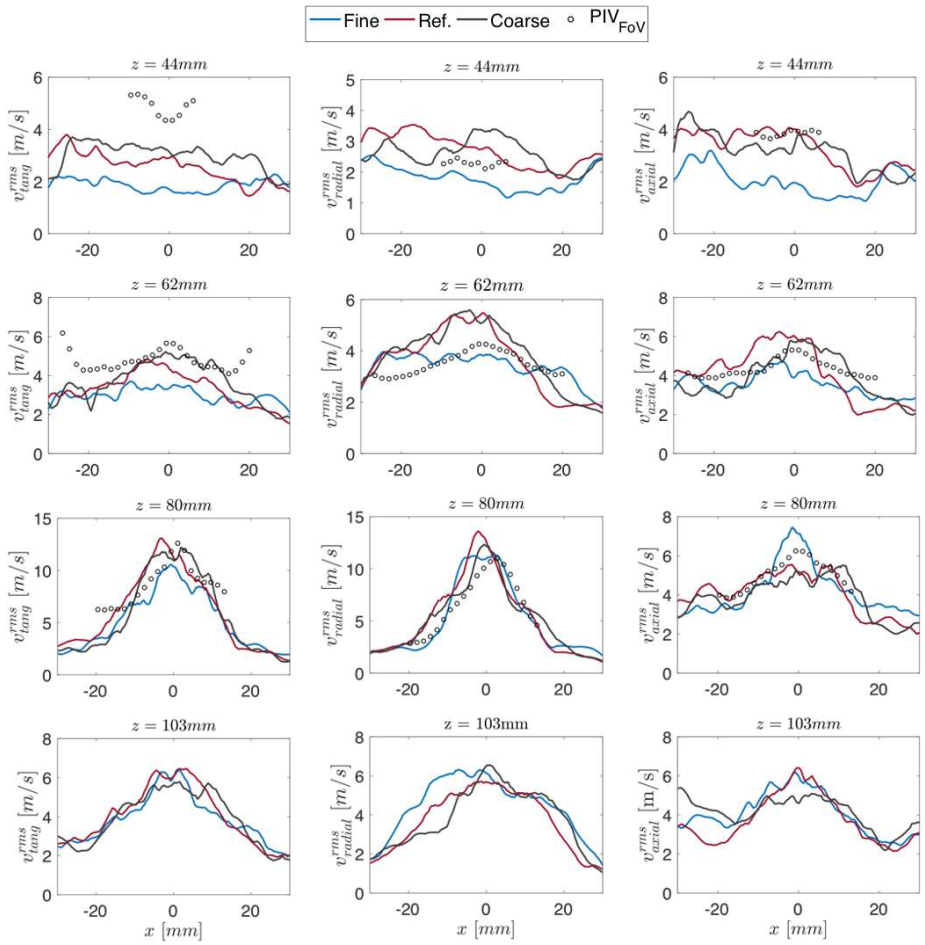

Figure 6.32: *Resolved rms velocity components profiles under reacting conditions obtained with the three grids (fine grid in blue, reference grid in red and coarse grid in gray) compared to the experimental measurement (symbols - Geigle et al. (2017)) in the vicinity of the secondary zone (40 < z < 80 mm).*

The observed instability is probably due to numerical issues. In the primary combustion and the post-flame zones, the fine grid predicts higher temperatures (about 10%) compared to the other grids, as highlighted by the black iso-line of T = 2000 K. The low reverse flow within the IRZ leads to a slow recirculation of lean burner gases explaining such difference. Downstream, in the middle of the chamber (z > 44 mm), as well as in the secondary oxidation zone, all grids provide excellent agreement with experimental values in the combustor centerline.

For more detailed interpretation, the radial numerical and experimental temperatures are compared for different axial positions along the burner centerline in Fig. 6.34. An overall agreement with experimental values is obtained for all

grids. The predicted temperature is within the experimental uncertainties for all positions, except for z = 3 mm, where the temperature is over-predicted by all grids, especially for the coarse grid since the flame is located inside the injector. For z = 18 - 44 mm, the fine and the reference grids predict similar temperatures, while the coarse grid predicts lower temperature for x > 15 mm, due to the extended flame brush. Downstream, at z = 62 mm, the reference and the coarse grids predict similar temperatures higher than the fine grid. Finally, at z = 80 mm, the reference grid predicts a high temperature than the other grids.

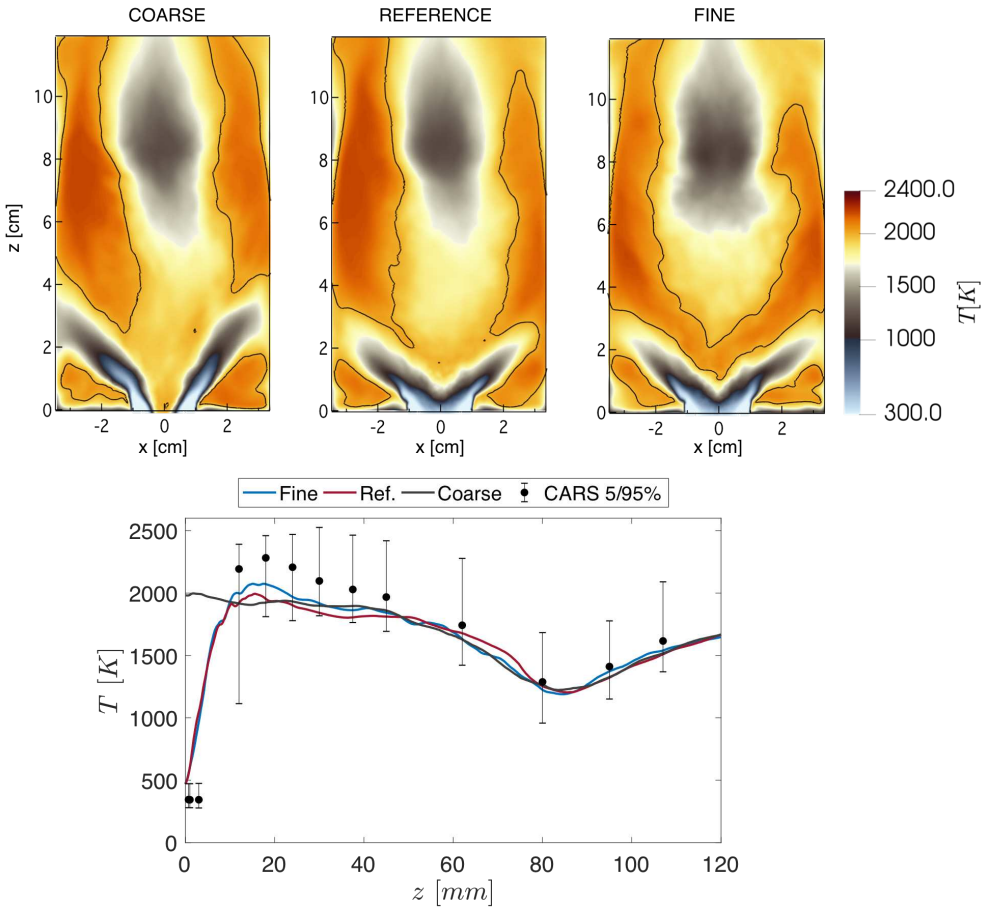

Figure 6.33: *Top: time-averaged temperature fields for the three grids (coarse, reference and fine from the left to the right) with the isoline of T= 2000 K. Bottom: temperature comparison along the burner centerline between grids (fine grid in blue, reference grid in red and coarse grid in gray) and experimental data (symbols - Geigle et al. (2015)).*

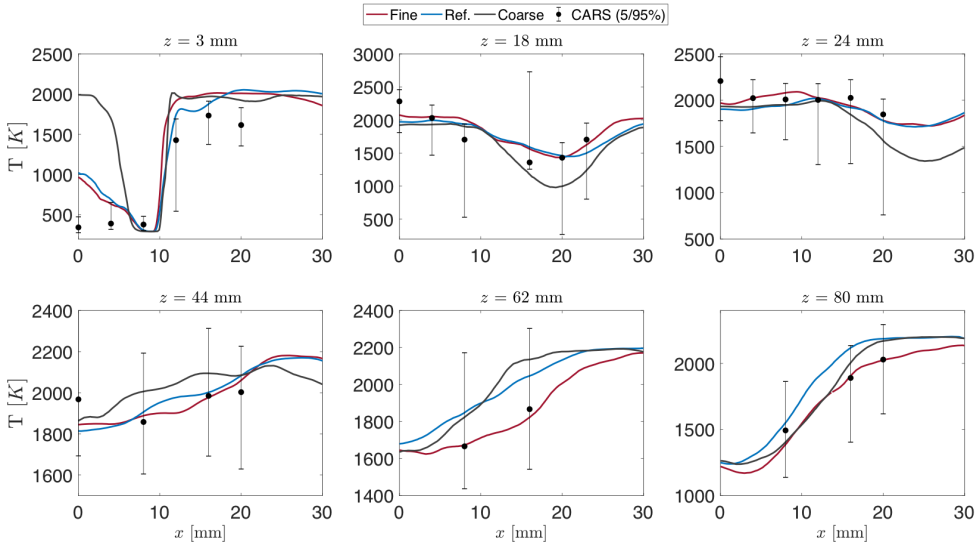

Figure 6.34: *Comparison of time-averaged radial profiles of temperature (fine grid in blue, reference grid in red and coarse grid in gray) and experimental data (symbols - Geigle et al. (2015)).*

The analysis of velocity and temperature reveals that the LES computations of the DLR burner is affected by the studied grid resolutions. Even if all grids capture the velocity field reasonably well in the primary zone, the secondary injection behavior is different for each grid. The coarse grid does not reproduce the experimental flame structure. Therefore, this grid is no longer considered in this work. Only the results from the fine and the reference grids are retained for the following analysis.

Mixture fraction

Figure 6.35 presents the time-averaged Z field with the iso-line of stoichiometric mixture $Z_{st} = 0.064$ for the fine and reference grids. The centerline Z profile predicted by both grids is also presented (Fig. 6.35 right). The centerline profiles are quite similar, with only small discrepancies in the primary zone (z $>$ 20 mm). The fine grid predicts a leaner mixture close to the stoichiometric value for z = 5 - 20 mm, while the reference grid presents a sharp profile in this zone. The 2D fields show that the primary mixing zone is slightly more compact in the reference grid than the fine grid. In the reference grid, the secondary jet dynamics enhance the reverse flow in the IRZ, and lean gases are transported towards the primary zone and penetrate this zone, as discussed in Section 6.1. On the other hand, in the fine grid, the secondary jets are driven by the induced tangential motion resulting in a moderate IRZ motion leading to lower recirculated lean gases. In addition to these observations, it can be

noted that both computations present an asymmetric field, notably near the primary injection. The jet inflow flapping induces such asymmetry due to the effect of the precessing vortex core (PVC) in the shear layer's vicinity inducing local rich-fuel pockets through unsteady jet inflow break down, as previously discussed in Section 6.1.

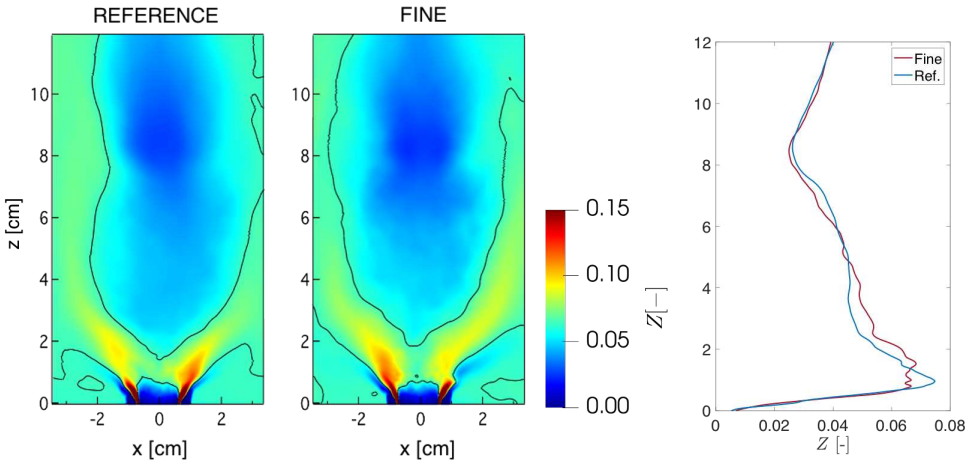

Figure 6.35: *Time-averaged mixture fraction fields for the reference and fine grids with the black line corresponding to the iso-line of stoichiometric mixture $Z_{st} = 0.064$. Mixture fraction profiles along the burner centerline for the fine (red line) and reference (blue line) grids are shown in the right.*

Mixing also occurs at the subgrid scale. Accordingly to the β-pdf model, used to account for subscale mixing processes, the effect of the turbulence on mixture fraction at the subgrid-scale is represented by the segregation factor, defined as the normalized mixture fraction variance (see Chapter 1). Therefore, when $S_z = 0$, the variance is null, meaning that the reactants are perfectly mixed, and the combustion subgrid model is not applied. On the contrary, when $S_z = 1$, the variance is maximum, and the subgrid-scale model is applied. Figure 6.36 shows a typical instantaneous (top) field and the time-averaged (bottom) segregation factor for each numerical grid. In the IRZ and secondary injection, S_z is close to zero since mixing in these zones occurs between combustion products and the air from the second injection stage. Then no subgrid combustion model is applied. In the primary zone, fuel and air are injected separately, the segregation factor presents strong fluctuations, revealing the mixing processes between air and fuel. Even if the resolution is quite similar between the fine and the reference grids, the mixing seems to occur slightly downstream for the reference case, which might explain the difference in the thickness of the mixing-reaction zone (Fig. 6.35).

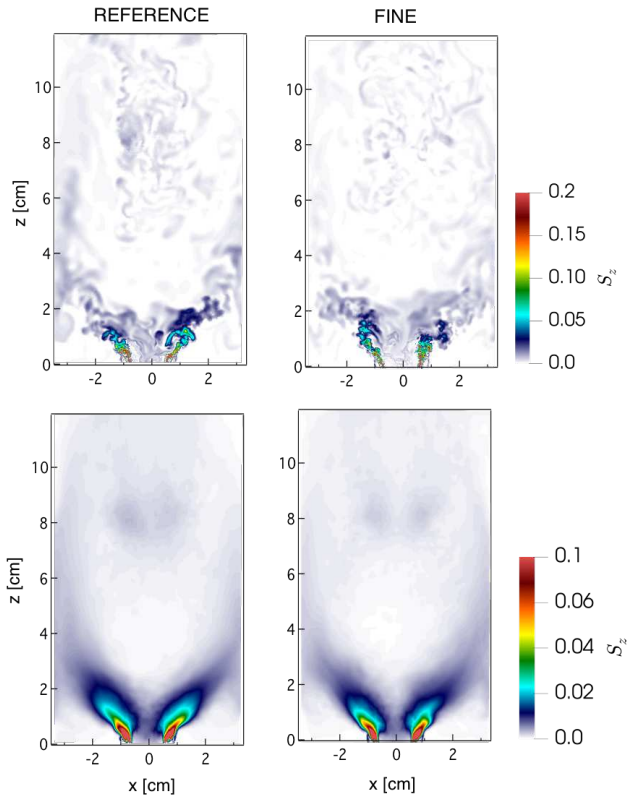

Figure 6.36: *Instantaneous (top) and mean (bottom) segregation factor for the reference (left) and fine (right) grids.*

6.3.3 Analysis of the probability density function

An overview of the local instantaneous flame behavior is obtained here by comparing temperature (Fig. 6.37) and mixture fraction (Fig. 6.38) probability density function (pdf). For the temperature, the experimental pdfs are also considered. At the centerline (x = 0 mm) for z = 3 mm (Fig. 6.37a), both grids predicts similar temperature events. Compared to the experimental pdf, higher temperature events are observed in both grids, revealing that the flame position is lower than the experimental one and it is oscillating as an effect of the PVC, as already discussed in Section 6.2 for the reference grid. The mixture fraction pdf (Fig. 6.38a) is mostly representative of unburned gas for both grids. Downstream, at z = 12, 18 and 24 mm (x = 0 mm - Fig. 6.37b-d) for both grids, the numerical temperature pdfs are shifted towards lower temperatures compared to the experimental pdf. The over-prediction of radiative heat losses due to the optically thin assumption used in this simulation (Rodrigues, 2018) may explain this under-estimation. For the reference grid, even lower temperature events are observed due to the secondary injection impact in the gas

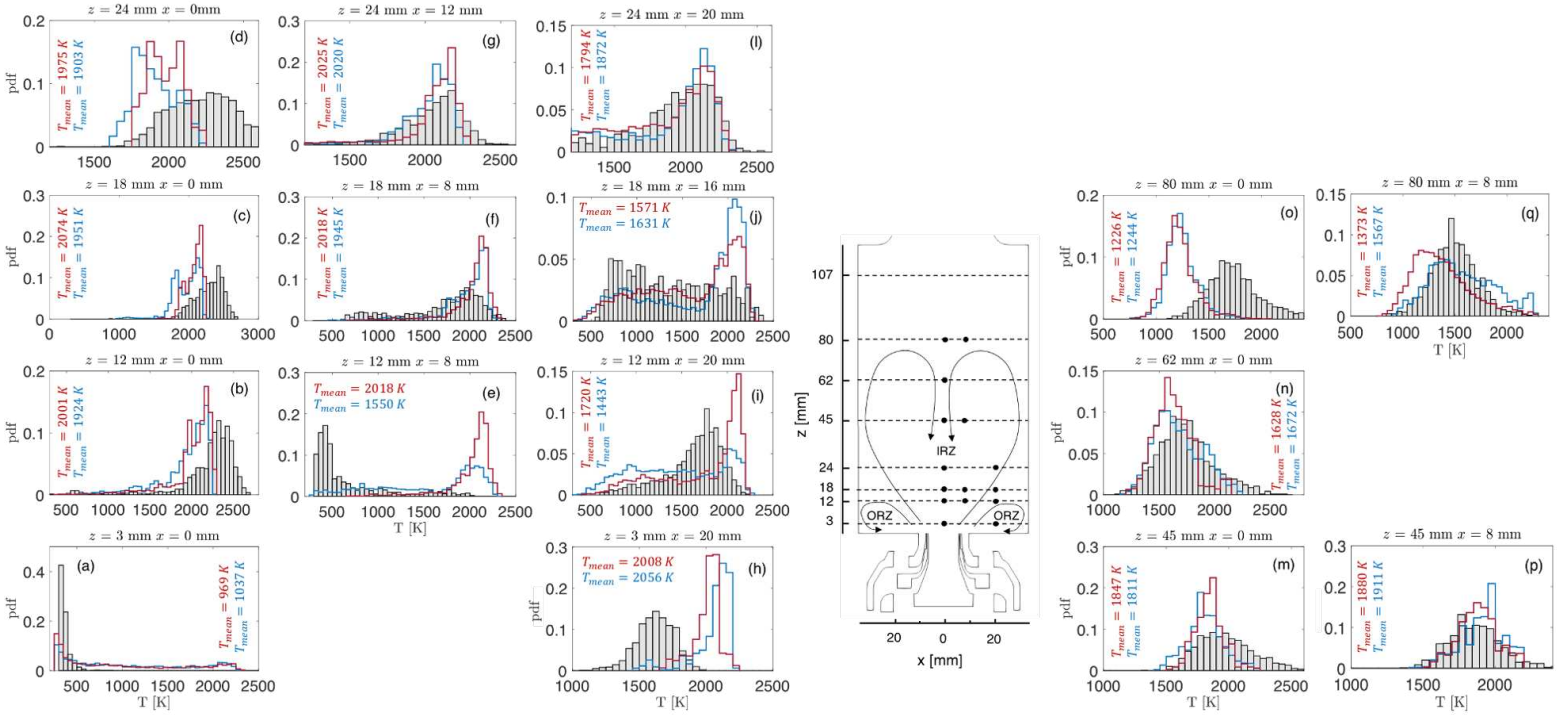

Figure 6.37: *Temperature probability density function for the fine grid (red) and reference grid (blue) compared to the measured temperature probability density function (gray - Geigle et al. (2015)). The locations where the pdf are compared are indicated in the schematic illustration of the DLR burner (in the center of the figure).*

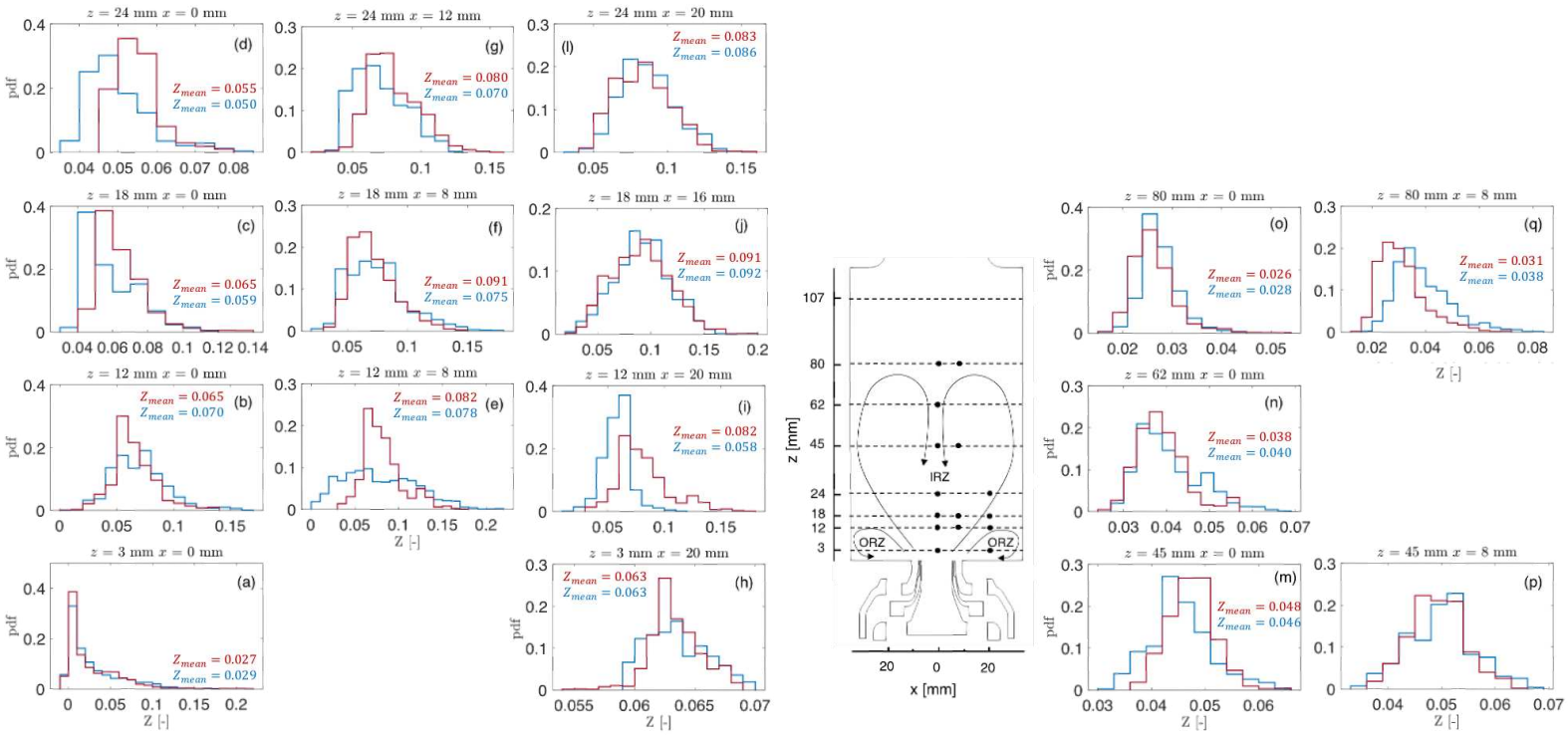

Figure 6.38: *Mixture fraction probability density function for the fine grid (red) and reference grid (blue). The locations where the pdf are compared are indicated in the schematic illustration of the DLR burner (in the center of the figure).*

recirculation into the IRZ, leading to mean values lower than for the fine grid. The mixture fraction pdf confirms this (Fig. 6.38b-d), showing that the reference grid predicts leaner mixture fraction events than the fine grid. Downstream, at z = 45 mm and x = 0 mm (Fig. 6.37m and 6.38m) in the upper part of the IRZ and in the vicinity of the secondary zone at z = 62 and 80 mm (x = 0 mm - Fig. 6.37n-o and 6.38n-o) the gas composition is leaner and more homogeneous than in the primary injection for both grids as revealed by mixture fraction distribution. The predicted temperature distribution is in good agreement with the experimental one for both grids for z = 45 and 62mm, but for z = 80 mm numerical pdfs display slightly narrow distributions shifted towards lower temperatures.

Outside the centerline at z = 80 and 45 mm (x = 8 mm - Fig. 6.37p-q), temperature pdfs are in good agreement with experimental ones for both grids, but the temperature pdf from the fine grid is slightly shifted towards lower temperatures. The mixture fraction pdfs are quite similar between grids for z = 45 mm, while for z = 80 mm, the pdf is slightly shift towards rich mixture fraction for the reference grid. This differences is ascribed to the different description of the secondary injection with impacts the IRZ behavior. Upstream at z = 24 mm (x = 12 and 20 mm, respectively in Fig. 6.37g and Fig. 6.37l), both grids present quite similar temperature and mixture fraction pdfs. The temperature pdfs are in quite good agreement with the experimental one. At z = 18 mm x = 16 mm (Fig. 6.37j), the temperature fluctuation due to the intermittent flame presence, is reasonably well captured by the simulations, but numerical pdfs predict high temperatures events, notably the reference grid. At this position both grids predict similar pdfs. At z = 18 mm x = 8 mm both temperature and mixture fraction pdfs are similar between grids, and the temperature distribution are in good agreement with the experimental one, even if simulation predicts more high temperature events. At z = 12 mm x = 8 mm (Fig. 6.38e), both grids present a poor agreement with experimental distribution, high-temperature events are numerically predicted while experimental pdf presents an opposite behavior. Such discrepancies might be due to the flame position, which is predicted slightly upstream by the simulations compared to the experimental position. The mixture fraction pdf (Fig. 6.38f) shows that mixture fraction events are mainly at the stoichiometric value ($Z_{st} = 0.064$) for the fine grid, while the reference grid predicts a broader distribution. At z = 12 mm and x = 20 mm (Fig. 6.37i), when compared to the experimental pdf, both grids predict higher temperature events but the fine grid predicts higher temperatures than the reference grid. The mixture fraction pdfs (Fig. 6.38i) shows that the stoichiometric value characterizes the fine grid ($Z_{st} = 0.064$), suggesting that the flame is intermittently present at this position. In contrast, for the reference grid, a broader distribution is predicted with mixture fractions events higher than Z = 0.1. At z = 3 mm and x = 20mm (Fig. 6.37h), localized in the ORZ, the temperature pdfs agreement with the experimental pdf is not

satisfactory. Both numerical calculations predict higher temperature events, whereas mixture fraction is quite similar (Fig. 6.38h). Such high-temperature events are probably an effect of the thermal boundary condition. The thermal wall conditions are known to affect the flame stabilization, and it can even induce flame topology changing (Guiberti et al., 2015; Rodrigues, 2018). It should be reminded that the experimental temperature imposed on bottom wall is 650 K but presents an uncertainty of about +/- 100 K (private communications with DLR). An over-prediction of the bottom wall temperature may explain the hotter ORZ and the lower flame position.

The analysis of temperature and mixing probability density function shows that the flames statistically behave differently for the two grids, especially for $z < 24$ mm, i.e., where soot is mainly produced. It can then be expected that soot prediction will be affected since soot production is strongly correlated to the local flow conditions, as discussed in the previous section for the reference grid. This point will be investigated in the following also for the fine grid. Additionally, the discrepancies with the experimental measurements are quite significant for both grids. It should be pointed out that the simulations and experiments do not consider the same range of length scales due to the different grid and experimental resolutions. The considered subgrid scales models may differently affect the numerical results. Additionally, simulation considers only a few ms while experiments are based on more extensive physical time.

6.3.4 Soot statistics

Figure 6.39 shows the time-averaged fields of number density of particles (N_p) and soot volume fraction (f_v) for the fine and reference grids. Globally, the maximum values of N_p and f_v are quite similar between grids. Both soot fields are asymmetric for the two grids, but with opposite sides, in analogy with the results for the mixture fraction distribution (Fig. 6.35). Compared to the measured soot volume fraction, both grids underpredict the soot load by a factor about 6.

As shown in the previous section, the particle number density is related to the gas phase through the PAH concentration that presents a more homogenous spatial distribution than soot volume fraction, as in the experimental observations (Geigle et al., 2015; Helou et al., 2020). Figure 6.40 shows the PAHs fields obtained numerically and experimentally. Geigle et al. (2015) provided information on PAH concentration considering two (A2) to four-rings (A4) species. The measured PAHs are mainly found in the lower part of the combustor in the inner and outer shear layer, as shown in Fig. 6.40. The experimental asymmetric field was explained by laser absorption (Geigle et al., 2015). In the simulations, A2 and A4 species are mainly located in the inner shear layer. However, large soot precursors are numerically predicted in the outer/inner shear-layers and

along the wall, as shown by the A7 (aromatic species with seven rings) field in Fig. 6.40. Therefore, large soot precursors seem to be essential to retrieve soot nucleation along the chamber walls. However, OH is also found along the wall. Consequently, the competition between oxidation and nucleation/condensation determines the soot concentration in this zone as already shown in the previous section. The fine grid predicts slightly high PAH concentration than the reference grid, but it is globally similar between grids explaining the similarity obtained for N_p. This result is in opposition to the numerical observations from Chong et al. (2018). According to these authors, PAH concentration decreases with grid resolution due to its sensibility to the scalar dissipation rate. However, a direct comparison between the current simulations and the literature is not trivial since the used gaseous and soot models, the numerical methods and the grids are quite different.

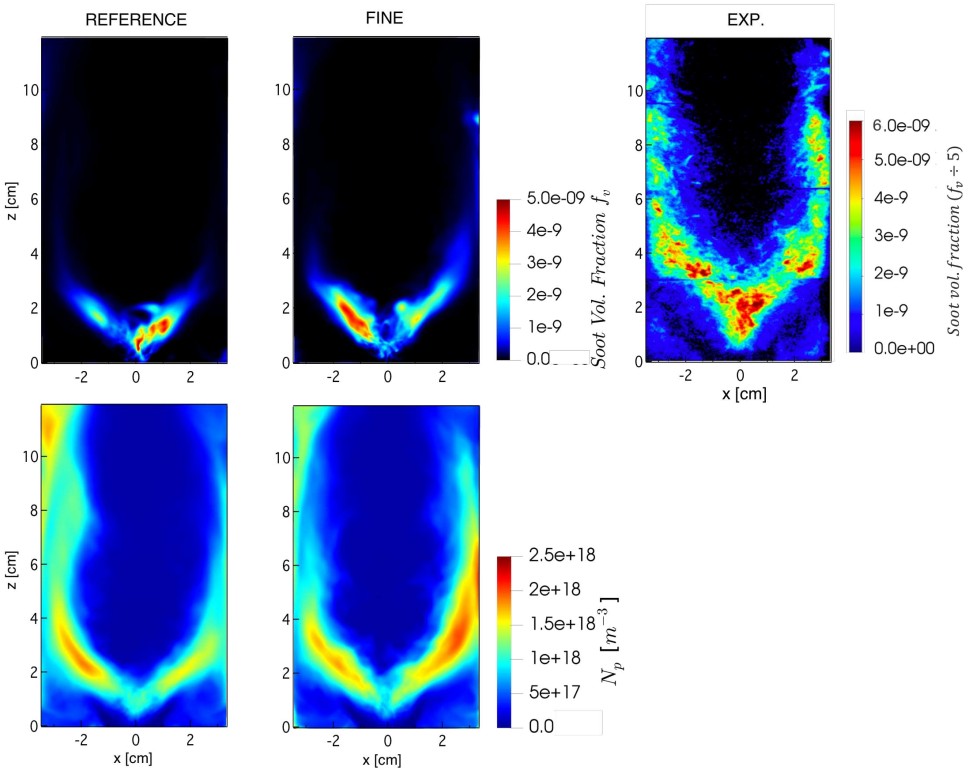

Figure 6.39: *Time-averaged fields of soot volume fraction f_v (top) and the particle number density N_p (bottom) for the reference and fine grids. The experimental soot volume fraction (Geigle et al., 2013), (ISF, 2019) field is shown on the right.*

The radial profiles of f_v in Fig. 6.41 provides additional information on the f_v spatial distribution. At z = 4 mm, the soot volume fraction is underpredicted by a factor 2 in the center of the IRZ for both grids. At z = 10 mm, whereas

the reference grid still predicts soot in the center of the IRZ, the f_v

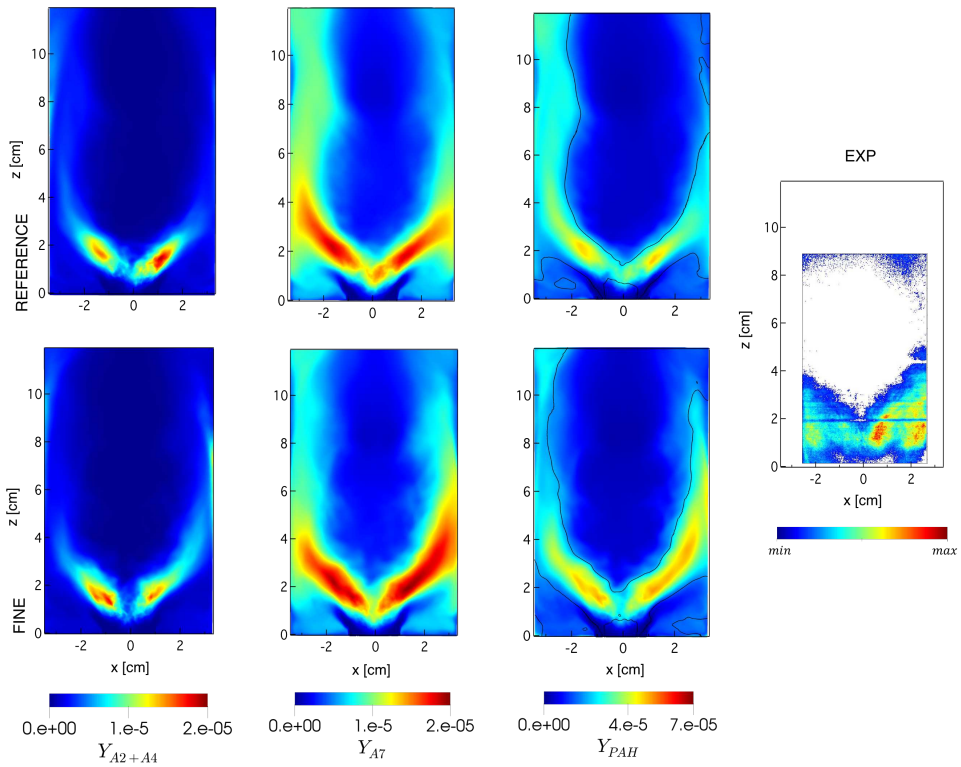

Figure 6.40: *Time-averaged fields of PAH species mass fraction (A2+A4, A7 and the transported lumped PAH from the left to the right) for the reference (top) and fine (bottom) grids. Experimental PAHs field from Geigle et al. (2015) is shown on the right.*

profile starts to open in the mean V-shape for the fine grid but the reference grid presents a qualitative better agreement with experiments. At this position, both grids underpredict the experimental f_v value by a factor 5. At z = 12 mm, both grids predict soot in the inner shear layer, while experiments present a one peak profile centered in the combustor's axis until z = 26 mm. At z = 24 mm, soot volume fraction decreases significantly in the simulation, with a factor 10 between the fine grid and experimental profiles and a factor about 20 for the reference grid. Downstream, at z = 45 mm, the soot concentration is higher for the fine grid compared to the reference grid. At the same time, compared to the experimental profiles, soot is rarely predicted by the simulations. Only small nascent particles are found, suggesting a lack of physical description of soot production in this configuration. This feature is currently observed in the literature (Franzelli et al., 2015; Felden et al., 2018; Grader et al., 2018). A possible explanation is an overestimation of the oxidation ratio used in the model whose reaction constants are based on an empirical reaction

efficiency (El-Leathy et al., 2002; Xu et al., 2003), estimated from a co-flow laminar diffusion flame. The use of empirical parameters can lead to unphysical behavior. In the future, a sensibility analysis of the oxidation reaction efficiency could be interesting to evaluate the impact of the oxidation model on soot prediction in the DLR burner. Complementary, in the SOPRANO project framework, the DLR team is currently experimentally studying the oxidation process (Bierkandt et al., 2019). It will hopefully bring a new insight into it to help the modelers in the future. Another possible explanation could be attributed to the limitations of the turbulent combustion models and the description of the thermochemical space.

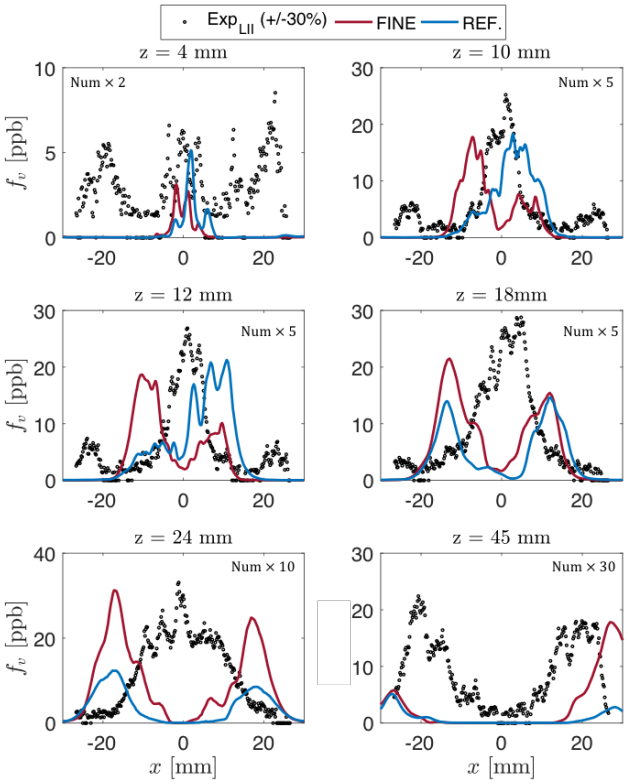

Figure 6.41: *Comparison of time-averaged soot volume fraction radial profiles between the two grids (fine in red and reference in blue) and experimental data (black symbols - (Geigle et al., 2015)) for different heights above the burner. For sake of visualization, the numerical results are multiplied by different factors, as indicated on the top of each graph.*

The discrepancies in the temperature and mixture fraction fluctuations might partially explain the discrepancies between the two computations at these positions. Figure 6.42 shows the temperature, mixture fraction, number particle density and soot volume fraction pdfs conditioned by soot presence ($f_v > 1$

ppb) at four different locations in the sooting zone where large discrepancies in soot volume fraction prediction are observed between computations. As already discussed in the previous section, soot is highly correlated to the gaseous quantities, notably the mixture fraction. The mean mixture fraction is about 0.1 for all locations for both grids (see Table 6.4). The conditioned mean temperature presents larger discrepancies (see Table 6.4) between the two grids with ΔT = 173, 93, 81 and 26 K for z = 3, 12, 18 and 24 mm, respectively. The pdf of particle number density presents a high variability between grids in response to the temperature and mixture fraction discrepancies. Instantaneous values of soot volume fraction f_v is mainly lower than 5 ppb. At z = 3 and 18 mm, the mean f_v is quite similar between the two grids while it strongly differ between grids for z = 12 and 24 mm (see Table 6.4). The soot intermittency, defined as the probability to found $f_v > 1$ ppb, is quite different between grids at the four considered probes, as shown in Table 6.5. This suggests that soot particles experience different thermochemical conditions (temperature and gas composition) along the flow pathlines leading to different probabilities of soot occurrence, eventually to different total soot production.

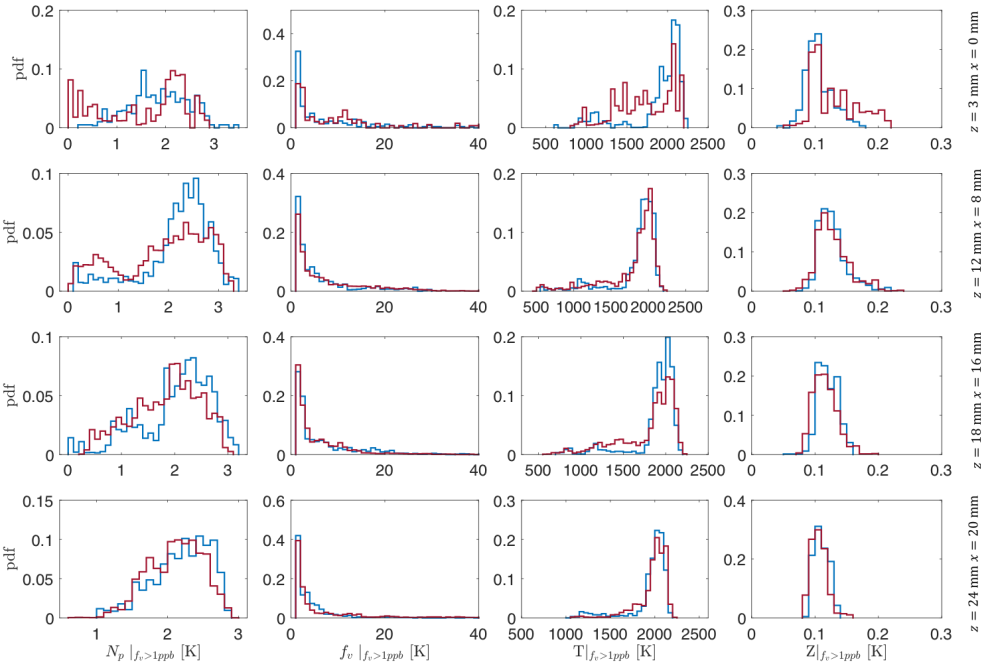

Figure 6.42: *Temperature, mixture fraction, number density of particle and soot volume fraction pdfs conditionned by the presence of soot ($f_v > 1$ ppb) at four different locations in the sooting zone for the fine (red) and reference (blue) grids.*

Table 6.4: *Gaseous and soot time-averaged values conditioned by the presence of soot (f_v > 1 ppb) at different probes in the sooting zone. Blue values for the reference case and red values for the fine case.*

z | x [mm]	T$\|_{f_v>1ppb}$ [K]		Z$\|_{f_v>1ppb}$ [-]		f_v $\|_{f_v>1ppb}$ [ppb]	
	REF. GRID	FINE GRID	REF. GRID	FINE GRID	REF. GRID	FINE GRID
3 | 0	1889	1716	0.10	0.13	12.2	12.9
12 | -8	1844	1791	0.12	0.12	6.0	10.0
18 | -16	1883	1802	0.12	0.11	7.3	7.0
24 | -20	1952	1978	0.11	0.10	4.5	7.4

Table 6.5: *Soot intermittency obtained with the reference and fine grids.*

z | x [mm]	FINE GRID	REF. GRID
3 | 0	3.80%	9.87%
12 | -8	34.27%	18.63%
18 | -16	32.78%	24.46%
24 | -20	23.42%	20.46%

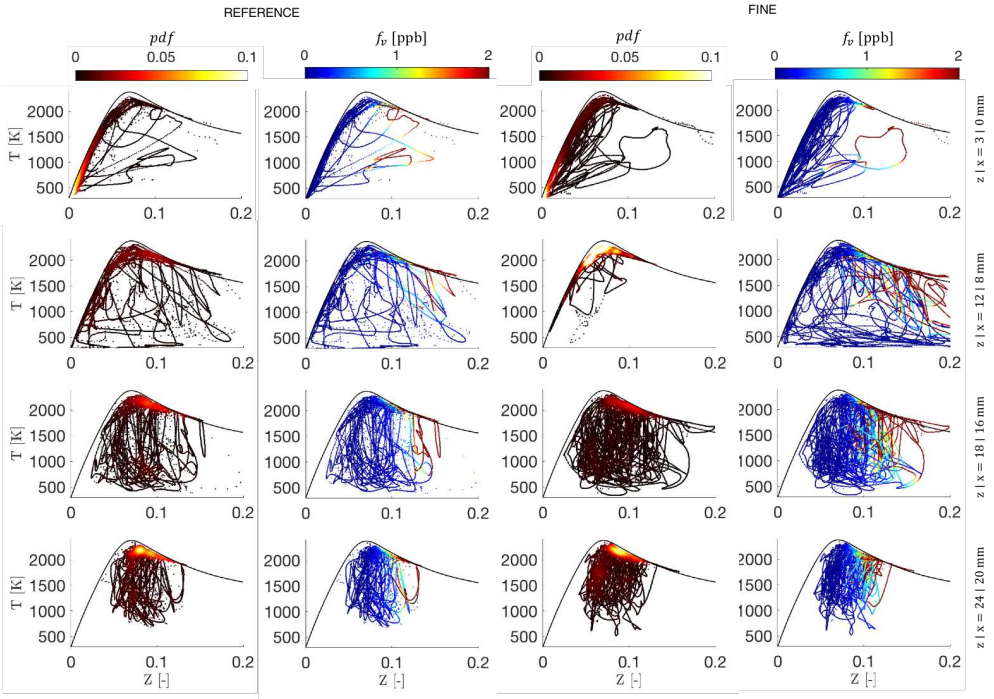

Figure 6.43: *Scatter plot of temperature in the mixture fraction space colored by the joint T-Z probability density function (first and third columns) and colored by f_v (second and fourth columns) for the reference (left) and fine (right) grids.*

Figure 6.43 shows the scatter plots of temperature in the mixture fraction space for the same locations of the pdfs colored by the joint T-Z pdf. Statistically, the thermochemical states accessed in both grids are quite similar. However, soot is present in some distinct rare thermochemical states which are not necessarily accessed in the same way in the two simulations, as shown in the scatter plots colored by f_v. These events are characterized by relatively high temperatures and mixture fraction as already observed in the pdfs in Figs. 6.42 and seem to be differently accessed by the two grids. Such rare thermochemical conditions could explain the high soot intermittency and low soot load in this configuration, as already discussed in Section 6.2. However, as discussed in Section 6.2, it is important to remind that such discrepancies may be also due to a lack of statistical convergence of the solid phase.

6.4 Conclusion

In this chapter, a statistical analysis of the LES simulation of the DLR burner was discussed. It was found that reaching a statistical convergence is challenging due to the presence of unsteady large flow structures, which affects soot production. Three unsteady phenomena have been identified in the DLR burner. First, a coherent large-scale instability, typical of swirling flows, known as precessing vortex core (PVC), was characterized via a power density spectrum. This coherent structure affects the mixing in the primary combustion zone through the inflow fuel jet's roll-up. Besides, the PVC drives the root flame position that oscillates near the burner inlet. Second, the secondary air dynamics characterized by an unsteady interaction between the radial jets induce an intermittent localization of the root of inner recirculation zone. In opposition to the PVC, the jet dynamics do not behave as a coherent structure. It is likely characterized by a low frequency, whose quantitative characterization is not straightforward with the available statistics. More computation time may be necessary to characterize the unsteady interaction between the secondary jets, which is out of the scope of this work. Finally, the turbulence effect on soot production introduces additional difficulty to get statistical convergence of soot quantities.

It was found that statistics based on 40 ms are sufficient to reproduce the main reactive flow characteristics. However, convergence is more challenging to reach concerning the prediction of the IRZ and secondary air injection. This is because the IRZ is affected by the downward flow contribution from the intermittent secondary jets. However, 60 ms is sufficient to obtain a statistical convergence of the gaseous phase. On the contrary, soot fields require a longer averaging time due to their intermittent nature strongly dependent on time flow history. The statistical convergence of the gas phase does not assure the convergence of soot volume fraction, which is very sensitive to local reactive

flow fluctuations since only rare thermochemical states lead to soot production occurrence.

The sensitivity of soot and gaseous scalars on grid resolution was also investigated in this chapter by performing LES simulations on three numerical grids with different spatial resolutions. The comparison between grids shows that the three grids correctly describe the swirl flow structure in the primary zone. In contrast, the mesh resolution impacts the flow dynamics description in the secondary air injection affecting the IRZ motion. The strength of the IRZ decreases when grid resolution increases, affecting mixing until the primary combustion zone. The stronger IRZ in the coarse grid induces a non-physical flame instability and flashback due to the substantial reactant dilution for the coarse case. Then, only the results from the fine and the reference grids were compared. The time-averaged soot field analysis shows that the soot load is quite similar between fine and reference grids. However, a different spatial distribution is observed which is correlated with the mixture fraction field affected by the PVC motion and the propagation of the lean gases in the primary zone.

It worth to be mentioned that LES uses a spatial filter based on the mesh size so that it is intrinsically sensitive to the mesh resolution and numerical errors (Pope, 2004). Even though subgrid models should cover the unresolved scales, results dependent on the grid resolution may indicate that the subgrid models retained in this work may have to be improved for gas turbine flows, notably when a secondary air dilution is accounted for. It should also be taken into account that numerical errors and the artificial numerical viscosity equally depend on grid resolution, and they can strongly impact the results. Thereby, characterizing the dependence of the results on grid resolution is highly recommended and should be systematically performed to quantify the reliability of the LES results for sooting turbulent flames. Therefore, the current study provides precious support for LES simulation and data interpretation in the forthcoming chapters. Although the observed highly unstable secondary jet dynamics observed in the reference grid, this grid is retained in the following since the mean reacting flow features are quite well reproduced for a reduced CPU cost compared to the fine grid.

Finally, it should be recognized that the intrinsic complexity of this configuration complicates the soot modeling evaluation. The case without the secondary injection may be preferred in the future as reference case to overcome the difficulty in simulating the secondary jet dynamics.

Chapter 7

Impact of the HACA-RC* model in a LES of the DLR burner

This chapter investigates the effects of the HACA-RC surface reactions model, previously introduced in Chapter 3, when used in the LES of the DLR burner. This configuration operating at technically relevant conditions has been broadly used to evaluate soot models (Gallen et al., 2018; Felden et al., 2018; Franzelli et al., 2018; Chong et al., 2019). Its complex flame structure, presenting multiple combustion regimes, makes this configuration a good candidate to evaluate the effect of the HACA-RC* model, developed to account for soot production in both premixed and diffusion flames. Besides, surface reactions were found to be the principal soot mechanism in the DLR burner (Chong et al., 2019). Then two LES simulations of the DLR burner, one with the reference HACA-RC model and another with the new HACA-RC*, are performed. First, in Section 7.2, an a priori analysis on the impact of the model in turbulent conditions is carried out based on the local flame structure. Then, the effect of the new model on the prediction of the global soot quantities (f_v and N_p) is presented in Section 7.3. By considering the coupling between soot and gas phase, the gaseous variables (axial velocity, temperature and mixture fraction) are also investigated. Finally, the soot source terms are compared, and differences between simulations are discussed. Part of the discussion presented in this chapter has been published as: "Impact of the reaction mechanism model on soot growth and oxidation in laminar and turbulent flames", in Proceedings of ASME Turbo Expo 2019: Turbomachinery Technical Conference and Exposition.*

Contents

.

7.1 Introduction

The numerical prediction of soot production, i.e., the net product of formation and destruction phenomena, in applied systems, is essential but particularly challenging for many reasons. First, the involved processes, i.e., nucleation, condensation, surface growth, oxidation and coagulation, are complex with a heterogeneous nature that is still not entirely well understood even under laminar conditions. Second, most technical devices often work under specific operating conditions, leading to multi-regime combustion (premixed and non-premixed). This makes the problem extremely complex since the soot model has to reproduce soot production in both premixed and non-premixed regimes without any parameter fitting depending on the investigated case. Finally, the model has to be simple enough to perform Large Eddy Simulations (LES) of the industrial configurations in terms of CPU time.

Therefore, to perform LES of industrial configurations, it is essential to dispose of a model with the following characteristics: (1) it should provide a reasonable prediction of soot volume fraction in both premixed and diffusion flames and (2) it should be possible to consistently couple it with the state-of-the-art LES models, specifically with the tabulation technique. In this context, this work aims to show how relevant it could be for LES the modification of one of the soot processes models so that the description of laminar flames is improved. Among the different processes, a focus is put on the description of soot surface reactions since they can significantly contribute to the total soot mass yield in turbulent jet flame (Rodrigues et al., 2018) and in confined swirled flames (Chong et al., 2018; Mueller and Pitsch, 2013).

In Chapter 3, a model for the soot surface reactions mechanism, called HACA-RC*, was proposed to improve soot volume fraction prediction in laminar counterflow non-premixed ethylene-air flames by introducing a new reaction enhancing soot reactivity. Indeed, new zones of reactions are identified using CH_3

radicals in addition to the reference H species. When coupled with the sectional strategy (introduced in Chapter 1), the model was validated in different laminar premixed and non-premixed flames. In this chapter, the HACA-RC* is coupled with a three-equation soot model (described in Chapter 1), a more simple and lower CPU-demanding soot model.

The chapter is organized as follows. In Section 7.2, an *a priori* analysis based on instantaneous fields is performed as a first attempt to evaluate the impact of the HACA-RC* model in the soot prediction in the DLR burner. Then, in Section 7.3 *a posteriori* analysis of the time-averaged soot quantities and source terms from two LES simulations (with the reference model and with the HACA-RC* model) are carried out to evaluate the impact of the proposed model on soot prediction.

7.2 A *priori* analysis

In swirling combustors, where fuel and oxidizer are injected separately, as in the DLR burner, the flame structure is conditioned by the turbulent mixing between the reactants. However, perfect mixing is hardly reached, leading to local mixture inhomogeneities. Consequently, multiple burning regimes (premixed and non-premixed) often coexist (Masri, 2015). The local flame structure might impact soot prediction, particularly the soot surface growth, classically described by HACA-based models whose behavior in laminar flames depends on the combustion regime, as discussed in Chapter 2. Here, the response of the HACA-based models to the structure of the flame in turbulent context is analyzed.

A first attempt to characterize the reaction zone can be made by looking at the instantaneous OH field. Figure 7.1 compares the numerical instantaneous and time-averaged OH fields to instantaneous and ensemble-averaged OH intensity from OH-PLIF measurements (Geigle et al., 2015). Two strongly wrinkled OH-fronts (highest OH mass fraction in Fig. 7.1) can be distinguished in the instantaneous fields: the first flame front (FF1 indicated in the instantaneous numerical field in 7.1) is located near the burner injectors, and the second flame front (FF2 in 7.1) is located downstream in the inner recirculation zone. In the mean fields, the OH fronts are no longer distinguishable due to the intense wrinkling of the instantaneous OH fronts by the high turbulent flow in quite good agreement with experimental OH field.

The Takeno flame index (H. Yamashita and Takeno, 1996) is used here to characterize the flame structure and the combustion regime. The normalized Takeno flame index (Reveillon and Vervisch, 2005), defined Eq. (7.1), is used to identify zones burning in premixed or in diffusion regimes, based on the sign

of reactive species gradients.

$$I_T = \left(\frac{\nabla Y_O \cdot \nabla Y_F}{| \nabla Y_O \cdot \nabla Y_F |} \right)_{\dot{\omega}_{Y_C} > \epsilon} \tag{7.1}$$

where ∇Y_F and ∇Y_O are the mass fraction gradients of fuel and oxygen respectively. Then positively aligned gradients correspond to the premixed flame ($I_T = 1$) while the opposing gradients denote the diffusion flames (I_T = -1). In order to highlight the burning zones by masking the values where only mixing is occurring, I_T is conditioned by the source term of progress variable $\dot{\omega}_{Yc}$, which represents the heat release ($\dot{\omega}_{Y_C} > \epsilon$ with $\epsilon = 1.0\ s^{-1}$).

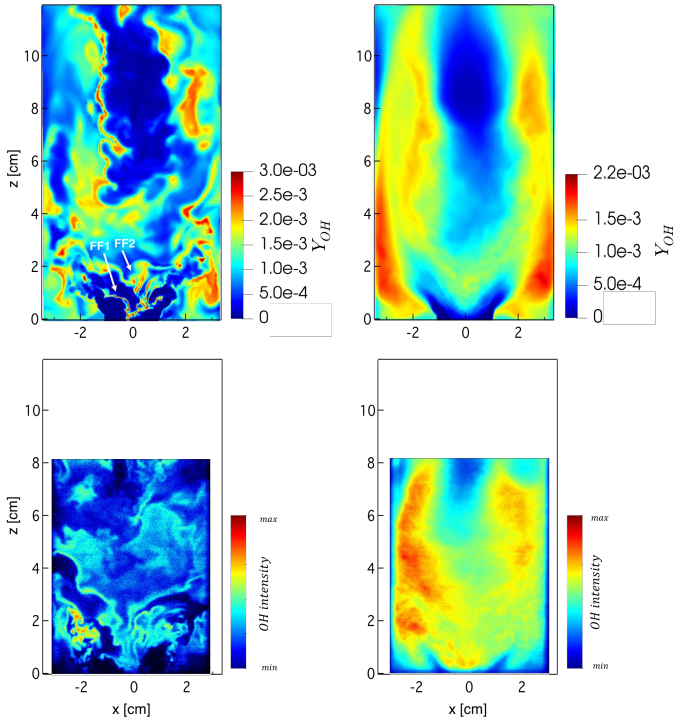

Figure 7.1: *Comparison of instantaneous (left) and mean (right) OH fields numerically predicted (top) and experimentally measured (bottom - Geigle et al. (2015)) at the combustor mid-plan. The double OH fronts FF1 and FF2 are indicated in the instantaneous OH fileds.*

The instantaneous and time-averaged Takeno's index is represented in Fig. 7.2. Both premixed (blue regions) and non-premixed (red regions) combustion modes coexist, as already reported by Stohr et al. (2018) and Felden et al. (2018). The combustion structure presents a stratified reacting zone with three distinct burning layers. The first zone, very close to the injectors, is characterized

by a non-premixed flame, corresponding to the FF1 flame front in Fig. 7.1. Downstream, the swirling flow enhances the mixture between reactants, and a premixed regime establishes. Finally, the third zone is burning in the non-premixed mode, corresponding to the second OH front FF2 in Fig. 7.1. This second front results from the reaction between fuel-rich burned gases and the lean gases from the secondary injection. The existence of both combustion regimes suggests a wide range of mixture and their inhomogeneities in the thermochemical space, characteristic of partially-premixed flames (Masri, 2015).

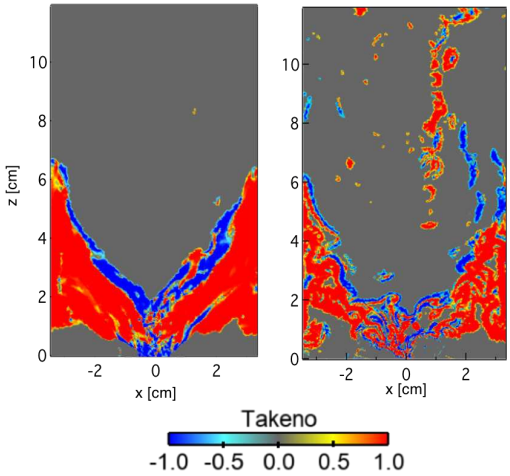

Figure 7.2: *Time-averaged (left) and instantaneous (right) Takeno index fields conditioned by the progress variable source ($\dot{\omega}_{Y_C} > \epsilon = 1.0s^{-1}$) term at the combustor mid-plan. Blue regions are burning in diffusion regime, while the red regions are burning in premixed regime.*

Scatters plots of temperature as a function of the mixture fraction colored by the normalized $\dot{\omega}_{Yc}$ and by I_T are shown in Fig. 7.3 for burning zone split in three regions: a black zone for $\dot{\omega}_{Yc} > 50s^{-1}$, a grey zone for $3s^{-1} < \dot{\omega}_{Yc} < 50s^{-1}$ and a blue zone where $1s^{-1} < \dot{\omega}_{Yc} < 3s^{-1}$. The stoichiometric mixture fraction $Z_{st} = 0.064$ (solid line), the global mixture fraction corresponding to the equivalence ration $\phi_g = 0.86$ (dotted line) and the injected mixture fraction corresponding to $\phi_{inj} = 1.2$ (dashed blue line) are also display. Also, the flamelet with the highest strain rate (dotted black line) and the adiabatic equilibrium state (solid black line) are shown. In general, the scatter plots present a significant variation of temperature in the mixture fraction space, reflecting a large variability of thermochemical states due to the unsteady mixing typical of gas turbine combustors (Ax et al., 2010; Meier et al., 2010; Boxx et al., 2010; Stopper et al., 2013). The non-perfect mixing leads to the existence of a non-reacted mixture at low temperatures (gray and blue zones), completely burned mixture near the adiabatic flame temperature and partially-premixed combustion at

moderate temperature (black and gray zones). Globally, close to the adiabatic temperature, both diffusion and premixed regions are observed with lower reaction source terms. At moderate temperatures, where the reaction source terms are high, the premixed mode predominates while at low temperatures (in gray and blue zones), $\dot{\omega}_{Yc}$ is very close to the threshold value ϵ, and unburned gases are found.

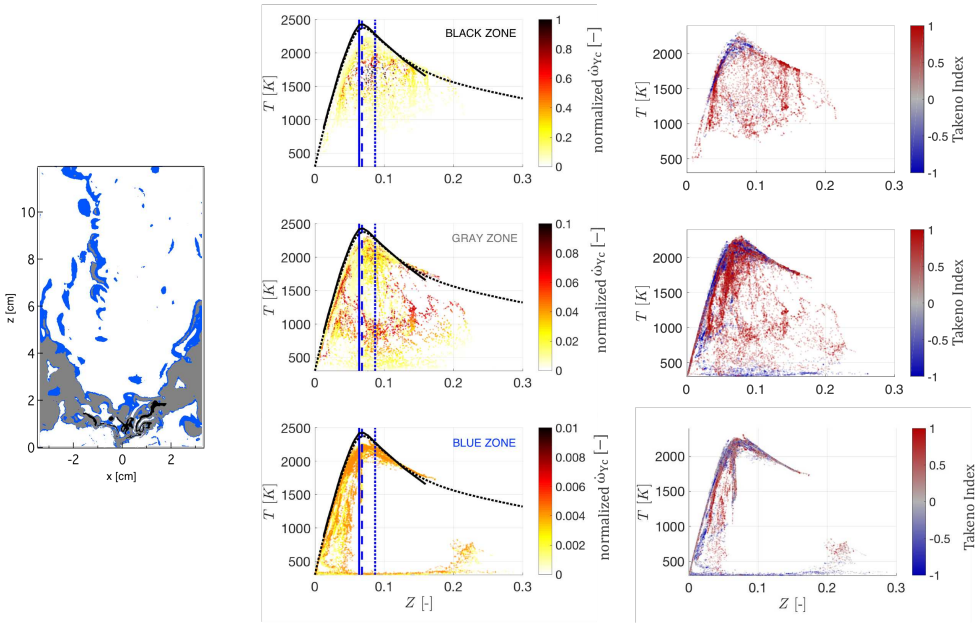

Figure 7.3: *Scatter plot of temperature as a function of the mixture fraction Z colored by the normalized source terms of progress variable (left, red-yellow) and the Takeno index (right, red-blue). The solid, dashed and dotted blue vertical lines represents the stoichiometric mixture fraction $Z_{st} = 0.064$, the global mixture fraction $Z_{global} = 0.055$ (corresponding to $\phi_g = 0.86$) and the primary injection mixture fraction $Z_{inj} = 0.077$ (corresponding to $\phi_{inj} = 1.2$), respectively. The flamelet with the highest strain rate (dotted black line) and the adiabatic equilibrium state (solid black line) are also shown. The source terms of progress variable $\dot{\omega}_{Y_C}$ is normalized by the maximum value from the black zone.*

For further information, the local gas composition is analyzed for the main reaction zone (black zone in Fig. 7.3). The profiles of species C_2H_4, O_2, CO and CO_2 and source term of the progress variable along the flame front at two different locations are shown Fig. 7.4. It is observed that premixed combustion is present at the boundary of unburned premixed gases. In contrast, non-premixed combustion is present between the unburned gases and the rich burned gases from the premixed flame, where CO burns with O_2. A similar local flame structure was obtained by (Stohr et al., 2018). It was found that a premixed flame enriches the diffusion flame with CO and H_2, corroborating

the observed flame structure in the DLR burner. According to them soot is found between a premixed and diffusion fronts in agreement with experimental observations in a laminar partially premixed flame (Carbone et al., 2015).

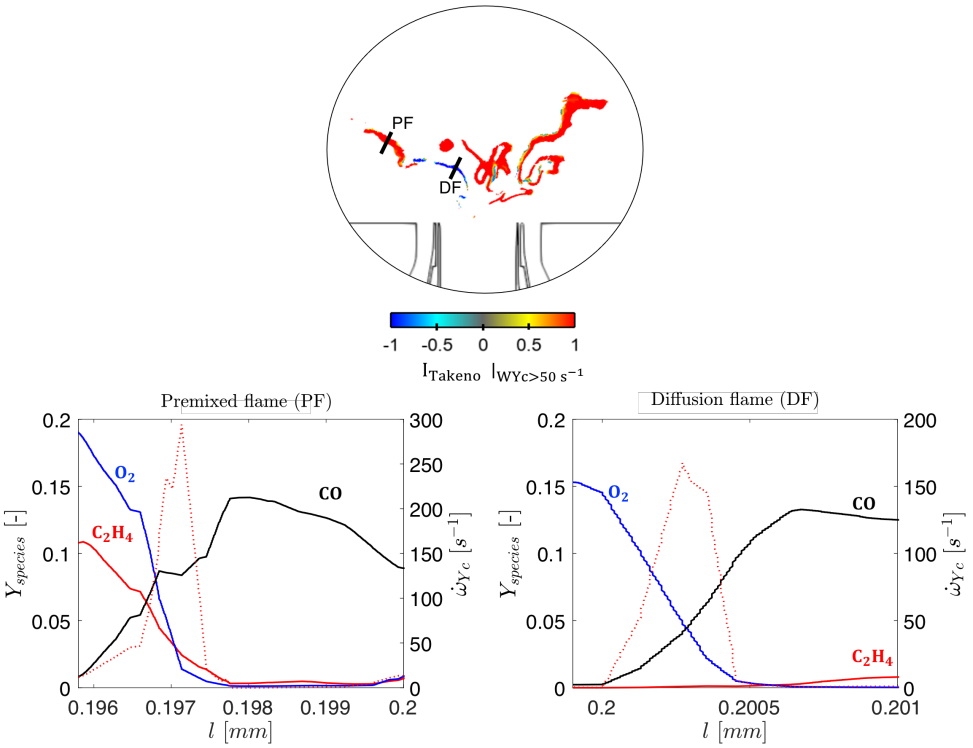

Figure 7.4: *Top: Takeno index field conditioned by the progress variable source term ($\dot{\omega}_{YC} > 50\ s^{-1}$ - black zone in Fig. 7.3). Blue regions are burning in diffusion regime, while the red regions are burning in premixed regime. Bottom: profiles of species mass fraction C_2H_4, O_2 and CO (red, blue, black solid lines respectively) and progress variable source term (dotted red line) as a function the segment length along the flame front corresponding to premixed (left) and non-premixed flame front (right).*

Figure 7.5 compares the surface reaction source terms (oxidation and surface reactions), using the reference HACA-RC and the HACA-RC* models for the same instant, correspond to the solution in Fig. 7.4. Surface growth is observed in rich-fuel zones (black iso-line Z = 0.1) and increases by a factor 2 with the HACA-RC* model compared to the reference solution, which is compatible with the increasing trend observed in the laminar flames (see Chapter 3). Although the model response depends on the time flow history, this first evaluation reveals the potential effect of the HACA-RC* model in soot prediction in the DLR burner.

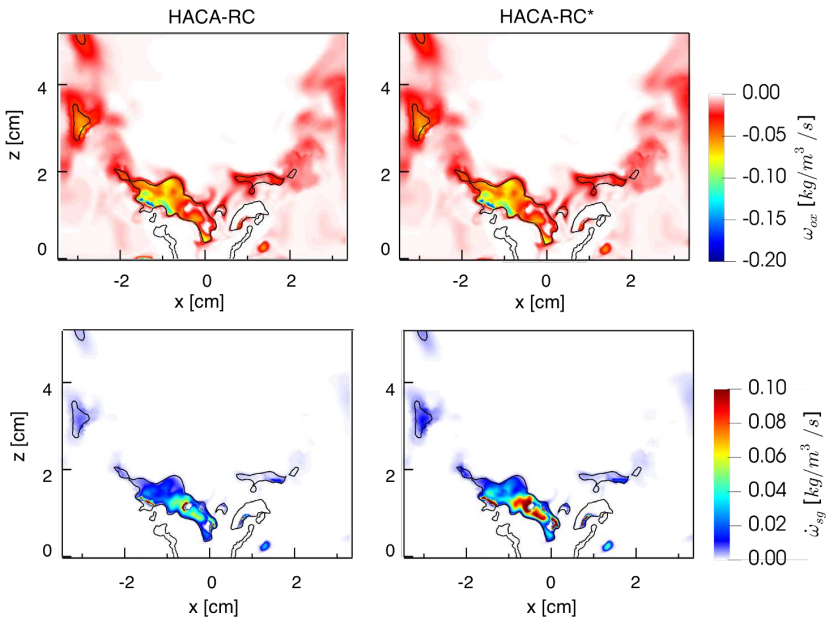

Figure 7.5: *Instantaneous surface growth (bottom) and oxidation (top) source terms with HACA-RC (left) and HACA-RC* (right) with iso-line of Z = 0.1 in black.*

Figure 7.6 shows the local temperature and gas composition in the sooting zone correspond to the premixed and non-premixed front showed in Fig. 7.4. Looking through the flame fronts, the radical CH_3 (dotted blue line in Fig. 7.6), a key species in the surface activation in the HACA-RC* model, is formed at high temperature (red line in Figs. 7.6). The C_2H_2, the surface growth species, is subsequently formed, similarly to the laminar flame structure. In opposition to the laminar structure, H and CH_3 coexist, but CH_3 concentration is much higher than H concentration as observed under laminar conditions in Chapter 3. Soot volume fraction (solid black line in top graphs in Fig. 7.6) is found in the post-flame zone at relatively high temperatures coinciding with the zone of high concentrations of C_2H_2 (solid blue line). Figure 7.6 also shows that surface growth rates increases when using the HACA-RC* model in both premixed and non-premixed conditions. For the studied solution, the effect of the model appears to be slightly high at non-premixed conditions, surface growth increases by a factor 1.4 with the HACA-RC* while for the premixed flame surface growth is increased by a factor 2.

In principle, the HACA-RC* model has been developed to enhance soot particles reactivity in non-premixed flames by identifying new zones of reactions using CH_3 radicals in addition to the H species. However, in the DLR flame, CH_3 and H species are localized in the same regions due to the swirl induces a strong turbulent mixing leading to partially-premixed burning zones. In this case, the surface growth rate mainly increases due to tabulated reaction constants based

on C_2H_4-O_2 counterflow non-premixed flames. It should be pointed out that although the tabulated model correctly reproduces temperature based on a specific flame archetype, pollutant emissions as soot particles might be more sensitive to partially premixing, as already implied by Wick et al. (2017). It is then recognized that a specific tabulated approach (Domingo et al., 2002; Duboc et al., 2019) or finite rate chemistry should be considered to accurately describe the complex combustion in this burner in future studies. However, considering the state-of-the-art soot models in turbulent flames, the RPFV approach is an excellent compromise to access reliable soot predictions that take into account large PAHs since similar flame structures have been observed when using finite rate chemistry description (Stohr et al., 2018; Felden et al., 2018).

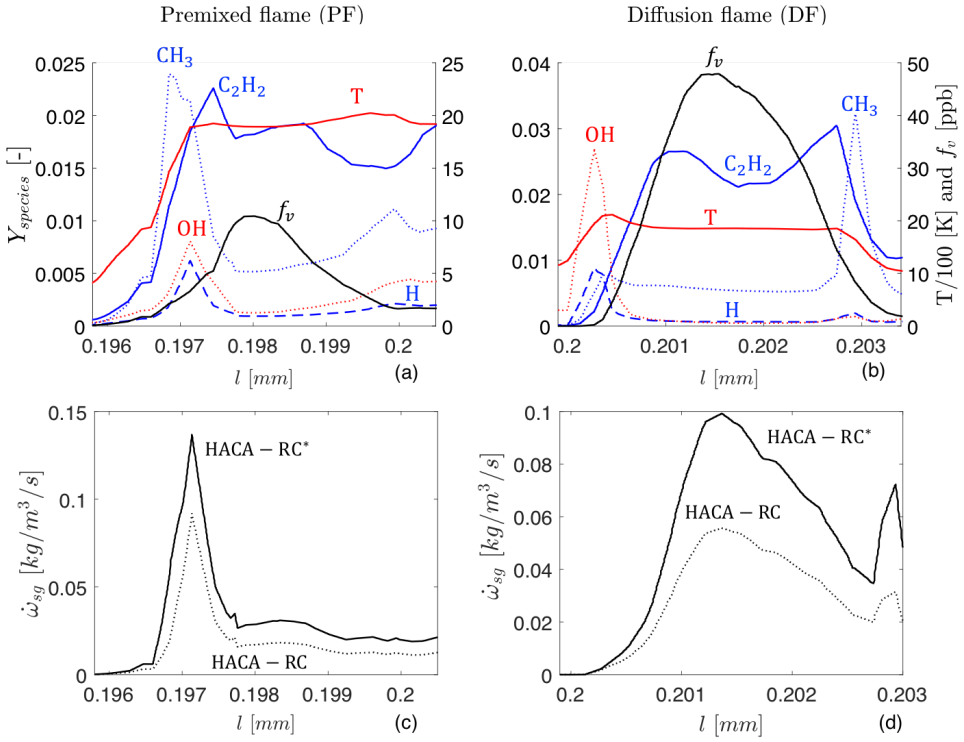

Figure 7.6: *Top: Temperature profile and HACA species (C_2H_2, CH_3; H and OH) at the flame front from Fig. 7.4. Bottom: Surface growth source terms for HACA-RC* (solid lines) and HACA-RC (dotted lines) simulations, respectively. l represents the segment length along the flame front.*

7.3 A *posteriori* analysis

An *a posteriori* analysis is performed based on the time-averaged fields of gas and solid phases. The simulations were carried out using the reference set-up

described in Chapter 6. Statistics were collected over 60 ms for each simulation, for a total computation time of 90 ms.

7.3.1 Soot statistics: N_p and f_v

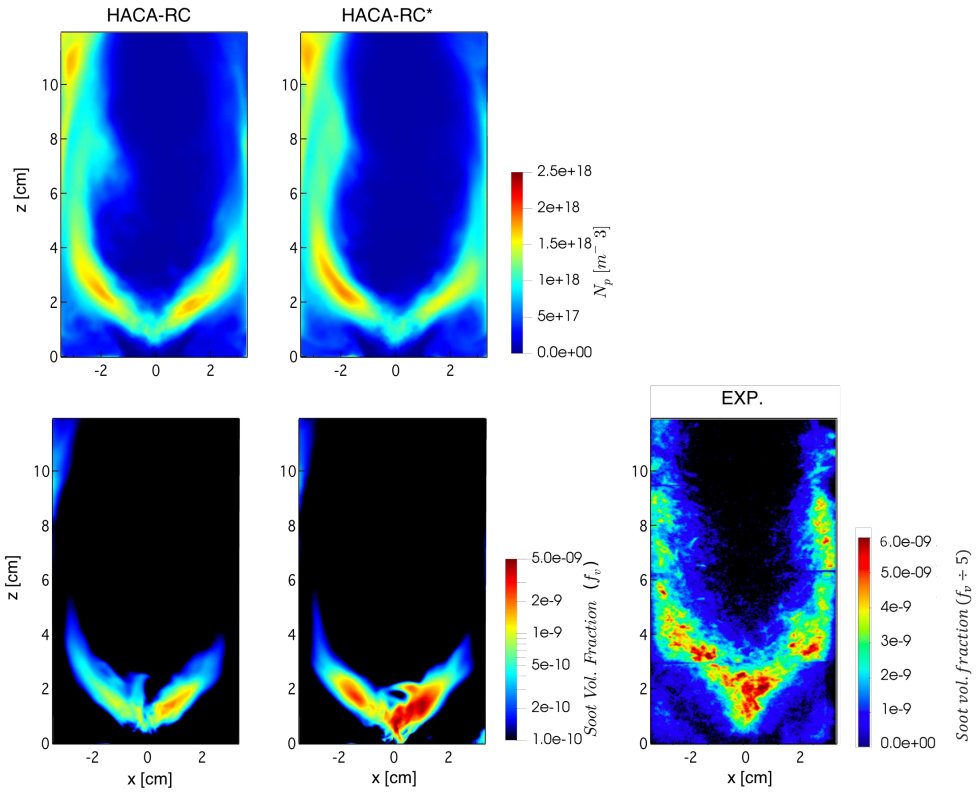

Figure 7.7: *Time-averaged particle number density (N_p - top) and soot volume fraction (f_v - bottom) obtained with the HACA-RC (left) and the HACA-RC* model (right). The experimental f_v field is shown in the bottom right (Geigle et al., 2015).*

Figure 7.7 compares time-averaged particles number density N_p (top) and soot volume fraction f_v (bottom) fields obtained using the HACA-RC (left) and the HACA-RC* (right) reaction mechanisms. The soot volume fraction obtained with the HACA-RC* is about three times higher than the soot yield from the HACA-RC case, while the particle number density is quite similar between the two computations. The increase of soot volume fraction is consistent with the increasing tendency observed for the laminar flames (Chapter 3), where a factor of three was obtained for the tested non-premixed laminar flames as well as *a priori* analysis on the turbulent flame. On the other hand, it should be reminded that the accuracy of the results strongly depends on numerous models used in the simulation, as the turbulence-chemistry interaction model,

the physical and kinetics soot sub-models, the chemistry model as well as the temporal statistical convergence discussed in Chapter 6. Therefore, obtaining a better prediction of the experimental measurements while using the HACA-RC* model is insufficient to conclude its quality concerning turbulent flames. In order to better understand this prediction, it is crucial to understand if this may be related to a different gas phase prediction, possibly due to the numerical uncertainties according to the statistical analysis discussed in Chapter 6 or/and a possible retro-coupling of the solid phase on the gas phase. For that, the effect of the HACA-RC* model on gas and solid phases statistics is discussed in details in the following.

7.3.2 Reactive flow statistics

Velocity

The mean axial velocity field obtained with the two simulations is compared in Fig. 7.8. The mean fields are very similar between simulations in the swirling zone and the inner recirculation zone, as well as in the vicinity of the secondary air injection. The similarity between mean velocity fields suggests that the dynamics of the side jets are statistically similar between the two computations, according to the statistical analysis performed in Chapter 6.

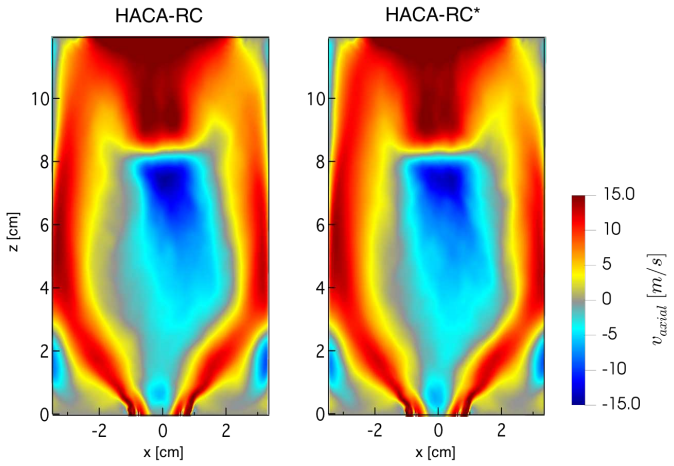

Figure 7.8: *Time-averaged axial velocity fields.*

Temperature

In principle, soot particles may contribute to radiation transfer and, consequently, affect the temperature field. Therefore, it can be expected that increasing f_v when using the HACA-RC* model could enhance soot radiation

and, consequently, change the temperature field. It is the only physical coupling between soot and gas phases for the used numerical strategy. However, it was demonstrated by Rodrigues (2018) and more recently by Monclard et al. (2020), using a Monte-Carlo calculation, that soot particles do not have a significant contribution in total radiative transfer in this configuration due to the small soot load (only a few [*ppb*] in the mean and few [*ppm*] in instantaneous solutions). Even if the soot volume fraction is increased by a factor 10, the impact on the total emitted and absorbed radiative power remains small (Monclard et al., 2020). Figure 7.9 shows that the radiative power from soot particles is less than 0.1% of the total time-averaged radiative power for the simulation with the reference HACA-RC model, while when using the HACA-RC* model, it is about 1% of the total radiative power, which is still low compared to the gas-phase contribution.

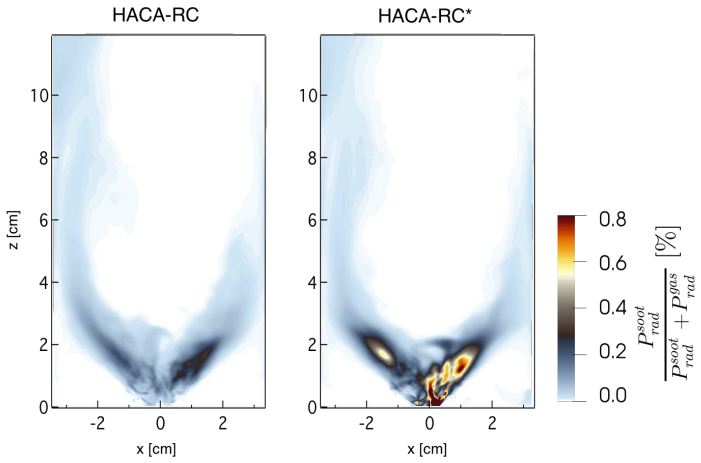

Figure 7.9: *Contribution of soot particles to the radiative power obtained with the HACA-RC (left) and the HACA-RC* (right).*

The time-averaged axial temperature profile obtained with the HACA-RC and the HACA-RC* are shown in Figure 7.10. A good agreement with experimental measurements (symbols) is obtained for both computations (solid lines), with small discrepancies between simulations. The lifted experimental flame position and the post-flame temperature are quite well reproduced for both cases. The decrease in the temperature approaching the secondary injection is also correctly captured. As already said, the prediction of lower temperatures in the post-flame zone is due to the overprediction of radiative losses under the optically thin assumption (Rodrigues, 2018).

Figure 7.11 compared the temperature pdfs for different locations in the chamber, as indicated in Fig. 7.10. Consistently with the time-averaged fields (Fig 7.10), no major discrepancies are observed between temperature pdfs pre-

dicted by the two simulations, which present similar distribution and mean values.

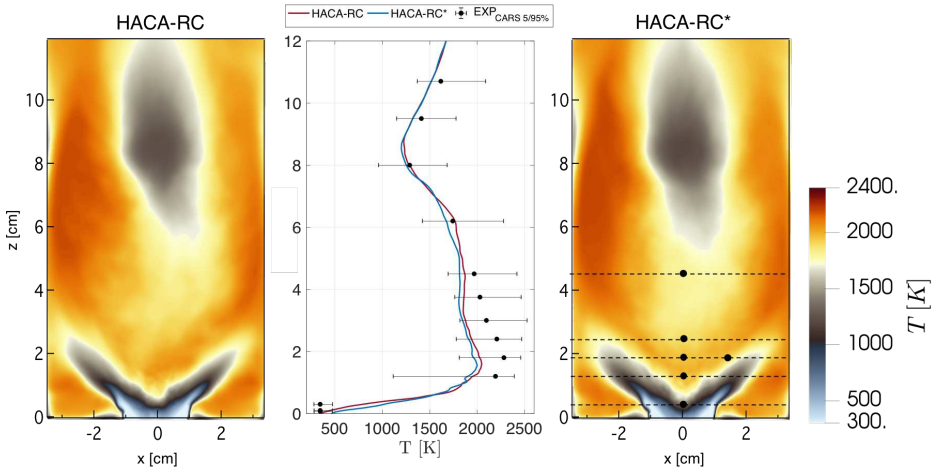

Figure 7.10: *Time-averaged temperature fields with HACA-RC (left) and HACA-RC* (right) and the comparison with experimental temperature (Geigle et al., 2015) in the combustor centerline (center). The black dots in the HACA-RC* field indicate the position for the pdfs shown in Figs. 7.11 and 7.13.*

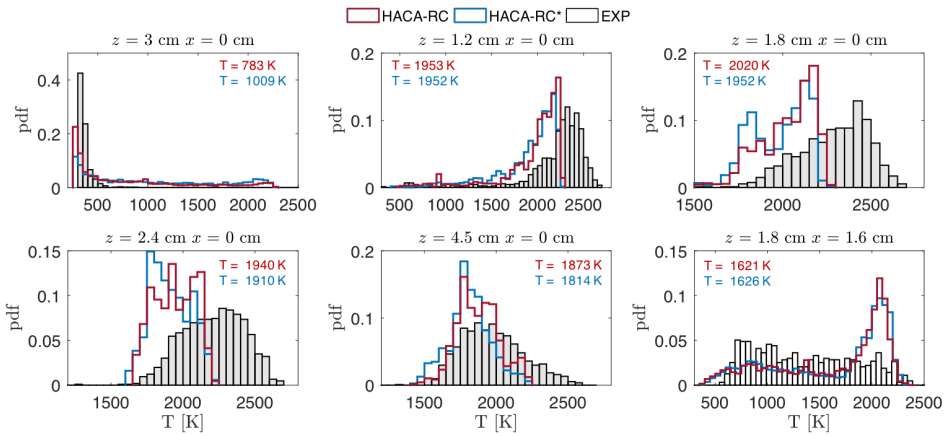

Figure 7.11: *Probability density function of the temperature with HACA-RC (red) and HACA-RC* (blue) at locations indicated in Fig. 7.10. Experimental temperature pdfs (Geigle et al., 2015) are shown in gray.*

Mixture fraction and species

Figure 7.12 shows the time-averaged fields of mixture fraction. In analogy with temperature, the time-averaged mixture fraction fields are similar between the

two simulations in terms of magnitude and spatial distribution. The similar asymmetric mixture fraction fields provide confidence in the similarity of the PVC and secondary injection dynamics effect in mixing. Figure. 7.13 presents the corresponding probability density function (second and fourth rows) for different positions in the chamber (as indicated in Fig. 7.10). Similarly to temperature, the mixture fraction pdfs are also globally similar between the two simulations.

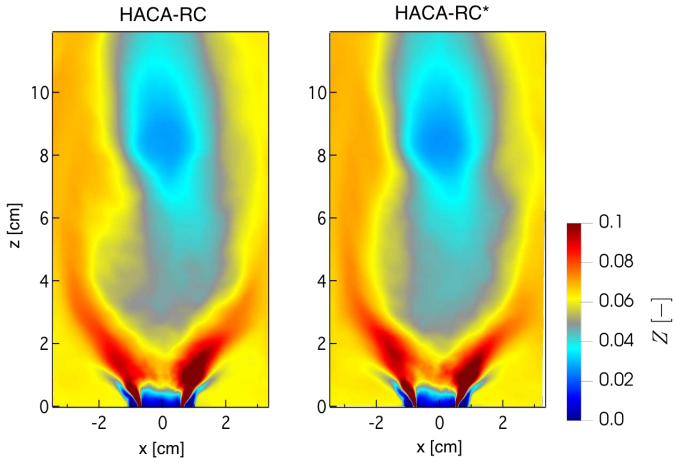

Figure 7.12: *Time-averaged fields of mixture fraction obtained with HACA-RC (left) and HACA-RC* (right).*

.

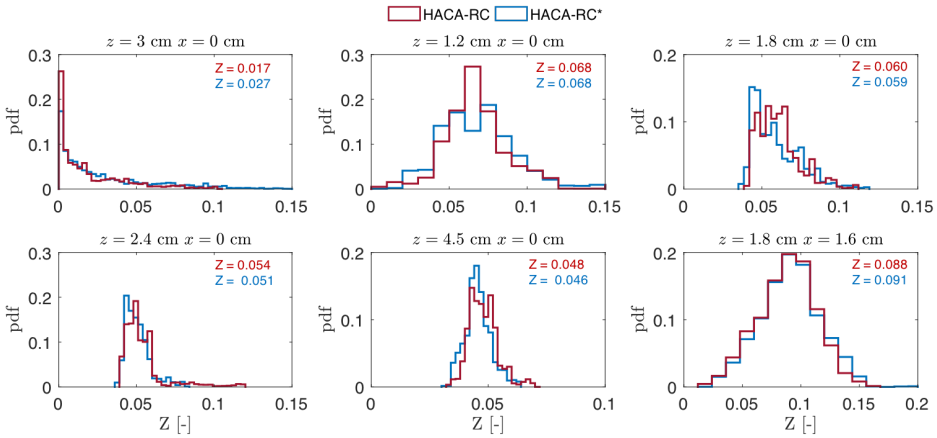

Figure 7.13: *Probability density function of the mixture fraction for HACA-RC (red) and HACA-RC* (blue) computations at locations indicated in Fig. 7.10.*

Finally, Fig. 7.14 shows the time-averaged fields of the PAH, C_2H_2, H and CH_3

mass fraction species. The similarity between HACA-species fields confirms that the simulations are statistically similar for the gas phase. However, the PAH fields are slightly different. Note that the mass fraction of C_2H_2, H and CH_3 are read from the same look-up table while the PAH is transported due to its higher sensibility to scalar dissipation rate (Bisetti et al., 2012).

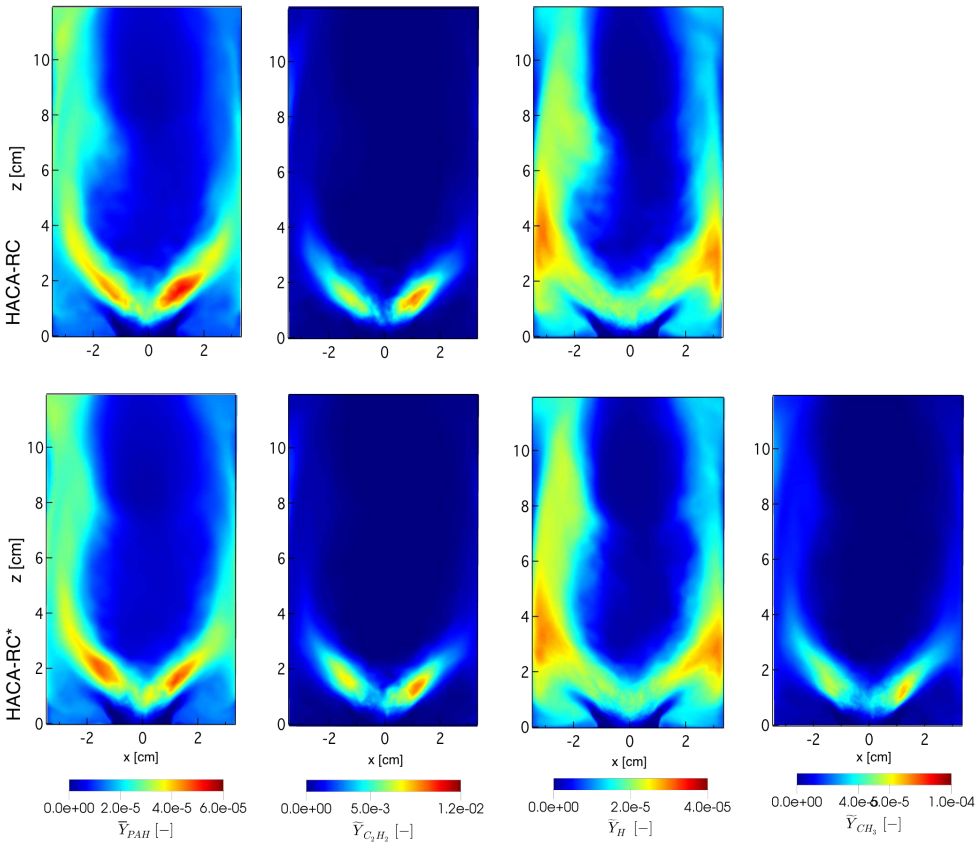

Figure 7.14: *Time-averaged fields of species (PAH, C_2H_2, H) mass fraction for both HACA-RC and HACA-RC* cases. CH_3 is not included in the HACA-RC model (top) therefore it is only show for the HACA-RC* case (bottom).*

7.3.3 Analysis of soot production

Figure 7.15 compares the soot mass source terms (nucleation, condensation, surface growth and oxidation) obtained using the reference HACA-RC (top) and the new HACA-RC* (bottom) models. Coagulation, contributing to the particle number density, is also compared. No significant differences are detected for the nucleation. Similar conclusions are obtained for condensation, even though changes may have been expected due to its soot size dependency.

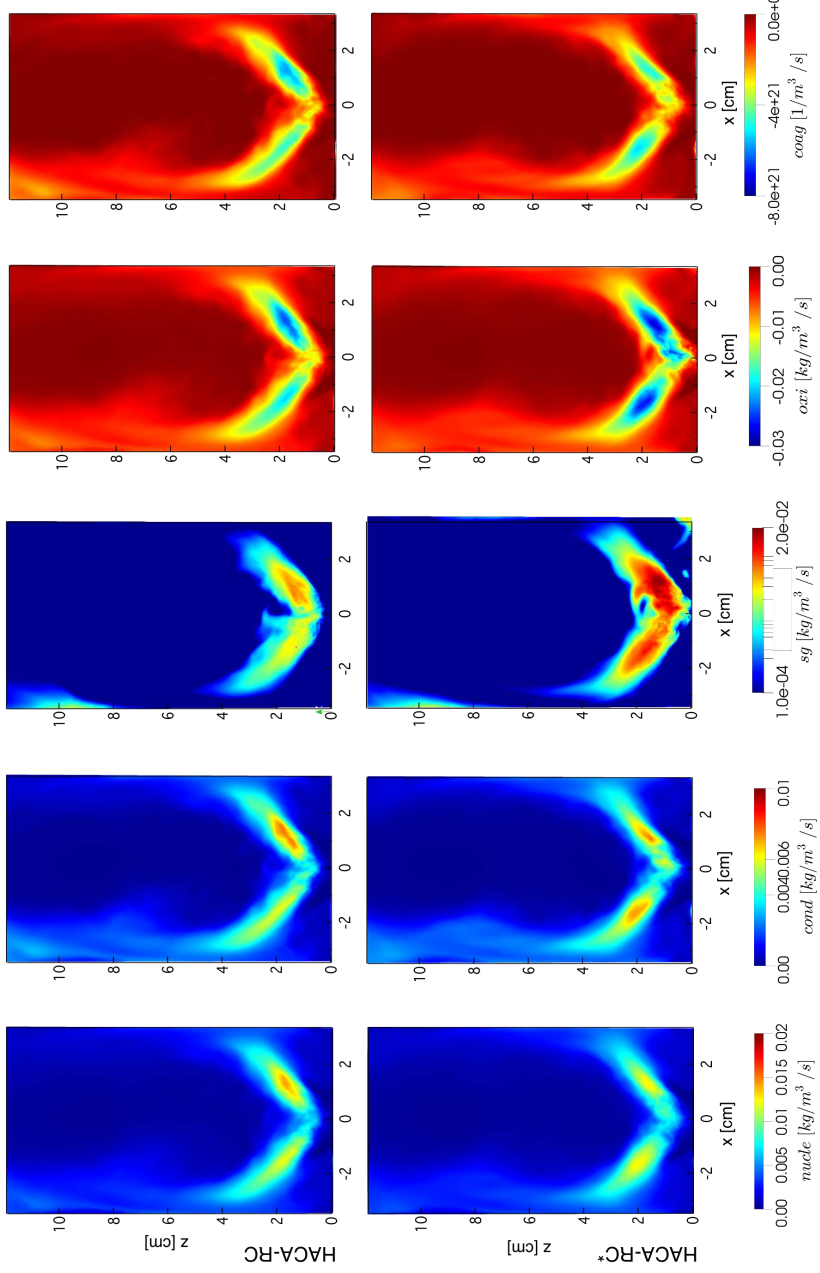

Figure 7.15: *Comparison between mass soot source terms obtained with the HACA-RC (top) and HACA-RC* (bottom) from left to right nucleation, condensation, surface growth, oxidation and coagulation (particle number density source term). Surface growth source term is shown in log-scale.*

These observations are in opposition to the laminar flame behavior, where nucleation reduces as dimers are further consumed by condensation due to the increase in soot particle size. For coagulation, no relevant differences are observed either, although its dependence on the particle size. On the contrary, the source term of surface growth increases by a factor 3 using the HACA-RC*. At the same time, oxidation also increases since the HACA-RC* model activates the particle surface to react with both growth and oxidation species.

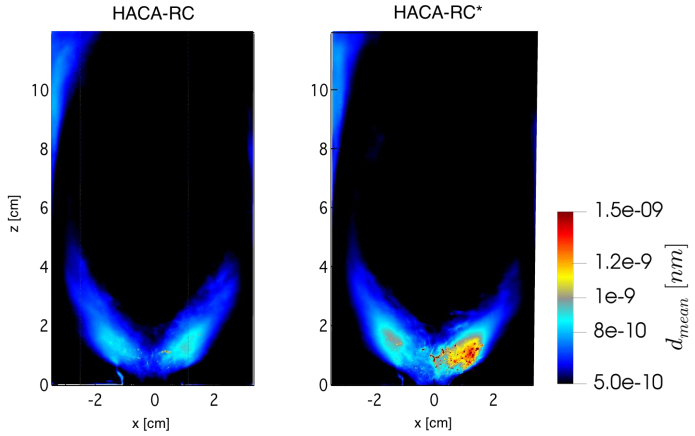

Figure 7.16: *Time-averaged mean particle diameter with HACA-RC (left) and HACA-RC* (right).*

These results are not surprising considering the low soot load characteristic of this flame. Although soot mass increases with the HACA-RC* model, soot particle yield remains very small. Note that the nucleation and the surface growth have a similar contribution to soot mass in the HACA-RC* case, whereas, for the HACA-RC case, surface growth is lower, while oxidation is high in both cases compared to the other mechanisms. This is characteristic of the early formation stage of particles, as observed in laminar flames (Chapter 3). Then, even if the mean diameter obtained with the HACA-RC* model is almost twice the one from the reference model (Fig. 7.16), the soot particles are still very small. Diameters of a few nanometers, typical of young particles, are observed instead of mature soot particles generally composed of large aggregates reaching several hundred nanometers characterizing laminar flames (Joo et al., 2018). The small size of soot particles might be partially attributed to the small residence time encountered by the soot particles formed close to the region of the PVC (Geigle et al., 2017), but also due to the strong soot particles oxidation.

Figure 7.17 shows the net source terms by progressively including soot processes: surface reactions $\dot{\omega}_{sg+ox}$, surface reactions with nucleation $\dot{\omega}_{sg+ox+nu}$ and the total mass source term $\dot{\omega}_{Y_s}$. Due to the high oxidation rate, $\dot{\omega}_{sg+ox}$ is negative everywhere in the sooting zone for both cases. By adding nucleation

($\dot{\omega}_{sg+ox+nu}$), the net source term becomes positive for the HACA-RC* case in the zone of high surface growth. This zone corresponds to high C_2H_2 concentrations located slightly upstream to the zone of high PAH concentration (see Fig. 7.14). By including condensation ($\dot{\omega}_{Y_s}$), the global source term becomes positive in the zone of high f_v for the HACA-RC, but also in the zone of high PAH concentration in both cases. Then, the soot mechanisms appear to be relevant in different zones. The combination of the growth mechanisms further contributes to f_v when using the HACA-RC* model, similarly to prior numerical observations in the DLR burner (Chong et al., 2018, 2019) and a real-scale gas turbine combustor (Mueller and Pitsch, 2013).

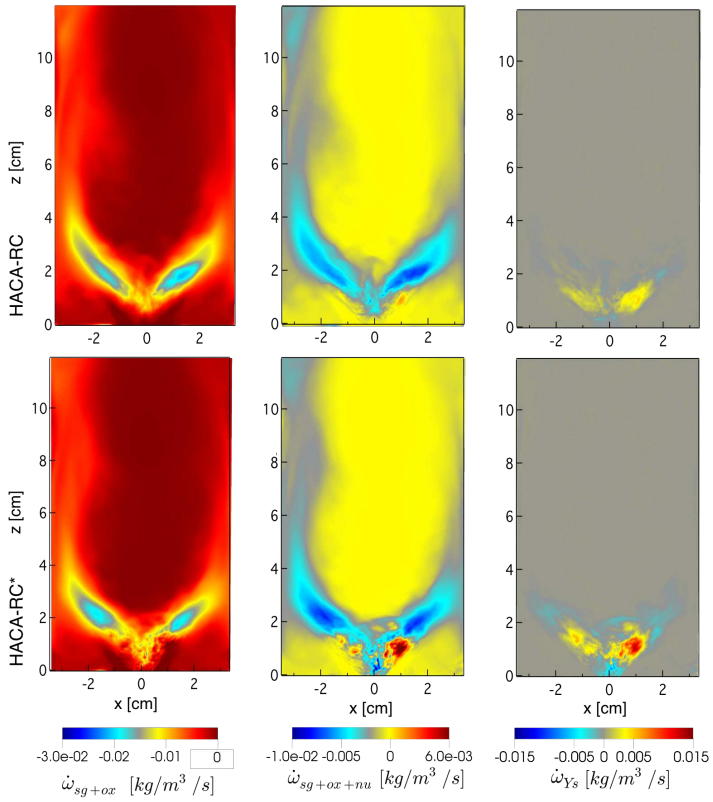

Figure 7.17: *Net mass source terms with HACA (top) and HACA-RC* (bottom): left column corresponds to the net surface reactions $\dot{\omega}_{sg+ox}$ (oxidation + surface growth), the middle column includes nucleation $\dot{\omega}_{sg+ox+nu}$ and the right column corresponds to the total soot mass source term, including condensation $\dot{\omega}_{Y_s}$.*

7.4 Conclusion

The numerical prediction of soot volume fraction in turbulent flames is challenging due to the complexity of the soot production that involves physical and

chemical processes that interacts in a non-linear way with the turbulent combustion fluctuations. The state-of-the-art in CFD modeling of such complex phenomena still lacks even under laminar conditions. Among the processes involved in soot production, the present work evaluates the impact of the surface reactions model, the HACA-RC* model, in LES soot prediction in the DLR burner.

A *priori* analysis revealed that soot particles are formed in both fuel-rich premixed and non-premixed combustion zones and soot surface growth increases when using the HACA-RC* model, consistent with the trend obtained for laminar flames in Chapter 3. However, the spatial species distribution is quite different from the laminar conditions. The HACA-RC* model does not detect new zones of surface reactions as expected from laminar flames but only enhances the reaction zones already identified by the reference HACA-RC model. The proposed HACA-RC* modification may have a more relevant interest in other turbulent configurations where H and CH_3 may not overlap, likely in turbulent jet non-premixed flames.

The *a posteriori* analysis of soot statistics (60 ms) shows that the time-averaged maximum soot volume fraction f_v is three times higher than the reference model due to the substantial increases in the surface reaction rate. The other source terms do not seem to be modified by the HACA-RC* model, even if f_v, and then soot particle size, increases. Indeed, soot particles remain very small in this configuration which is characteristic of the early formation stage of particles observed for laminar flames (Chapter 3). This could partially explain the low soot load in this configuration.

Although a better agreement with experimental data is obtained when using the HACA-RC* model, it should be reminded that the quantitative conclusions from this study depend on the specific used models for both soot and gas phases, as well as the corresponding model assumptions and parameters. Therefore, the impact of the HACA-RC* model, coupled with other gaseous and soot models, should be verified since its performances strongly depend on the prediction of CH_3 and C_2H_2 mass fraction. It can be done, in a first attempt, in laminar canonical flames.

Finally, it seems essential to mention that this study was carried out before quantifying the LES reliability of the soot prediction in the DLR burner presented in Chapter 6. The present study was performed based on the state-of-the-art LES simulations of the DLR burner, where statistics are based on time-averaged of maximum 60 ms except for Chong et al. (2018). Therefore, for qualitative conclusions, longer simulation time would be necessary, requiring massive CPU resources. Alternatively, a strategy to evaluate the soot model in turbulent flames is proposed in the next chapter and could also be applied to this investigation to clearly quantify the effect of the HACA-RC* model.

Chapter 8

Impact of the subgrid soot model

Chapter 6 illustrated the difficulties in evaluating model performances specific to soot prediction in turbulent flames by considering soot production in the DLR aero-engine combustor. It was proven that soot production occurs only for scarce local gaseous conditions. To obtain a consistent quantitative comparison, a much long physical time is required to guarantee a statistical representation of the sooting events implying a very high CPU cost. Therefore, soot models evaluation based on two distinct LES is CPU prohibitive. Alternatively, a new strategy to rigorously evaluate soot models in turbulent flames is proposed here and its capability is proven by investigating the soot subgrid intermittency model (Mueller and Pitsch, 2011). This study was recently proposed and recommended to the Turbo Expo 2021 conference publication: "Validating Soot Models in LES of Turbulent Flames: The Contribution of Soot Subgrid Scales Models to Prediction of Soot Production in an Aero-Engine Model Combustor."

This chapter is organized based on the paper structure. First, a new statistical analysis based on 110 ms is performed revealing the difficult in reaching convergence for the solid phase and consequently the evaluation of soot models. Then, in Section 8.3, a new strategy based on a unique LES simulation, where the set of soot equations is duplicated is proposed. For a unique set of gaseous equations, one set accounts for the reference soot model, the other accounting for the soot model under interest. Following this strategy, when solid phase retro-coupling with the gas phase is negligible, as in the studied case, this strategy enables soot scalars to experience a unique temporal and spatial gas phase evolution.

Therefore, the model evaluation can be straightforwardly handled since soot model effect can be evaluated by comparing the instantaneous model response without attending soot statistics. Finally, in Section 8.4 the strategy is used to evaluate the impact of the soot subgrid intermittency model (Mueller and Pitsch, 2011) on the prediction of soot production in the DLR combustor.

Contents

8.1 Introduction

The complex physical processes underlying soot production are today not fully understood even under laminar conditions so that the numerical prediction of soot production is quite challenging. When considering turbulent flows, the modeling becomes more complex by the strong soot-flame-turbulence interactions at the origin of an intermittent soot presence in space and time. Indeed, soot production was found to be affected by turbulence in two major ways. First, soot precursors are characterized by long chemical time scales compared to turbulence, resulting in a more delayed response to turbulence fluctuations than other major species (Bisetti et al., 2012; Attili et al., 2014, 2015). Consequently, due to the PAH sensitivity to the local dissipation rate, soot production can be inhibited in the high dissipation rate zone, while high soot production can be found in low dissipation rate zones. Second, soot particles are characterized by a high Schmidt number, i.e., soot molecular diffusivity is negligible compared to gaseous species. Soot particles are then confined in thin structures of different length scales convected and deformed by the turbulent flow field (Bisetti et al., 2012; Attili et al., 2014; Franzelli et al., 2017; Geigle et al., 2013). Additionally, its interaction with turbulent flow leads to high temporal and spatial intermittency since soot particles experience different thermochemical conditions (temperature and gas composition) along the flow pathlines, promoting or inhibiting soot production (Geigle et al., 2017; Stohr et al., 2018).

When proposing new models for turbulent sooting flames, a classical approach consists in their development under laminar conditions and the evaluation of their performances by comparing the results from two numerical simulations of turbulent target flames: one using a reference model and the other with the

model under scope (Franzelli et al., 2015; Felden et al., 2018; Chong et al., 2019; Tardelli et al., 2019). However, a clear quantification of the effect of the model can be complex (Tardelli et al., 2019) since soot events are extremely rare under turbulent conditions so that only qualitatively trends can be analyzed when considering the computational times classically used for gaseous flames (i.e. tens of ms).

In this framework, the goals of this work are threefold. First, the difficulties in evaluating the performances of new models for soot production in turbulent flames are deeply characterized by considering the DLR burner (Geigle et al., 2013, 2017, 2015), one of the turbulent target flames of the International Sooting Flame Workshop (ISF, 2019), representative of a gas turbine combustor. The strong intermittent behavior of soot production is shown to be due to the unsteadiness of the flow (Geigle et al., 2017; Stohr et al., 2018; Grader et al., 2020), governing the rare occurrence of local gaseous conditions leading to soot production. The analysis of time-averaged and instantaneous gaseous and solid quantities revealed the issues in obtaining a statistical description of rare sooting events compared to gaseous quantities. This behavior is intrinsic to sooting turbulent flames so that the only possibility to obtain a consistent quantitative evaluation of soot models is to perform two distinct simulations for a quite very long physical time to guarantee a statistical representation of the sooting events (Chong et al., 2018), requiring a very high computational cost. In an industrial context, this strategy is not affordable.

Therefore, the second aim of this work is to propose a new strategy based on a unique LES simulation, where the set of soot equations are duplicated with one set accounting for the soot reference model. In contrast, the other set relies on the new model under the scope. This strategy enables soot scalars to experience the same temporal and spatial gas phase evolution so that the same rare sooting events are considered with both models. In this way, the response of the model to specific soot events can be evaluated easily by isolating the soot model from the uncertainties on gaseous models and numerical errors, provided that solid phase retro-coupling is negligible. Besides, by considering a unique set of gaseous equations, the final CPU cost will be smaller than the classical approach based on two distinct simulations.

Finally, the last objective consists of evaluating the contribution of a soot subgrid-scale model to soot prediction in the DLR combustor to illustrate the potential of the proposed unique gas phase approach. Among the few models for soot subgrid scales that can be found in the literature, (Lindstedt and Louloudi, 2005; Aksit and Moss, 2006; El-Asrag et al., 2007; Mueller and Pitsch, 2011; Donde et al., 2013), the intermittency model developed by Mueller and Pitsch (Mueller and Pitsch, 2011) is the most used when soot subgrid scales are taken into account (Mueller and Pitsch, 2012, 2013; Rodrigues et al., 2018; Koo et al., 2016; Franzelli et al., 2018), probably due to its easiness of implementa-

tion and its low computational cost. However, to our knowledge, the effect of the model on soot prediciton has never been deeply evaluated on LES of soot production in the DLR burner (ISF, 2019). Thanks to the proposed strategy analysis, the first indications of the role of the subgrid intermittency model on soot prediction in the DLR burner are finally provided.

8.2 Analysis of soot production

A reference LES simulation of the DLR burner was performed over 140 ms using the numerical set up, presented in Chapter 5 (with the reference grid, the HACA-RC* for the surface reaction model and the soot subgrid intermittency model). Statistics were collected over the last 110 ms corresponding to twelve flow-through times (estimated based on the inflow velocity and the combustor's axial length) which is almost twice the statistics discussed in Chapter 6 and also longer than the time interval considered on most of the works on LES of the DLR burner found in literature (Franzelli et al., 2015; Felden et al., 2018; Koo et al., 2016; Franzelli et al., 2018; Dupoirieux and Bertier, 2016; Wick et al., 2017; Eberle et al., 2018; Grader et al., 2018; Rodrigues, 2018; Gallen et al., 2018), except for (Chong et al., 2018), which considered 200 ms.

Figure 8.1 shows the temporal evolution of temperature, mixture fraction and PAHs mass fraction, averaged over all the domain and normalized by their time-averaged values $\hat{\phi}(t)$ defined as:

$$\hat{\phi}(t) = \{\phi\}/ < \phi > \tag{8.1}$$

where $\{\phi\}(t) = \int_V \phi(t)\, dV$ and $< \phi >= \int_t \{\phi\}(t)\, dt$.

An oscillation of less than 1% can be observed for these gaseous quantities. The temporal evolution of soot quantities (number density of particles $\hat{N}_p$, total soot surface $\hat{s}_s$ and soot volume fraction $\hat{f}_v$) are also shown in Fig. 8.1. N_p evolution presents small fluctuations in amplitude, similarly to PAHs. On the contrary, the total soot surface s_s and f_v presents a higher variability. The soot volume fraction $\hat{f}_v$ presents the highest variability reaching 40 % of the mean value. This trend can be considered the first evidence of the intermittent soot signature, mainly governed by the flame-soot-turbulence interactions. Therefore, it is important to remind that three sources of unsteadiness of soot production have been identified in the DLR burner (aas discussed in Chapter 6): (1) a coherent large-scale motion, known as precessing vortex core (PVC), that can affect the mixing, potentially inducing or inhibiting soot formation. (Eberle et al., 2015; Geigle et al., 2017; Stohr et al., 2018; Grader et al., 2020); (2) the slow dynamics of the secondary jet (Grader et al., 2020) that modify the

position of the root of the inner recirculation zone, affecting the flame position and, consequently, the gaseous quantities experienced by particles along their trajectory; (3) the effect of turbulent eddies displacing and deforming soot ligaments (Geigle et al., 2017; Stohr et al., 2018).

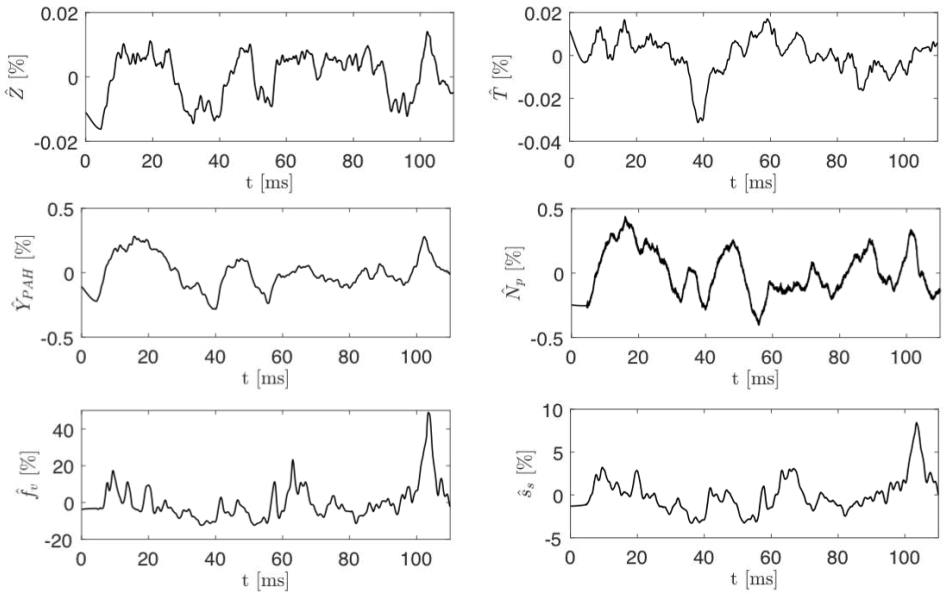

Figure 8.1: *Temporal evolution of spatially-averaged gaseous (top - temperature, mixture fraction and pah mass fraction) and soot variables (bottom - particle number density, total soot surface and soot volume fraction) normalized by their respective mean values.*

In order to quantify the effect of the intermittent soot volume fraction dynamics on soot statistics, the time-averaging interval t_{av} is progressively increased. The resultant time-averaged temperature fields are shown in Fig. 8.2 for t_{av} = 40, 60, 80, 110 ms. Results along the centerline are compared to the experimental data (symbols) in Fig. 8.3. It can be seen that 60 ms are sufficient to obtain a statistical time-averaged description of the temperature in the primary reaction zone (where most soot production occurs). Furthermore, a good agreement with experiments is observed although the prediction of lower temperatures in the post-flame zone due to the optically thin assumption (Rodrigues, 2018). Therefore, it might be concluded that 60 ms are enough to perform time-averaged statistics as done in some previous papers (Eberle et al., 2018; Grader et al., 2018). However, when looking at soot quantities, the conclusions are not the same.

Figure 8.4 shows the four cumulative time-averaged fields for particle number density and soot volume fraction. Concerning the particle number density,

results seem to converge over 80 ms, whereas even 110 ms are not sufficient for the statistical description of the soot volume fraction. Note that on the left side of the at t_{av} = 40 ms soot volume fraction is very low and increase with time-averaging, as indicate the white isoline of f_v = 1 ppb.

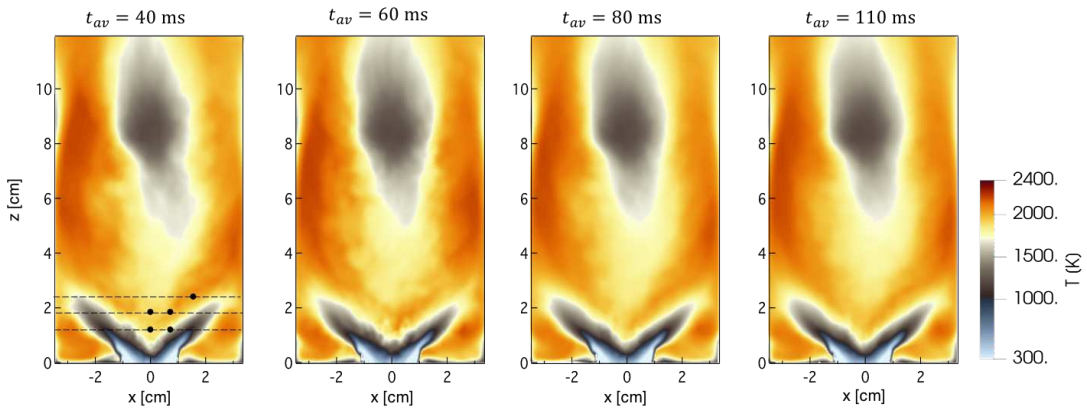

Figure 8.2: *(Time-averaged temperature sequence up to 110 ms. Five probes in the sooting zone (z < 30 mm) are indicated at the 40 ms field.*

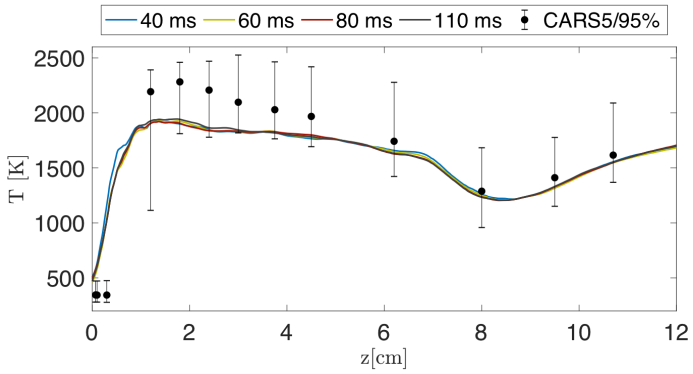

Figure 8.3: *Temperature profile along the centerline of the chamber: 40 ms (solid blue line), 60 ms (dotted blue line), 80 ms (black solid line) and 110 ms (dotted black line). Black circles correspond to the experimental data (Geigle et al., 2015; ISF, 2019).*

Figure 8.5 (left) shows the temperature probability density function at five different locations in the sooting zone (z < 30 mm). The pdfs are quite similar for the different t_{av} values. However, if the temperature pdfs are conditioned by the presence of soot (f_v > 1 ppb) as shown in Fig. 8.5 (right), it is found that pdfs differ between the different time-averaging periods. In particular, differences are observed in the layer between fresh gases and the outer recirculation zone (for z|x = 12|8 and 18|8 mm) where high velocity fluctuation are

expected and at the root of the inner recirculation zone (z|x = 18|0 mm) whose position is strongly affected by the dynamics of the secondary air injection. Such discrepancies suggest that particles will experience statistically different thermochemical gaseous history depending on the considered time-averaged periods. To quantify it, Table 8.1 presents the difference on temperature, mixture fraction and soot volume fraction time-averaged at different t_{av} against t_{av} = 110 ms non-dimensionalized by the value obtained at t_{av} = 110 ms at the considered locations. It confirms that the gas phase is statistically converged from 60 ms. The difference between mean values is about only 2% after 40 ms for the temperature and less than 10 % for the mixture fraction. On the contrary, soot volume fraction presents a high variability (more than 40 %). If the conditioned mean values are considered, also shown in Table 8.1, time-averaged results present a higher variability depending on t_{av}. Therefore, it can be concluded that a statistical description of the gaseous phase is not observed when considering only the occurrence of soot events to perform statistics. It should be noticed that in some extreme cases, such as for probe at z|x = 18| 0 mm no sooting event is observed during the first 40 ms, clearly illustrating the issues of statistics when describing the solid phase compared to a purely gaseous flame.

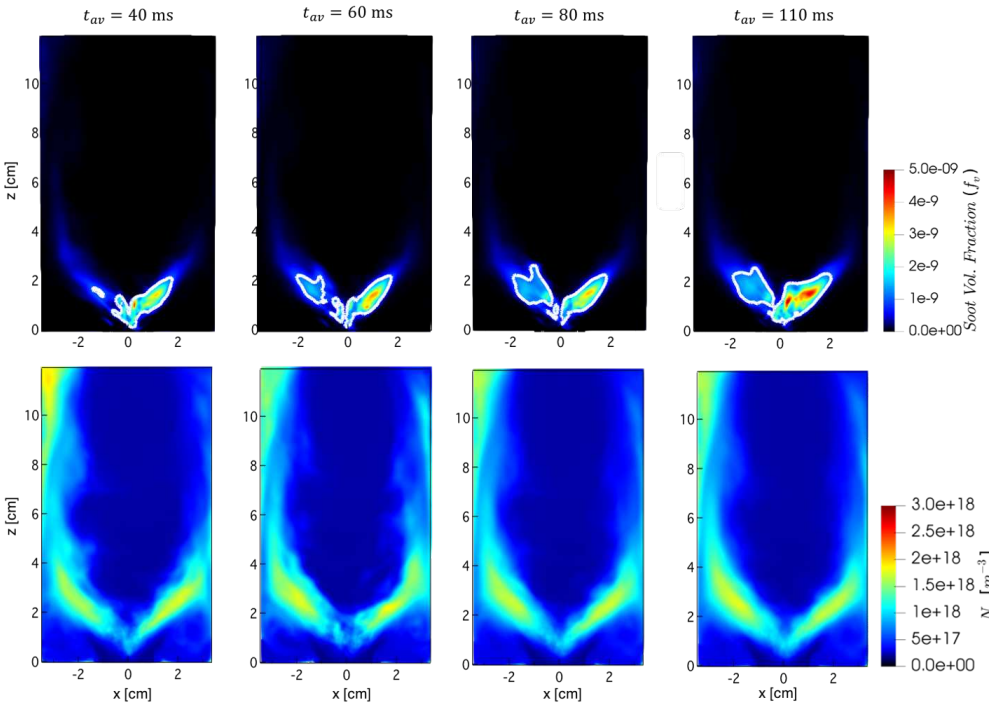

Figure 8.4: *Left: time-averaged soot volume fraction with isoline of f_v = 1 ppb (top) and particle number density (bottom) sequence for different time-averaging intervals.*

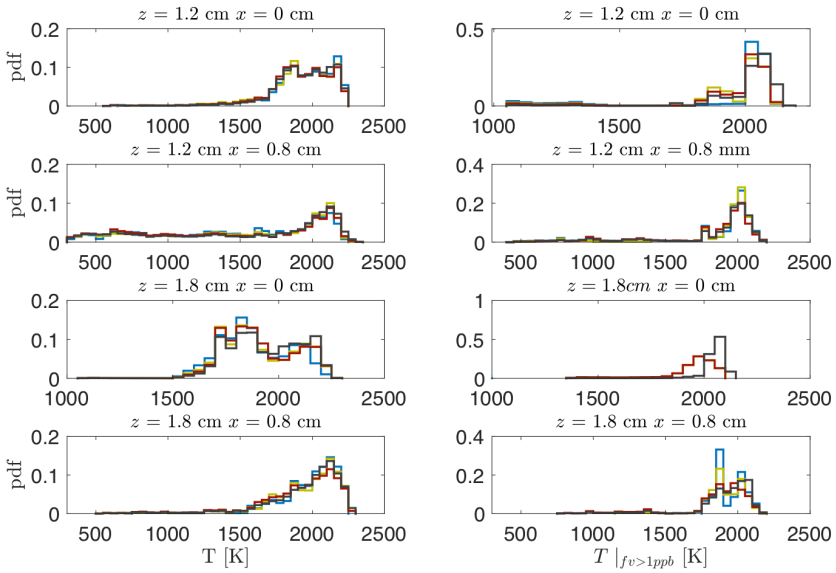

Figure 8.5: *Left: temperature probability density function considering different time-averaging intervals of 40 ms (blue), 60 ms (green), 80 ms (red) and 110 ms (black) at different locations in the sooting zone (z< 30 mm) as indicated in Fig. 8.2. Right: the respective temperature probability density function conditioned by the presence of soot (f_v > 1 ppb).*

Table 8.1: *Relative difference between time-averaged gaseous and soot values ($\mid \phi_{t_{av}} - \phi_{t_{av}} \mid / \phi_{t_{av}=110ms}$, for t_{av} = 40, 60, 80 ms) at probes in the sooting zone (z > 30 mm).*

z | x	T [%]			Z [%]			f_v [%]		
[mm]	40 ms	60 ms	80 ms	40 ms	60 ms	80 ms	40 ms	60 ms	80 ms
12 | 0	0	1.1	1.2	0	1.5	3.0	65.2	47.2	54.2
12 | 8	14.0	1.1	5.0	0	4.5	0	44.2	54.7	9.4
18 | 0	2.7	1.8	1.5	12.3	7.0	7.0	-	80.0	84.0
18 | 8	1.2	0.25	2.0	10.3	9.0	2.6	70.2	61.1	3.3
	T$\mid_{f_v>1bbp}$ [%]			Z$\mid_{f_v>1bbp}$ [%]			$f_v \mid_{f_v>1bbp}$ [%]		
12 | 0	4.9	4.6	3.2	0	2.5	0	60.0	20.2	30.6
12 | 8	2.6	3.8	0.04	3.1	4.7	3.1	47.0	47.2	19.6
18 | 0	-	5.5	5.5	-	14.7	14.7	-	43.8	43.8
18 | 8	2.2	0	2.9	4.8	3.2	4.8	43.6	40.0	5.2

Figure 8.6 shows the scatter plot of temperature as a function of the mixture fraction colored by the joint T-Z probability for probes at z = 12, 18 mm, x = 8 mm. Statistically, the thermochemical states accessed during the three time-averaged periods are quite similar, notably after 60 ms. However, soot is found only for rare thermochemical states, as shown by the conditioned scatter plots colored by the soot volume fraction also in Fig. 8.6. Such rare thermochemical

conditions are localized in space and are affected by the unsteady PVC and IRZ motions, explaining the high soot intermittency in this configuration. In specific, soot intermittency, defined as the probability to found $f_v > 1$ ppb, is equal to 9.3%, 15.3%, 5.8% and 17.5% at z|x = 12|0, 12|8, 18|0 and 18|8 mm, respectively, based on 110 ms time-averaged results. Therefore, a long averaging time, whose duration is strongly related to soot intermittency, is needed to get a statistical description of the soot volume fraction compared to the gaseous phase. This implies a high CPU cost that is today not affordable to perform parametric studies or model sensitivity analysis in an industrial context. As an exemple, to obtain 10 ms in the specific case 45000 CPU hours (run on Intel E5-1920 processors) are required.

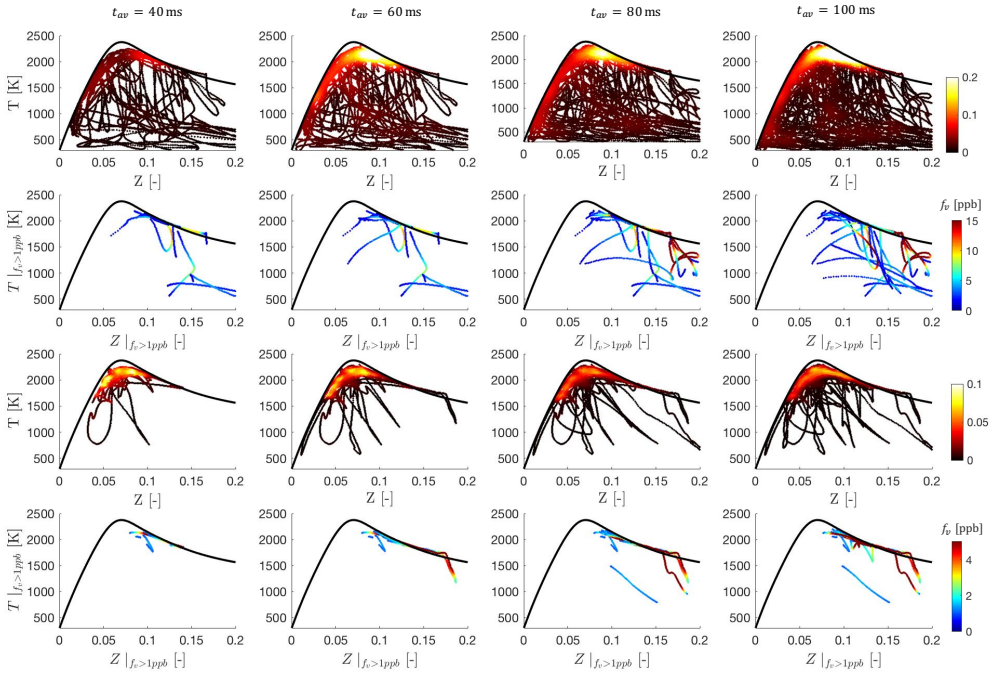

Figure 8.6: *Scatter plot of temperature as function of the mixture fraction colored by the joint t-z probability for t_{av} 40, 60, 80 and 110 ms and the corresponding scatter plot of temperature as function of the mixture fraction conditioned by soot presence ($f_v > 1$ ppb) and colored by the soot volume fraction. First two rows: z|x = 12|8 mm. Last two rows: z|x = 18|8 mm.*

8.3 "Unique" gas phase approach

In a first attempt to quantify the effect of the soot intermittency subgrid model developed by Mueller and Pitsch (2011) on soot production in the DLR burner, a second LES without soot subgrid scale model (NO SGS) has been performed.

Figure 8.7 shows the soot volume fraction averaged over $t_{av} = 60$ ms, which, as already said, corresponds to a time-averaged period longer than what is generally considered in the literature for the DLR configuration (Franzelli et al., 2015; Felden et al., 2018; Koo et al., 2016; Franzelli et al., 2018; Dupoirieux and Bertier, 2016; Wick et al., 2017; Eberle et al., 2018; Grader et al., 2018; Rodrigues, 2018; Gallen et al., 2018). The results from the LES with soot subgrid scale model (SGS) for t_{av}=60 ms are also reported. The NO-SGS computation predicts less f_v than the SGS. The difference between f_v predictions normalized by the f_v with the soot subgrid-scale model, ε, revealed that in some regions, the difference reaches a factor 3. On the contrary, the particle number density fields are quite similar (not shown).

$$\varepsilon = \frac{f_v^{sgs} - f_v^{no-sgs}}{f_v^{sgs}} \tag{8.2}$$

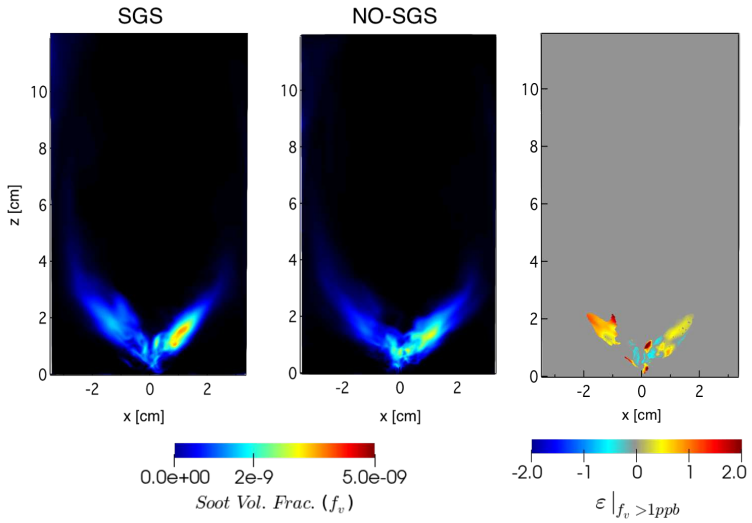

Figure 8.7: *Time-averaged soot volume fraction obtained with two distinct LES one with the subgrid-scale soot model (sgs) and the other without (no-sgs) and the difference ϵ between time-averaged f_v predictions for $f_v > 1$ ppb.*

At this stage, based on the previous statistical analysis, it is impossible to assess whether the differences in soot volume fractions are due to a lack of statistics on rare sooting events or to the contribution of the soot subgrid model. A long time simulation (surely longer than 110 ms) would indeed be necessary to capture a statistically representative number of soot events that discriminate the model contribution.

Assuming that the retro-coupling of the solid phase on the gaseous phase is negligible, as is the case in the DLR burner (Rodrigues, 2018; Monclard et al.,

2020), the proposed approach is based on a unique LES transporting a duplicated set of soot equations, one set accounting for the soot reference model, the other treated with the model under the scope. In this work, the intermittency soot subgrid-scale model (described in Chapter 4) is applied to the first set of equations, whereas no soot subgrid model is considered for the second set of equations. Therefore, the sets of equations, from the three-equation model, write as:

First set considering the soot subgrid intermittency model:

$$\frac{\partial \overline{\rho}\widetilde{Y_s}}{\partial t} + \nabla \cdot (\overline{\rho}(\widetilde{\mathbf{u}} + \widetilde{\mathbf{v}_{th}})\widetilde{Y_s}) = \nabla \cdot (\overline{\rho} D^t \nabla \widetilde{Y_s}) + \overline{\rho}\widetilde{\dot{\omega}}_{Y_s}^{sgs}$$

$$\frac{\partial \widetilde{N_s}}{\partial t} + \nabla \cdot ((\widetilde{\mathbf{u}} + \widetilde{\mathbf{v}_{th}})\widetilde{N_s}) = \nabla \cdot \left(\overline{\rho} D^t \nabla \widetilde{\left(\frac{\widetilde{N_s}}{\rho} \right)} \right) + \widetilde{\dot{\omega}}_{N_s}^{sgs}$$

$$\frac{\partial \widetilde{S_s}}{\partial t} + \nabla \cdot ((\widetilde{\mathbf{u}} + \widetilde{\mathbf{v}_{th}})\widetilde{S_s}) = \nabla \cdot \left(\overline{\rho} D^t \nabla \widetilde{\left(\frac{\widetilde{S_s}}{\rho} \right)} \right) + \widetilde{\dot{\omega}}_{S_s}^{sgs}$$

Duplicated set without the soot subgrid intermittency model:

$$\frac{\partial \overline{\rho}\widetilde{Y_{s_2}}}{\partial t} + \nabla \cdot (\overline{\rho}(\widetilde{\mathbf{u}} + \widetilde{\mathbf{v}_{th}})\widetilde{Y_{s_2}}) = \nabla \cdot (\overline{\rho} D^t \nabla \widetilde{Y_{s_2}}) + \overline{\rho}\widetilde{\dot{\omega}}_{Y_{s_2}}^{no-sgs}$$

$$\frac{\partial \widetilde{N_{s_2}}}{\partial t} + \nabla \cdot ((\widetilde{\mathbf{u}} + \widetilde{\mathbf{v}_{th}})\widetilde{N_{s_2}}) = \nabla \cdot \left(\overline{\rho} D^t \nabla \widetilde{\left(\frac{\widetilde{N_{s_2}}}{\rho} \right)} \right) + \widetilde{\dot{\omega}}_{N_{s_2}}^{no-sgs}$$

$$\frac{\partial \widetilde{S_{s_2}}}{\partial t} + \nabla \cdot ((\widetilde{\mathbf{u}} + \widetilde{\mathbf{v}_{th}})\widetilde{S_{s_2}}) = \nabla \cdot \left(\overline{\rho} D^t \nabla \widetilde{\left(\frac{\widetilde{S_{s_2}}}{\rho} \right)} \right) + \widetilde{\dot{\omega}}_{S_{s_2}}^{no-sgs}$$

where $\widetilde{\mathbf{v}_{th}}$ is the thermophoresis velocity and D^t is the soot turbulent diffusivity, both defined in Chapitre 4 (Section 4.5).

An unique set of gaseous equations is transported (Chapter 4). Therefore, both sets of soot equations experience the same unique temporal and spatial gas phase evolution, allowing to isolate the soot model effects from the uncertainties on gaseous models and numerical sensitivities.

In the following the contribution of the soot subgrid intermittency model (Mueller and Pitsch, 2011) on the soot production is evaluated using the proposed new strategy.

8.4 The effect of the soot subgrid model on soot production

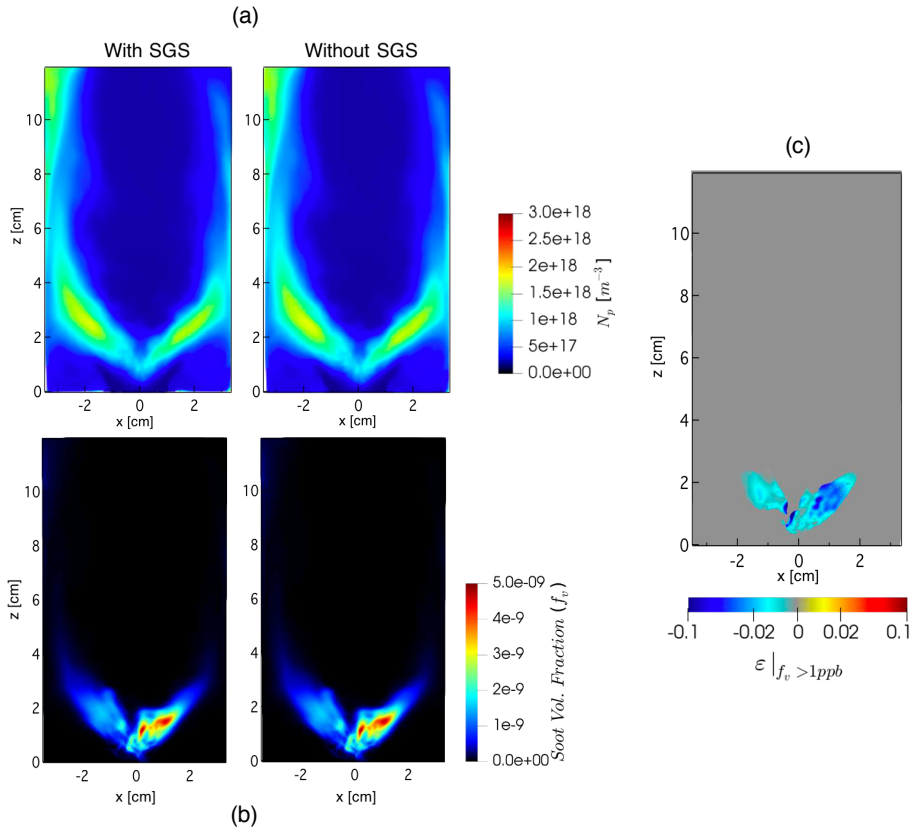

Figure 8.8: *Tiime-averaged soot volume fraction obtained unique gas phase approach and the difference ϵ between time-averaged f_v predictions for $f_v > 1$ ppb.*

Figure 8.8 compares the particle number density (a) and the soot volume fraction (b) fields obtained with the two sets of soot equations with and without the soot subgrid-scale model, respectively, for $t_{av} = 110$ ms. The fields are very similar between the two cases as confirmed by the normalized difference between f_v prediction, ϵ shown in Fig. 8.8c. The f_v prediction with and without the soot subgrid model using the proposed approach leads to contradictory conclusions compared to results of Fig. 8.7, obtained by performing to separate LES. Such discrepancies are most probably due to a lack of statistical convergence of the intermittent soot events.

Figure 8.9 shows the radial profiles of ϵ (normalized f_v Eq. (8.2)) for three heights in the sooting zone. No relevant differences can be identified on the profiles. This seems to indicate that by imposing the same thermochemical

history to the soot particles it is possible to quickly identify the differences on their responses to the same rare sooting events. In particular, the ϵ field in Fig. 8.8c, shows that f_v predicted without the soot subgrid-scale model is about 2% higher than with the soot subgrid-scale model in the region where f_v is higher than 1 ppb. In some localized regions of high soot load, f_v predictions can present a difference of 10 % suggesting that the model effect appears more relevant for high soot load. The effect on the mean Np is negligible (not shown).

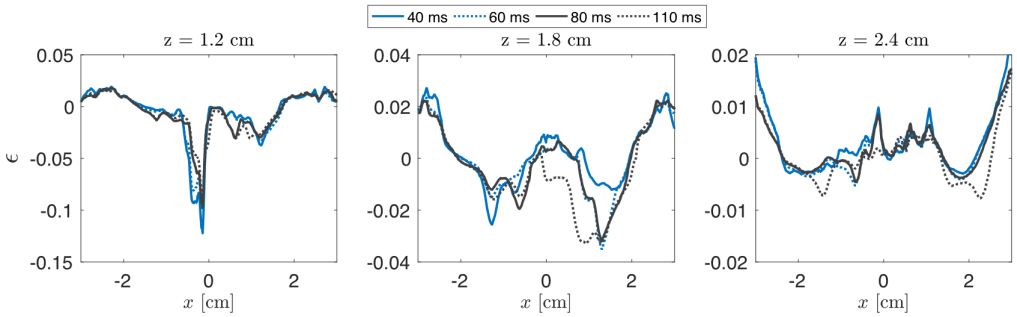

Figure 8.9: *Radial profiles of the normalized f_v difference ϵ for $f_v > 1$ ppb.*

The main advantage of this approach is the possibility to investigate the model influence in the instantaneous soot fields without waiting for the statistical convergence of the solid phase quantities. Figure 8.10 compares instantaneous soot volume fraction and particle number density obtained with and without the soot subgrid-scale model using the 'unique' gas-phase approach. Particle number density is slightly affected by the soot subgrid-scale model. It can be observed in Fig. 8.11 that the sources term driving particle number density (nucleation and coagulation) are very similar. However, the set without the soot subgrid-scale model predicts high soot volume fraction for high f_v load, as observed in the mean field in Fig. 8.9. It is ascribed to the higher surface growth and condensation rates (Fig. 8.11), which depends on the particle size. Similar to the surface growth, oxidation is also slightly high without the soot subgrid-scale model.

It is important to note that most of the soot events composing the scatter plots are characterized by low soot load where the effect of the soot intermittency model appears to be negligible. It is confirmed by the cumulative distribution function shown in Fig. 8.12 which reveal that soot is mainly characterize by low soot load ($f_v < 10$ ppb) with similar prediction with and without the soot subgrid intermittency model, at least for the observed soot events. Even if, in order to definitely conclude, the statistical convergence should be attained for the soot fields, the observed trends indicate that the intermittency soot subgrid model has a low impact on the soot prediction in the DLR burner.

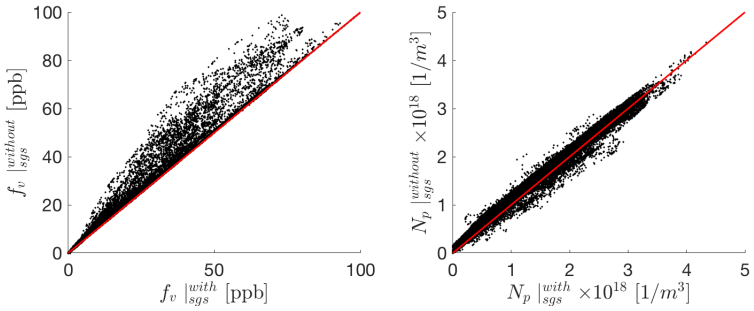

Figure 8.10: *Comparison of several instantaneous (22 instants in 40 ms) particle number density (right) and soot volume fraction (left) obtained with (absciss) and without (ordinate) the soot intermittency model.*

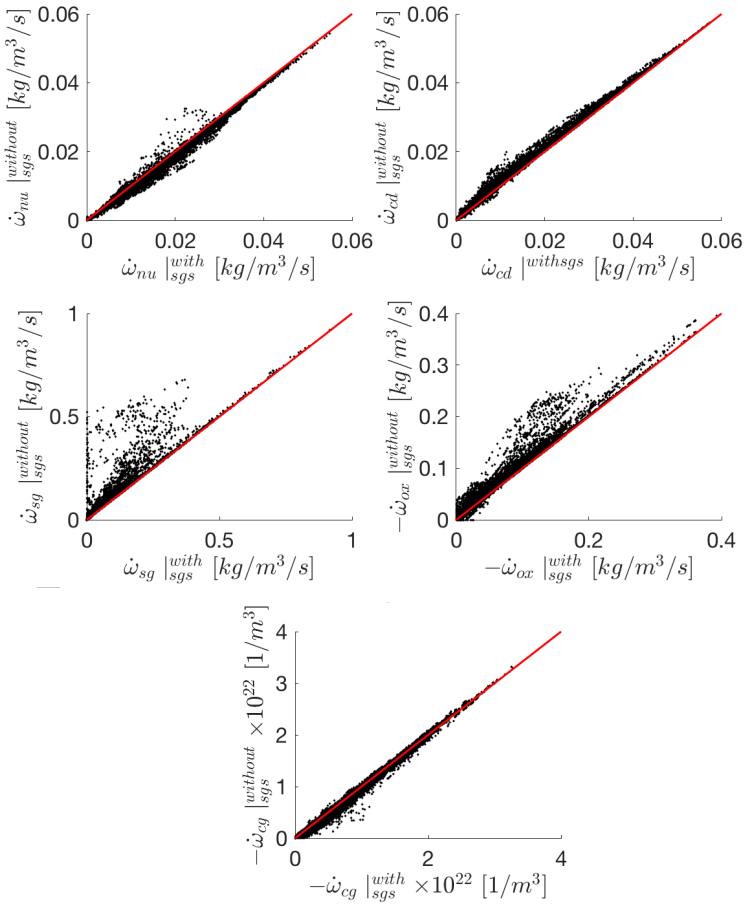

Figure 8.11: *Comparison of several instantaneous (22 instants in 40 ms) soot source terms obtained with (absciss) and without (ordinate) the soot intermittency model. Top: nucleation $\dot{\omega}_{nu}$ and condensation $\dot{\omega}_{cd}$. Center: surface growth $\dot{\omega}_{sg}$ and oxidation $\dot{\omega}_{ox}$. Bottom: coagulation $\dot{\omega}_{cg}$.*

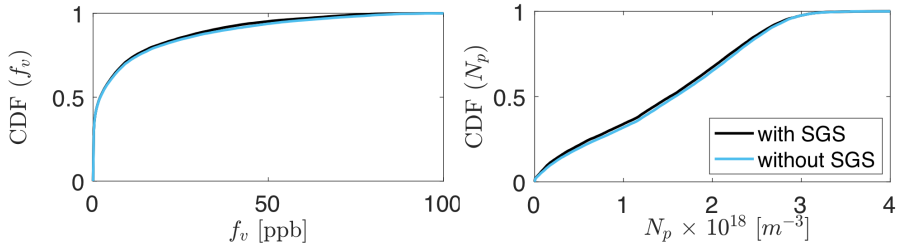

Figure 8.12: *Cumulative distribution function of soot volume fraction (left) and particle number density (right) for the scatters in Fig.* **??**.

8.5 Conclusion

Soot production in turbulent flames is characterized by an intermittent nature in space and time. The numerical prediction of sooting turbulent flames is then quite challenging not only for modeling issues but also to obtain a statistical description of the solid phase. Considering the DLR burner, it was found that 60 ms time-averaging, generally considered in previous publications, is sufficient to guarantee the statistical convergence of the gas phase. However, a much longer averaging time is needed for a reliable statistical description of the soot volume fraction (more than 110 ms). This is because soot events are rare since specific thermochemical conditions of the gaseous phase are required to promote soot production. Therefore, ensuring statistical gas phase convergence is not enough to obtain accurate soot prediction in configurations presenting high soot intermittency, preventing a reliable model evaluation. To address this issue, a new strategy to evaluate soot modeling in turbulent flame was proposed.

In order to discriminate the effect of soot models by comparing results from a reference description and a new model, it is essential to ensure that particles experience the same temporal and spatial gas phase evolution. For this, a unique gas phase approach has been proposed by transporting a new set of soot scalars for the new model in addition to the reference set. The approach has been applied to investigate the effect of Mueller and Pitsch's soot intermittency subgrid model on soot prediction in the DLR burner. The analysis of instantaneous and time-averaged results indicates a low impact of the soot subgrid-scale model in the considered configuration. A mean difference of about 2% between time-averaged soot volume fraction f_v predictions was obtained, which can be considered quite low when considering the models uncertainties.

Overall, the proposed strategy is attractive to evaluate soot models, notably when simple soot models are used without retro-coupling of soot fields on the gas phase, allowing comparison of models response to the same gaseous conditions. Additionally, the new approach is characterized by a reduced CPU cost,

compared to the two-simulation approach. In the presented case, while the two-simulation strategy required 90000 CPU hours per 10 ms (45000 CPU hours to each simulation run on Intel E5-1920 processors), the proposed approach required only 56000 CPU hours per 10 ms.

Conclusion

Understanding soot particle formation is of primary importance in developing low emission devices due to its harmful impact on health and the environment. Numerical simulation is a powerful tool to study the processes involved in soot production in combustion systems. The Large Eddy Simulation (LES) approach was retained in this thesis to investigate soot production in an aero-engine combustor. However, predicting soot production in such complex systems using an LES formalism represents a great scientific challenge for many reasons:

- In-depth knowledge and the modeling of the complex physico-chemical processes involved in soot production are still lacking.
- Multiple combustion regimes coexist in technical devices, presenting an additional difficulty for high fidelity simulations.
- Soot particles are confined in very thin structures interacting with turbulence. Because of their size, these structures may not be resolved on the LES grids, so that specific soot subgrid-scale models are required.
- Finally, the validation of newly developed models is difficult due to the non-linear interactions between such multi-physical phenomena and the massive computational resources required for a reliable statistical representation.

In the context of the SOPRANO European project, the main objective of this thesis is to evaluate the reliability of the LES formalism for turbulent sooting flames in an aero-engine model combustor, the DLR burner, to improve the soot prediction and contribute to the development of low-emission aircraft systems. For that purpose, three LES issues for turbulent sooting flames were investigated. First, statistical convergence was discussed, then the grid resolution effect on gaseous and soot statistics was studied, and finally, the effect of soot models on soot prediction in turbulent conditions is evaluated by investigating the effect of the soot surface reaction model and the soot subgrid intermittency model.

The first part of this thesis concerned soot modeling and prediction in lami-

nar flames. The reference sectional approach due to Rodrigues et al. (2017), coupled with detailed chemistry, was evaluated in laminar premixed and non-premixed ethylene-air flames. Although this model provides a good prediction of soot volume fraction and particle size distribution in premixed conditions, it fails in non-premixed flames. Indeed, an accurate model response to the different combustion regimes is primordial when considering configuration under technical conditions, where multiple combustion regimes coexist. Despite the huge efforts made by the scientific community to develop accurate soot models, large gaps in understanding soot formation still exist. Among the soot processes, the surface growth model may not be well described in non-premixed flames. Therefore, an improved model, called HACA-RC*, was proposed for the soot growth mechanism. In the reference model, the soot surface is activated by the H abstraction via surface reaction with H, which coexists with the soot growth species (C_2H_2). The addition of a new H-abstraction reaction by soot surface reaction with the radical CH_3, which further spatially overlaps with C_2H_2, leads to a higher soot particle surface reactivity enabling the reproduction of the experimental soot yield in both premixed and non-premixed regimes. As a perspective, the dependence on temperature of the new reaction may be considered to improve the model quality and precision. However, it also requires an improvement of the understanding of soot processes and properties in non-premixed flames.

In the second part of this thesis, an LES simulation of an aero-engine model combustor, the DLR burner, was performed. In this case, a three-equation model is used to describe the solid phase as it provides similar accuracy for a lower CPU cost compared to the sectional approach. First, the reliability of the LES formalism was quantified through statistical analysis. This analysis revealed that numerical convergence is quite challenging to be achieved in the considered burner since it is characterized by a complex flow structure and a highly intermittent soot production. It was shown that soot production occurs only for scarce local gaseous conditions. Therefore, for a reliable statistical representation of soot occurrence, a longer time-averaging is required implying a massive CPU cost. The sensitivity of results to grid resolution was also investigated in three grids with different spatial resolutions. It was found that negligible differences in the gas phase structure due to the different grid resolutions may lead to significant soot prediction discrepancies. However, a longer physical time should be simulated to conclude on the grid resolution on soot prediction, which was not affordable in the scope of this thesis.

Then, the impact of soot modeling in soot prediction in the DLR burner via LES was investigated. First, the impact of the improved surface reaction HACA-RC* model was evaluated. The statistical analysis of the soot yields shows that the maximum soot volume fraction increases by a factor of three compared to the reference model due to the substantial increase of the surface reaction rates. However, the HACA-RC* model could not detect new zones of surface

reactions as expected from laminar flames but only enhance reaction rates in the reaction zones already identified by the reference HACA-RC model. The proposed HACA-RC* modification may have a more relevant interest in other turbulent configurations where H and CH_3 may not overlap, likely in turbulent jet non-premixed flames. Although a better agreement of the soot volume fraction peak with experimental data is obtained when using the HACA-RC* model, quantitative conclusions may depend on the specific used models for solid and gas phases and the corresponding model assumptions and parameters. Therefore, the impact of the HACA-RC* model, coupled with other gaseous and soot models, should be verified. In a first attempt, model evaluation can be done in laminar canonical flames.

Finally, the impact of the soot subgrid intermittency model was also evaluated. However, soot model evaluation based on two different simulations, currently employed for the purely gaseous phase, provides only the tendency of soot yield as a consistent quantitative evaluation requires a longer physical time to guarantee a statistical representation of the rare soot events. Motivated by the difficulties in evaluating soot model performances in turbulent flames using the classic strategy, a new strategy based on a unique LES transporting a duplicated set of soot equations was proposed. Both sets, one accounting for the soot reference model, the other treated with the model under the scope, experience the same unique temporal and spatial gas phase evolution. Therefore, it was possible to isolate the soot model effects from the uncertainties on gaseous models and numerical sensitivities rigorous model evaluation. Thanks to this approach, the first indications of the soot intermittency model contribution to soot prediction in the investigated burner were proposed. It was found that the model contribution seemed to be negligible in the studied configuration.

This work highlighted the difficulties in predicting soot particles in complex configurations under relevant conditions using the LES approach. It should be recognized that the intrinsic complexity of this configuration complicates the soot model evaluation. In order to overcome the difficulty in simulating the secondary jet dynamics, the operating condition without the secondary air injection may be preferred in the future as a reference case. Even if LES is a promising tool to predict soot production in industrial combustors, the parametric studies necessary to the development of soot models are associated today to extremely high CPU cost. In addition, the non-linear interactions between such multi-physical phenomena are extremely difficult to characterize in an LES framework, which relies on subgrid-scale models and simplified physical descriptions. On the other hand, Direct Numerical Simulation (DNS) is a powerful tool to study soot production parallel to the experimental approach and to contribute to the development of LES closure models specific for sooting flames which still require much effort. In this optic, an academic configuration adapted to the evaluation of soot subgrid-scale models through DNS has been designed at the end this thesis work. It consists of a turbulent sooting counterflow 2D

flame subjected to isotropic homogenous turbulence. An a priori analysis of the intermittency subgrid model, used for the LES simulations performed during the present work, is presented in Appendix A, providing a preliminary study about its contribution to soot prediction. In the perspective of the presented work, this new configuration is expected to provide a new database for parametric studies, an essential step for soot model development and understanding of soot production in turbulent conditions.

Appendix A

A priori analysis of the intermittency soot subgrid model

Direct Numerical Simulation (DNS) is a powerful tool to study turbulent combustion in a complement of experimental observations. The DNS results are useful in the development of subgrid-scale models required by the Large Eddy Simulation (LES) approaches (Boger et al., 1998; Moureau et al., 2011; Domingo and Vervisch, 2017), even when simple canonical flames are used (Proch et al., 2017). Here, a DNS of a turbulent 2D counterflow non-premixed ethylene-air sooting flame is performed. The results are used as a database for a priori analysis of the intermittency model (Mueller and Pitsch, 2011), currently used in LES simulations of sooting flames, in order to provide a first evaluation of its ability in using the quantities solved in an LES to reproduce the effects of the subgrid scales.

A.1 Introduction

DNS is a valuable tool to understand turbulent combustion as well as the physical and chemical mechanisms involved in soot production. Nevertheless, when considering turbulent sooting flames, few DNS studies can be found in the literature. Lignell et al. (2007) have performed the first DNS of a two-dimensional non-premixed sooting ethylene flame in a temporally evolving shear layer using a reduced chemical mechanism and a semi-empirical soot model. It was found that in turbulent flames, soot can be observed in a broader region in the mixture fraction space compared to laminar flames due to differential diffusion and turbulent transport effects. The relative position of soot to flame

impacts soot reactivity and radiative properties. This study was later extended to a three-dimensional configuration (Lignell et al., 2008). The flame dynamics was found to be similar in both 2D and 3D cases, but enhanced mixing rates in the 3D cases affect soot distribution in the mixture fraction space. Yoo and Im (2007) have studied the soot dynamics in a turbulent counterflow ethylene-air flame. Semi-global gas and semi-empirical soot models were used to reduce the computational cost. It was found that turbulence can affect soot in two main ways: increasing flame volume leading to higher levels of soot and transporting soot away from the flame zone resulting in lower soot load. Afterward, Bisetti et al. (2012) have performed a DNS of a two-dimensional non-premixed sooting n-heptene flame, using a chemical mechanism considering the PAH formation pathways up to naphthalene and the HMOM approach (Mueller et al., 2009) for the soot description. Radiative heat transfer from soot was neglected due to the low soot load obtained by nitrogen dilution in the fuel. They concluded that naphthalene is strongly sensitive to scalar dissipation compared to C_2H_2, then the C_2H_2-based nucleation may misrepresent the effect of turbulent mixing on soot production. Similarly to Lignell et al. (2007), this study was extended to a three-dimensional case (Attili et al., 2014), where a Lagrangian approach was used to characterize soot dynamics coupled with the classical Eulerian grid-based solver for the gas phase. This strategy limits the needs in high spatial resolution and enables the investigation of the particle time history. However, a large number of notional particles is required. While reactive scalars show a homogenous-like spatial distribution, the soot mass fraction presents a strong spatial variability due to the combination of different phenomena: the PAH sensitivity to dissipation rate, the non-linearity of soot source terms and the low mass diffusivity of soot particles and differential diffusion with respect to the gaseous species. More recently, Arias et al. (2015) have performed a DNS of a non-premixed ethylene-air flame, using the ABF chemistry including PAHs up to pyrene (Appel et al., 2000) for the gas phase description and MOMIC aroach for soot description. The temporal analysis reveals that soot oxidation is the main mechanism for soot suppression and it is highly sensitive to velocity fluctuations, in contradiction with Bisetti et al. (2012), who stated that PAH sensitivity to scalar dissipation is responsible for the decrease in soot mass. This divergence in results was attributed to the fact that Bisetti et al. (2012) studied the early phase of soot evolution when nucleation is predominant while Arias et al. (2015) investigate the effect of the turbulence on soot production after the transitional interval. Therefore, the effect of turbulence on soot production may depend on the soot evolution stage and the physical model retained for gas and solid phases.

Additionally, the development of LES models are generally based on DNS results. An *a priori* analysis based on the filtered DNS results is a key step in the development and evaluation of subgrid-scale models. The soot subgrid intermittency model (Mueller and Pitsch, 2011), used in the LES presented in

this manuscript, was developed using a DNS database of a temporally evolving non-premixed n-heptane flame Bisetti et al. (2012) was used. However, only the early stages of soot formation were considered. The observed features of the obtained soot subgrid-scale model, classically applied in fully developed turbulent flames, should still be confirmed by looking at different DNS configurations and physical models. Therefore, in order to evaluate the generality of the conclusions proposed by Mueller and Pitsch (2011), the present study investigates the soot subgrid intermittency model by performing a *priori* analysis of a DNS database of a two-dimensional counterflow configuration considering a different soot formation process description. Experimental and numerical researchers have extensively used counterflow flames to study soot formation in laminar conditions (Kennedy et al., 1990; Lindstedt, 1994; Wang et al., 2015; Rodrigues et al., 2017; Xu et al., 2018). However, to our knowledge, only the work from Yoo and Im (2007) can be found in the literature when considering turbulent sooting conditions. This configuration provides computational modeling and a cost advantage over the classical jet flame due to its compactness and might be of most relevance to study flame-soot-turbulence interaction (Coppola et al., 2009).

A.2 Configuration description and numerical methods

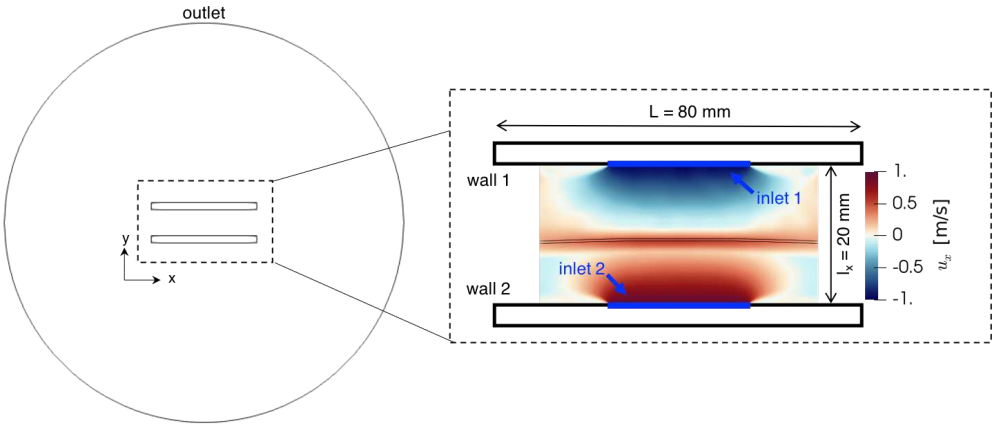

Figure A.1: *Schematic 2D counterflow geometry colored by the axial velocity and reaction zone (black isoline of the source term of progress variable $\dot{\omega}_{Y_C} = 10\ s^{-1}$) for the reference laminar flame.*

The configuration selected for the study, represented in Figure A.1, is a counterflow turbulent 2D flame. The geometry is composed of two inlets though fuel (inlet 1) and oxidizer (inlet 2) are injected. The inlets are separated by a

distance of $l_x = 20$ mm and are surrounded by walls (black lines in Fig. A.1). Therefore, the fluid domain size where the counterflow flame is established (the zoomed region in Fig. A.1) is 80 mm vs. 20 mm, with the width of the inlet (blue lines in Fig. A.1) of 20 mm. The fuel stream consists of ethylene diluted with 20% of nitrogen (in volume) at 300 K and the oxidizer is air (21 % oxygen and 79 % nitrogen) at 300 K. An ambient atmosphere with a diameter fifty times the inlet length is included in order to impose a pressure boundary condition far from the inlets avoiding numerical instability and achieving a stable flame.

The grid is composed of 3 million triangular cells. The counterflow fluid domain (zoomed zone in Fig. A.1) contains 1.2 million homogeneous cells with size $h_{DNS} = 50$ μm for the edges of the tetrahedrons. In the atmosphere, the cell size smoothly increases, reaching 10 mm at the outlet.

The unsteady Navier-Stokes equations for continuity, momentum, temperature are described in Chapter 1. In order to make the DNS affordable, the gas phase is described using the FPV approach (Ihme and Pitsch, 2008) presented in Chapter 4 (Section 4.3). Therefore, instead of transporting multiple species, two variables parameterize the look-up table: the mixture fraction Z and the reaction progress variable Y_C. The corresponding flamelet library is generated using the detailed mechanism KM2 (Wang et al., 2013) with 202 species and 1351 reactions, enabling soot precursors formation up to seven aromatic rings. Unity Lewis number is considered for all species, including PAH. Although differential diffusion is important for the soot precursors due to its impact on the soot load, it is expected not to affect the evolution of soot particles significantly (Bisetti et al., 2012; Attili et al., 2014). Moreover, soot production can also be strongly affected by the use of a tabulation method for PAH description since their concentration is highly sensitive to strain rate (Mueller and Pitsch, 2012; Attili et al., 2016). However, here we are more interested in the effect of small scales on the processes governing soot evolution once particles are formed, i.e., we are not considering nucleation, which is mainly governed by PAH dimerization. Although condensation is also dependent on PAH concentration, it has been observed that accounting for the physical model retained in this manuscript, its contribution to the total soot volume fraction is negligible compared to surface growth.

The solid phase is described using the three-equation model (Franzelli et al., 2018), introduced in Chapter 1. Nucleation, condensation, coagulation, and surface reactions (oxidation and surface growth) phenomena are considered source terms. Surface reactions are described using the recent HACA-RC* model (Tardelli et al., 2019) (Chapter 3). Despite the model simplifications, it can be argued that the presented study provides a valuable preliminary evaluation of the phenomena governing turbulence-chemistry-soot interaction.

Finally, radiation is not included in this study, even though the contribution

of radiative heat loss from gas and solid phases may not be negligible (Pitsch et al., 1998; Narayanan and A.Trouvé, 2009).

The transported equations are solved using the explicit AVBP code (Schonfeld and Rudgyard, 1999) . The third-order in space and fourth-order time finite element TTG4A scheme (Donea et al., 1987) is retained for the simulations with a CFL number of 0.7.

A.3 Initialization of the HIT field

Before injects turbulence a counterflow steady laminar flame is established. For that, the mixture fraction field is initialized using an one-dimensional flamelet solution with a prescribed strain rate a = 100 s^{-1}, corresponding to about 1/15 of the extinction strain rate. Once initialized, the progress variable and temperature are mapped from the mixture fraction space onto the x-direction to reconstruct the initial fields. The initial mixture fraction and progress variable profiles are shown in Fig. A.2. Finally, the velocity field ($\mathbf{u} = u(x,y)e_x + v(x,y)e_y$) is initialized.

The axial velocity at the fuel inlet is defined as:

$$v_{fuel}(x,y) = ay \tag{A.1}$$

To obtain similar momentum at both inlets and a stable flame in the middle of the domain, the velocity in the oxidizer side writes:

$$v_{ox}(x,y) = -\sqrt{(}\frac{\rho_{fuel}}{\rho_o x})ay \tag{A.2}$$

Similarly, the transverse velocity is defined as:

$$u_f(x,y) = ax \qquad u_{ox}(x,y) = -\sqrt{(}\frac{\rho_{fuel}}{\rho_o x})ax \tag{A.3}$$

The soot scalars are not initialized so that no soot is present at the beginning of the simulation. A stable converged sooting flame is obtained after 20 ms of the simulation (corresponding to two flow time). The reaction zone δ_r (estimated as the half height of the source term of the progress variable $\dot{\omega}_{Y_C}$) is resolved over 5 points ($\delta_r = 5\ h_{DNS}$), the thermal thickness ($(T_b - T_u)/\mid \nabla T \mid_{max}$ where b and u are burned and unburned states, respectively) is $\delta_{th} = 22\ h_{DNS}$, while the soot volume fraction layer thickness δ_{f_v} (estimated as the half height of the soot volume fraction f_v) is $\delta_{f_v} = 10\ h_{DNS}$.

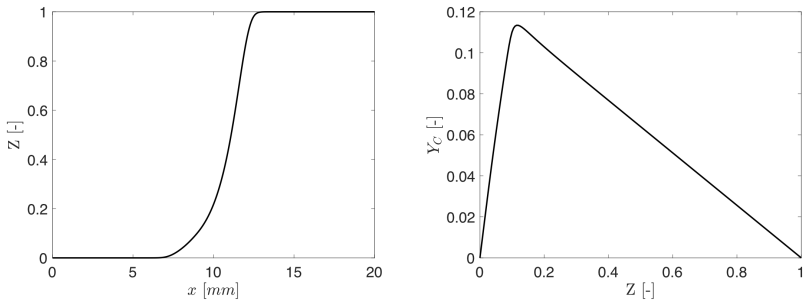

Figure A.2: *One-dimensional flamelet used to initialize the two-dimensional flames.*

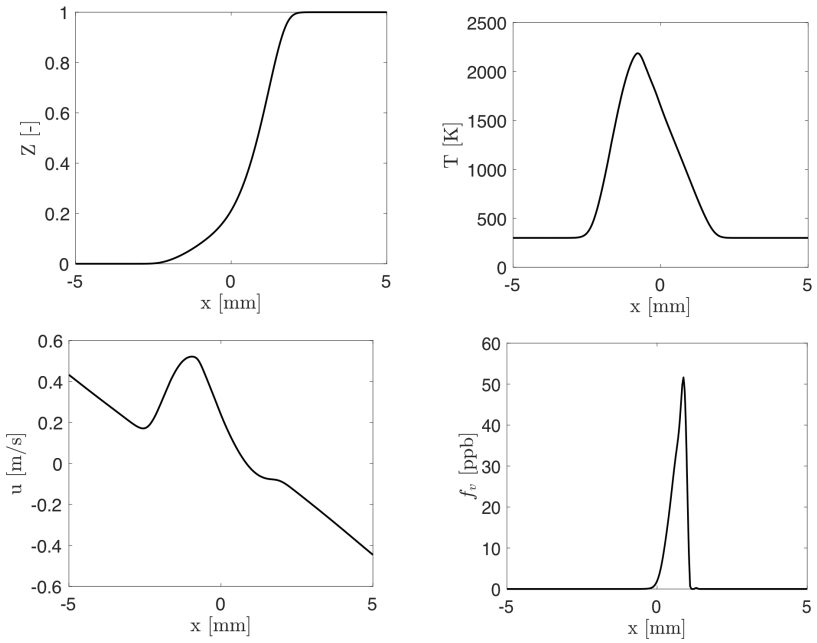

Figure A.3: *Centerline profiles of mixture fraction, temperature, axial velocity and soot volume fraction.*

Once the steady flame is established (Fig A.3), the injection of homogeneous isotropic turbulence is activated at the two inlets by prescribing velocity fluctuation u' (u'_{fuel} and u'_{ox}) and integral length scale l_t according to the AVBP procedure based on Passot and Pouquet (1987). For that, Navier-Stokes Characteristic Boundary Conditions (Poinsot and Lele, 1992) are used to prescribe the boundary conditions with imposed temperature (T), bulk velocity (u_{fuel} and u_{ox}), and scalars (Z, Y_C, Y_s, N_s, S_s) values at the inlets and pressure at the outlet. In order to feed the turbulent eddies, the turbulent velocity fluctuation (u'_{fuel} and u'_{ox}) and the integral length scale l_t are also imposed at the inlets. For the wall, an adiabatic non-slip boundary condition is used.

Two different turbulent cases were considered. For a similar turbulent Reynolds number ($R_t = l_t u'/\nu$), CASE I presents an integral length scale half of that CASE II and the turbulence intensity (I = u/u') is twice the CASE II. Therefore, the differences in turbulence time scales can be expected to impact mixing and soot dynamics differently. The calculation parameters and characteristic values of the two cases are summarized in Table A.1. The simulations are advanced up to 40 ms and 60 ms, with a time step Δ t = 2 10^{-8} s for CASE I and CASE II, respectively. They correspond to four and five flow time ($\tau_{flow} = l_x/2u_0$, l_x is the distance between inlets and u_0 is the bulk velocity) and about 50 and 19 integral time scales ($\tau_{eddy} = l_t/u'$), for the CASE I and II, respectively. This is long enough for the velocity and scalar fields to forget the initial conditions. The Kolmogorov length scale η_k computed with the parameters from injection ($\eta_k = l_t Re_t^{-3/4}$) are 42 μm and 84 μm, for CASE I and CASE II, respectively. From cold calculation, it has been observed that downstream, approaching the stagnation plane, η_K increases by a factor 2. Under reactive conditions, due to the increase in viscosity, the smallest scales are dissipated near the vicinity of the flame front, where soot is produced. Therefore, it can be considered that the grid resolution is fine enough to resolve the turbulent flow scales.

Table A.1: *Computational parameters and characteristic spatial and time scales of the injected turbulence at both inlets for the two test cases.*

Parameters	CASE I	CASE II
h_{DNS} [μm]	50	
l_x [mm]	20	
t_{sim} [ms]	40	60
l_t [mm]	0.8	1.6
u	1.0	0.5
u'	1.0	0.5
Re_t	50	50
τ_{eddy} [ms]	0.8	3.2

A.4 Analysis of the turbulent soot production

Figure A.4 shows the temporal evolution of the volume-integrated temperature, particle number density, soot volume fraction and mean soot surface. The injected turbulent eddies are fully convected into the domain after 10 and 5 τ_{eddy} for CASE I and CASE II, respectively, and start to interact with the initially laminar flame and the planar soot fields. For both cases, the temporal

evolution of the volume-integrated particle number density appears to be correlated to the temporal evolution of the volume-integrated temperature in the zone of T > 1500 K. In contrast, the volume-integrated soot volume presents a sharp increase followed by a drastically decrease. For CASE I, the total soot volume fraction reaches a maximum value after 28 τ_{eddy}, while for CASE II, with different turbulence intensity and τ_{eddy} (Table A.1), the total soot volume fraction reaches its maximum value, that is lower than in CASE I, after 17 τ_{eddy}. Attili et al. (2015) have found that soot volume fraction is sensitive to the Damkohler number, the ratio between the turbulent time scale and the chemical time scale. In contrast, the particle number density was found to be not significantly affected by the Damkohler number.

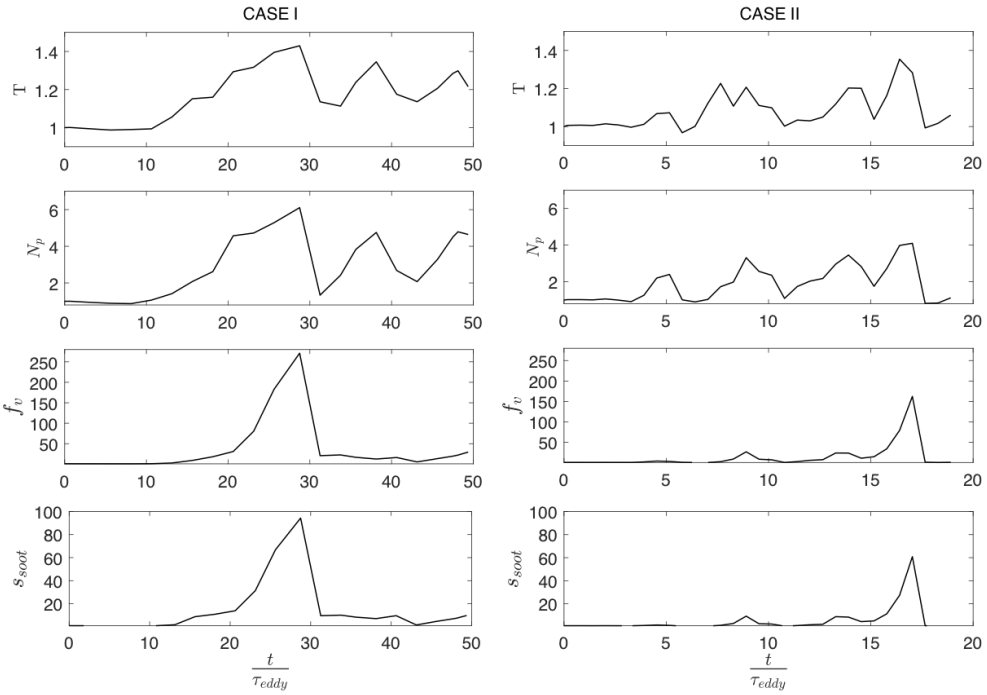

Figure A.4: *Temporal evolution of the flame volume-integrated temperature, particle number density, soot volume fraction and mean surface normalized by the respective laminar values for CASE I (left) and CASE II (right). Time is normalized by the characteristic time scale τ_{eddy} of the integral length scale.*

To further investigation of the soot dynamics, the volume-integrated soot source terms are shown in Figure A.5. Consistent with the particle number temporal evolution, the volume-integrated nucleation and coagulation rates present a temporal evolution correlated to the volume-integrated temperature evolution in both CASE I and CASE II. The same is observed for condensation as it is coupled with flame evolution via its dependence on PAH concentration. For a

high volume-integrated temperature, these three mechanisms present a higher rate. Surface reactions appear to be significantly affected by the turbulence. Besides dependence on species concentration and temperature, surface reactions depend on the particle size. It can be noted that, the higher volume-integrated surface reaction rate occurs at the same time as the higher volume-integrated mean soot surface shown in Fig. A.4. The peak of total soot volume fraction also coincides with the mean soot surface peak, suggesting that soot load is mainly governed by surface growth, which presents a rate two times higher than condensation.

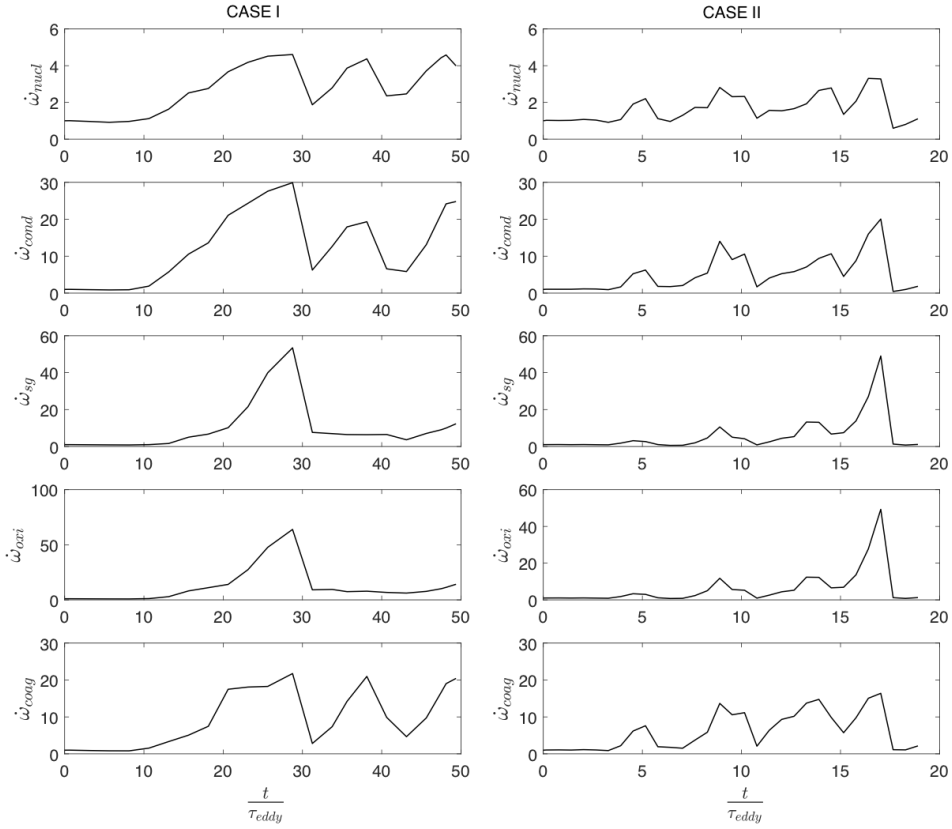

Figure A.5: *Temporal evolution of the flame volume-integrated soot source terms normalized by the respective laminar values for CASE I (left) and CASE II (right).*

The local turbulence effect on the soot volume fraction evolution f_v is illustrated by the scatter plots of f_v as a function of the mixture fraction and temperature in Fig. A.6 colored by the different source terms for different instants after 10 and 5 τ_{eddy} for CASE I and CASE II, respectively. Soot volume fraction peak and dispersion are quite different between the two cases. For CASE I, which presents a high turbulence intensity, f_v is widely spread in the mixture fraction

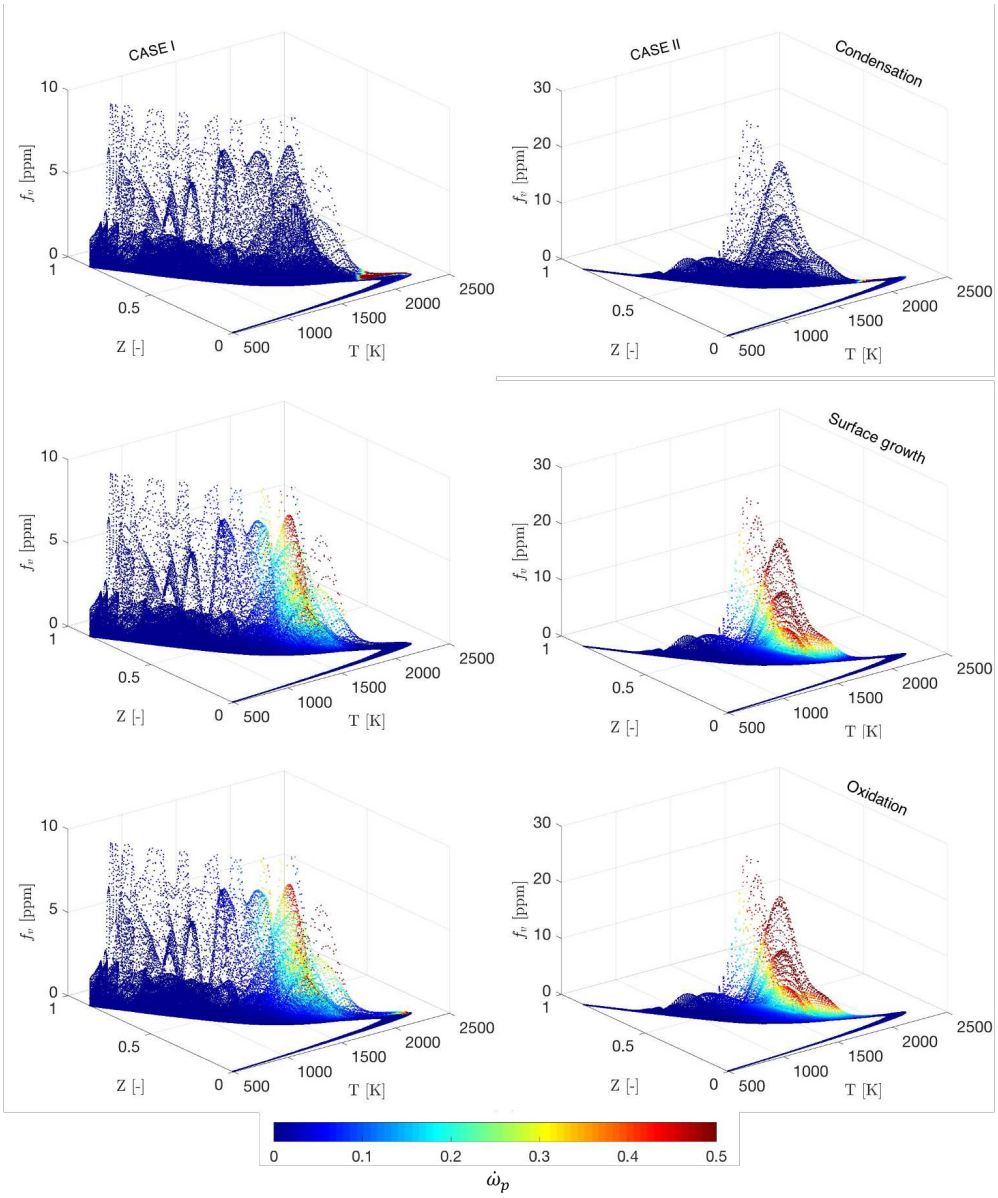

Figure A.6: *Scatter plots of soot volume fraction f_v as a function of mixture fraction and temperature colored by the source terms ($\dot{\omega}_p$ with p = condensation - top, surface growth - middle and oxidation - bottom) for CASE I (left) and CASE II (right). Source terms are normalized by their respective observed maximum value ($\omega_{cond,max} = 1.310^{-3}$ and 6.5710^{-4}, $\omega_{sg,max} = 10.23$and10.57 and $\omega_{ox,max} = -2.5310^{-1}$ and -2.410^{-1} for CASE I and CASE II, respectively).*

space compared to the laminar flame where maximum soot volume fraction (f_v = 50 ppb) is observed for Z = 1. In contrast, for CASE II, the soot volume fraction is observed in a narrow mixture fraction range, but in magnitude, the

soot volume fraction is much higher than in CASE I. For CASE I, the smaller turbulent structures with high turbulent intensity lead to a strong differential diffusion and thus to soot dispersion in the mixture fraction space as already numerically evidenced by Yoo and Im (2007) in a similar flame configuration. The scatter plots also reveal that condensation occurs mainly at high-temperature (T≈ 2000 K) zones and high mixture fraction (Z ≈ 0.1). Surface reactions (surface growth and oxidation) occur on broader temperature (around T≈ 1500 K) and mixture fraction ranges (Z ≈ 0.2-0.4) contributing to soot load in this zones.

Figure A.7 shows the 3D scatter plots of particle number density as a function of temperature and mixture fraction colored by the nucleation rate. Nucleation occurs at a relatively high mixture fraction and temperature, confirming that the presence of soot particles outside these conditions is then due to turbulent transport. Finally, Fig. A.8 shows that coagulation rate seems to be more sensitive to the particle number density than by their soot load, in agreement with the observations from Mueller and Pitsch (2011). The highest coagulation rates are observed at the highest particle number density and relatively high temperatures since it depends on the size and density of particles.

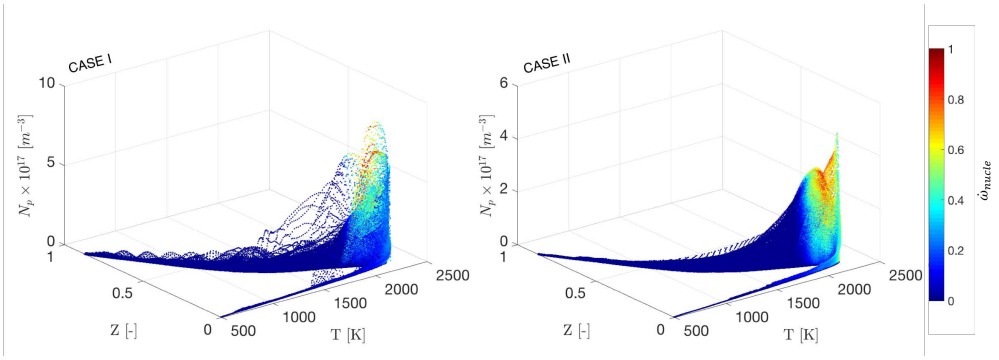

Figure A.7: *Scatter plots of particle number density N_p as a function of mixture fraction and temperature colored by the normalized nucleation rate for CASE I (left) and CASE II (right). Nucleation is normalized by the observed maximum value ($\omega_{nu,max} = 1.2010^{-3}$ and 6.3610^{-4} for CASE I and CASE II, respectively).*

This analysis illustrated the complexity of the turbulence effect on soot production. Although the evident temporal and spatial variability of soot volume fraction currently interpreted as the soot intermittency, a unique solution is initially considered for the *a priori* analysis in analogy with the work of Mueller and Pitsch (2011). In order to avoid the initial flame transient stage, the solutions at 24 and 36 ms are retained for CASE I and CASE II, respectively. It corresponds to 2 τ_{flow} + 5 τ_{eddy}. These solutions contain enough soot structures (filaments and pockets) to enable the analysis. The corresponding instantaneous fields of vorticity, source term of the progress variable and soot volume

fraction are shown in Fig. A.9 for the two cases.

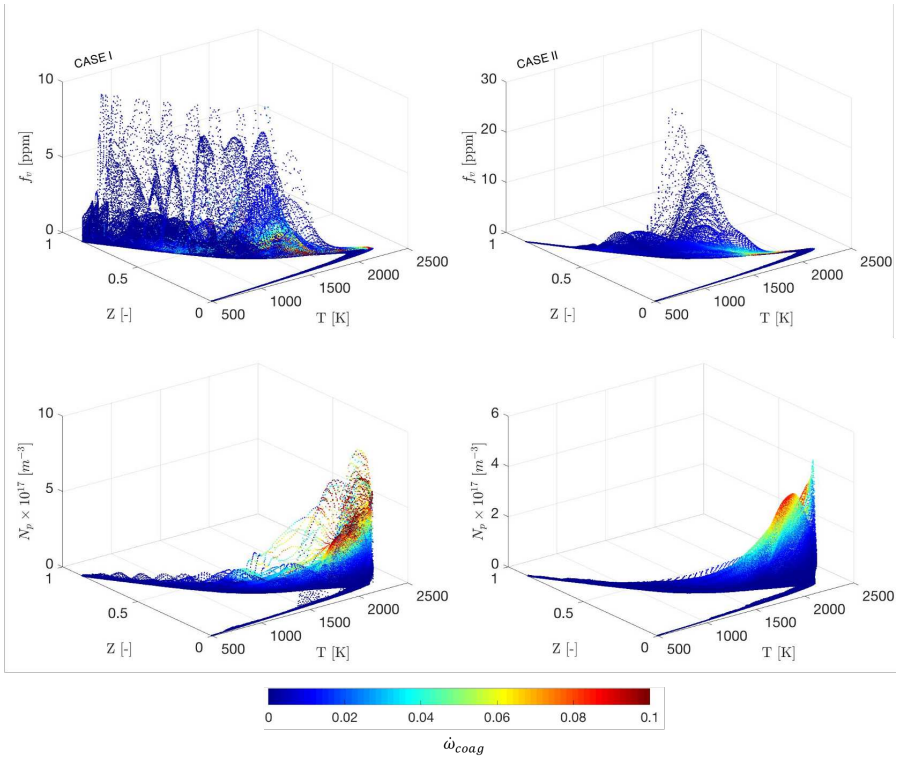

Figure A.8: *Scatter plots of soot volume fraction f_v (top) and particle number density N_p (bottom) as a function of mixture fraction and temperature colored by the coagulation source term for CASE I (left) and CASE II (right). Coagulation rate is normalized by the respective observed maximum value ($\omega_{coag,max} = -5.9610^{20}$ and -2.9810^{20} for CASE I and CASE II, respectively).*

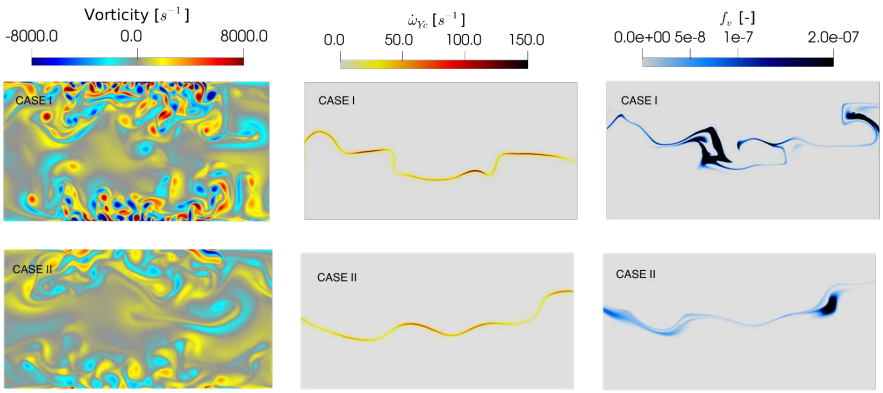

Figure A.9: *Instantaneous fields of vorticity (left), source term of the progress variable (middle) and soot volume fraction (right) for CASE I (top) and CASE II (bottom).*

A.5 *A priori* post-processing technique

For comparison with the LES model, the DNS solutions were filtered. The Gaussian filtering is thus performed based on a truncated Taylor expansion of the moments of the filter (Moureau et al., 2011; Domingo and Vervisch, 2017), leading to a diffusion-like equation:

$$\overline{\mathcal{Q}} = \mathcal{Q} + \frac{\Delta}{\gamma}\frac{\partial^2 \mathcal{Q}}{\partial x_i^2} \tag{A.4}$$

where Δ is the filter width and γ depends on the filter (for a 1D Gaussian filter $\gamma = 24$). This equation is then explicitly solved using a series of sub-steps in order to alleviate the pseudo Fourier condition (Moureau et al., 2011).

Four different filter widths are considered here: Δ = 23, 32, 45 and 64 h_{DNS} (with h_{DNS} = 50 μm) leading to Δ = 2.3 - 6.4 δ_{th} (with δ_{th} = 0.5 mm) and Δ = 4.6 - 12.8 δ_{fv} (with δ_{fv} = 0.25 mm) in CASE I and Δ = 1.9 - 5.3 δ_{th} (with δ_{th} = 0.6 mm) and Δ = 2.3 - 6.4 δ_{fv} (with δ_{fv} = 0.5 mm) in CASE II. The filter size ratios are summarized in Table A.2. From the filtered fields, the mixture fraction variance Z_v is reconstructed $Z_v = \widetilde{Z^2} - \widetilde{Z}^2$. Then, Z_v, $\widetilde{Z}$ and $\widetilde{Y}_C$ provide the access to the look-up table as done for a LES computation.

Table A.2: *Length scales and filter size ratios.*

	CASE I				CASE II			
Δ/h_{DNS}	23	32	45	64	23	32	45	64
Δ/δ_{th}	2.3	3.2	4.5	6.4	1.9	2.7	3.8	5.3
Δ/δ_{f_v}	4.6	6.4	9.0	12.8	2.3	3.2	4.5	6.4

The Pope criterion (Pope, 2000) is here retained to quantify the filtering effect on the turbulent field. It is defined as:

$$I_{LES} = \frac{k_{res}}{k_{DNS}} \tag{A.5}$$

where k_{res} is the resolved turbulent kinetic energy obtained by filtering the DNS solution $k_{res} = 0.5\overline{\rho}(\widetilde{u}^2 + \widetilde{v}^2)$ ($\overline{\rho}$ is the filtered gaseous density) and k_{DNS} is the total turbulent kinetic energy, considering both resolved and not-resolved scales $k = 0.5\rho(u^2 + v^2)$ from the unfiltered DNS solution. I_{LES} is bounded between 0 and 1 corresponding to a RANS and a DNS simulation, respectively.

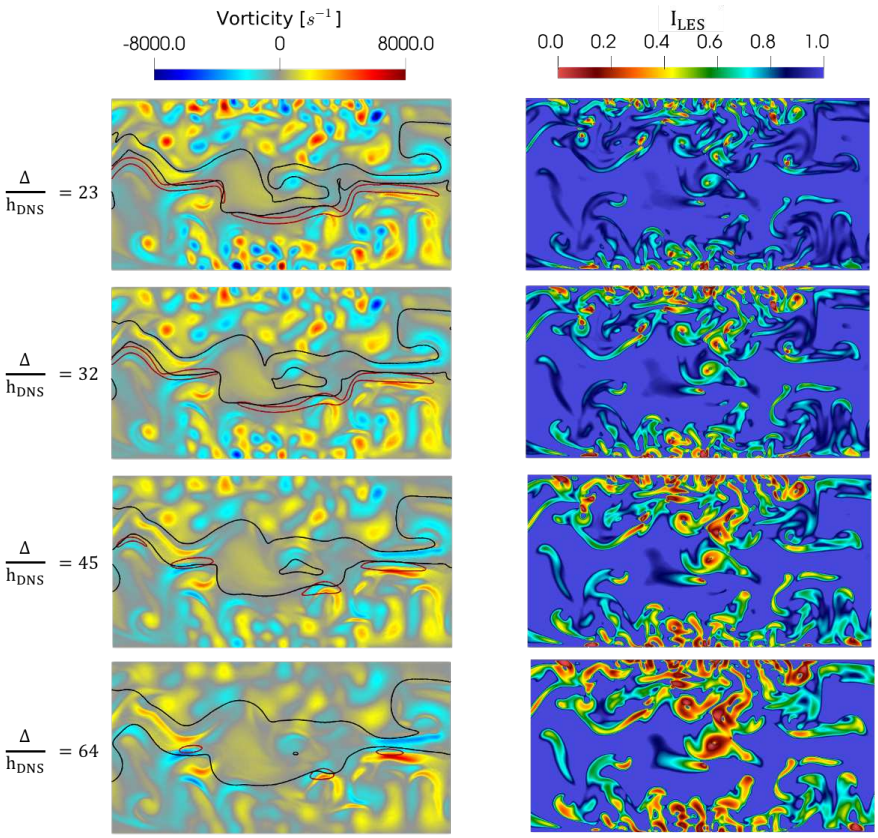

Figure A.10: *Left: Filtered vorticity field superposed by the black isoline of filtered source term progress variable ($\tilde{\dot{\omega}}_{Yc} = 10s^{-1}$) and the red isoline of filtered soot volume fraction ($\overline{f}_v$ = 1 ppb) for CASE I for different filter width Δ/h_{DNS}. Right: Corresponding I_{LES} fields.*

According to Pope (2000), LES should resolve at least 80% of the turbulent kinetic energy. Figures A.10 and A.11 show the filtered vorticity and the LES criterion fields obtained with different filter width for CASE I and CASE II, respectively. For CASE I, I_{LES} is satisfied for Δ/h_{DNS} up to 32, except near the inlets. For higher filter width, I_{LES} is no longer satisfied in the domain and the turbulent flow structure is no longer distinguishable, as shown by the filtered vorticity fields. For CASE II, the turbulent integral scales are high and I_{LES} is satisfied for filter width lower than $\Delta/h_{DNS} = 64$. Note that in the proximity of the flame front, the flow suffers from re-laminarization due to the thermal expansion leading to an increase in the fluid viscosity dissipating the turbulent eddies. Therefore, for the *a priori* analysis the filter width $\Delta/h_{DNS} = 32$ is retained for both cases.

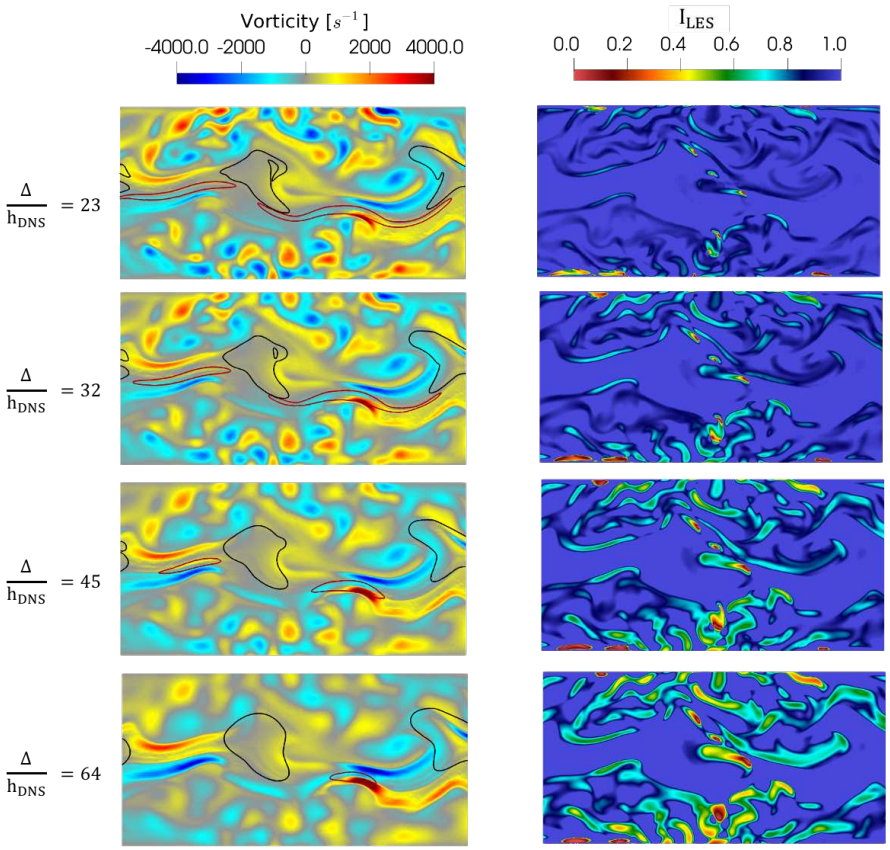

Figure A.11: *Left: Filtered vorticity field superposed by the black isoline of filtered source term progress variable ($\widetilde{\dot{\omega}}_{Yc} = 10s^{-1}$) and the red isoline of filtered soot volume fraction ($\overline{f}_v$ = 1 ppb) for CASE II for different filter widths Δ/h_{DNS}. Right: Corresponding I_{LES} fields.*

A.6 A *priori* analysis of the soot subgrid scale model

A.6.1 Soot intermittency

The soot subgrid-scale model proposed by Mueller and Pitsch (2011) is based on the soot intermittency I, i.e, the probability of finding f_v smaller than a specified threshold at any given location and time. Therefore, the first step is to verify that the definition for the retained intermittency $\bar{I}_{LES}$ reconstructed from the LES filtered fields provides a good estimation for the filtered DNS intermittency $\bar{I}_{DNS}$. Mueller and Pitsch (2011) defined the filtered intermittency $\bar{I}_{LES}$ by Eq. (A.6).

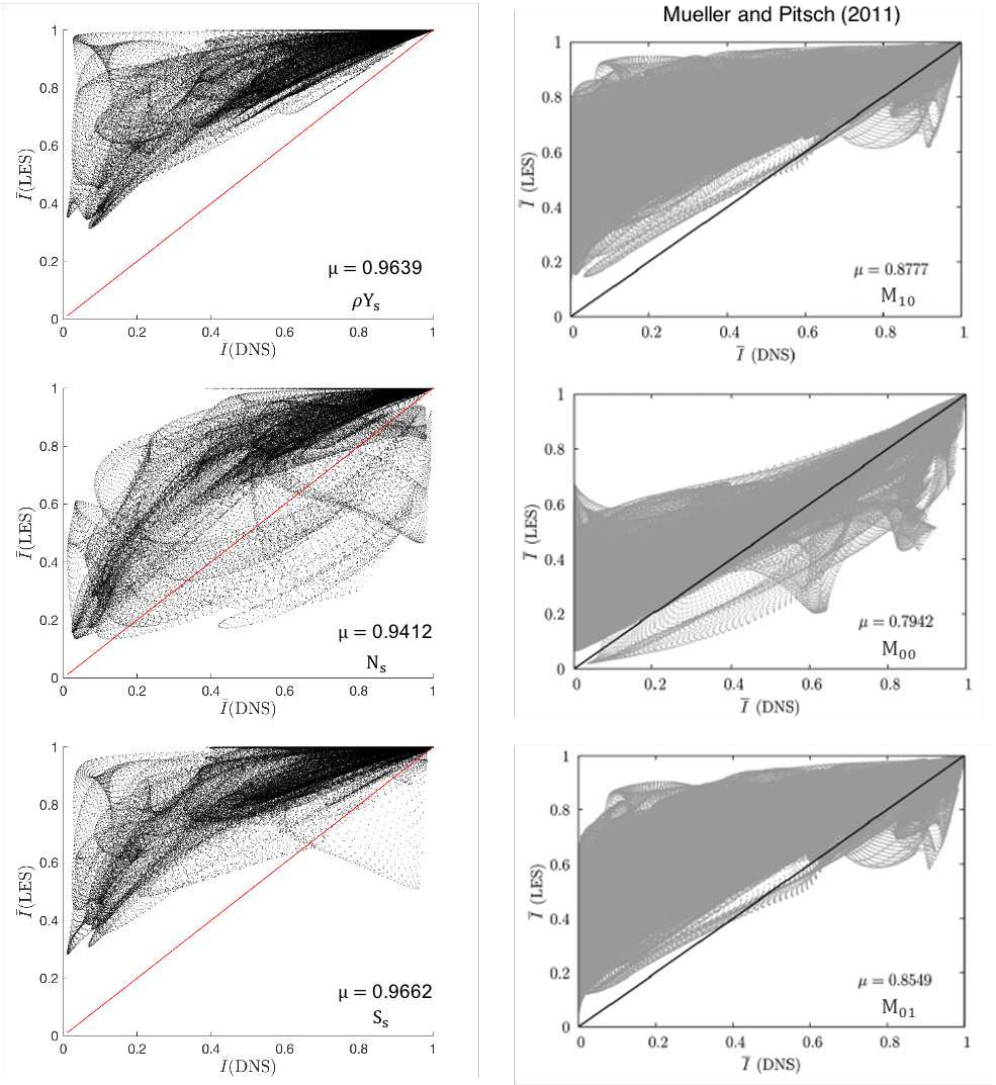

Figure A.12: *Filtered intermittency (from CASE I at t = 24 ms) evaluated with different subfilter ω definitions compared to the results from Mueller and Pitsch (2011) for $\Delta/h_{DNS} = 32$. The red line represents the filtered DNS, the "reference" model. The exact mean intermittency from the present filtered DNS is 0.898. In Mueller and Pitsch (2011) the exact mean is 0.751. For each model evaluation the mean intermittency is indicated in each graph.*

$$\overline{I}_{LES} = \begin{cases} 1 & \text{si } f_v^* < 0.1 ppb \\ \omega & \text{si } f_v^* > 0.1 ppb \end{cases} \tag{A.6}$$

where $f_v^* = \overline{f}_v/(1-\omega)$ is the filtered soot volume fraction associated with the

sooting mode of the presumed PDF (Eq. (4.61) in Chapter 4) and ω is the subfilter sensor representing the spatial intermittency of the soot scalars. The threshold of 0.1 ppb is an arbitrary value and has also been retained in this work to be consistent with the post-processing analysis of Mueller and Pitsch (2011).

The accuracy of the $\bar{I}_{LES}$ to reproduce $\bar{I}_{DNS}$ depends on the choice of the quantity $\overline{\Psi}_s$ used to defined the subgrid filter ω.

$$\omega = 1 - \frac{\overline{\Psi}_s^2}{\overline{\Psi}_s^2} \tag{A.7}$$

where $\overline{\Psi}_s$ is a transported soot scalar.

Mueller and Pitsch (2011) have evaluated the soot subgrid sensor ω using the transported soot scalars Ψ_s corresponding to the three first moments of the NDF, obtained with the HMOM soot model. Here ω is recalculated based on three soot scalars, $\overline{\rho}\widetilde{Y}_s$, $\overline{N}_s$ and $\overline{S}_s$ from the three-equation soot model (Franzelli et al., 2018), which corresponds to the moments ($\overline{M}_{10}$, $\overline{M}_{00}$ and $\overline{M}_{01}$) used by Mueller and Pitsch (2011). Figure A.12 shows the comparison between the soot intermittency obtained with the LES model for the three definitions of ω and the filtered DNS representing the "reference" model. The results extracted from Mueller and Pitsch (2011) are also shown in Fig. A.12. In the present results, the LES model tends to overpredict the intermittency independently of the ω definition, similarly to what has been observed by Mueller and Pitsch (2011).

For further comparison, Fig. A.13 shows the cumulative distribution function (CDF) for each ω evaluation for CASE I and CASE II. For CASE I, the CDF is slightly better captured using the subfilter ω evaluated with the particle number density N_s. Overall, due to the overprediction of the mean intermittency, the LES models provide low accurate CDF. For CASE II, the three evaluations present a similar poor accuracy level. In the case of the model of Mueller and Pitsch (2011), also shown in Fig. A.13, the model based on N_s presents a better agreement with DNS, notably for large soot intermittency values ($\overline{I} > 0.6$). According to Mueller and Pitsch (2011), the resolution of the fine structure of the sooting mode in the cell grid is not nearly as important as identifying the non-sooting and sooting modes. In fact, the bimodal PDF identifies only the presence of soot particles in the small scales. The soot distribution sub-structures are neglected, as reported in a very recent work realized by the Mueller research team (Berger et al., 2020).

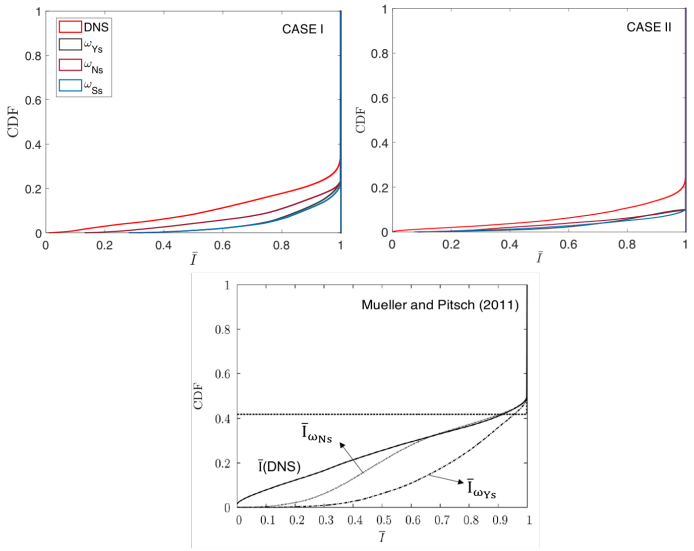

Figure A.13: *Cumulative Distribution Function (CDF) of the filtered intermittency for CASE I at t = 24 ms (top left), CASE II at t = 36 ms (top right) and for Mueller and Pitsch (2011) case (bottom). The dotted line in the Mueller and Pitsch (2011) graph is the mean intermittency evaluated using a single delta distribution (not considered in the present study).*

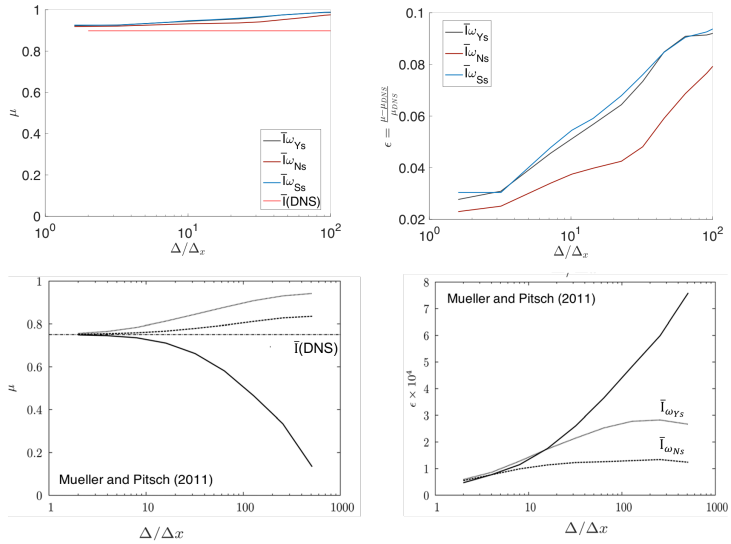

Figure A.14: *Effect of the filter width on the mean filtered intermittency and normalized error of the intermittency for CASE I at t = 24 ms (top) compared to the study of Mueller and Pitsch (2011) (bottom). The solid line in the Mueller and Pitsch (2011) graphs is the mean intermittency evaluated using a single delta distribution (not considered in the present study).*

The mean intermittency and the normalized error as a function of the filter width are shown in Fig. A.14 for each model evaluation for the CASE I and for the case studied by Mueller and Pitsch (2011). In opposition to the study performed by Mueller and Pitsch (2011), mean intermittency does not present a significant variation with the filter width for the present case. Even for small filter widths, the mean intermittency is over-predicted and the error keeps increasing with filter width. Overall, in opposition to the study performed by Mueller and Pitsch (2011), the three LES model evaluations provide very poor accuracy for soot intermittency, even though the evaluation based on the particle number density presents a slightly better prediction.

A.6.2 Coagulation

Once the most adequate choice for Ψ_s identified ($\bar{\Psi}_s = M_{00}$ in Mueller and Pitsch (2011)), the coagulation source term was the second quantity used by (Mueller and Pitsch, 2011) to evaluate the intermittency model for two main raisons. First, this source term controls the number of particles, which affects the definition of the intermittency sensor itself. Second, in the development of the soot intermittency model, only coagulation terms appears to be directly ω dependent. Recall that coagulation source term obtained with the LES model writes as:

$$\overline{\dot{\omega}}_{coag}(LES) = \frac{\dot{\omega}_{coag}(\overline{\Psi}_s)}{(1-\omega_{\Psi_s})} \tag{A.8}$$

whereas

$$\overline{\dot{\omega}}_{coag}(DNS) = \overline{\dot{\omega}_{coag}(\Psi_s)} \tag{A.9}$$

Figure A.15 compares the coagulation source terms ($\overline{\dot{\omega}}_{coag}$) obtained with the different definitions of ω and the corresponding results ($\overline{\dot{M}}_{0,0}^{coag}$) from Mueller and Pitsch (2011). Note that the same log scale is adopted to compare the obtained results with the model evaluation performed by Mueller and Pitsch (2011). The coagulation rate range is higher in the flame studied here than in the flame studied by Mueller and Pitsch (2011). Probably because in the Mueller and Pitsch (2011) case, only the first stage of soot formation was considered where only small particles are probably present, while in the present study, surface growth is the main contributor to soot mass yield, which may result in larger particles sizes and consequently a higher collision rate, as discussed in Section A.3. For the present flame, the scatter is broader with a larger geometric standard deviation of σ. Note that in Mueller and Pitsch (2011) the

coagulation seems to deviate from the DNS solution for high coagulation rate, which is dissimulated by the log scale.

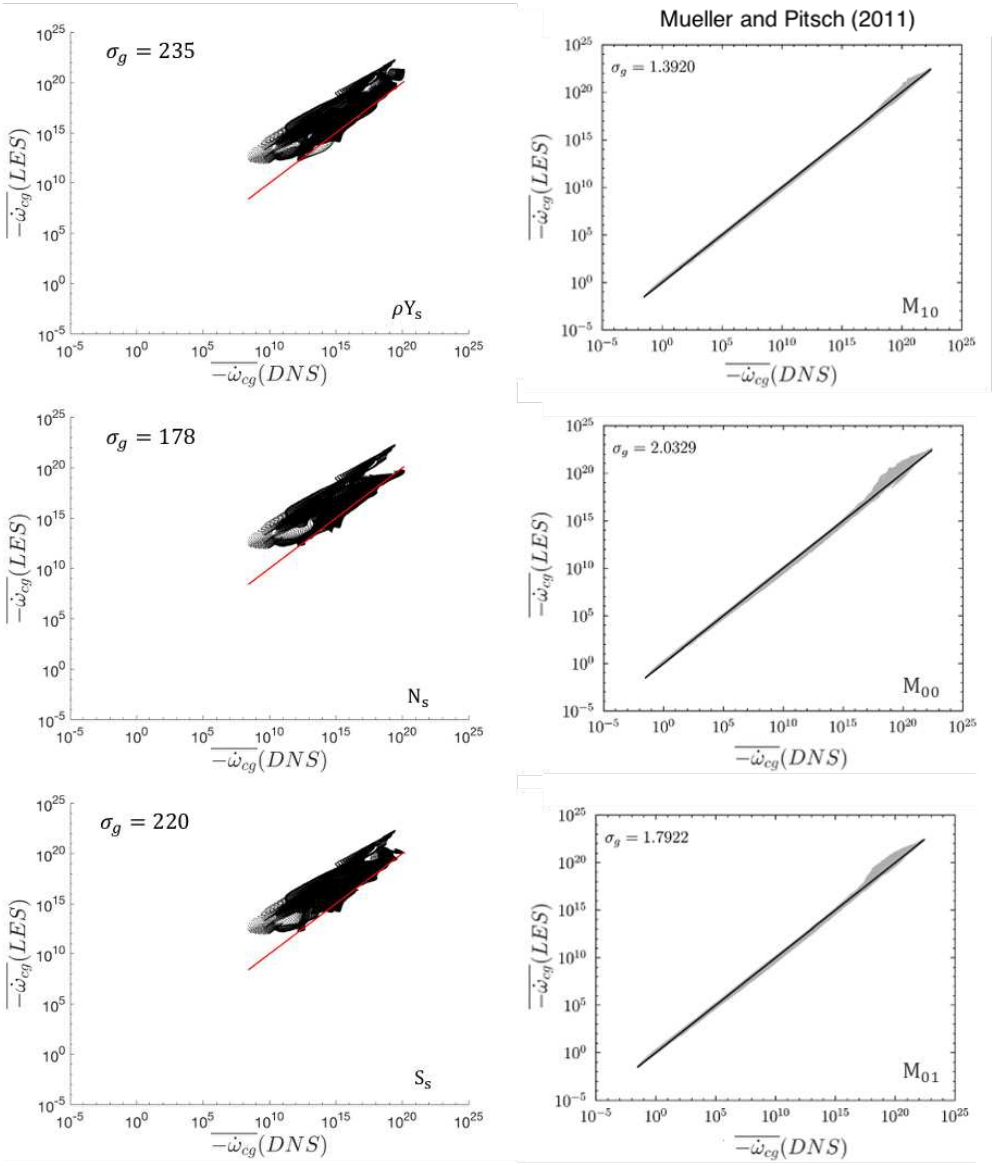

Figure A.15: *Filtered coagulation source term from CASE I at t = 24 ms evaluated with different subfilter ω evaluation compared to the study of Mueller and Pitsch (2011). The red line represents the filtered DNS, the "reference" model. Geometric standard deviation:* $\sigma_g = \exp(1/N \sum_{n=1}^{N} ln(\dot{\omega}_{coag}^{LES}/\dot{\omega}_{cg}^{DNS})^2)$*, where N is the number of points.*

Figure A.16 shows the CDF of coagulation source term for the two cases studied

here and for the Mueller and Pitsch (2011) case. The LES model overpredicts the DNS reference solution with the three ω evaluations for the presented two cases. These results are not in agreement with the one obtained in Mueller and Pitsch (2011) where ω evaluated from the number density of particles can capture the small soot scales quite well.

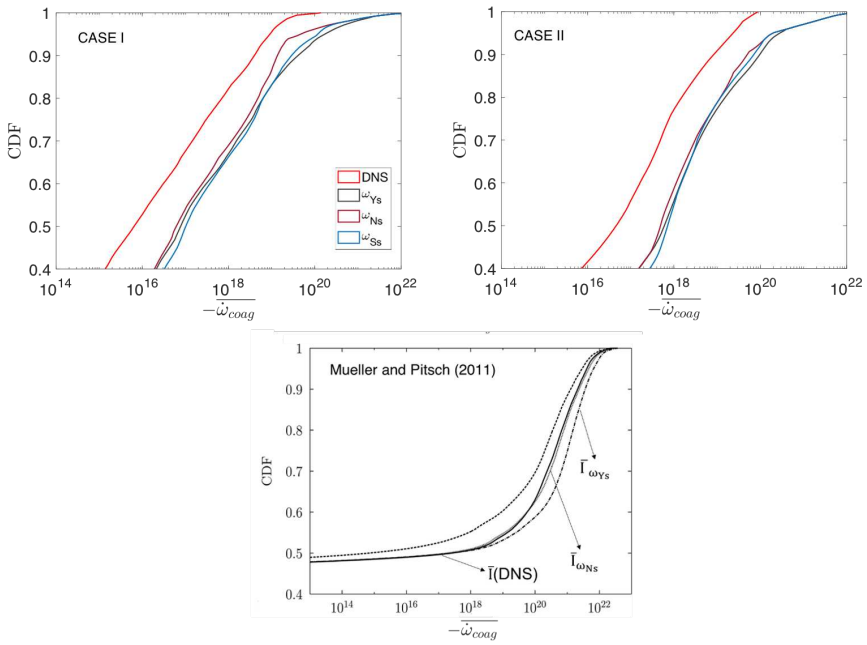

Figure A.16: *Cumulative Distribution Function (CDF) of the filtered coagulation source term for all cases and the Mueller and Pitsch (2011) case. The dotted line in the Mueller and Pitsch (2011) graph is the mean intermittency evaluated using a single delta distribution (not considered in the present study)*

A.6.3 Soot source terms

Mueller and Pitsch (2011) have not considered the other source terms in their study. According to them, nucleation was not considered because it mostly depends on the turbulent combustion model via PAH, as well as condensation. Surface growth was neglected based on Bisetti et al. (2012), who stated that soot growth by surface reactions is small compared to condensation in the flame studied by Mueller and Pitsch (2011) and simulation was stopped before oxidation predominates. However, the soot intermittency subgrid model is used in the literature in turbulent flames where oxidation levels can be significant, as in the DLR burner. Thus, the present study considers the whole soot evolution stages and not only the first ones.

Figure A.17 shows the comparison between mass source terms ($\dot{\omega}^p_{Y_s}$) for p =

condensation (cd), surface growth (sg) and oxidation (ox) obtained with the LES model and the filtered DNS at t = 24, 36 ms for CASE I and CASE II, respectively, with $\Delta/\Delta h_{DNS} = 32$. For CASE II, $\Delta/h_{DNS} = 64$ is also considered as it represents the same length ratio between the filter width and the integral scale $\Delta/l_t = 2$ (l_t at the injection) obtained with $\Delta/h_{DNS} = 32$ for CASE I. Remember that, according to the model formulation described in Chapter 4, the intermittency soot model is not directly applied to these source terms. In this case, the filtered LES source terms writes as: $\overline{\dot{\omega}}^p_\Psi = \dot{\omega}^p_\Psi(\overline{\Psi})$. For CASE I, condensation and oxidation are significantly affected by the smaller turbulent scales. Surface growth is mainly affected by high values. For CASE II ($\Delta/l_t = 2$), characterized by larger turbulent structures, the source terms are also poorly described. Surface growth and oxidation are highly underpredicted, while condensation is overpredicted, notably at low values. For CASE II with an equivalent Δ/l_t ratio, while condensation and oxidation are underpredicted, surface growth is overpredicted. Compared to the soot intermittency, the soot source terms seem very sensitive to the filter width. Note that the condensation and surface growth rates values reached with Δ/l_t=1 and $\Delta/l_t = 2$ are very different.

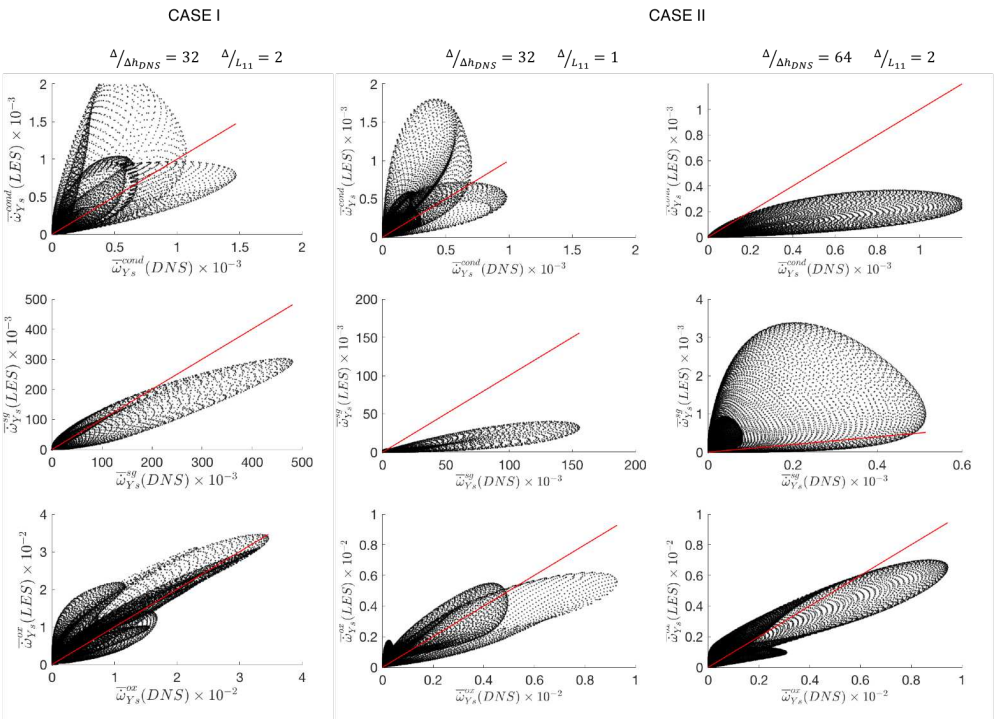

Figure A.17: *Filtered source terms of nucleation, condensation and surface reactions from CASE I at t = 24 ms (left) and from CASE II at t = 36 ms(right), conditioned by the presence of soot particle with a threshold of 0.1 ppb. The red line represents the filtered DNS, the "reference" model.*

It should be reminded that the intermittency subgrid-scale model assumes statistical independence between soot and gaseous scalars. This assumption can hardly be verified for oxidation that has a time scale of the order of magnitude of the combustion phenomenon. Very recently, Yang et al. (2019) have extended the intermittency model in order to address the oxidation time scale issue and Berger et al. (2020) have proposed a log-normal distribution to accounts for the sub-structure of the soot distribution at the subgrid. An investigation of these new versions on the present configuration will be of great interest.

Overall, the *a priori* analysis of the soot intermittency and soot source terms calls into question the robustness of the intermittency subgrid-scale model. By comparison with the study from Mueller and Pitsch (2011), the model response appears to strongly depend not only on the turbulence conditions but also on some other variables such as the flame configuration, the fuel, the physical models that have to be clearly identified. While for a heptane-air non-premixed jet flame from Mueller and Pitsch (2011) the model seems to *a priori* perform well, in the ethylene-air counterflow flame studied in the present work, the accuracy of the model is *a priori* quite low, questioning then its general use in fully-turbulent sooting flames.

A.7 Conclusion

The DNS approach is a valuable tool for understanding turbulent combustion. A large amount of work has used DNS to study the combustion in turbulent conditions and the obtained results were used to develop LES models (Vreman et al., 1996; Moureau et al., 2011; Proch et al., 2017; Domingo and Vervisch, 2017). This approach can also be valuable to investigate the mechanism involved in soot production and its interaction with turbulence and chemistry (Bisetti et al., 2012; Attili et al., 2015, 2016; Lucchesi et al., 2017) and may contribute to the development of LES closure models specific for sooting flames (Mueller and Pitsch, 2011).

The soot subgrid intermittency model due to Mueller and Pitsch (2011), used for the LES simulations previously presented in this manuscript, has been investigated here based on *a priori* analysis of the DNS database of a 2D counterflow sooting flame subjected to isotropic homogeneous turbulence. The compactness of the counterflow configuration results in low computational CPU costs compared to the classical jet flames currently used in the DNS soot modeling studies (Bisetti et al., 2012; Attili et al., 2015, 2016; Lucchesi et al., 2017). Its low CPU cost makes this configuration a good candidate to investigate soot-flame-turbulence interactions. Additionally, at high turbulent conditions, as in gas turbine environments, this configuration may provide meaningful knowledge about flame-turbulence-soot interactions (Coppola et al., 2009).

In analogy with the work of Mueller and Pitsch (2011), two quantities were used to evaluate the LES model performance, the soot intermittency and the coagulation rate. In addition to these two quantities, the mass source terms were also considered in the present work. The *a priori* analysis of the soot LES model showed very low accuracy for the intermittency and the coagulation source term for the presented calculations, in opposition with the better accuracy obtained by Mueller and Pitsch (2011) using the particle number density for the soot subgrid sensor definition. Concerning the other source terms not investigated by Mueller and Pitsch (2011), the model also provides a poor description. Besides, the mass source terms appear very sensitive to the filter width. In Mueller and Pitsch (2011), the effects of the soot subgrid-scale model on surface growth and oxidation were neglected as only the first stages of soot formation were considered. However, a recent study Yang et al. (2019) proposed a new intermittency LES model to account for small scales effect on oxidation by considering its dependence on the mixture fraction. This is a crucial issue for soot prediction in turbulent flames, notably when oxidation is strongly presented in the DLR burner. Therefore, this LES model should also be investigated in the 2D counterflow configuration to evaluate its generality in future works. Overall, the *a priori* analysis brings into question the universality of the soot subgrid intermittency model and reinforces the importance of validating soot models in a wide range of flame configurations. For the studied flame, 39000 hours CPU with 720 cores was necessary to obtain 40 ms. Therefore, canonical configurations allow performing DNS studies at low CPU costs so that parametric studies are accessible to verify the generality of the observed trends.

Synthèse en Français

Introduction

Les particules de suies sont connues pour avoir des effets néfastes sur la santé et l'environnement, par conséquence les normes deviennent de plus en plus restrictives afin de réduire leurs émissions. Pour cela, la compréhension du phénomène de production de ces particules est urgent afin de contribuer au développement de technologies plus propres. Cependant, la prédiction de la production des suies dans une chambre de combustion à l'aide d'une approche de type Simulation aux Grandes échelles (Large Eddy Simulation - LES) représente un défi de taille pour plusieurs raisons. La modélisation des processus physico-chimiques impliqués dans la production de ces particules fait encore défaut aujourd'hui, même pour les flammes en conditions laminaires. Ensuite, dans les dispositifs présentant un intérêt pratique, telles que les turbines à gaz, des régimes de combustion multiples coexistent, ce qui présente une difficulté supplémentaire à la modélisation haute-fidélité de tels phénomènes. De plus, dans des conditions turbulentes les particules de suies, caractérisées par une faible diffusivité, sont confinées dans des structures soumises au transport turbulent. En raison de leurs tailles, un modèle de sous-maille est nécessaire pour décrire ces structures pouvant avoir des tailles inferieur à la taille du maillage. Pour finir, la validation de nouveaux modèles est difficile lorsqu'on considère ce type de flamme en raison du couplage non-linéaire entre les différents phénomènes coexistant (rayonnement, mélange entre les réactives, présence de structures cohérentes à grande échelle, etc) et du besoin d'importantes ressources de calcul pour obtenir une représentation statistique fiable de la production intermittente de suies.

Objectives de la thèse

1. Proposer un modèle capable de décrire la production de suie dans les flammes de suie laminaires et turbulentes.
2. Quantifier la fiabilité du formalisme LES pour prédire la production de suie lorsqu'il est appliqué dans une chambre de combustion modèle d'un

moteur aéronautique, le brûleur DLR.

3. Identifier une stratégie pour quantifier l'effet des modèles de suie sur la prédiction LES de la production de suie dans le brûleur DLR.
4. Évaluer l'effet d'un mécanisme nouvellement développé pour les réactions de surface des particules de suie dans les flammes laminaires et turbulentes.
5. Évaluer l'effet du modèle d'intermittence de sous-maille pour la suie sur leur prédiction dans le brûleur DLR.

Plan de la thèse

La première partie de ce manuscrit est consacrée à la modélisation et à la simulation des flammes laminaires avec production de suie. Dans le Chapitre 1, les différents modèles et équations sont présentés ainsi que les mécanismes physiques et chimiques de production de suie et les différentes méthodologies numériques de prédiction de suie trouvées dans la littérature. L'approche sectionnelle (Rodrigues et al., 2017), retenue pour les simulations laminaires y est décrite en détail. Dans le Chapitre 2, le modèle sectionnel couplé à une chimie détaillé (plus de 1000 réactions et 200 espèces chimiques (Wang et al., 2013)) est évalué dans des flammes laminaires d'éthylène-air prémélangées et non-prémélangées. Bien qu'il fournisse une bonne prédiction de la fraction volumique de suie dans des conditions prémélangées, il échoue dans des flammes non-prémélangées. Ainsi, dans le Chapitre 3, dans la deuxième partie de ce manuscrit, un modèle réactionnel appelé HACA-RC* est proposé afin d'améliorer la prédiction de la production de suie dans des flammes non-prémélangées. Couplé à la stratégie sectionelle, le modèle proposé est testé sur plusieurs flammes laminaires, présentant une bonne prédiction de la fraction volumique dans les deux régimes de combustion.

La troisième partie est consacrée à la simulation LES d'un brûleur quasi-industriel, le brûleur expérimentalement étudié au DLR Geigle et al. (2013, 2015, 2017). Fonctionnant à une pression élevée avec une oxydation secondaire de l'air, ce brûleur a été conçu pour fournir une base de données expérimentale étendue servant à l'évaluation des modèles de suie dans des conditions techniquement pertinentes. Il a été récemment élu comme flamme cible dans la base de données de référence de l'International Sooting Flame (ISF) Workshop. Le dispositif est présenté en détail dans le Chapitre 4 ainsi que sa mise en donnée dans le code AVBP. Le formalisme LES utilisé, présenté dans le Chapitre 3, est basé sur une approche tabulée pour la phase gazeuse (Ihme and Pitsch, 2008) et sur le modèle de suie à trois équations (Franzelli et al., 2018) pour la description de la phase solide. Le modèle à trois-équation (décrit dans le Chapitre 1) fournit une précision similaire à la méthode sectionnelle

pour un coût CPU inférieur (Franzelli et al., 2018). Premièrement, la fiabilité du formalisme LES est évaluée dans le Chapitre 6. Pour cela, une analyse statistique de la phase gazeuse et de la phase solide, révèle qui atteindre la convergence statistique de la phase solide est difficile dans cette configuration, étant donnée la complexité de l'écoulement et la forte intermittence de la production des particules de suies très sensible aux fluctuations locales de la phase gazeuse. Il a été montré que des conditions thermochimiques spécifiques sont nécessaires à la production de suie. Associé à écoulement fortement turbulent et à la présence d'instabilités hydrodynamiques, l'occurrence de ces conditions est rare et intermittent. Par conséquent, atteindre la convergence statistique de ce phénomène demande un temps physique très long. La sensibilité des résultats à la résolution spatiale est aussi étudiée. Des différences dans la structure de la phase gazeuse, due à des résolutions de maillage différentes, entraînent des écarts importants dans la prédiction de la fraction volumique. Les différences dans la structure de la phase gazeuse et dans la prédiction de suie, peuvent être attribuées non seulement aux différences entre les maillage étudiés mais également au manque de convergence statistique de la phase solide. Un maillage plus fin, pourrait apporter une réponse à ce questionnement, mais dans le contexte industriel dans lequel cette thèse est insérée, le coût du calcul ne permet pas cela. Ensuite, dans le Chapitre 7 et 8, l'impact des modèles de suies est également examiné. Dans le Chapitre 7, il est montré que la fraction volumique maximale de suie est multipliée par trois avec le modèle HACA-RC* en raison de l'augmentation substantielle de la croissance en surface. Afin de prendre en compte le caractère intermittent des suies sur l'évaluation des modèles, une nouvelle stratégie pour évaluer la réponse des modèles de suie est proposée (Chapitre 8). Basée sur une LES unique où l'ensemble d'équations décrivant les suies est dupliqué (un ensemble représente le modèle de référence et l'autre le modèle à évaluer) cela permet aux deux ensembles d'interagir avec la même évolution temporelle et spatiale que la phase gazeuse et ainsi d'évaluer la réponse des modèles au même évènement rare sans atteindre la convergence statistique. Grâce à cette approche, les premières indications de la contribution du modèle d'intermittence de sous-maille (Mueller and Pitsch, 2011) pour la phase solide à la prédiction des suies dans le brûleur DLR sont proposées.

Motivée par les difficultés rencontrées pour prédire de façon fiable la production de suies et évaluer les performances des modèles de suies dans la flamme turbulente considérée avec l'approche LES, une l'analyse a priori du modèle d'intermittence basée sur une Simulation Numérique Directe d'une flamme contre-courant turbulente 2D est réalisée. Cette analyse, présentée dans l'Annexe A, fournit des informations préliminaires sur la contribution du modèle d'intermittence de sous-maille à leur prédiction. De plus, ces données réprésentent une nouvelle base de données pour des études paramétriques. Ainsi le développement de cette étude ouvre une perspective dans la compréhension de la production des suies dans des conditions turbulentes.

Conclusions générales

La production de suie dans des flammes turbulentes est caractérisée par une nature intermittente dans l'espace et le temps. La prédiction numérique de suie dans les flammes turbulentes est donc assez difficile, non seulement pour des questions de modélisation, mais aussi pour obtenir une description statistique de la phase solide. En considérant le brûleur DLR, il a été constaté qu'un moyennage temporel de 60 ms, généralement considéré dans les publications précédentes, est suffisant pour garantir la convergence statistique de la phase gazeuse. Cependant, un temps de moyennage beaucoup plus long est nécessaire pour une description fiable de la fraction volumique de suie (plus de 110 ms). Ceci est dû au fait que les événements de suie sont rares puisque des conditions thermochimiques spécifiques et rares de la phase gazeuse sont requises pour favoriser la production de suie. Par conséquent, assurer la convergence statistique de la phase gazeuse n'est pas suffisant pour garantir la convergence statistique de la phase solide, caractérisée par une forte intermittence. Dans ce cas, une moyenne temporelle plus longue est nécessaire pour représenter statistiquement l'apparition de suie et, par conséquent, permettre une évaluation fiable du modèle.

Une nouvelle stratégie pour caractériser l'effet des modèles de suie dans une flamme turbulente a été proposée pour répondre à ce problème. Afin de discriminer l'effet des modèles de suie en comparant les résultats d'une description de référence et d'un nouveau modèle, il est essentiel de s'assurer que les particules connaissent la même évolution temporelle et spatiale que la phase gazeuse. Pour cela, une approche "unique" de la phase gazeuse a été proposée en transportant un nouvel ensemble de scalaires représentant la phase solide avec le nouveau modèle en plus de l'ensemble de référence. L'approche a été appliquée pour étudier l'effet du modèle de sous-maille d'intermittence de suie sur leur prédiction dans le brûleur DLR. L'analyse des résultats instantanés et moyennés dans le temps indique un faible impact du modèle sous-grille de suie dans la configuration considérée. Dans l'ensemble, la stratégie proposée est intéressante pour évaluer les modèles de suie, notamment lorsque des modèles de suie simple sont utilisés sans rétro-couplage des champs de suie sur la phase gazeuse, ce qui permet de comparer la réponse des modèles aux mêmes conditions gazeuses.

Cette étude met en évidence les difficultés en prédire la production des particules de suie et apporte principalement une réflexion sur la méthodologie d'évaluation de la modélisation de ce phénomène complexe dans les flammes turbulents. Dans ce contexte, un modèle réactionnel pour les flammes laminaires et turbulents multi-régime a été proposé ainsi qu'un changement de paradigme dans l'évaluation des modèles de production des particules de suie dans les flames turbulents. Ces travaux font l'objet de deux communications à Turbo Expo (Turbomachinery Technical Conference & Exhibition, éditions 2019 et 2021). Beaucoup reste encore a faire pour la comphrèesion de tel

phénomène et sa prédiction dans les dispositifs présentant un intérêt pratique. Le formalisme DNS, proposé à la fin de cette étude, semble ainsi être une bonne option pour le dévelopement et évaluation des modèles de suie dans les flammes turbulents.

Bibliography

(2019). International sooting flame workshop. URL: https://www.adelaide.edu.au/cet/isfworkshop/data-sets. *(p. 185, 215, 216, 218)*

Abid, A. D., J. Camacho, D. A. Sheen, and H. Wang (2009). Quantitative measurement of soot particle size distribution in premixed flames – the burner-stabilized stagnation flame approach. *Combustion and Flame 156*(10), 1862 – 1870. *(p. 50, 54, 55)*

Airbus (2019). Global market forecast: Cities, airports & aircraft 2019-2038. Technical report, Airbus. *(p. 4)*

Aksit, I. and J. Moss (2006). A hybrid scalar model for sooting turbulent flames. *Combustion and Flame 145*(1-2), 231–244. *(p. 39, 113, 114, 215)*

Appel, J., H. Bockhorn, and M. Frenklach (2000). Kinetic modeling of soot formation with detailed chemistry and physics: laminar premixed flames of c2 hydrocarbons. *Combustion and Flame 121*(1), 122 – 136. *(p. 7, 23, 29, 31, 74, 78, 79, 80, 102, 234)*

Arias, P. G., V. R. Lecoustre, S. Roy, Z. Luo, D. C. Haworth, T. Lu, A. Trouvè, and H. G. Im (2015). Dynamics of flow-soot interaction in wrinkled non-premixed ethylene-air flames. *Combustion Theory and Modelling 19*(5), 568–586. *(p. 234)*

Attili, A., F. Bisetti, M. E. Mueller, and H. Pitsch (2014). Formation, growth, and transport of soot in a three-dimensional turbulent non-premixed jet flame. *Combustion and Flame 161*(7), 1849 – 1865. *(p. 48, 97, 110, 114, 150, 214, 234, 236)*

Attili, A., F. Bisetti, M. E. Mueller, and H. Pitsch (2015). Damkohler number effects on soot formation and growth in turbulent nonpremixed flames. *Proceedings of the Combustion Institute 35*(2), 1215 – 1223. *(p. 97, 114, 150, 214, 240, 255)*

Attili, A., F. Bisetti, M. E. Mueller, and H. Pitsch (2016). Effects of non-unity lewis number of gas-phase species in turbulent nonpremixed sooting flames. *Combustion and Flame 166*, 192 – 202. *(p. 97, 112, 236, 255)*

Aubagnac-Karkar, D., A. E. Bakali, and P. Desgroux (2018). Soot particles inception and pah condensation modelling applied in a soot model utilizing a sectional method. *Combustion and Flame 189*, 190 – 206. *(p. 7, 79, 87)*

Aubagnac-Karkar, D., J.-B. Michel, O. Colin, P. E. Vervisch-Kljakic, and N. Darabiha (2015). Sectional soot model coupled to tabulated chemistry for diesel rans simulations. *Combustion and Flame 162*(8), 3081 – 3099. *(p. 7, 30, 37, 97)*

Ax, H., U. Stopper, W. Meier, M. Aigner, and F. GŸthe (2010, 03). Experimental Analysis of the Combustion Behavior of a Gas Turbine Burner by Laser Measurement Techniques. *Journal of Engineering for Gas Turbines and Power 132*(5). 051503. *(p. 197)*

B. Kärcher (2018). Hybrid transported-tabulated chemistry for partially premixed combustion. *Nature Communications*, 1–17. *(p. 4)*

Balthasar, M. and M. Kraft (2003). A stochastic approach to calculate the particle size distribution function of soot particles in laminar premixed flames. *Combustion and Flame 133*(3), 289 – 298. *(p. 36)*

Balthasar, M., F. Mauss, M. Pfitzner, and A. Mack (2000). Implementation and Validation of a New Soot Model and Application to Aeroengine Combustors. *Journal of Engineering for Gas Turbines and Power 124*(1), 66–74. *(p. 97, 102)*

Berger, L., A. Wick, A. Attili, M. E. Mueller, and H. Pitsch (2020). Modeling subfilter soot-turbulence interactions in large eddy simulation: An a priori study. *Proceedings of the Combustion Institute*. *(p. 114, 249, 255)*

Bierkandt, T., P. OBwald, T. Schripp, and M. Kohler (2019). Experimental investigation of soot oxidation under well-controlled conditions in a high-temperature flow reactor. *Combustion Science and Technology 191*(9), 1499–1519. *(p. 187)*

Bisetti, F., G. Blanquart, M. E. Mueller, and H. Pitsch (2012). On the formation and early evolution of soot in turbulent nonpremixed flames. *Combustion and Flame 159*(1), 317 – 335. *(p. 19, 48, 65, 95, 97, 110, 113, 150, 152, 207, 214, 234, 235, 236, 253, 255)*

Blacha, T., M. D. Domenico, P. Gerlinger, and M. Aigner (2012). Soot predictions in premixed and non-premixed laminar flames using a sectional approach for pahs and soot. *Combustion and Flame 159*, 181–193. *(p. 36)*

Blanquart, G. and H. Pitsch (2007). *A joint volume-surface-hydrogen multivariate model for soot formation*. Berlin, Heidelberg: Springer Berlin Heidelberg. *(p. 7, 21, 22, 23, 38)*

Bodor, A. L., B. Franzelli, T. Faravelli, and A. Cuoci (2019). A post processing technique to predict primary particle size of sooting flames based on a chemical discrete sectional model: Application to diluted coflow flames. *Combustion and Flame 208*, 122 – 138. *(p. 36)*

Boger, M., D. Veynante, H. Boughanem, and A. Trouvè (1998). Direct numerical simulation analysis of flame surface density concept for large eddy simulation of turbulent premixed combustion. *Symposium (International) on Combustion 27*(1), 917 – 925. Twenty-Seventh Sysposium (International) on Combustion Volume One. *(p. 233)*

Bolla, M., Y. M. Wright, K. Boulouchos, G. Borghesi, and E. Mastorakos (2013). Soot formation modeling of n-heptane sprays under diesel engine conditions using the conditional moment closure approach. *Combustion Science and Technology 185*(5), 766–793. *(p. 35, 97)*

Bond, T. C., S. J. Doherty, D. W. Fahey, P. M. Forster, T. Berntsen, B. J. DeAngelo, M. G. Flanner, S. Ghan, B. Karcher, D. Koch, S. Kinne, Y. Kondo, P. K. Quinn, M. C. Sarofim, M. G. Schultz, M. Schulz, C. Venkataraman, H. Zhang, S. Zhang, N. Bellouin, S. K. Guttikunda, P. K. Hopke, M. Z. Jacobson, J. W. Kaiser, Z. Klimont, U. Lohmann, J. P. Schwarz, D. Shindell, T. Storelvmo, S. G. Warren, and C. S. Zender (2013). Bounding the role of black carbon in the climate system: A scientific assessment. *Journal of Geophysical Research: Atmospheres 118*(11), 5380–5552. *(p. 4)*

Bouaniche, A., L. Vervisch, and P. Domingo (2019). A hybrid stochastic/fixed-sectional method for solving the population balance equation. *Chemical Engineering Science 209*, 115198. *(p. 39)*

Bourguignon, D. (2018). Pollution sources and impacts, eu legislation and international agreements. Technical report, European Parliamentary Research Service. *(p. 3)*

Boxx, I., M. Stohr, C. Carter, and W. Meier (2010). Temporally resolved planar measurements of transient phenomena in a partially pre-mixed swirl flame in a gas turbine model combustor. *Combustion and Flame 157*(8), 1510 – 1525. *(p. 123, 197)*

Brookes, S. and J. Moss (1999). Predictions of soot and thermal radiation properties in confined turbulent jet diffusion flames. *Combustion and Flame 116*(4), 486 – 503. *(p. 35, 39, 114, 129, 133)*

Buseck, P. R., K. Adachi, A. Gelencsér, E. Tompa, and M. Pósfai (2012). Are black carbon and soot the same? *Atmospheric Chemistry and Physics Discussions 12*, 24821–24846. *(p. 6)*

Cailler, M., N. Darabiha, D. Veynante, and B. Fiorina (2017). Building-up vir-

tual optimized mechanism for flame modeling. *Proceedings of the Combustion Institute 36*(1), 1251 – 1258. *(p. 102)*

Camacho, J., C. Liu, C. Gu, H. Lin, Z. Huang, Q. Tang, X. You, C. Saggese, Y. Li, H. Jung, L. Deng, I. Wlokas, and H. Wang (2015). Mobility size and mass of nascent soot particles in a benchmark premixed ethylene flame. *Combustion and Flame 162*(10), 3810 – 3822. *(p. 50, 55, 56, 57, 87, 88)*

Carbone, F., F. Cattaneo, and A. Gomez (2015). Structure of incipiently sooting partially premixed ethylene counterflow flames. *Combustion and Flame 162*(11), 4138 – 4148. *(p. 199)*

Celnik, M., R. Patterson, M. Kraft, and W. Wagner (2007). Coupling a stochastic soot population balance to gas-phase chemistry using operator splitting. *Combustion and Flame 148*(3), 158 – 176. *(p. 36)*

Chong, S. T., M. Hassanaly, H. Koo, M. E. Mueller, V. Raman, and K. P. Geigle (2018). Large eddy simulation of pressure and dilution-jet effects on soot formation in a model aircraft swirl combustor. *Combustion and Flame 192*, 452 – 472. *(p. 102, 127, 133, 167, 185, 194, 210, 211, 215, 216)*

Chong, S. T., V. Raman, M. E. Mueller, P. Selvaraj, and H. G. Im (2019). Effect of soot model, moment method, and chemical kinetics on soot formation in a model aircraft combustor. *Proceedings of the Combustion Institute*. *(p. 102, 127, 129, 133, 193, 210, 215)*

Colin, O. and M. Rudgyard (2000). Development of high-order taylor-galerkin schemes for les. *Journal of Computational Physics 162*(2), 338 – 371. *(p. 138)*

Colmán, H. M., A. Cuoci, N. Darabiha, and B.Fiorina (2019). A reduced virtual chemistry model for soot prediction in hydrocarbon-air flames. *27^{th} International Colloquium on the Dynamics of Explosions and Reactive Systems*. *(p. 102)*

Coppola, G., B. Coriton, and A. Gomez (2009). Highly turbulent counterflow flames: A laboratory scale benchmark for practical systems. *Combustion and Flame 156*(9), 1834 – 1843. *(p. 235, 255)*

Cuoci, A., A. Frassoldati, T. Faravelli, and E. Ranzi (2008). Frequency response of counter flow diffusion flames to strain rate harmonic oscillations. *Combustion Science and Technology 180*(5), 767–784. *(p. 8, 65)*

D'Anna, A. (2008). Detailed kinetic modeling of particulate formation in rich premixed flames of ethylene. *Energy & Fuels 22*(3), 1610–1619. *(p. 36)*

Darabiha, N. (1992). Transient behaviour of laminar counterflow hydrogen-air diffusion flames with complex chemistry. *Combustion Science and Technology 86*(1-6), 163–181. *(p. 54, 103)*

Decroix, M. E. and W. L. Roberts (2000). Transient flow field effects on soot volume fraction in diffusion flames. *Combustion Science and Technology 160*(1), 165–189. *(p. 65, 66, 68, 69, 85)*

Dellinger, N. (2019, September). *Modélisation de la formation et de l'évolution des particules de suie en approche hybride Euler-Lagrange pour la simulation de foyers aéronautiques*. Thesis, Sorbonne Université. *(p. 39)*

Dellinger, N., N. Bertier, F. Dupoirieux, and G. Legros (2020). Hybrid eulerian-lagrangian method for soot modelling applied to ethylene-air premixed flames. *Energy 194*, 116858. *(p. 39)*

Derjaguin, B., A. Storozhilova, and Y. I. Rabinovich (1966). Experimental verification of the theory of thermophoresis of aerosol particles. *Journal of Colloid and Interface Science 21*(1), 35 – 58. *(p. 19)*

Dickson, N. (2019, 2). Icao standards and recommended practices on local air quality. URL: https://www.icao.int/Meetings/ENVSymposium/Presentations/. Online; accessed 20-October-2020. *(p. 5)*

Domenico, M. D., P. Gerlinger, and M. Aigner (2010). Development and validation of a new soot formation model for gas turbine combustor simulations. *Combustion and Flame 157*(2), 246 – 258. *(p. 127, 133)*

Domingo, P. and L. Vervisch (2017). Dns and approximate deconvolution as a tool to analyse one-dimensional filtered flame sub-grid scale modelling. *Combustion and Flame 177*, 109 – 122. *(p. 233, 245, 255)*

Domingo, P., L. Vervisch, and K. Bray (2002). Partially premixed flamelets in les of nonpremixed turbulent combustion. *Combustion Theory and Modelling 6*(4), 529–551. *(p. 123, 201)*

Donde, P., V. Raman, M. E. Mueller, and H. Pitsch (2013). Les/pdf based modeling of soot-turbulence interactions in turbulent flames. *Proceedings of the Combustion Institute 34*(1), 1183 – 1192. *(p. 114, 215)*

Donea, J., L. Quartapelle, and V. Selmin (1987). An analysis of time discretization in the finite element solution of hyperbolic problems. *Journal of Computational Physics 70*(2), 463 – 499. *(p. 237)*

Duboc, B., G. Ribert, and P. Domingo (2019). Hybrid transported-tabulated chemistry for partially premixed combustion. *Computers & Fluids 179*, 206 – 227. *(p. 201)*

Dupoirieux, F. and N. Bertier (2016). Methodology for the numerical prediction of soot formation in turbulent reactive flows and application to aircraft engine combustors. *International Journal of Sustainable Aviation 2*, 15. *(p. 126, 132, 216, 222)*

Dworkin, S. B., Q. Zhang, M. J. Thomson, N. A. Slavinskaya, and U. Riedel (2011). Application of an enhanced pah growth model to soot formation in a laminar coflow ethylene/air diffusion flame. *Combustion and Flame 158*(9), 1682 – 1695. *(p. 31)*

EASA (2019). European aviation environmental report. Technical report, European Union Aviation Safety Agency. *(p. 3, 4)*

Eaves, N., S. Dworkin, and M. Thomson (2015). The importance of reversibility in modeling soot nucleation and condensation processes. *Proceedings of the Combustion Institute 35*(2), 1787 – 1794. *(p. 7, 79)*

Eberle, C., P. Gerlinger, K. P. Geigle, and M. Aigner (2015). Numerical investigation of transient soot evolution processes in an aero-engine model combustor. *Combustion Science and Technology 187*(12), 1841–1866. *(p. 97, 127, 139, 140, 141, 142, 144, 216)*

Eberle, C., P. Gerlinger, K. P. Geigle, and M. Aigner (2018). Toward finite-rate chemistry large-eddy simulations of sooting swirl flames. *Combustion Science and Technology 190*(7), 1194–1217. *(p. 114, 127, 132, 216, 217, 222)*

EEA (2020). Transport: increasing oil consumption and greenhouse gas emissions hamper eu progress towards environment and climate objectives. Technical report, European Environment Agency. *(p. 2)*

El-Asrag, H., T. Lu, C. Law, and S. Menon (2007). Simulation of soot formation in turbulent premixed flames. *Combustion and Flame 150*(1), 108 – 126. *(p. 38, 114, 215)*

El-Leathy, A., F. Xu, and G. Faeth (2002). *Soot surface growth and oxidation in laminar unsaturated-hydrocarbon/air diffusion flames. (p. 187)*

Epstein, P. S. (1924, Jun). On the resistance experienced by spheres in their motion through gases. *Phys. Rev. 23*, 710–733. *(p. 19)*

Felden, A., L. Esclapez, E. Riber, B. Cuenot, and H. Wang (2018). Including real fuel chemistry in les of turbulent spray combustion. *Combustion and Flame 193*, 397 – 416. *(p. 102)*

Felden, A., P. Pepiot, L. Esclapez, E. Riber, and B. Cuenot (2019). Including analytically reduced chemistry (arc) in cfd applications. *Acta Astronautica 158*, 444 – 459. *(p. 102)*

Felden, A., E. Riber, and B. Cuenot (2018). Impact of direct integration of analytically reduced chemistry in les of a sooting swirled non-premixed combustor. *Combustion and Flame 191*, 270 – 286. *(p. 35, 128, 132, 186, 193, 196, 201, 215, 216, 222)*

Fiorina, B., R. Vicquelin, P. Auzillon, N. Darabiha, O. Gicquel, and D. Vey-

nante (2010). A filtered tabulated chemistry model for les of premixed combustion. *Combustion and Flame 157*(3), 465 – 475. *(p. 102)*

Floyd, J., A. M. Kempf, A. K. 1, and R. H. Ram (2009). A simple model for the filtered density function for passive scalar combustion les. *Combustion Theory and Modelling 13*(4), 559–588. *(p. 109)*

Franzelli, B., A. Cuoci, A. Stagni, M. Ihme, T. Faravelli, and S. Candel (2017). Numerical investigation of soot-flame-vortex interaction. *Proceedings of the Combustion Institute 36*(1), 753 – 761. *(p. 214)*

Franzelli, B., B. Fiorina, and N. Darabiha (2013). A tabulated chemistry method for spray combustion. *Proceedings of the Combustion Institute 34*(1), 1659 – 1666. *(p. 102)*

Franzelli, B., E. Riber, B. Cuenot, and M. Ihme (2015). Numerical Modeling of Soot Production in Aero Engine Combustors Using Large Eddy Simulations. *Proceedings of ASME Turbo Expo Volume 4B: Combustion, Fuels and Emissions*. *(p. 102, 126, 131, 132, 186, 215, 216, 222)*

Franzelli, B., P. Scouflaire, and S. Candel (2015). Time-resolved spatial patterns and interactions of soot, pah and oh in a turbulent diffusion flame. *Proceedings of the Combustion Institute 35*(2), 1921 – 1929. *(p. 8)*

Franzelli, B., A. Vie, and N. Darabiha (2018). A three-equation model for the prediction of soot emissions in les of gas turbines. *Proceedings of the Combustion Institute*. *(p. 10, 15, 38, 40, 47, 49, 50, 52, 95, 98, 102, 112, 114, 116, 129, 132, 137, 193, 215, 216, 222, 236, 249, 258, 259)*

Frenklach, M. (1996). On surface growth mechanism of soot particles. *Symposium (International) on Combustion 26*(2), 2285 – 2293. *(p. 7, 27, 29)*

Frenklach, M. (2002). Method of moments with interpolative closure. *Chemical Engineering Science 57*(12), 2229 – 2239. Population balance modelling of particulate systems. *(p. 38)*

Frenklach, M. and H. Wang (1991). Detailed modeling of soot particle nucleation and growth. *Symposium (International) on Combustion 23*(1), 1559–1566. *(p. 22, 27, 28, 29, 31, 74, 80)*

Gallen, L. (2020, July). *Prediction of soot particles in Gas Turbine Combustors using Large Eddy Simulation*. Phd thesis, Institut National Polytechnique de Toulouse. *(p. 39, 102, 128)*

Gallen, L., A. Felden, E. Riber, and B. Cuenot (2018). Lagrangian tracking of soot particles in les of gas turbines. *Proceedings of the Combustion Institute*. *(p. 35, 39, 102, 128, 132, 193, 216, 222)*

Galley, D., S. Ducruix, F. Lacas, and D. Veynante (2011). Mixing and sta-

bilization study of a partially premixed swirling flame using laser induced fluorescence. *Combustion and Flame 158*(1), 155 – 171. *(p. 141, 142)*

Geigle, K. P., R. Hadef, and W. Meier (2013). Soot formation and flame characterization of an aero-engine model combustor burning ethylene at elevated pressure. *Journal of Engineering for Gas Turbines and Power 136*(2), 021505–021505–7. *(p. 8, 9, 10, 119, 120, 121, 122, 123, 124, 131, 150, 165, 185, 214, 215, 258)*

Geigle, K. P., R. Hadef, M. Stöhr, and W. Meier (2017). Flow field characterization of pressurized sooting swirl flames and relation to soot distributions. *Proceedings of the Combustion Institute 36*(3), 3917 – 3924. *(p. 9, 10, 119, 120, 121, 122, 123, 124, 139, 140, 141, 144, 150, 172, 173, 175, 176, 209, 214, 215, 216, 217, 258)*

Geigle, K. P., M. Köhler, W. O'Loughlin, and W. Meier (2015). Investigation of soot formation in pressurized swirl flames by laser measurements of temperature, flame structures and soot concentrations. *Proceedings of the Combustion Institute 35*(3), 3373 – 3380. *(p. 9, 10, 119, 120, 121, 122, 124, 177, 178, 181, 187, 195, 196, 202, 205, 215, 218, 258)*

Geigle, K. P., W. O'Loughlin, R. Hadef, and W. Meier (2015). Visualization of soot inception in turbulent pressurized flames by simultaneous measurement of laser-induced fluorescence of polycyclic aromatic hydrocarbons and laser-induced incandescence, and correlation to oh distributions. *Applied Physics B 119*(4), 717 – 730. *(p. 119, 121, 122, 124, 125, 127, 170, 184, 186)*

Gicquel, L., G. Staffelbach, and T. Poinsot (2012). Large eddy simulations of gaseous flames in gas turbine combustion chambers. *Progress in Energy and Combustion Science*. *(p. 97, 150)*

Giusti, A., S. Gkantonas, J. M. Foale, and E. Mastorakos (2018). Numerical Investigation of Flame Structure and Soot Formation in a Lab-Scale Rich-Quench-Lean Burner. *Volume 4B: Combustion, Fuels, and Emissions*. *(p. 146)*

Grader, M., C. Eberle, P. Gerlinger, and M. Aigner (2018). LES of a Pressurized, Sooting Aero-Engine Model Combustor at Different Equivalence Ratios With a Sectional Approach for PAHs and Soot. *Proceedings of ASME Turbo Expo Volume 4A: Combustion, Fuels, and Emissions*. *(p. 128, 132, 186, 216, 217, 222)*

Grader, M., Z. Yin, K. P. Geigle, and P. Gerlinger (2020). Influence of flow field dynamics on soot evolution in an aero-engine model combustor. *Proceedings of the Combustion Institute*. *(p. 215, 216)*

Guiberti, T., D. Durox, P. Scouflaire, and T. Schuller (2015). Impact of heat

loss and hydrogen enrichment on the shape of confined swirling flames. *Proceedings of the Combustion Institute 35*(2), 1385 – 1392. *(p. 184)*

Guo, H., P. M. Anderson, and P. B. Sunderland (2016). Optimized rate expressions for soot oxidation by oh and o2. *Fuel 172*, 248 – 252. *(p. 8)*

H. Yamashita, M. S. and T. Takeno (1996). *A numerical study on flame stability at the transition point of jet diffusion flames.* *(p. 195)*

Harris, S. J. (1990). Surface growth and soot particle reactivity. *Combustion Science and Technology 72*(1-3), 67–77. *(p. 28)*

Helou, I. E., A. W. Skiba, and E. Mastorakos (2020). Experimental investigation of soot production and oxidation in a lab-scale richÐquenchÐlean (rql) burner. *Flow Turbulence Combustion.* *(p. 145, 146, 184)*

Hwang, J. and S. Chung (2001). Growth of soot particles in counterflow diffusion flames of ethylene. *Combustion and Flame 125*(1), 752 – 762. *(p. 8, 28, 60, 62, 70, 73, 74, 75, 76, 77, 78, 79, 80, 81, 82, 90)*

ICAO (2019). Environmental report. Technical report, Organisation de l'aviation civile internationale. *(p. 5)*

IEA (2020). Key world energy statistics. Technical report, International Energy Agency. *(p. 1, 2)*

Ihme, M. and H. Pitsch (2008). Modeling of radiation and nitric oxide formation in turbulent nonpremixed flames using a flamelet/progress variable formulation. *Physics of Fluids 20*(5). *(p. 10, 95, 102, 103, 106, 111, 114, 137, 236, 258)*

IPCC (1999). Ipcc special report: Aviation and the global atmosphere. Technical report, Intergovernmental Panel on Climate Change. *(p. 5)*

Ivanova, E. M., B. E. Noll, and M. Aigne (2012). A Numerical Study on the Turbulent Schmidt Numbers in a Jet in Crossflow. *Journal of Engineering for Gas Turbines and Power 135*(1). 011505. *(p. 144, 150)*

J, H. S. and W. A. M (1985). Chemical kinetics of soot particle growth. *Annual Review of Physical Chemistry 36*(1), 31–52. *(p. 28)*

J., S. R., M. G. W., and G. J. W. (1987). Structural analysis of soot agglomerates. *Langmuir 3*(2), 272–281. *(p. 21)*

Jaegle, F., O. Cabrit, S. Mendez, and T. Poinsot (2010). Implementation methods of wall functions in cell-vertex numerical solvers. *Flow, Turbulence and Combustion 85*(2), 245–272. *(p. 135)*

Jaravel, T., E. Riber, B. Cuenot, and G. Bulat (2017). Large eddy simulation of an industrial gas turbine combustor using reduced chemistry with accurate

pollutant prediction. *Proceedings of the Combustion Institute 36*(3), 3817 – 3825. *(p. 102)*

Jaravel, T., E. Riber, B. Cuenot, and P. Pepiot (2018). Prediction of flame structure and pollutant formation of sandia flame d using large eddy simulation with direct integration of chemical kinetics. *Combustion and Flame 188*, 180 – 198. *(p. 102)*

Joo, P. H., B. Gigone, E. A. Griffin, M. Christensen, and Ã–mer L. GÃ¼lder (2018). Soot primary particle size dependence on combustion pressure in laminar ethylene diffusion flames. *Fuel 220*, 464 – 470. *(p. 209)*

Kartaev, E., V. Emelkin, M. Ktalkherman, S. Aulchenko, and S. Vashenko (2018). Upstream penetration behavior of the developed counter flow jet resulting from multiple jet impingement in the crossflow of cylindrical duct. *International Journal of Heat and Mass Transfer 116*, 1163 – 1178. *(p. 144)*

Kazakov, A. and M. Frenklach (1998). Dynamic modeling of soot particle coagulation and aggregation: Implementation with the method of moments and application to high-pressure laminar premixed flames. *Combustion and Flame 114*(3), 484 – 501. *(p. 26)*

Kee, R. J., J. A. Miller, G. H. Evans, and G. Dixon-Lewis (1989). A computational model of the structure and extinction of strained, opposed flow, premixed methane-air flames. *Symposium (International) on Combustion 22*(1), 1479 – 1494. *(p. 103)*

Kennedy, I. M., W. Kollmann, and J.-Y. Chen (1990). A model for soot formation in a laminar diffusion flame. *Combustion and Flame 81*(1), 73 – 85. *(p. 34, 235)*

Khosousi, A. and S. B. Dworkin (2015). Soot surface reactivity during surface growth and oxidation in laminar diffusion flames. *Combustion and Flame 162*(12), 4523 – 4532. *(p. 28, 74)*

Klein, M. (2005). An attempt to assess the quality of large eddy simulations in the context of implicit filtering. *Flow Turbulence Combustion 75*, 131 – 147. *(p. 167)*

Koo, H., V. Raman, M. E. Mueller, and K. Geigle (2016). *LES of a sooting flame in a pressurized swirl combustor. (p. 127, 215, 216, 222)*

Köylü and G.M. Faeth and T.L. Farias and M.G. Carvalho (1995). Fractal and projected structure properties of soot aggregates. *Combustion and Flame 100*(4), 621 – 633. *(p. 21)*

Kuklinska, K., L. Wolska, and J. Namiesnik (2015). Air quality policy in the u.s. and the eu - a review. *Atmospheric Pollution Research 6*(1), 129 – 137. *(p. 3)*

Lecocq, G., I. Hernandez, D. Poitou, E. Riber, and B. Cuenot (2013). Soot prediction by large-eddy simulation of complex geometry combustion chambers. *Comptes Rendus Mecanique 341*(1), 230 – 237. Combustion, spray and flow dynamics for aerospace propulsion. *(p. 126)*

Lelieveld, J., K. KlingmŸller, A. Pozzer, U. Pöschl, M. Fnais, A. Daiber, and T. MŸnzel (2019, 03). Cardiovascular disease burden from ambient air pollution in Europe reassessed using novel hazard ratio functions. *European Heart Journal 40*(20), 1590–1596. *(p. 2)*

Leschowski, M., K. A.Thomson, D. R. Snelling, C. Schulz, and G. J.Smallwood (2015). Frequency response of counter flow diffusion flames to strain rate harmonic oscillations. *Applied Physics B 119*(4), 685–696. *(p. 8)*

Leung, K., R. Lindstedt, and W. Jones (1991). A simplified reaction mechanism for soot formation in nonpremixed flames. *Combustion and Flame 87*(3), 289 – 305. *(p. 35, 39, 126, 128, 133)*

Liati, A., B. T. Brem, L. Durdina, M. Vögtli, Y. Arroyo Rojas Dasilva, P. Dimopoulos Eggenschwiler, and J. Wang (2014). Electron microscopic study of soot particulate matter emissions from aircraft turbine engines. *Environmental Science & Technology 48*(18), 10975–10983. *(p. 6, 20, 21)*

Lien, F., H. Liu, E. Chui, and C. McCartney (2009). Development of an analytical β-function pdf integration algorithm for simulation of non-premixed turbulent combustion. *Flow Turbulence and Combustion 83*(2), 205–226. *(p. 107, 137)*

Lignell, D. O., J. H. Chen, and P. J. Smith (2008). Three-dimensional direct numerical simulation of soot formation and transport in a temporally evolving nonpremixed ethylene jet flame. *Combustion and Flame 155*(1), 316 – 333. *(p. 234)*

Lignell, D. O., J. H. Chen, P. J. Smith, T. Lu, and C. K. Law (2007). The effect of flame structure on soot formation and transport in turbulent nonpremixed flames using direct numerical simulation. *Combustion and Flame 151*(1), 2 – 28. *(p. 97, 233, 234)*

Lindstedt, P. R. (1994). *Simplified Soot Nucleation and Surface Growth Steps for Non-Premixed Flames*. Berlin, Heidelberg: Springer Berlin Heidelberg. *(p. 35, 74, 113, 235)*

Lindstedt, R. and S. Louloudi (2005). Joint-scalar transported pdf modeling of soot formation and oxidation. *Proceedings of the Combustion Institute 30*(1), 775 – 783. *(p. 35, 113, 215)*

Lowe, J. S., J. Y. Lai, P. Elvati, and A. Violi (2015). Towards a predictive model for polycyclic aromatic hydrocarbon dimerization propensity. *Proceedings of the Combustion Institute 35*(2), 1827 – 1832. *(p. 7)*

Lu, T. and C. K. Law (2005a). A directed relation graph method for mechanism reduction. *Proceedings of the Combustion Institute 30*(1), 1333 – 1341. *(p. 102)*

Lu, T. and C. K. Law (2005b). A directed relation graph method for mechanism reduction. *Proceedings of the Combustion Institute 30*(1), 1333 – 1341. *(p. 114)*

Lucchesi, M., A. Abdelgadir, A. Attili, and F. Bisetti (2017). Simulation and analysis of the soot particle size distribution in a turbulent nonpremixed flame. *Combustion and Flame 178*, 35 – 45. *(p. 50, 255)*

Marchal, C. (2008). *Soot formation and oxidation modelling in an automotive engine*. Phd thesis, Université d'Orléans. *(p. 7, 27)*

Marchisio, D. L. and R. O. Fox (2005). Solution of population balance equations using the direct quadrature method of moments. *Journal of Aerosol Science 36*(1), 43 – 73. *(p. 38)*

Marchisio, D. L., J. T. Pikturna, R. O. Fox, R. D. Vigil, and A. A. Barresi (2003). Quadrature method of moments for population-balance equations. *AIChE Journal 49*(5), 1266–1276. *(p. 38)*

Masri, A. (2015). Partial premixing and stratification in turbulent flames. *Proceedings of the Combustion Institute 35*(2), 1115 – 1136. *(p. 123, 143, 195, 197)*

Mauss, F., K. Netzell, and H. Lehtiniemi (2006). Aspects of modeling soot formation in turbulent diffusion flames. *Combustion Science and Technology 178*(10-11), 1871–1885. *(p. 28, 29)*

Mauss, F., T. Schäfer, and H. Bockhorn (1994). Inception and growth of soot particles in dependence on the surrounding gas phase. *Combustion and Flame 99*(3), 697 – 705. 25th Symposium (International) on Combustion Papers. *(p. 29, 31, 32, 75, 80)*

Meier, W., I. Boxx, and M. Stohr (2010). Laser-based investigations in gas turbine model combustors. *Experiments Fluids 49*, 865 – 882. *(p. 197)*

Mercier, R., V. Moureau, D. Veynante, and B. Fiorina (2015). Les of turbulent combustion: On the consistency between flame and flow filter scales. *Proceedings of the Combustion Institute 35*(2), 1359 – 1366. *(p. 102)*

Meyers, J., B. J. Geurts, and M. Baelmans (2003). Database analysis of errors in large-eddy simulation. *Physics of Fluids 15*(9), 2740–2755. *(p. 174)*

Michael, F. (2002). Reaction mechanism of soot formation in flames. *Phys. Chem. Chem. Phys. 4*, 2028–2037. *(p. 19, 31, 74, 80, 114)*

Michelsen, H. (2017). Probing soot formation, chemical and physical evolution, and oxidation: A review of in situ diagnostic techniques and needs. *Proceedings of the Combustion Institute 36*(1), 717 – 735. *(p. 6, 8)*

Migliorini, F., K. A.Thomson, and G. J. Smallwood (2011). Investigation of optical properties of aging soot. *Applied Physics B 104*(2), 273–283. *(p. 8)*

Miller, J. A. and C. F. Melius (1992). Kinetic and thermodynamic issues in the formation of aromatic compounds in flames of aliphatic fuels. *Combustion and Flame 91*(1), 21 – 39. *(p. 79)*

Modest, M. F. (1991). *Radiatif Heat Transfer* (Third Edition ed.). Boston: Academic Press. *(p. 137)*

Moin, P., K. Squires, W. Cabot, and S. Lee (1991). A dynamic subgrid-scale model for compressible turbulence and scalar transport. *Physics of Fluids A: Fluid Dynamics 3*(11), 2746–2757. *(p. 133)*

Monclard, K. T., O. Gicquel, and R. Vicquelin (2020, 06). Impact of Soot Radiative Properties, Pressure and Soot Volume Fraction on Radiative Heat Transfer in Turbulent Sooty Flames. In *Proceedings of the ASME Turbo Expo 2020: Turbomachinery Technical Conference and Exposition*. *(p. 204, 222)*

Moss, J., C. Stewart, and K. Syed (1989). Flowfield modelling of soot formation at elevated pressure. *Symposium (International) on Combustion 22*(1), 413 – 423. *(p. 35)*

Moureau, V., P. Domingo, and L. Vervisch (2011). From large-eddy simulation to direct numerical simulation of a lean premixed swirl flame: Filtered laminar flame-pdf modeling. *Combustion and Flame 158*(7), 1340 – 1357. *(p. 233, 245, 255)*

Mueller, M., G. Blanquart, and H. Pitsch (2009). Hybrid method of moments for modeling soot formation and growth. *Combustion and Flame 156*(6), 1143 – 1155. *(p. 19, 23, 30, 38, 47, 49, 95, 102, 114, 115, 133, 234)*

Mueller, M. E. and H. Pitsch (2011). Large eddy simulation subfilter modeling of soot-turbulence interactions. *Physics of Fluids 23*(11), 115104. *(p. 10, 95, 114, 115, 116, 128, 137, 213, 214, 215, 221, 223, 233, 234, 235, 243, 247, 248, 249, 250, 251, 252, 253, 255, 256, 259)*

Mueller, M. E. and H. Pitsch (2012). Les model for sooting turbulent nonpremixed flames. *Combustion and Flame 159*(6), 2166 – 2180. *(p. 38, 79, 102, 109, 110, 111, 114, 115, 150, 215, 236)*

Mueller, M. E. and H. Pitsch (2013). Large eddy simulation of soot evolution in an aircraft combustor. *Physics of Fluids 25*(11), 110812. *(p. 7, 38, 97, 102, 114, 194, 210, 215)*

Narayanan, P. and A.Trouvé (2009). Radiation-driven flame weakening effects in sooting turbulent diffusion flames. *Proceedings of the Combustion Institute 32*(1), 1481 – 1489. *(p. 237)*

Narayanaswamy, K., H. Pitsch, and P. Pepiot (2015). A chemical mechanism for low to high temperature oxidation of methylcyclohexane as a component of transportation fuel surrogates. *Combustion and Flame 162*(4), 1193 – 1213. *(p. 7, 23, 133)*

Nau, P., Z. Yin, K. P. Geigle, and W. Meier (2017). Wall temperature measurements at elevated pressures and high temperatures in sooting flames in a gas turbine model combustor. *Applied Physics B 123*(12). *(p. 9, 121, 122, 135)*

Neoh, K. G., J. B. Howard, and A. F. Sarofim (1981). *Soot Oxidation in Flames*, pp. 261–282. Boston, MA: Springer US. *(p. 28, 29)*

Netzell, K., H. Lehtiniemi, and F. Mauss (2007). Calculating the soot particle size distribution function in turbulent diffusion flames using a sectional method. *Proceedings of the Combustion Institute 31*(1), 667 – 674. *(p. 30, 37, 42, 50, 97)*

Nguyen, T., F. Laurent, R. Fox, and M. Massot (2016). Solution of population balance equations in applications with fine particles: Mathematical modeling and numerical schemes. *Journal of Computational Physics 325*, 129 – 156. *(p. 38)*

Nicoud, F. and F. Ducros (1999). Subgrid-scale stress modelling based on the square of the velocity gradient tensor. *Flow, Turbulence and Combustion 62*(3), 183–200. *(p. 133)*

Nicoud, F., H. B. Toda, O. Cabrit, S. Bose, and J. Lee (2011). Using singular values to build a subgrid-scale model for large eddy simulations. *Physics of Fluids 23*(8), 085106. *(p. 101, 133, 138)*

Okyay, G. (2016). *Impact of the morphology of soot aggregates on their radiative properties and the subsequent radiative heat transfer through sooty gaseous mixtures*. Phd thesis, Université Paris-Saclay. *(p. 6, 20, 21)*

Ong, J. C., K. M. Pang, J. H. Walther, J.-H. Ho, and H. K. Ng (2018). Evaluation of a lagrangian soot tracking method for the prediction of primary soot particle size under engine-like conditions. *Journal of Aerosol Science 115*, 70 – 95. *(p. 39)*

Paccati, S., D. Bertini, L. Mazzei, S. Puggelli, and A. Andreini (2020). Large-eddy simulation of a model aero-engine sooting flame with a multiphysics approach. *Flow Turbulence Combustion*. *(p. 129, 131, 133)*

Passot, T. and A. Pouquet (1987). Numerical simulation of compressible homogeneous flows in the turbulent regime. *Journal of Fluid Mechanics 181*, 441Ð466. *(p. 238)*

Pepiot-Desjardins, P. and H. Pitsch (2008). An efficient error-propagation-based reduction method for large chemical kinetic mechanisms. *Combustion and Flame 154*(1), 67 – 81. *(p. 102)*

Peters, N. (2000). *Turbulent Combustion*. Cambridge University Press. *(p. 97)*

Pierce, C. D. and P. Moin (2004). Progress-variable approach for large-eddy simulation of non-premixed turbulent combustion. *Journal of Fluid Mechanics 504*, 73Ð97. *(p. 103, 104, 105)*

Pitsch, H. (2000). Unsteady flamelet modeling of differential diffusion in turbulent jet diffusion flames. *Combustion and Flame 123*(3), 358 – 374. *(p. 112)*

Pitsch, H. (2006). Large-eddy simulation of turbulent combustion. *Annual Review of Fluid Mechanics 38*(1), 453–482. *(p. 97)*

Pitsch, H., M. Chen, and N. Peters (1998). Unsteady flamelet modeling of turbulent hydrogen-air diffusion flames. *Symposium (International) on Combustion 27*(1), 1057 – 1064. Twenty-Seventh Sysposium (International) on Combustion Volume One. *(p. 237)*

Pitsch, H. and L. Duchamp de Lageneste (2002). Large-eddy simulation of premixed turbulent combustion using a level-set approach. *Proceedings of the Combustion Institute 29*(2), 2001 – 2008. *(p. 167)*

Poinsot, P. and D. Veynante (2005). *Theoretical and Numerical Combustion*. Edwards, 2nd Edition. *(p. 16, 97, 98, 99, 101, 109)*

Poinsot, T. and S. Lele (1992). Boundary conditions for direct simulations of compressible viscous flows. *Journal of Computational Physics 101(1)*, 104–129. *(p. 135, 238)*

Pope, S. B. (2000). *Turbulent Flows*. Cambridge University Press. *(p. 96, 98, 245, 246)*

Pope, S. B. (2004). Ten questions concerning the large-eddy simulation of turbulent flows. *New Journal of Physics 6*, 35–35. *(p. 150, 167, 191)*

Proch, F., P. Domingo, L. Vervisch, and A. M. Kempf (2017). Flame resolved simulation of a turbulent premixed bluff-body burner experiment. part i: Analysis of the reaction zone dynamics with tabulated chemistry. *Combustion and Flame 180*, 321 – 339. *(p. 233, 255)*

Reveillon, J. and L. Vervisch (2005). Analysis of weakly turbulent dilute-spray flames and spray combustion regimes. *Journal of Fluid Mechanics 537*, 317Ð347. *(p. 195)*

Richter, H., S. Granata, W. H. Green, and J. B. Howard (2005). Detailed modeling of pah and soot formation in a laminar premixed benzene/oxygen/argon low-pressure flame. *Proceedings of the Combustion Institute 30*(1), 1397 – 1405. *(p. 36)*

Richter, H. and J. Howard (2000). Formation of polycyclic aromatic hydrocarbons and their growth to soot - a review of chemical reaction pathways. *Progress in Energy and Combustion Science 26*(4), 565 – 608. *(p. 7)*

Rigopoulos, S. (2019). Modelling of soot aerosol dynamics in turbulent flow. *Flow, Turbulence and Combustion 103*(3), 565–604. *(p. 34)*

Rodrigues, P. (2018, June). *Multi-physics modelling of turbulent sooting flames including thermal radiation and wall heat transfer*. Phd thesis, Université Paris-Saclay. *(p. 22, 23, 27, 40, 47, 54, 103, 104, 105, 107, 110, 128, 129, 132, 135, 136, 138, 180, 184, 204, 216, 217, 222)*

Rodrigues, P., B. Franzelli, R. Vicquelin, O. Gicquel, and N. Darabiha (2017). Unsteady dynamics of pah and soot particles in laminar counterflow diffusion flames. *Proceedings of the Combustion Institute 36*(1), 927 – 934. *(p. 7, 8, 10, 15, 28, 29, 30, 37, 40, 42, 43, 47, 50, 60, 63, 65, 73, 75, 77, 81, 230, 235, 258)*

Rodrigues, P., B. Franzelli, R. Vicquelin, O. Gicquel, and N. Darabiha (2018). Coupling an les approach and a soot sectional model for the study of sooting turbulent non-premixed flames. *Combustion and Flame 190*, 477 – 499. *(p. 7, 37, 38, 40, 50, 52, 79, 95, 97, 102, 111, 112, 114, 115, 128, 129, 150, 194, 215)*

Saggese, C., S. Ferrario, J. Camacho, A. Cuoci, A. Frassoldati, E. Ranzi, H. Wang, and T. Faravelli (2015). Kinetic modeling of particle size distribution of soot in a premixed burner-stabilized stagnation ethylene flame. *Combustion and Flame 162*(9), 3356 – 3369. *(p. 36, 55, 56)*

Salenbauch, S., A. Cuoci, A. Frassoldati, C. Saggese, T. Faravelli, and C. Hasse (2015). Modeling soot formation in premixed flames using an extended conditional quadrature method of moments. *Combustion and Flame 162*(6), 2529 – 2543. *(p. 38, 47)*

Saxon, A. and D. Diaz-Sanchez (2005). Air pollution and allergy: you are what you breathe. *Nature Immunology*, 223–226. *(p. 4)*

Schluter, J. and T. Schonfeld (2000). Les of jets in cross flow and its application to a gas turbine burner. *Flow, Turbulence and Combustion 177*(65). *(p. 144, 150)*

Schonfeld, T. and M. Rudgyard (1999). Steady and unsteady flow simulations using the hybrid flow solver avbp. *AIAA Journal 37*, 1378 – 1385. *(p. 99, 138, 237)*

Schuetz, C. A. and M. Frenklach (2002). Nucleation of soot: Molecular dynamics simulations of pyrene dimerization. *Proceedings of the Combustion Institute 29*(2), 2307 – 2314. *(p. 7, 22)*

Shaddix, C. R., J. Zhang, R. W. Schefer, J. Doom, J. C. Oefelein, S. Kook, L. M. Pickett, and H. Wang (2010). Understanding and predicting soot generation in turbulent non-premixed jet flames. *Sandia Report*. *(p. 150)*

Singh, J., M. Balthasar, M. Kraft, and W. Wagner (2005). Stochastic modeling of soot particle size and age distributions in laminar premixed flames. *Proceedings of the Combustion Institute 30*(1), 1457 – 1465. *(p. 31, 36, 74)*

Slavinskaya, N. A., U. Riedel, S. B. Dworkin, and M. J. Thomson (2012). Detailed numerical modeling of pah formation and growth in non-premixed ethylene and ethane flames. *Combustion and Flame 159*(3), 979 – 995. *(p. 7, 23, 80, 133)*

Smoluchowski, M. (1916). Versuch einer mathematischen theorie der koagulationskinetik kolloider lšsungen. *(p. 25)*

Smyth, K. C. and C. R. Shaddix (1996). The elusive history of m = 1.57-0.56i for the refractive index of soot. *Combustion and Flame 107*(3), 314 – 320. *(p. 110, 137)*

Stohr, M., C. Arndt, and W. Meier (2015). Transient effects of fuel-air mixing in a partially-premixed turbulent swirl flame. *Proceedings of the Combustion Institute 35*(3), 3327 – 3335. *(p. 140, 143)*

Stohr, M., I. Boxx, C. D. Carter, and W. Meier (2012). Experimental study of vortex-flame interaction in a gas turbine model combustor. *Combustion and Flame 159*(8), 2636 – 2649. Special Issue on Turbulent Combustion. *(p. 141, 142)*

Stohr, M., K. Geigle, R. Hadef, I. Boxx, C. Carter, M. Grader, and P. Gerlinger (2018). Time-resolved study of transient soot formation in an aero-engine model combustor at elevated pressure. *Proceedings of the Combustion Institute*. *(p. 97, 123, 139, 140, 141, 142, 144, 149, 152, 196, 198, 201, 214, 215, 216, 217)*

Stopper, U., W. Meier, R. Sadanandan, M. Stohr, M. Aigner, and G. Bulat (2013). Experimental study of industrial gas turbine flames including quantification of pressure influence on flow field, fuel/air premixing and flame shape. *Combustion and Flame 160*(10), 2103 – 2118. *(p. 197)*

Syred, N., W. Fock, T. O'doherty, and A. J. Griffiths (1997). The effect of the precessing vortex core on combustion in a swirl burner. *Combustion Science and Technology 125*(1-6), 139–157. *(p. 123, 141)*

Tardelli, L. P., B. Franzelli, P. Rodrigues, and N. Darabiha (2019). Impact

of the Reaction Mechanism Model on Soot Growth and Oxidation in Laminar and Turbulent Flames. *Proceedings of ASME Turbo Expo Volume 4A: Combustion, Fuels, and Emissions*. *(p. 137, 215, 236)*

Thong, C. X., P. A. M. Palt, and B. B. Dally (2005). Flow dynamics of multilateral jets injection into a round pipe flow. *Experiments in Fluids 15*(56). *(p. 144)*

Tracey, T. E., J. A. Sidey, and E. Mastorakos (2018). A lab-scale rich-quench-lean (rql) combustor for stability and soot investigations. *(p. 145)*

Vervisch, L., P. Domingo, G. Lodato, and D. Veynante (2010). Scalar energy fluctuations in large-eddy simulation of turbulent flames: Statistical budgets and mesh quality criterion. *Combustion and Flame 157*(4), 778 – 789. *(p. 167, 174)*

Veshkini, A., S. B. Dworkin, and M. J. Thomson (2014). A soot particle surface reactivity model applied to a wide range of laminar ethylene/air flames. *Combustion and Flame 161*(12), 3191 – 3200. *(p. 7, 8, 31, 74)*

Veshkini, A., N. A. Eaves, S. B. Dworkin, and M. J. Thomson (2016). Application of pah-condensation reversibility in modeling soot growth in laminar premixed and nonpremixed flames. *Combustion and Flame 167*, 335 – 352. *(p. 7, 79, 87)*

Vicquelin, R. (2010, June). *Tabulated chemistry for turbulent combustion modeling and simulation*. Phd thesis, Ecole Centrale Paris. *(p. 109)*

Violi, A. (2004). Modeling of soot particle inception in aromatic and aliphatic premixed flames. *Combustion and Flame 139*(4), 279 – 287. *(p. 7)*

Vreman, A. W. (2004). An eddy-viscosity subgrid-scale model for turbulent shear flow: Algebraic theory and applications. *Physics of Fluids 16*(10), 3670–3681. *(p. 133)*

Vreman, B., B. Geurts, and H. Kuerten (1996). Comparison of numerical schemes in large-eddy simulation of the temporal mixing layer. *International journal for numerical methods in fluids 22*(4), 297–312. *(p. 174, 255)*

Wang, H. (2011). Formation of nascent soot and other condensed-phase materials in flames. *Proceedings of the Combustion Institute 33*(1), 41 – 67. *(p. 7, 8, 23)*

Wang, H., D. Du, C. Sung, and C. Law (1996). Experiments and numerical simulation on soot formation in opposed-jet ethylene diffusion flames. *Symposium (International) on Combustion 26*(2), 2359 – 2368. *(p. 28)*

Wang, H. and A. Laskin (1988). A comprehensive kinetic model of ethylene and acetylene oxidation at high temperatures. Technical report, Progress Report for an AFOSR New World Vista Program. *(p. 133)*

Wang, H. and A. Laskin (1998). A comprehensice kinetic model of ethylene and acetylene oxidation at high temperatures. *Internal Report of the Department of Mechanical and Aerospace Engineering Princeton University*. *(p. 133)*

Wang, Y. and S. H. Chung (2016). Strain rate effect on sooting characteristics in laminar counterflow diffusion flames. *Combustion and Flame*. *(p. 8, 66, 67, 68, 69, 85, 86)*

Wang, Y., A. Raj, and S. H. Chung (2015). Soot modeling of counterflow diffusion flames of ethylene-based binary mixture fuels. *Combustion and Flame 162*(3), 586 – 596. *(p. 22, 235)*

Wang, Y., A. D. Raj, and S.-H. Chung (2013). A pah growth mechanism and synergistic effect on pah formation in counterflow diffusion flames. *Combustion and Flame*. *(p. 7, 23, 24, 55, 75, 79, 80, 81, 102, 103, 111, 133, 137, 236, 258)*

Welch, P. (1967). The use of fast fourier transform for the estimation of power spectra: A method based on time averaging over short, modified periodograms. *IEEE Transactions on Audio and Electroacoustics 15*(2), 70–73. *(p. 142)*

Wick, A., F. Priesack, and H. Pitsch (2017). Large-Eddy Simulation and Detailed Modeling of Soot Evolution in a Model Aero Engine Combustor. *Proceedings of ASME Turbo Expo Volume 4A: Combustion, Fuels and Emissions*. *(p. 126, 132, 201, 216, 222)*

Xu, F., A. El-Leathy, C. Kim, and G. Faeth (2003). Soot surface oxidation in hydrocarbon/air diffusion flames at atmospheric pressure. *Combustion and Flame 132*(1), 43 – 57. *(p. 6, 20, 21, 28, 29, 187)*

Xu, L., F. Yan, M. Zhou, Y. Wang, and S. H. Chung (2018). Experimental and soot modeling studies of ethylene counterflow diffusion flames: Non-monotonic influence of the oxidizer composition on soot formation. *Combustion and Flame 197*, 304 – 318. *(p. 74, 235)*

Xuan, Y. and G. Blanquart (2014). A flamelet based a priori analysis on the chemistry tabulation of polycyclic aromatic hydrocarbons in non-premixed flames. *Combustion and Flame 161*(6), 1516 – 1525. *(p. 79)*

Xuan, Y. and G. Blanquart (2015). Effects of aromatic chemistry turbulence interactions on soot formation in a turbulent non-premixed flame. *Proceedings of the Combustion Institute 35*(2), 1911 – 1919. *(p. 55, 79)*

Yan, F., M. Zhou, L. Xu, Y. Wang, and S. H. Chung (2019). An experimental study on the spectral dependence of light extinction in sooting ethylene counterflow diffusion flames. *Experimental Thermal and Fluid Science 100*, 259 – 270. *(p. 8, 61)*

Yang, S., J. K. Lew, and M. E. Mueller (2019). Large eddy simulation of soot evolution in turbulent reacting flows: Presumed subfilter pdf model for soot-turbulence-chemistry interactions. *Combustion and Flame 209*, 200 – 213. *(p. 39, 114, 255, 256)*

Yapp, E. K., D. Chen, J. Akroyd, S. Mosbach, M. Kraft, J. Camacho, and H. Wang (2015). Numerical simulation and parametric sensitivity study of particle size distributions in a burner-stabilised stagnation flame. *Combustion and Flame 162*(6), 2569 – 2581. *(p. 7, 19)*

Yoda, M. and H. E. Fiedler (1996). The round jet in a uniform counterflow: flow visualization and mean concentration measurements. *Experiments in Fluids* (21). *(p. 144)*

Yoo, C. and H. G. Im (2007). Transient soot dynamics in turbulent non-premixed ethylene-air counterflow flames. *Proceedings of the Combustion Institute 31*(1), 701 – 708. *(p. 234, 235, 243)*

Young, K. J. and J. B. Moss (1995). Modelling sooting turbulent jet flames using an extended flamelet technique. *Combustion Science and Technology 105*(1-3), 33–53. *(p. 113)*

Yuan, L. L., R. L. Street, and J. H. Ferziger (1999). Large eddy simulations of a round jet in crossflow. *Journal of Fluid Mechanics 379*, 71–104. *(p. 144, 150)*

Zerbs, J., K. P. Geigle, O. Lammel, J. Hader, R. Stirn, R. Hadef, and W. W. Meier (2009). The influence of wavelength in extinction measurements and beam steering in laser-induced incandescence measurements in sooting flames. *Applied Physics B 96*(4), 683–694. *(p. 8)*

Zhang, Q., H. Guo, F. Liu, G. Smallwood, and M. Thomson (2009). Modeling of soot aggregate formation and size distribution in a laminar ethylene/air coflow diffusion flame with detailed pah chemistry and an advanced sectional aerosol dynamics model. *Proceedings of the Combustion Institute 32*(1), 761 – 768. *(p. 19, 37)*

Zhao, B., Z. Yang, M. V. Johnston, H. Wang, A. S. Wexler, M. Balthasar, and M. Kraft (2003). Measurement and numerical simulation of soot particle size distribution functions in a laminar premixed ethylene-oxygen-argon flame. *Combustion and Flame 133*(1), 173 – 188. *(p. 50)*

université PARIS-SACLAY
ECOLE DOCTORALE
Sciences mécaniques et énergétiques, matériaux et géosciences (SMEMAG)

Titre: Étude de la stratégie LES pour la prédiction de la production des suies dans une chambre de combustion de type aéronautique.

Mots clés: combustion, suies, turbulence, LES, modlisation, sous-maille

Résumé: La prédiction de la production des suies à l'aide de la Simulation aux Grandes Echelles (SGE) représente un défi scientifique pour plusieurs raisons. La modélisation des processus physico-chimiques impliqués dans la production de ces particules fait encore défaut. Ensuite, dans les dispositifs présentant un intérêt pratique, des régimes de combustion multiples coexistent, ce qui présente une difficulté supplémentaire à la modélisation de tels phénomènes. De plus, les particules de suies sont confinées dans des structures soumises au transport turbulent. En raison de leur taille, un modèle de sous-maille est nécessaire. Pour finir, la validation de nouveaux modèles est difficile lorsqu'on considère ce type de flamme en raison du couplage non-linéaire entre les différents phénomènes et du besoin d'importantes ressources de calcul pour obtenir une représentation statistique fiable. L'objectif principal de cette thèse, réalisée dans le cadre du projet Européen SOPRANO, est d'évaluer la fiabilité du formalisme SGE pour la prédiction des suies dans une configuration de type aéronautique (le brûleur DLR). Initialement, un modèle amélioré du mécanisme réactionnelle pour des particules de suie est proposé, permettant une bonne prédiction de la fraction volumique dans les flammes laminaires prémélangées et non-prémélangées, ce qui est essentiel pour les configurations turbulentes à multi-régimes comme la configuration étudié. Ensuite, une simulation SGE de la production des suies dans le brûleur DLR est réalisé avec une chimie tabulée et un modèle de suies à trois équation. Une analyse statistique révèle que les évènements gazeux favorables à la production de suies sont rares résultant dans une forte intermittence. Par conséquent, atteindre la convergence statistique de ce phénomène demande un temps physique très long. Ainsi, une nouvelle stratégie pour évaluer la réponse des modèles de suie prenant en compte son caractère intermittent dans les flammes turbulentes est proposé. Basée sur une LES unique où l'ensemble d'équations décrivant les suies est dupliqué (un ensemble représente le modèle de référence et l'autre le modèle à évaluer) cela permet aux deux ensembles d'interagir avec la même évolution temporelle et spatiale de la phase gazeuse et ainsi d'évaluer la réponse des modèles au même évènement rare sans atteindre la convergence statistique. Grâce à cette approche, les premières indications de la contribution du modèle d'intermittence de sous-maille pour la phase solide à la prédiction des suies dans le brûleur DLR sont proposées.

Title: Investigating the LES strategy for the prediction of soot production in an aero-engine combustor.

Keywords: combustion, soot, turbulence, LES, modeling, subgrid-scale

Abstract: Predicting soot production in industrial systems using a Large Eddy Simulation (LES) approach represents a great challenge for many reasons. First, in-depth knowledge and modeling of the complex physico-chemical processes involved in soot production are still lacking. Second, multiple combustion regimes coexist in technical devices, presenting an additional difficulty for high fidelity simulations. Third, soot particles are confined in very thin structures interacting with turbulence. Because of their size, these structures may not be resolved on the LES grids, so specific soot subgrid-scale models are required. Finally, the validation of newly developed models is difficult due to the non-linear interactions between such multi-physical phenomena and the massive computational resources required for a reliable statistical representation. In the framework of the SOPRANO European Project this thesis aims to investigate the reliability of the LES formalism for the prediction of soot production in an aero-engine model combustor, the DLR burner. First, an improved soot model with a new soot surface reaction mechanism is proposed, enabling the reproduction of the experimental soot yield in laminar premixed and non-premixed flames, which is essential for multi-regime turbulent configurations as the DLR burner. Then the reliability of the LES formalism, based on a tabulated chemical model and a three-equation soot model, is evaluated through statistical analysis. This analysis reveals that soot occurrence is rare as it requires specific flow conditions rarely observed in the studied configuration. Therefore, numerical convergence is quite challenging to be achieved when considering soot production. Since unaffordable CPU cost is required for a reliable soot prediction, a new strategy based on a unique LES transporting a duplicated set of soot equations is proposed to rigorously investigate soot models in turbulent flames. One set accounts for the soot reference model, while the other is treated with the model under the scope. Therefore, both sets experience the same unique temporal and spatial gas phase evolution allowing the analysis of the instantaneous model response to rare gaseous events leading to soot production without attaining convergence. Thanks to this approach, the first indications of the soot intermittency model contribution to soot prediction in the DLR burner are proposed.

Université Paris-Saclay
Espace Technologique / Immeuble Discovery
Route de l'Orme aux Merisiers RD 128 / 91190 Saint-Aubin, France